UNIVERSITY OF TRENTO

DEPARTMENT OF PHYSICS

PH.D. THESIS IN PHYSICS

The longitudinal control for the Advanced Virgo Plus gravitational wave detector

Supervisor:
Prof. Antonio Perreca
Cosupervisor:
Dr. Maddalena Mantovani

Candidate:
Michele Valentini
XXXIV Cycle
January 2023

Contents

1 Detecting Gravitational Waves with ground-based interferometers **3**
1.1 Gravitational waves and their detection 3
1.2 Sources of gravitational waves and observations 5
1.2.1 Sensitivity of the detectors for CBC signals 6
1.3 The interferometers and their optical response 7
1.3.1 Michelson interferometer response 7
1.3.2 Fabry-Perot cavities 14
1.3.3 Recycling cavities 19
1.3.4 Putting everything together in a real interferometer 21
1.4 The LIGO-Virgo-KAGRA collaboration 24
1.4.1 A brief history of ground-based GW detectors 25
1.4.2 The detector network and the Observing runs 26
1.4.3 Current status and future prospects 27

2 Controlling a GW interferometer **31**
2.1 Keeping an optical resonator locked 32
2.1.1 Sensing the detuning of optical cavities 32
2.1.2 Double (“2f”) and triple (“3f”) demodulations 36
2.2 Controlling Linear Time-Invariant systems 37
2.3 Advanced Virgo Plus Sensing and Control 44
2.3.1 The AdV+ Optical scheme 45
2.3.2 Longitudinal DOFs 48
2.3.3 Control sidebands 50
2.4 Conclusions: 50

3 Locking the detector **51**
3.1 AdV+ lock acquisition procedure overview 52
3.1.1 Main steps 53
3.1.2 Starting conditions 54
3.2 Arm cavities lock and the Auxiliary Laser System 55
3.2.1 Independent arm cavity lock 56
3.2.2 The auxiliary laser system 56
3.2.3 Arms lock with the ALS 60
3.3 Lock of the Central Interferometer 62
3.3.1 Alignment of the CITF mirrors 63
3.3.2 Trigger logic and engagement of the CITF lock 65
3.4 CARM offset reduction and final working point 67
3.4.1 Main obstacles in reducing the CARM offset 69

3.4.2 Reaching Low-Noise operation 75
3.5 Conclusions 78

4 Steady-state longitudinal control of Advanced Virgo Plus 81
4.0.1 Chapter Summary 81
4.1 AdV+ configuration highlights and its Finesse representation 82
4.1.1 Simulation model simplifications and limitations 83
4.2 Accuracy requirements 84
4.2.1 DARM and MICH 85
4.2.2 PRCL 85
4.2.3 CARM and frequency stabilization loop 85
4.2.4 SRCL 87
4.2.5 Accuracy requirements results: 88
4.3 LSC residual noise projections 88
4.3.1 Methodology 89
4.3.2 Resulting projections and further studies 93
4.4 Optimal error signals for the O4 run 95
4.4.1 Control side-bands, ports, and available error signals 96
4.4.2 Study overview 97
4.4.3 Sensing matrices 99
4.5 Conclusions and commissioning results 102
4.5.1 Commissioning results 102

5 An alternative lock acquisition procedure: *"Twin Variable Finesse"* 105
5.1 The *Twin Variable Finesse* lock acquisition 106
5.1.1 Independent arm lock 106
5.1.2 Small Michelson lock 106
5.1.3 Arm control basis change 106
5.1.4 Lock of the PR cavity 107
5.1.5 MICH offset reduction and dark fringe 109
5.1.6 Lock of SRCL 109
5.1.7 DC readout and low-noise operation 110
5.2 Validation of the “twin variable finesse” lock acquisition 110
5.2.1 Study overview 112
5.2.2 Extent of the simulated misalignment 113
5.2.3 Sideband recycling 115
5.2.4 Optical gains 116
5.2.5 Demodulation phases and cross-couplings 118
5.2.6 Impact on the DARM transfer function 120
5.3 Limits of the simulations 121
5.3.1 Ideal interferometer 121
5.3.2 Misalignment range 122
5.4 Conclusions 122

6 Conclusions 125
Acknowledgements 127

A Effects of misalignments on the CITF longitudinal error signals 129
A.1 Simulation details and limits . . . 129
A.1.1 Optimally matched interferometer . . . 130
A.1.2 Base simulation of misaligned interferometer and convergence check 130
A.1.3 Simulation of the longitudinal DOFs sweeps . . . 132
A.1.4 Optimization and study of the error signals . . . 133
A.2 Results . . . 134
A.2.1 Optical Gain variation . . . 134
A.2.2 Error signal shapes and zero-crossing . . . 135
A.2.3 Optimal demodulation phase variations . . . 143
A.2.4 Cross couplings . . . 146

B Detailed study of LSC error signals 153
B.1 DARM: B1p 56 MHz . . . 153
B.2 CARM and SSFS: B2 6 MHz (I) . . . 157
B.3 MICH: B2 56 MHz (Q) . . . 161
B.4 PRCL: B2 8 MHz . . . 165
B.5 SRCL: B2 56 MHz (I) . . . 167

Acronyms 171

Bibliography 175

Abstract

Ground-based gravitational wave detectors are evolving at a rapid pace. In the five years that followed the first direct detection of gravitational waves, the Advanced LIGO and Advanced Virgo experiments have been subject to substantial upgrades, increasing their sensitivities by many times and allowing them to detect dozens of other gravitational wave signals. Third-generation ground-based interferometers (Einstein Telescope and Cosmic Explorer) and space-based detectors (such as LISA) are being researched and planned to enter into function in the second half of the next decade. If successful, these experiments will allow the detection of thousands of signals coming from an ever-increasing range of cosmological sources. In the meantime, second-generation interferometers are approaching the conclusion of ambitious upgrades started with the end of the third observing run "O3" in march 2020.

The work of this thesis revolves around the planning and the commissioning of the "Advanced Virgo plus" upgrade project, which aims to increase the detector's sensitivity by a factor of two, allowing a ten times higher detection rate than the previous configuration. In particular, the main topic is the update of the interferometer longitudinal sensing and control scheme required by the upgrade in the detector's optical configuration. The design and simulation of the new control scheme carried out in constant collaboration with the "Interferometer Sensing and Control" team, started years before the actual implementation of the upgrades. Following that, I participated in the full-time commissioning of the upgraded configuration, which started in January 2021 and is currently ongoing.

We will first explain the new interferometer configuration, then go into the details of the lock-acquisition procedure, presenting the results of the related simulation studies and the commissioning. A particular focus will also be given to the simulations of the interferometer's state at the end of the lock acquisition, called "steady-state". In addition to the study and implementation of the current lock-acquisition procedure, the thesis will present simulation activities to study an alternative lock-acquisition technique that has not yet been implemented.

Chapter 1 of the thesis introduces gravitational wave detection and the detectors' operating principles.

Chapter 2 will dive deeper into topics related to the control of the main suspended optics of the interferometer.

Chapter 3 explains the newly implemented lock-acquisition procedure for the lock of Advanced Virgo Plus, showing the most relevant studies carried out during the design phase and the results obtained during the commissioning. An in-depth study regarding the impact of misalignments during a particularly crucial part of the lock acquisition is reported in appendix A.

Chapter 4 focuses on the control strategy of the AdV+ interferometer in the steady-state configuration, that is, the final configuration in which the interferometer has completed the lock acquisition and is ready to detect gravitational waves. A more details study of each of the longitudinal error signals used during this phase is given in B.

Chapter 5 will overview a different lock acquisition technique that can be potentially applied to AdV+ or similar gravitational wave interferometers. This technique potentially gives several advantages with respect to the one currently implemented, including cheaper and simpler to-commission hardware. Simulation studies to verify the feasibility of this technique gave encouraging results. However, simple experiments on the actual interferometer are needed to obtain complete validation and can be carried out once the AdV+ interferometer dark-fringe configuration is sufficiently stable.

Chapter 1

Detecting Gravitational Waves with ground-based interferometers

Gravitational Wave science is a broad subject, covering topics like astrophysics, cosmology and fundamental physics. The technical complexity of the current gravitational wave detectors involves expertise from a multitude of fields: linear optics, laser science, quantum optics, material science, electronics, vacuum science, mechanical engineering and control system theory. In this chapter, we will introduce the basics of gravitational wave detection, giving context to the studies treated in this thesis.

We will start with a brief overview of the effect of gravitational waves, their possible sources and how the sensitivity of a detector to Compact Binary Cohalescence (CBC) signals is defined. This will allow us to obtain an understanding of how the LIGO-Virgo-KAGRA network of gravitational-wave detectors operated in the past years, alternating between periods of uninterrupted data acquisition (observing runs) with periods dedicated to the upgrade and commissioning of the detectors. Finally, we will treat the optical configuration of the ground-based gravitational-wave interferometers, focusing on the impact of the main components on the overall sensitivity of the detector.

1.1 Gravitational waves and their detection

Gravitational Waves (GWs) are often defined as “ripples in the space-time” or “periodic compressions and dilatations of the space”. These generic formulations help in picturing this phenomenon in an intuitive way since a complete discussion requires an understanding of gravitation in the framework of general relativity. A formal introduction to this topic is well outside the scope of this thesis; nevertheless, we will show how representing GWs as perturbations of the space-time metric leads to representing their effect as a measurable variation of distance between objects in the space. The following steps are inspired by the explanation given in [1], while more formal derivations can be found in many related textbooks such as [2] and [3].

Gravitational waves can be formalized starting from the linearisation of Einstein field equations. This linearisation is allowed as long as we consider events far from strong gravitational field sources, where the space-time metric $g_{\mu\nu}$ (i.e. the solution to the equations) can be approximated to the one of a flat Minkowski space $\eta_{\mu\nu}$ plus a term representing a small perturbation $h_{\mu\nu}$.

$$g_{\mu\nu} = \eta_{\mu\nu} + h_{\mu\nu} \tag{1.1}$$

where

$$\eta_{\mu\nu} = \begin{pmatrix} -1 & 0 & 0 & 0 \\ 0 & 1 & 0 & 0 \\ 0 & 0 & 1 & 0 \\ 0 & 0 & 0 & 1 \end{pmatrix} \tag{1.2}$$

The metric $g_{\mu\nu}$ can then be used to compute the interval between two points in the space-time.

$$ds^2 = g_{\mu\nu} dx^\mu dx^\nu \tag{1.3}$$

By using the Lorenz gauge and by remembering to consider that we are studying the case in which the reference frame is far away from the source of perturbation, the general solution of the perturbation can then be written as a superposition of plane waves. These plane waves are known as **gravitational waves**. In the Transverse-Traceless (TT) gauge [3] they can be represented as:

$$h_{\mu\nu} = A_{\mu\nu} \cos\left[\omega_{gw} t - k_{gw} z\right] \tag{1.4}$$

with

$$A_{\mu\nu} = \begin{pmatrix} 0 & 0 & 0 & 0 \\ 0 & h_+ & h_\times & 0 \\ 0 & h_\times & -h_+ & 0 \\ 0 & 0 & 0 & 0 \end{pmatrix} \tag{1.5}$$

being the polarization tensor that represents the spatial effect of a GW while ω_{gw} and k_{gw} are respectively the angular frequency and wave vector of the GW. h_+ and $h_\times$ are two independent polarization modes, also known as "*plus*" and "*cross*" modes.

We will now finally show that the effect of these perturbations $h_{\mu\nu}$ of the space-time metric can be observed as a simultaneous compression and stretching of the space in two perpendicular directions, both of which are orthogonal to the direction of propagation of the wave.

We can observe this effect by computing the proper distance between two points in the space when a GW is influencing it. The proper distance L' is defined in equation 1.6 as the integral of the metric interval ds^2 (1.3). Considering, for simplicity, one point at the origin and one at distance L along the x axis, one can use 1.1, 1.2, 1.4 and 1.5 to obtain:

$$L' := \int |ds^2|^{\frac{1}{2}} \tag{1.6}$$

$$= \int_0^L |g_{11}|^{\frac{1}{2}} dx^1 \tag{1.7}$$

$$=\simeq L|g_{11}[x=0]|^{\frac{1}{2}} \tag{1.8}$$

$$=\simeq L(1 + h_+ \cos\left[\omega_{gw} t\right]) \tag{1.9}$$

Extending this to a 2-dimensional case, where the points considered are separated by ΔL_x and ΔL_y as in [1] one gets:

$$\begin{pmatrix} \Delta L'_x \\ \Delta L'_y \end{pmatrix} = \begin{pmatrix} \Delta L_x \\ \Delta L_y \end{pmatrix} + \frac{1}{2} \begin{pmatrix} h_+ & h_\times \\ h_\times & -h_+ \end{pmatrix} \begin{pmatrix} \Delta L_x \\ \Delta L_y \end{pmatrix} \cos\left[\omega_{gw} t + k_{gw} z\right] \tag{1.10}$$

One can now see how the distance between the two points depends then on the phase and polarisation of the GW, as represented in figure 1.1. Section 1.3 will show how interferometric detectors can use this effect to observe GWs.

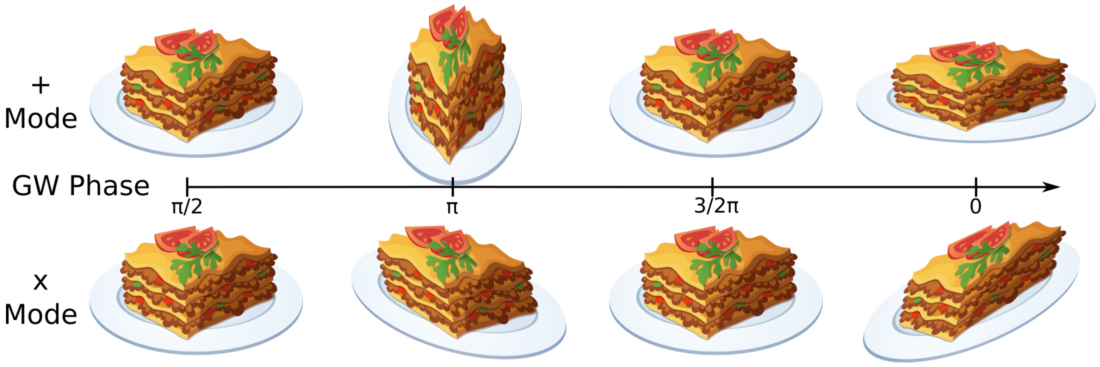

Figure 1.1: Greatly magnified representation of the strain effect of the two different GW polarisations h_+ and $h_\times$ on an object. On a more realistic scale, the strain of a typical GW would give compressions and dilatations of the order of 10^{-21} with respect to the original object size, which would not be appreciable by eye.

1.2 Sources of gravitational waves and observations

Gravitational waves are the result of cosmological events involving a rapidly changing mass-quadrupole moment [2]. While, in principle, this opens the possibility of observing GWs generated by a multitude of different physical phenomena, only events involving masses on the astrophysical scale have the possibility of having tangible effects on the space-time metric. Amidst those, the most likely astrophysical sources that satisfy the quadrupole moment condition and can generate gravitational-wave signals are:

- Compact Binary Coalescences CBCs,
- rapidly rotating isolated Neutron Star (NS),
- core-collapse supernovae,
- stochastic GW background.

In addition to these possible sources, the search of gravitational waves is also open on detecting sources and emission mechanisms that are currently unknown to science.

Currently, only gravitational-wave transients generated from the coalescence of binary systems of compact objects CBCs have been directly observed. In particular, as of January 2022, 90 gravitational wave signals [4] [5] have been identified with high confidence[1]. In the absence of ElectroMagnetic (EM) counterparts to the detection and of other ways to observe the effects of matter on the signal (matter signatures), it is impossible to be certain of the exact type of compact objects involved in a merger [4]. However, the estimated mass of the objects involved in the coalescence can infer a distinction between Black Hole (BH) and NS objects. Indeed, it is possible to define

---

[1] An overview on how the likelihood of an event having astrophisical origin is estimated is given in [6] and [7].

a maximum mass for a NS, either from equations of state obtained from theoretical models or from the distribution of the observed galactic NSs, assuming a limit given by the astrophysical processes forming the compact binaries [8]. In all these cases, the maximum mass for a NS object is estimated to be between 2 and 2.5 Solar Masses ($M_\odot$) [8]. This leads to categorising the GW observations as originated by either Binary Black Hole (BBH) (if $m_1, m_2 > 3M_\odot$), Binary Neutron Star (BNS) (if $m_1, m_2 < 3M_\odot$) or Neutron-Star-Black-Hole (NSBH) merger events (if $m_1 > 3M_\odot, m_2 < 3M_\odot$) [4].

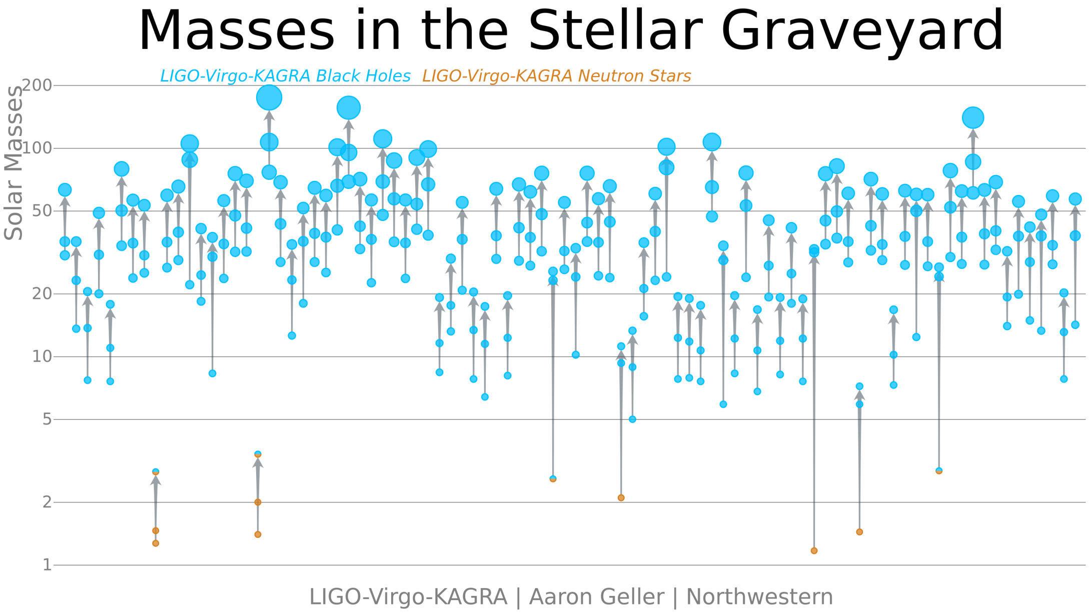

Figure 1.2: Detected compact object masses. The vertical axis represents the mass of the involved objects in solar masses $M_\odot$. The color of the circles identifies each object as black hole (blue), neutron star (orange) or uncertain (half-blue /half-orange). Each arrow indicates a merger, starting from the two merging compact objects and pointing to the generated object. (Credits: LIGO-Virgo-KAGRA Collaborations/Frank Elavsky, Aaron Geller/Northwestern.)

As represented in figure 1.2, out of the 90 events detected in the past three observing runs, 2 of them (GW170817 also confirmed by electromagnetic emission follow-up and GW190425 [9]) and have a high probability of being BNS mergers, 2 (GW200105 and GW200115 [8]) are possible NSBH mergers. In contrast, all the others are likely to be BBH merger events.

1.2.1 Sensitivity of the detectors for CBC signals

Since the most well-known sources of gravitational wave signals are CBCs, a GW detector sensitivity is usually estimated starting with the comparison of the Amplitude Spectral Density (ASD) of the detector's strain signal (also called "detector sensitivity curve") with the signals expected by CBCs of representative masses. In particular, for a given modeled signal and detector sensitivity curve, it is possible to estimate the orientation-averaged space-time volume for which the given signal would have a Signal-to-Noise-Ratio (SNR) of 8 [10]. For this volume, it is then possible to obtain a characteristic **range** of the detector, as the radius of an euclidean sphere corresponding to this volume[2].

The so-called BNS, BBH, and NSBH range are the most commonly calculated inspiral ranges. These are computed using respectively the signal generated by the merger of 1.4 + 1.4 solar masses BNS system, 30 + 30 solar masses BBH system and 1.4 + 10 solar masses NSBH system. The use of these quantities allows a comparison of the performance of the different detectors and estimating the impact of the upgrades that are currently being implemented, and will be presented in section 1.4.

Nevertheless, one needs to remember that, due to the non-stationary and transient nature of several noises affecting the detectors [12], their real performance cannot be estimated using only these parameters. Their ultimate capability of detecting gravitational waves and of inferring astrophysical information will indeed be also affected by factors that are difficult to quantitatively predict in advance, such as:

- The rate of short noise transients (glitches) affecting the detector,
- the stationarity of the detector response,
- the detector duty-cycle, i.e., the amount of time a detector can remain in observing mode with respect to the duration of the interruptions.

1.3 The interferometers and their optical response

The configuration of the current ground-based GW interferometers is, in essence, based on the Michelson interferometer. However, to reach the sensitivity necessary for detecting gravitational waves, many radical differences with respect to this simple instrument have been implemented. This section will focus on explaining the optical configuration currently used by the second generation detectors, called the Dual-Recycled Fabry-Perot Michelson Interferometer (DRFPMI). Since the main topic of this thesis is tightly tied to the upgrade of the Advanced Virgo plus interferometer, we will use its parameters in the examples. However, the resulting considerations will also be valid for the Laser Interferometer Gravitational-Wave Observator (LIGO) and Kamioka Gravitational Wave Detector (KAGRA) interferometers.

1.3.1 Michelson interferometer response

A Michelson interferometer allows measuring the relative phase shift between the electromagnetic fields of the laser beams reflected by the mirrors in its two perpendicular arms. Any effect that induces differential arm length variations originates such a phase shift, including the strain $h[t]$ applied by a gravitational wave, which can therefore be measured with the interferometer. The effect of the GW strain on the interferometer depends on many parameters of the gravitational wave, including its amplitude, wavelength, and its direction and polarisation relative to the interferometer orientation. We will show that it also depends on one core parameter of the interferometer, which is the total length of the arms.

An in-depth description of the electromagnetic field inside an interferometer would require a representation of its transverse components and the superposition between

---

[2] Further details on how the volume and ranges are calculated, taking into account the "antenna pattern" of the detectors (i.e., the difference in sensitivity to signals arriving from different directions), the red-shift of the GW waveform and other relativistic effects are given in [11].

the different beam and cavity modes. For the sake of simplicity, however, in this chapter, we will limit ourselves to using a monochromatic plane-wave approximation. The effect of a GW on an interferometer mainly involves the longitudinal components of the EM field. Therefore, this simple notation allows studying many relevant aspects of a well-matched and tuned interferometer.

Following the observations in section 1.1, it can be shown that the effect of a GW on a Michelson interferometer can be also inferred using equation 1.6.

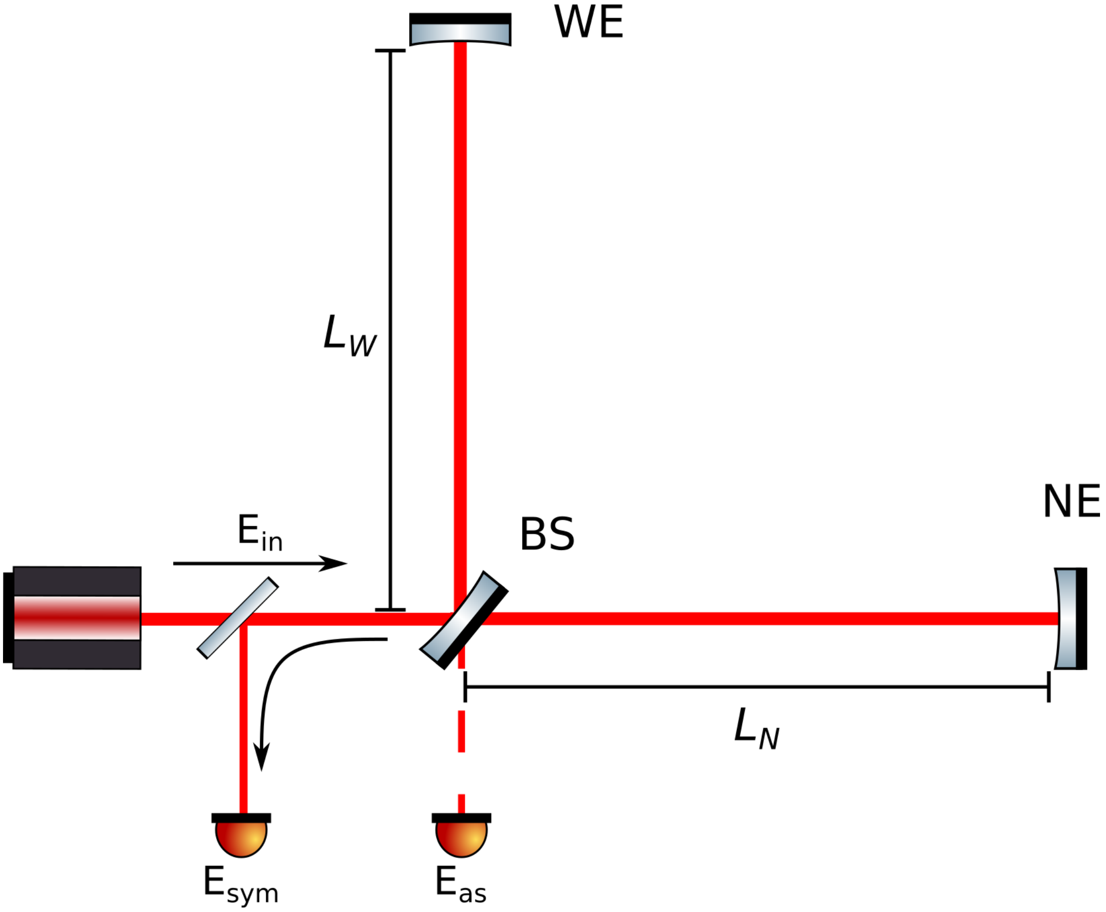

Figure 1.3: Optical scheme of a Michelson interferometer. The laser beam is injected towards the *Symmetric* port of the interferometer beam-splitter Beam-Splitter (BS). Two photodiodes (coloured in orange) collect the light transmitted towards the *Antisymmetric* port E_{as} and reflected from the *Symmetric* port E_{sym}.

The following will take into consideration an ideal Michelson interferometer such as the one represented in figure 1.3. The interferometer arms have respective lengths of L_N and L_W[3], with perfectly reflective mirrors (with no losses and no transmission) at the end of each. A monochromatic plane-wave laser with electric field $E_{in} = |E_{in}|e^{-i(\omega_0 t)+kz}$, frequency $\nu_0 = \frac{\omega_0}{2\pi}$ and wave-number $k = \frac{2\pi\nu}{c}$ is injected towards the "*Symmetric*" port (left side of the beam-splitter in figure 1.3 of the interferometer towards a 50/50 beam-splitter. The remaining port of the beam-splitter (bottom side in figure 1.3) is called the "*Antisymmetric*" port. We are considering a gravitational wave

---

[3] This notation originates from the orientation of the Virgo interferometer arms, which are approximately directed one towards North and one towards West.

travelling perpendicular with respect to the interferometer arms, and pure "+" polarization ($h_\times = 0$). Its strain amplitude[4] is given by $|h_+| \ll 1$. For simplicity, we suppose that the two interferometer arms are perfectly aligned with the x and y components of the GW "+" polarization. The change in optical phase of the field travelling trough each arm is therefore given by [1]:

$$\phi_N = 2kL_N + \frac{\omega_0}{2} \int_{t-2\frac{L_N}{c}}^{t} h_+[\tilde{t}]d\tilde{t} \tag{1.11}$$

Where $h_+[t] := h_+ \cos[\omega_{gw} t]$ is the projection of $h_{\mu\nu}$ along the interferometer arm. In the other arm, since it is perpendicular, the effect of the gravitational wave has opposite sign:

$$\phi_W = 2kL_W - \frac{\omega_0}{2} \int_{t-2\frac{L_W}{c}}^{t} h_+[\tilde{t}]d\tilde{t} \tag{1.12}$$

The beam-splitter recombines the two reflected beams, and the electric field at the antisymmetric port can be therefore written as:

$$E_{as} = |E_{in}| e^{-i(\omega_0 t + kz)} \frac{(e^{-i\phi_N} + e^{-i\phi_W})}{2} \tag{1.13}$$

$$= |E_{in}| \frac{e^{-i(\omega_0 t + kz)}}{2} e^{-2ikL_{\mathfrak{C}}} \left(e^{-i\left(kL_{\mathfrak{D}} + \frac{\omega_0}{2}\int_{t-2\frac{L_N}{c}}^{t} h_+[\tilde{t}]d\tilde{t}\right)} + e^{i\left(kL_{\mathfrak{D}} + \frac{\omega_0}{2}\int_{t-2\frac{L_W}{c}}^{t} h_+[\tilde{t}]d\tilde{t}\right)} \right)$$

$$\simeq |E_{in}| e^{-i(\omega_0 t + k(z+L_{\mathfrak{C}}))} \cos\left[kL_{\mathfrak{D}} + \frac{\omega_0}{2} \int_{t-2\frac{L_{\mathfrak{C}}}{c}}^{t} h_+[\tilde{t}]d\tilde{t} \right] \tag{1.14}$$

Where we replaced the single-arm lengths with the Differential ARM length (DARM) and Common ARM length (CARM) degrees of freedom (abbreviated in $L_{\mathfrak{D}}$ and $L_{\mathfrak{C}}$ respectively), commonly defined as:

$$L_{\mathfrak{D}} := DARM := L_N - L_W \tag{1.15}$$

$$L_{\mathfrak{C}} := CARM := \frac{L_N + L_W}{2} \tag{1.16}$$

We also approximated $L_N \simeq L_W \simeq L_{\mathfrak{C}}$ in the integration boundaries, which means supposing that the arm lengths are approximately equal. This is valid as long as $L_{\mathfrak{D}} \ll \lambda_{gw}$ and $L_{\mathfrak{D}} \ll L_{\mathfrak{C}}$.

Long wave approximation: if the period of a gravitational wave is much larger than the time taken by the light to travel across the arms, i.e. $\nu_{gw} \ll \frac{c}{2L_{\mathfrak{C}}}$,[5] one could consider $h[t]$ constant in that time-interval, and obtain a phase shift proportional to the arm length and to the laser frequency:

$$\Delta\phi_{gw}[t] := \omega_0 \int_{t-2\frac{L_{\mathfrak{C}}}{c}}^{t} h[\tilde{t}]d\tilde{t} \simeq 2\frac{\omega_0}{c} L_{\mathfrak{C}} h[t] \tag{1.17}$$

This approximation is valid for most of the gravitational waves within the detection bandwidth of current ground-based interferometers. Indeed, as explained in the

---

[4] Typical strain of GW reaching the earth are smaller than 10^{-21} [2].

[5] this also means that $\lambda_{gw} >> L_{\mathfrak{C}}$

following sections, above a few hundred Hz, the noise affecting the sensitivity of these instruments (shown in figures 1.13) increases steadily with the frequency due to quantum noise fluctuations. This noise hampers the detection of signals above a few kHz, while for kilometer-scale detectors, $\frac{c}{2L_{\mathfrak{C}}} > 10^4$ Hz.

Power and sensitivity: starting from equation 1.13 we can obtain the power measured by a photodetector placed at the antisymmetric port, which is proportional to $|E_{as}|^2$. The proportionality constant α takes in account the photodetector area and quantum efficiency, and is included in the term $P_{in} := \alpha|E_{in}|^2$, giving therefore:

$$P_{as} = P_{in} \cos^2 \left[kL_{\mathfrak{D}} + \frac{\Delta\phi_{gw}}{2} \right] \tag{1.18}$$

Which, in the aforementioned case of $\nu_{gw} \ll \frac{c}{2L_{\mathfrak{C}}}$, it becomes

$$P_{as} = P_{in} \cos^2 \left[k \left(L_{\mathfrak{D}} + L_{\mathfrak{C}} h[t] \right) \right] \tag{1.19}$$

A few interesting considerations about the sensitivity of the interferometer output with respect to CARM, DARM variations and with respect to a gravitational wave can be easiliy obtained from the derivatives of the measured power:

$$\frac{\partial P_{as}}{\partial L_{\mathfrak{C}}} = -kh[t] \sin \left[2k \left(L_{\mathfrak{D}} + L_{\mathfrak{C}} h[t] \right) \right] P_{in} \tag{1.20}$$

$$\frac{\partial P_{as}}{\partial L_{\mathfrak{D}}} = -k \sin \left[2k \left(L_{\mathfrak{D}} + L_{\mathfrak{C}} h[t] \right) \right] P_{in} \tag{1.21}$$

$$\frac{\partial P_{as}}{\partial h} = -kL_{\mathfrak{C}} \sin \left[2k \left(L_{\mathfrak{D}} + L_{\mathfrak{C}} h[t] \right) \right] P_{in} \tag{1.22}$$

- The sensitivity of a symmetrical Michelson interferometer with respect to common arm length ($L_{\mathfrak{C}}$) variations is extremely small with respect to the sensitivity to differential arm length ($L_{\mathfrak{D}}$) variations.
- At rest, the term $\sin \left[2k \left(L_{\mathfrak{D}} + L_{\mathfrak{C}} h[t] \right) \right]$ in the derivatives 1.20 can be simplified to $\sin \left[2kL_{\mathfrak{D}} \right]$. In this condition the maximum strain sensitivity ($\frac{\partial P_{as}}{\partial h}$) is obtained for $kL_{\mathfrak{D}} = \frac{\pi}{4} + N\frac{\pi}{2}$, which corresponds to the 'half fringe' condition. In the next paragraph we will show that however, the optimal interferometer signal to noise ratio is achieved at a different working point.
- The sensitivity to the strain ($\frac{\partial P_{as}}{\partial h}$) is proportional to the common arm length $L_{\mathfrak{C}}$.

Detection shot noise and optimal working point Choosing and maintaining the correct working point of the optics is a core factor in obtaining an interferometer capable of detecting gravitational waves. As hinted in the previous paragraph, for a simple Michelson interferometer like the one treated in this section, one of the most impacting choices is the choice of the DARM working point.

Up to now, we have considered the output of an interferometer that is not affected by any noise source. However, to analyze the choice of the optimal DARM working point, we need to consider one of the fundamental noise sources that affect the detector, which is the LASER shot noise. Shot noise affects the photodetector giving a white noise with Power Spectral Density (PSD) proportional the impinging power (a demonstration can be found here:[13]):

$$S_{nn} = 2\hbar\omega_0 P_{as} \tag{1.23}$$
$$= 2\hbar\omega_0 \alpha P_{in} \cos^2\left[kL_{\mathfrak{D}}\right] \tag{1.24}$$

The optimal DARM working point is chosen in order to maximize the SNR with respect to GW signals, which is $\frac{|\frac{\partial P_{as}}{\partial h}|}{\sqrt{S_{nn}}}$. Using equations 1.23 and 1.22 one therefore obtains:

$$SNR := \frac{k}{\sqrt{2\hbar\omega_0}}\sqrt{P_{in}}L_{\mathfrak{C}}|\sin\left[kL_{\mathfrak{D}}\right]| \tag{1.25}$$

From here, two important observations can be made: first, the Signal to Shot-Noise ratio increases with the input power. Second, the maximum SNR corresponds to the DARM working point given by $kL_{\mathfrak{D}} = \frac{\pi}{2} + n\pi$. This corresponds to the so-called **dark fringe** condition, in which no power is transmitted at the antisymmetric port of the interferometer. In this point, however, the linear component of the response to GW signals $|\frac{\partial P_{as}}{\partial h}|$ is also zero. In order to solve this issue (i.e., linearising the interferometer response), one of the possible solutions is to apply a small (a few picometers) offset on DARM. This allows a small portion of the carrier field to be transmitted to the antisymmetric port, which can be used to implement a homodyne detection scheme. This solution is currently used on all the ground-based GW interferometers and is called **"DC readout"** [14].

Linearization of the interferometer response and strain transfer function: In the previous paragraph, the dependence of the interferometer response on the frequency of the gravitational wave signal has been ignored thanks to the "low-frequency" GW approximation, i.e. , $\nu_{gw} \ll \frac{c}{2L_{\mathfrak{C}}}$.

While this is usually a perfectly valid assumption for ground-based detectors, we will now set it apart and introduce a representation of the interferometer response in the frequency domain. This representation will be instrumental in the following sections to understand the differences between interferometer configurations.

In order to proceed, the interferometer response needs to be linearized around its optimal working point. This approximation is valid as long as the chosen DARM offset $\delta L_{\mathfrak{D}}$ is large enough and $|h| \ll 1$.

In this condition

$$P_{as}[t] \simeq P_0 + \alpha\frac{\Delta\phi[t]}{2} \tag{1.26}$$
$$= P_0 + \alpha\frac{\omega_0}{2}\int_{t-2\frac{L_{\mathfrak{C}}}{c}}^{t} h[\tilde{t}]d\tilde{t} \tag{1.27}$$

Where the constant α contains the dependence on the DARM offset, CARM, the input power, and the detector area. It is relatively simple now to study the frequency response of the inteferometer $R_{mich}[\nu] := \frac{\hat{P}_{as}[\nu]}{\hat{h}[\nu]}$, where $\hat{P}_{as}$ and $\hat{h}[\nu]$ are the Fourier transforms of

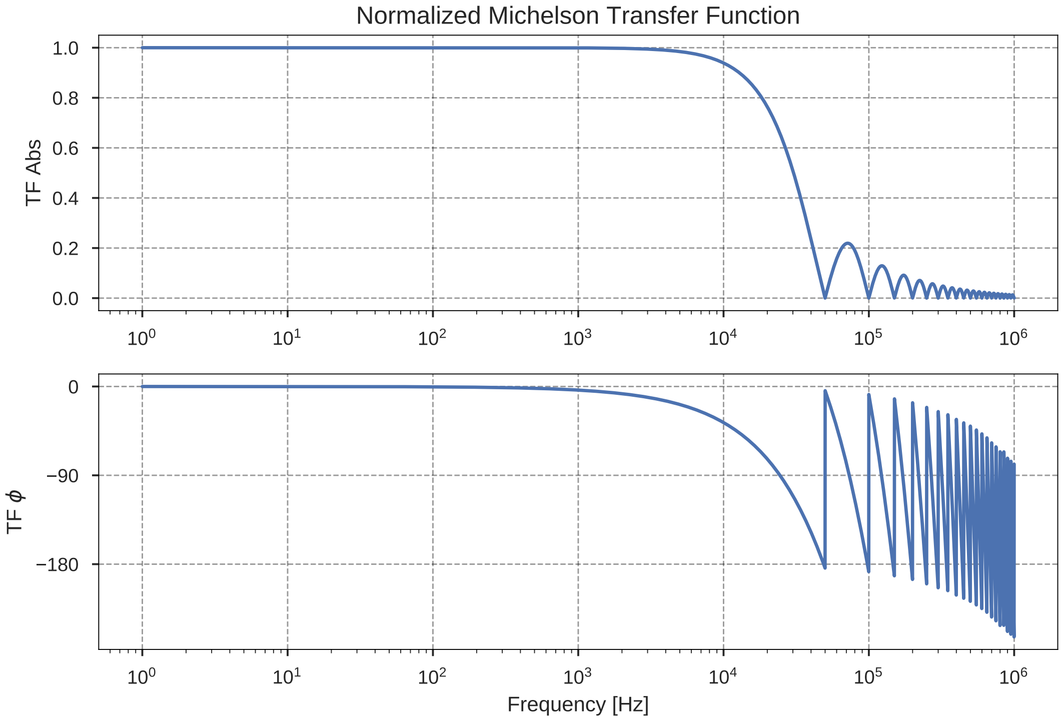

Figure 1.4: Normalized Michelson strain transfer function. One could notice the response approaching zero at frequency $\nu = \frac{2L_{\mathfrak{C}}}{c} = 50$ kHz.

P_{as} and h respectively. An easy way to do this is to first derive the linearized equation 1.26 and then to apply the Fourier transform to both terms as follows:

$$\frac{dP_{as}}{dt} = \alpha\frac{\omega_0}{2}\left(h[t] - h\left[t - 2\frac{L_{\mathfrak{C}}}{c}\right]\right) \tag{1.28}$$

$$i2\pi\nu\hat{P}_{as}[\nu] = \alpha\frac{\omega_0}{2}\hat{h}[\nu]\left(1 - e^{-i2\pi\frac{2L_{\mathfrak{C}}}{c}\nu}\right) \tag{1.29}$$

This gives us the following Transfer Function (TF) representing the simple Michelson response to h:

$$R_{mich}[\nu] = \alpha\frac{\omega_0}{2}\frac{1 - e^{-i2\pi\frac{2L_{\mathfrak{C}}}{c}\nu}}{i2\pi\nu} \tag{1.30}$$

The normalized result is plotted in figure 1.4, for an interferometer with $L_{\mathfrak{C}} = 3$ km. One can notice that the response is indeed flat for frequencies $\nu \ll \frac{c}{2L_{\mathfrak{C}}}$ and falls to zero at $\nu = \frac{c}{2L_{\mathfrak{C}}} = 50$ kHz and at every integer multiple of this frequency.

The importance of the frequency response becomes clearer once we remind that the shot noise at the detection photodiode is one of the main fundamental noise sources affecting the detector performance. Given the interferometer as a linear stationary system, the output at the antisymmetric port can now be written as function its frequency response : $P_{as}[\nu] = R[\nu]h[\nu]$. Therefore, we can use the same transfer function to convert the photodiode shot noise in its equivalent strain noise PSD.

$$S_{hh} = \frac{S_{P_{as}P_{as}}}{|R|^2} = \frac{2\hbar\omega_0 P_{as}}{|R|^2} \tag{1.31}$$

This shows us that the detector strain shot noise ASD $\sqrt{S_{hh}}$ is shaped by the inverse of the detector response. It is indeed intuitable that in the frequency regions in which the optical response to a GW signal is the lowest, the contribution of noises at the level of the photodetector becomes more relevant than the signal.

Phase modulation and GW sidebands: A very useful representation of the effect of a GW on the interferometer arm EM field can be obtained considering equations 1.11 and 1.12 in the case where $\nu \ll \frac{c}{2L_{\mathfrak{C}}}$. In this case, the effect of the GW on each arm EM field assumes the form of a proper phase modulation:

$$\begin{aligned} E_r^N[t] &= \frac{E_{in}}{2} e^{-i\omega_0 t + \phi_N[t]} \\ &= \frac{E_{in}}{2} e^{-i\left(\omega_0 t + 2kL_N + L_{\mathfrak{C}} \frac{\omega_0}{c} h[t]\right)} \\ &= \frac{E_{in}}{2} e^{-i[\omega_0 t + k(2L_N + L_{\mathfrak{C}} h[t])]} \end{aligned} \tag{1.32}$$

Considering now a monochromatic GW such as $h[t] = h_+ \cos[\omega_{gw} t]$, the reflected field can be expanded as:

$$E_r^N[t] = \frac{E_{in}}{2} e^{-i(\omega_0 t + 2kL_N)} \sum_{n=-\infty}^{\infty} i^n J_n[m] e^{-in\omega_{gw} t} \tag{1.33}$$

Where we defined $m := kL_{\mathfrak{C}} h_+$ and where $J_n[m]$ is the n-th Bessel function of the first kind. We can see that this is a superposition of a carrier field oscillating at the main laser angular frequency ω_0 plus an infinite number of sidebands with frequencies $\omega_0 + n\omega_{gw}$. Considering the realistic case in which $m = |kL_{\mathfrak{C}} h_+| \ll 1$[6], one could approximate the Bessel functions to $J_n[m] \simeq \frac{1}{n!}\left(\frac{m}{2}\right)^n$ and stop expansion at the first-order Bessel functions. In this case one would obtain an electric field with only two sidebands, one at angular frequency $\omega_0 + \omega_{gw}$ and one at $\omega_0 - \omega_{gw}$.

$$E_r^N[t] = \frac{|E_{in}|}{2} e^{-i(\omega_0 t + 2kL_N)} \left[1 + i\frac{m}{2}\left(e^{-i\omega_{gw} t} + e^{i\omega_{gw} t}\right)\right] \tag{1.34}$$

Similarly, due to the opposite phase of the GW strain applied on the other arm of the interferometer, we get

$$E_r^W[t] = \frac{|E_{in}|}{2} e^{-i(\omega_0 t + 2kL_W)} \left[1 - i\frac{m}{2}\left(e^{-i\omega_{gw} t} + e^{i\omega_{gw} t}\right)\right] \tag{1.35}$$

Which, once recombined at the beam-splitter, give the following output at the antisymmetric port:

$$E_{as}[t] = |E_{in}| e^{-i(\omega_0 t + 2kL_{\mathfrak{C}})} \left[\cos[kL_{\mathfrak{D}}] + i\sin[kL_{\mathfrak{D}}]\frac{m}{2}\left(e^{-i\omega_{gw} t} + e^{i\omega_{gw} t}\right)\right] \tag{1.36}$$

We can see now from here too that in the dark fringe condition ($kL_{\mathfrak{D}} = \frac{\pi}{2} + n\pi$) we have maximum transmission of the sidebands generated by GW signals towards the antisymmetric port, and maximum rejection of the carrier Direct Current (usually

---

[6] For an interferometer with 3 km long arms and a near-infrared laser with $\lambda \simeq 1\ \mu$m, a GW strain of 10^{-21} gives a modulation index $m \simeq 2 \cdot 10^{-11}$.

meant to indicate the constant component of a signal, as opposed to the high frequency components) (DC) field.

$$E_{as}[t] = i|E_{in}|e^{-i(\omega_0 t + 2kL_{\mathfrak{C}})}\frac{m}{2}\left(e^{-i\omega_{gw}t} + e^{i\omega_{gw}t}\right) \tag{1.37}$$

At the symmetric port, the relative phase applied to the arm fields when recombined is shifted by a factor π. Therefore, the behaviour of GW sidebands and carrier field is swapped, meaning that the carrier field is reflected towards this port. The importance of this difference will become relevant in the distinction between the effects of the Signal Recycling and the Power Recycling cavities.

One last note is that, in addition to a GW strain, there are many other different physical effects that can modulate the phase of an EM field and therefore generate sidebands such as the ones described in equation 1.34. These effects are widely used in the sensing and control systems of GW interferometers and will be treated in the following chapters.

1.3.2 Fabry-Perot cavities

One way to greatly enhance the sensitivity of a Michelson interferometer is to add an additional mirror at the input of each arm, effectively creating two Fabry-Perot (FP) cavities. In this configuration, called Fabry-Perot-Michelson, the field reflected from the cavities is the one that goes back into the beam-splitter and recombines with the field reflected by the other arm's cavity, as shown in figure 1.7. The resulting effect is that, as long as the laser beam is resonant or close enough to be resonant in a Fabry-Perot cavity, the reflected field's phase dependence on length variations (including the effect of GWs) is greatly magnified.

Static response of a FP cavity: To understand this, we can study the behaviour of a single Fabry-Perot cavity like the one shown in figure 1.5 in which a laser beam is injected towards the *"input mirror"* with reflectivity r_1 and transmissivity t_1, while the *"end mirror"* has reflectivity and transmissivity t_2 and r_2.

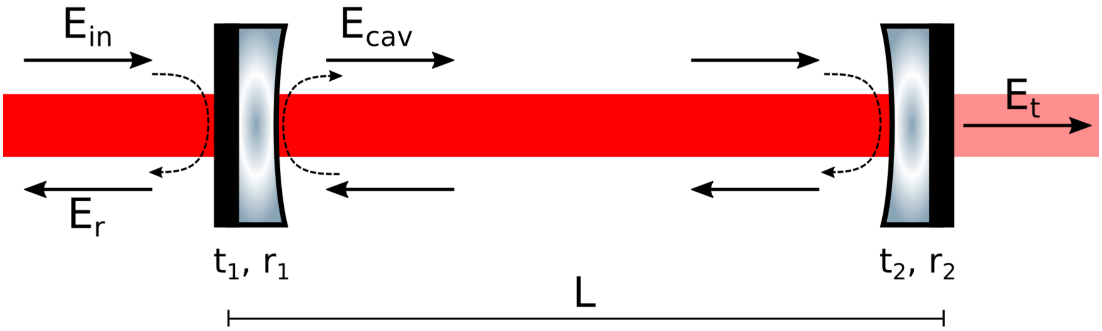

Figure 1.5: Schematic of a Fabry-Perot Cavity.

Equations 1.38 and 1.39 respectively represent the intra-cavity and the reflected electric fields, E_{cav} and E_r, as functions of the input field E_{in} and the cavity length L. The derivation of these results is quite straightforward and can be found in [15] and [13].

$$E_{cav} = \frac{t_1}{1 + r_1 r_2 e^{-2ikL}} E_{in} \tag{1.38}$$

$$E_r = i \frac{r_1 + r_2 (t_1^2 + r_1^2) e^{-2ikL}}{1 + r_1 r_2 e^{-2ikL}} E_{in} \tag{1.39}$$

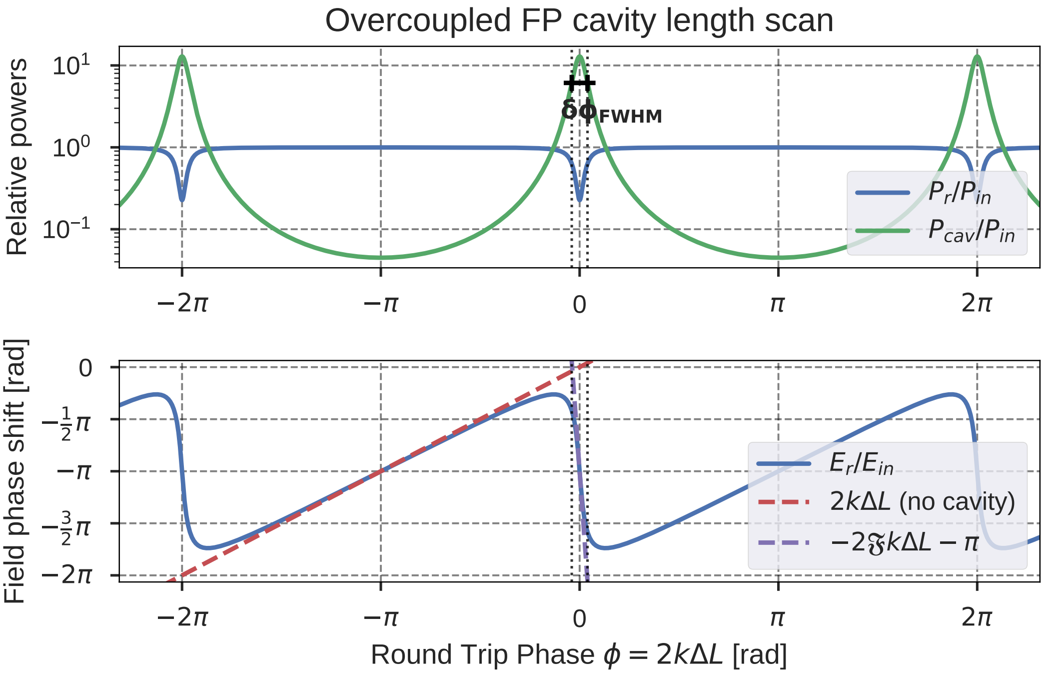

Figure 1.6: Behaviour of the reflected and intra-cavity fields inside an over-coupled FP cavity with respect to a length variation. The cavity in question has finesse $\mathfrak{F} \simeq 26$. The blue line represents the reflected field relative amplitude (top plot) and phase (bottom plot) with respect to the injected field. The green line represents the intra-cavity field relative amplitude. The bottom plot shows that, near the resonances, the reflected phase has a steep variation, with slope enhanced by a factor $\simeq -\mathfrak{F}$ (plotted in the violet dashed line) with respect to the phase shift of $2k\Delta L$ that would happen in the case of a field reflected by a single mirror (red dashed line)

The magnitude and phase of the reflected field are represented in figure 1.6 with respect to the complex exponential phase term $\phi := 2kL$. The fields have an obvious periodicity of $\Delta\phi = 2\pi$, corresponding to a length variation $\Delta L = \frac{2\pi}{2k} = \frac{\lambda}{2}$ or to a wavenumber variation of $\Delta k = \frac{2\pi}{2L}$. The latter is equivalent to periodicity in frequency, called Free Spectral Range (FSR) which in vacuum is:

$$\Delta\nu_{\mathrm{FSR}} = \frac{c}{2L} \tag{1.40}$$

Figure 1.6 also shows that indeed the phase of the reflected field has a steep variation close to the resonance condition $2kL = \pi + 2N\pi$. The slope of this variation depends mainly on two factors: the coupling of the cavity and its Finesse.

Cavity Finesse: Given $\delta\phi_{\text{FWHM}}$ the Full-Width-Half-Maximum (FWHM) of the intra-cavity power ($|E_{cav}|^2$), the cavity Finesse $\mathfrak{F}$ is defined as

$$\mathfrak{F} := \frac{2\pi}{\delta\phi_{\text{FWHM}}} = \frac{\Delta\nu_{\text{FSR}}}{\delta\nu_{\text{FWHM}}} = \frac{\pi}{2}\left(\arcsin\left[\frac{1-r_1r_2}{2\sqrt{r_1r_2}}\right]\right)^{-1} \simeq \pi\frac{\sqrt{r_1r_2}}{1-r_1r_2} \tag{1.41}$$

Cavity coupling: a Fabry-Perot cavity can behave in three different regimes according to the reflectivity and losses of its two mirrors. This regime influences the phase of the reflected field near the resonance greatly, as follows:

- **Undercoupled:** $r_1 > r_2(t_1^2 + r_1^2)$. In this regime, the phase shift of the reflected field is slightly enhanced with respect to the case of the beam reflected by a single mirror with no cavity.
- **Critically coupled:** $r_1 = r_2(t_1^2 + r_1^2)$. In this regime, the phase of the reflected field has a discontinuity at the resonance, abruptly changing phase by a factor π. Additionally, the amplitude of the reflected field reaches zero at resonance.
- **Overcoupled:** $r_1 < r_2(t_1^2 + r_1^2)$. **In this regime the phase shift of the reflected field is greatly enhanced, by a factor approximately equal to the finesse of the cavity** $\mathfrak{F}$, as shown in the example in figure 1.6. Additionally, if the reflectivity of the end mirror is high enough, most of the injected power is reflected back by the cavity even in the resonance condition. This feature is useful in FP-Michelson interferometers since power-losses through arm transmission reduce the shot-noise SNR at the detection port.

Frequency domain response of FP cavities: Using the sideband representation 1.34 introduced in section 1.3.1, it is possible to find the frequency response of an FP cavity to the sidebands generated in the FP cavity when affected by a GW with angular frequency ω_{gw}. Supposing that the sideband is generated at the end mirror, we get that their amplitude depends on the power circulating inside the cavity as follows:

$$E^0_{sb} = ir_2E_{cav}e^{-2ikL}\frac{m}{2}\left(e^{-i\omega_{gw}t} + e^{i\omega_{gw}t}\right) \tag{1.42}$$

Given $k_{gw} := \frac{\omega_{gw}}{c}$, the GW sidebands wave-numbers are $k^{\pm}_{sb} := k \pm k_{gw}$. Inside the cavity, each sideband acquires a round trip phase of $2k_{sb}L = 2(k \pm k_{gw})L$. Considering the positive sideband, at the level of the end mirror, the total sideband's field is given by:

$$E_{sb} = E^0_{sb} - E_{sb}\left(r_1r_2e^{-2ik_{sb}L}\right) = \frac{E^0_{sb}}{1 + r_1r_2e^{-2ik_{sb}L}} \tag{1.43}$$

Considering the cavity being at resonance condition $e^{-2ikL} = -1$ the denominator of 1.43 becomes:

$$\begin{aligned}
1 + r_1r_2e^{-2ik_{sb}L} &\simeq 1 - r_1r_2(1 - 2ik_{gw}L) \\
&\simeq 1 - (1 - \frac{\pi}{\mathfrak{F}})(1 - 2ik_{gw}L) \\
&\simeq -\frac{\pi}{\mathfrak{F}}\left(1 + 2\frac{\mathfrak{F}}{\pi}ik_{gw}L\right) \\
&= -\frac{\pi}{\mathfrak{F}}\left(1 + i\frac{\nu_{gw}}{\delta\nu_{\text{FWHM}}}\right)
\end{aligned} \tag{1.44}$$

Where we used the following approximations: GW frequency much smaller than the laser frequency ($k_{gw} \ll k$) and cavity with high Finesse, where $r_1 r_2 \simeq 1 - \frac{\pi}{\mathfrak{F}}$ and $\frac{\pi}{\mathfrak{F}} 2ik_{gw}L \ll 2ik_{gw}L$. The last step is obtained remembering the definition of finesse $\mathfrak{F} := \frac{\Delta\nu_{\mathrm{FSR}}}{\delta\nu_{\mathrm{FWHM}}}$ and of $\Delta\nu_{\mathrm{FSR}} = \frac{c}{2L}$. The same behaviour is applied to the negative frequency sideband, resulting in an overall cavity sideband-field of

$$E_{sb} \simeq -\frac{\mathfrak{F}}{\pi} \frac{E^0_{sb}}{1 + i\frac{2\nu_{gw}}{\delta\nu_{\mathrm{FWHM}}}} \tag{1.45}$$

As long as the frequency of the GW sidebands is small, their field is also enhanced by the cavity. It is however noteworthy that the equation 1.45 contains a simple pole at $\nu = \frac{\delta\nu_{\mathrm{FWHM}}}{2}$, which also affects the FP reflection field, in which the GW sidebands are transmitted. This means that the amplitude of the response rapidly decreases above the pole frequency.

Fabry-Perot Michelson interferometer: advantages and disadvantages. The observations made above for a single FP cavity can be extended to the case of a Fabry-Perot Michelson interferometer, in which two identical high-finesse overcoupled cavities are placed in each arm of the interferometer. For example, in the Advanced Virgo detector, the arm cavities have 3 km length and reflectivity $r_1^2 \simeq 0.986$ and $r_2^2 \simeq 0.99997$ for the input and end mirrors respectively, in both cases with very small losses $L = 1 - (r^2 + t^2) \simeq 27 \cdot 10^{-6}$ [16]. The resulting finesse is $\mathfrak{F} \simeq 450$, with a $\Delta\nu_{\mathrm{FSR}} \simeq 50$ kHz and cavity pole at $\frac{\delta\nu_{\mathrm{FWHM}}}{2} \simeq 50$ Hz.

The magnification of the reflected field phase-shift directly enhances the sensitivity of the interferometer against arm length variations, as can be seen in figure 1.10, where the response of a FP-Michelson interferometer is compared to a simple Michelson. The addition of the Fabry Perot cavity, however, introduces also several disadvantages. Indeed, while the overall frequency response of a complete Dual-Recycled-Fabry-Perot-Michelson interferometer is further modified by the Power Recycling (PR) and Signal Recycling (SR) cavities (as shown in the next section 1.3.3), **the arm cavity pole is the major contributor in limiting the detection bandwidth of the interferometer at high frequencies**.

Another disadvantage of adding high-finesse Fabry-Perot cavities in the arms is that both the arm length and the laser frequency need to be precisely controlled in order to maintain the resonance condition. Indeed, the sensitivity gain and linearity rapidly deteriorate if the laser frequency is not within the resonance peak FWHM. In the following chapters, we will explain in detail the sensing and control systems that allow to reach and maintain this condition.

Other issues that arise from the addition of high finesse Fabry-Perot arm cavities are related to the high power circulating in them. Indeed, from equation 1.38 one can see that the power circulating in the cavities is enhanced by a factor $\frac{t_1^2}{(1-r_1r_2)^2}$ when at resonance. In the current ground-based interferometers (in which the circulating power is further magnified by the PR cavity), this power reaches hundreds of kW. This generates the following issues, which need to be addressed by an appropriate design of the mirror control and thermal compensation systems:

- **Power-losses in the mirrors:** Despite the extremely low losses of the test-masses mirrors, due to the high amount of power circulating in the arm cavities at resonance, these losses absorb a large part of the input power. Indeed, considering

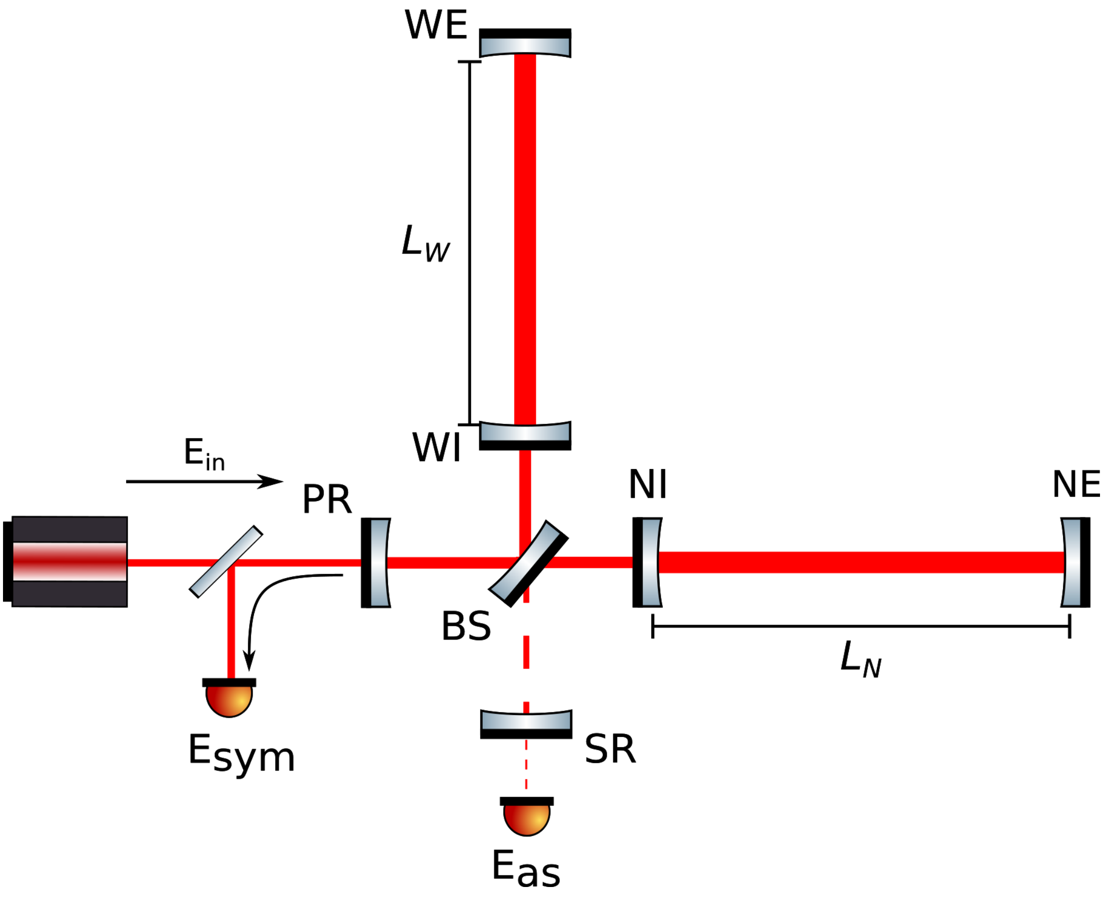

Figure 1.7: Simplified scheme of a Dual Recycled Fabry-Perot Michelson interferometer. One could note that the main differences with respect to a simple Michelson are the Fabry-Perot cavities in each arm and the Power Recycling and Signal recycling mirrors.

the losses of 27μ mentioned above for the Advanced Virgo Plus interferometer (in which the input power is 40 W), one could compute overall losses of 27 W over a circulating power of 500 kW.

- **Thermal Effects:** The absorption losses generate heat in the mirrors surfaces and substrates, which, together with the low dissipation caused by them being in vacuum, mean a substantial temperature increase of the mirrors. Due to the non-uniform heating profile of the laser beam hitting the mirror, this causes thermo-elastic deformation and thermal lensing effects. These effects, if not compensated, influence the mode-matching of the cavity, causing additional losses through scattering in high order modes.

- **Radiation Pressure:** The cavity mirrors, also called Test Masses (TMs), are suspended by complex multi-staged pendulum systems called superattenuators, which have the aim of decoupling them from ground motion. The superattenuators have extremely low stiffness, in order to have the test masses as close as possible to a free-falling state. As a side effect of this, even forces of the order of the mN[7], such as the optical-spring effects applied by radiation pressure in the

---

[7] The radiation pressure force is $\frac{2P}{c}$, which is 3 mN for a circulating power of 500 kW.

arm cavities, need to be taken into consideration by the angular and longitudinal control systems.

1.3.3 Recycling cavities

The last two main differences of the Dual-Recycled Michelson Interferometer (DRMI) configuration with respect to a simple Michelson interferometer are the Power Recycling Cavity (PRC) and the Signal Recycling Cavity (SRC). These cavities are defined by the PR and SR mirrors, located at the symmetric and antisymmetric ports of the interferometer, and the arm cavities input mirrors, as shown in figure 1.7.

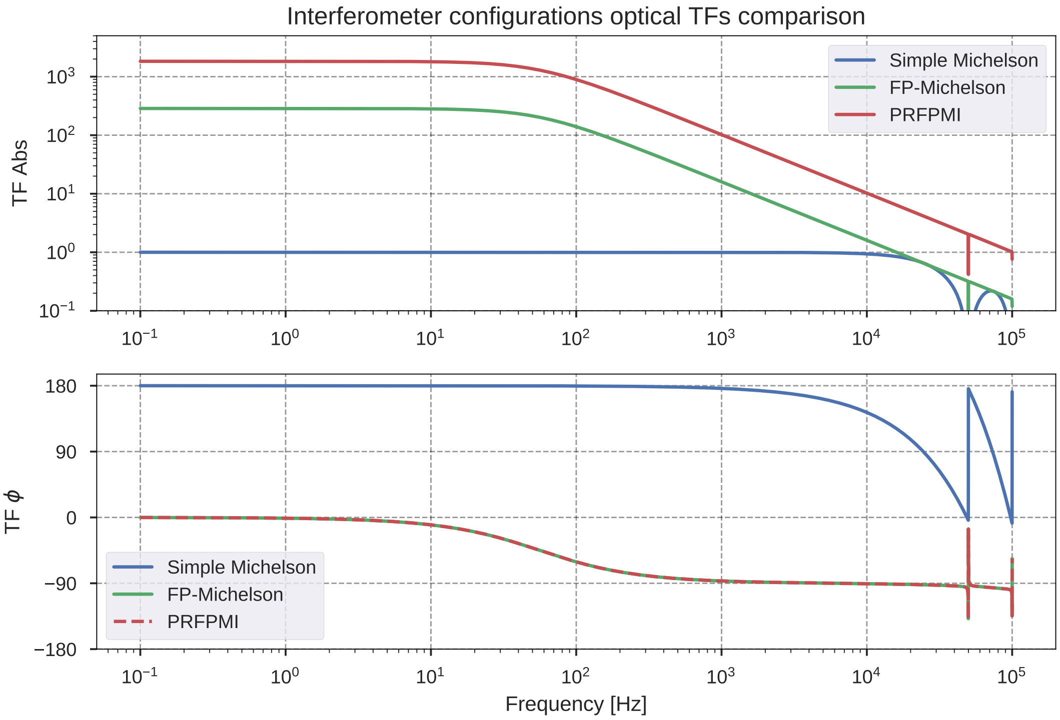

Figure 1.8: Simulated comparison of the optical response to strain transfer-function of different interferometer configurations. The blue line shows the response of a simple Michelson interferometer with 3 km long arms. The green line a Fabry-Perot Michelson configuration (with 3 km arm cavities of finesse of $\simeq 450$). The red line shows a similar configuration with the addition of a PR mirror, obtaining a Power-Recycled Fabry-Perot Michelson Power-Recycled Fabry-Perot Michelson Interferometer (PRFPMI). One could note that the addition of the PR cavity does not influence the phase nor the pole of the frequency response, but only enhances its magnitude. The parameters of the simulated configurations are based on the Advanced Virgo Plus interferometer design. For simplicity, no optomechanical interactions induced by radiation pressure have been considered in these simulations.

Power Recycling: In 1.3.1 we saw that GW interferometers operate very close to the dark fringe condition and that most of the laser power is reflected towards the symmetric port. Additionally, we showed how the $\mathrm{SNR}_{\mathrm{shot}}$ is proportional to P_{in}.

Both these observations are still valid for a Fabry-Perot Michelson interferometer. In a very simple explanation, adding a semi-transparent "Power Recycling Mirror“ at the symmetric port creates a coupled cavity system together with the arm FP cavities. When the PRC is resonant, its effect can be seen as an enhancement of reflectivity of the input mirrors for the carrier beam. This effectively increases the power circulating in the arm cavities, therefore, increasing the GW signal sidebands amplitude and improving the $\mathrm{SNR}_{\mathrm{shot}}$.

Since the sidebands created by GW signals are originated by a differential effect and therefore transmitted towards the antisymmetric port, do not interact directly with the PRC. Therefore, their amplitude is magnified by the power recycling gain, but their frequency response is not affected by the lower frequency of the coupled-cavity system pole. In summary, the addition of a PRC gives the same advantages given by increasing the finesse of the arm cavities without the disadvantage of a reduced detection bandwidth that would come by simply increasing the reflectivity of the test masses. Figure 1.8 shows the comparison between the optical transfer function of a Virgo-like FP-Michelson and a Power Recycled FP-Michelson interferometer. In the Advanced Virgo Plus interferometers, the PR mirror has a reflectivity of $r_{PR}^2 \simeq 0.95$ and the PRC length is 12 meters. At resonance, the cavity enhances the power circulating in the arms by a factor $G_{\mathrm{PRC}} \simeq 45$.

The addition of the PRC however presents also some noteworthy disadvantages: firstly, the power increase in the arm cavities caused by the PRC further accentuates the absorption, thermal effects and radiation pressure issues. Secondly, the PRC introduces additional longitudinal and angular degrees of freedom that need to be precisely controlled in order to maintain the resonance condition of the whole interferometer. The methods used to decouple and to control this additional Degree Of Freedom (DOF) from the other cavities DOFs will be a major topic discussed in the next chapters.

Signal Recycling: The addition of the Signal Recycling cavity is one of the main upgrades that is currently being implemented in the Advanced Virgo Plus interferometer. Indeed, while both Advanced LIGO detectors are working in a Dual-Recycled configuration since 2015, the Advanced Virgo detector operated in a Power-Recycled configuration up to now.

In a similar way to the PR mirror, the SR mirror creates an additional cavity that couples with the arm Fabry-Perot cavities, but this time the cavity interacts with the light going towards the antisymmetric port. This means that, close to the dark-fringe condition, the SR cavity interacts mostly with the GW signal sidebands, shaping the frequency response of the interferometer.

Depending on the length tuning of the cavity L_{SRC}, the SR cavity will affect the detector response in one of the three following ways, also represented in figure 1.9:

- **SRC resonant with the carrier:** $kL_{\mathrm{SRC}} = n\pi$ In this configuration, the transmissivity of the coupled Arm-SR cavity is increased for the carrier beam, together with its effective finesse and the gain at low frequencies. This configuration has the disadvantage of having a lower-frequency pole that further reduces the detection bandwidth.

- **SRC resonant with a specific GW sideband:** $(k + k_{GW})L_{\mathrm{SRC}} = n\pi$. In this configuration, the finesse coupled Arm-SR cavity is optimized for the enhancement and transmission of GW sidebands around a specific frequency, dependent on the exact tuning, at the disadvantage of signals at different frequencies.

- **SRC antiresonant to the carrier:** $kL_{\mathrm{SRC}} = \frac{\pi}{2} + n\pi$. In this configuration, the effective finesse of the coupled Arm-SR cavity is reduced both for the carrier and for GW sidebands. This effect reduces the maximum magnitude of the optical response. However, it has the advantage of increasing the bandwidth of detection of the interferometer by increasing the cutoff frequency of the cavity pole. This configuration is currently used by Advanced LIGO and is also being implemented in the Advanced Virgo plus detector.

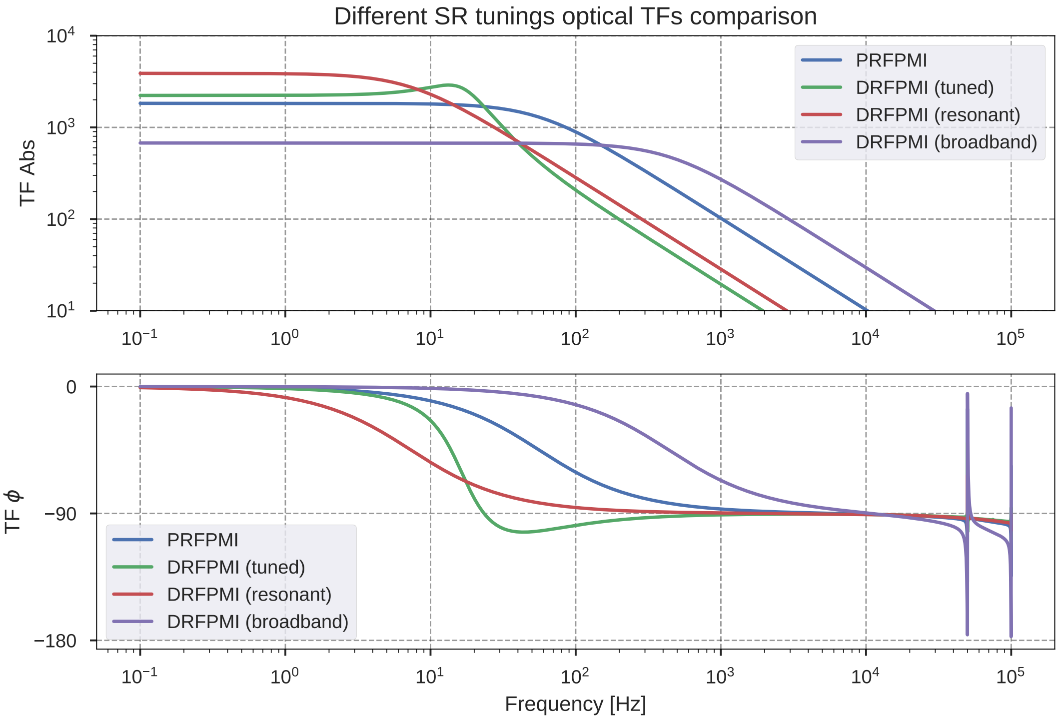

Figure 1.9: Simulated comparison of the optical response to strain transfer-function for different SR cavity tunings in the DRMI configuration, compared with the response of the Power-Recycled Michelson Interferometer (PRMI) configuration. All the simulated configurations are based on the Advanced Virgo Plus interferometer design parameters. For simplicity, no optomechanical interactions caused by radiation pressure have been considered in these simulations.

In the next chapters, we will see how the SR mirror further complicates the control scheme of the detector, impacting both the controllability of the system in the steady-state condition and the procedure that brings the various interferometer DOFs at their respective working points.

1.3.4 Putting everything together in a real interferometer

Figure 1.10 shows a comparison between the optical responses of the different ideal configurations presented in this chapter. As mentioned in paragraph 1.3.1, the optical response and the shot noise have a fundamental role in determining the overall

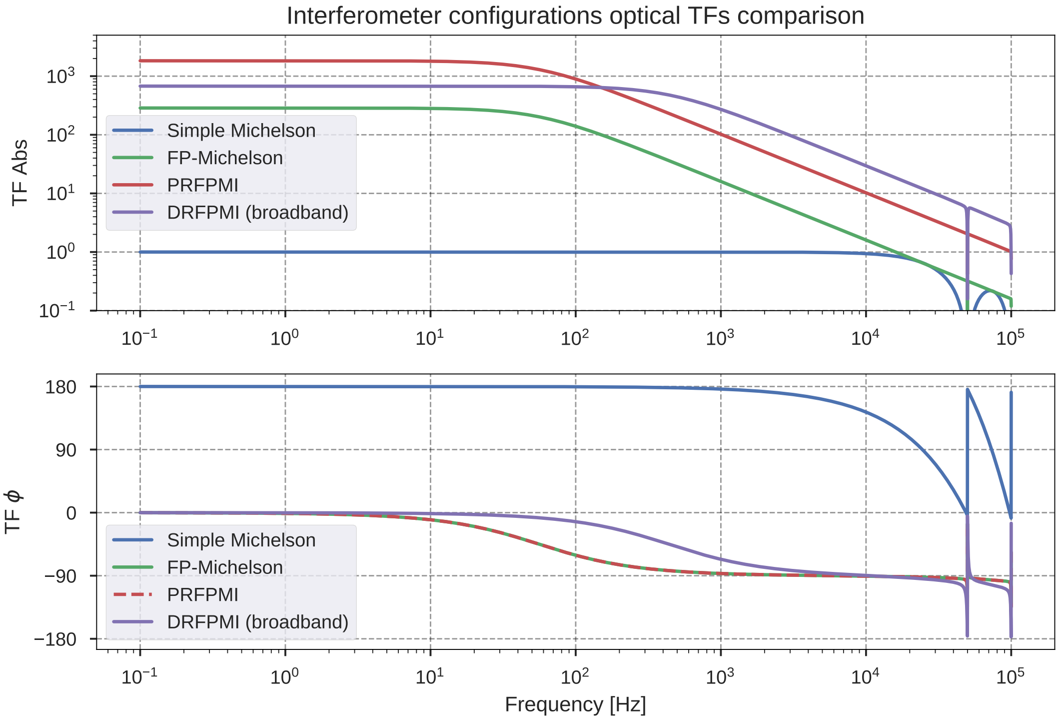

Figure 1.10: Simulated comparison of the optical response to strain transfer-function of different interferometer configurations. The blue line shows the response of a simple Michelson interferometer with 3km long arms. The green line a Fabry-Perot Michelson configuration (with 3 km arm cavities of finesse of 450). The red line shows a similar configuration with the addition of a PR mirror, obtaining a PRFPMI. Finally the purple line shows a Dual-Recycled Fabry-Perot Michelson in broadband configuration, which is used in the AdV+ and LIGO interferometers. The parameters of the simulated configurations are based on the Advanced Virgo Plus interferometer design. For simplicity, no optomechanical interactions induced by radiation pressure have been considered in these simulations.

sensitivity of the detector. However, many other noise sources need to be taken into consideration to obtain an accurate estimate of the sensitivity of a complex system such as a GW interferometer. First of all, the interferometer mirrors are not free-falling objects that are subject only to gravity. Several other forces influence their position, creating a mirror residual motion that, if not properly attenuated, overshadows the effect of GWs on the detector. The most common sources of residual mirror motion are:

- the laser beam radiation pressure;
- the (Newtonian) gravitational gradients caused by moving masses (including ground motion);
- impacts with residual gas particles;
- ground motion forces (caused by seismic, micro-seismic or anthropic sources) transmitted to the mirrors despite the superattenuators isolation;

- forces applied by the actuators (usually electromagnetic coils) to actively control the interferometer working point;
- force of external magnetic and electromagnetic fields interacting with metallic components of the superattenuator, suspension or with the electromagnetic actuators;
- electrostatic forces.

Expanding our view to the noise sources that do not affect the test mass position, but nevertheless affect the phase of the laser beam or the photodiode signals, we obtain a bewildering amount of other effects to take into consideration such as:

- Electronic shot noise of the detecting photodiode;
- Other electronic noises affecting the photodiode signals (e.g., Digital-to-analog conversion noise, modulation-demodulation, coupling with Radio Frequency (RF) EM waves);
- Interferometer laser light shot noise;
- Interferometer laser phase and amplitude noises;
- Roughness of the surface of the mirrors;
- Lase beam alignment and mode-matching in the various optical cavities;
- Mirrors surface and substrate thermal noise;
- Air temperature and local pressure variations, including sound waves, on the laser beam path;
- Noises affecting the sensing and control systems of the various interferometer components.

These noises are usually divided in two main categories: fundamental noises and technical noises. **Fundamental noises** are intrinsically connected to the physical phenomena that allow the operation of the interferometer. **Technical noises** originate instead from technical limitations of the interferometer's hardware.

In order to minimize the impact of the various noises, the ground-based gravitational-wave detectors evolved into increasingly complex instruments. The design of any upgrade on the system, therefore, requires a thorough estimate of the impact of the changes on all the components and noise sources. This activity takes into account theoretical models, experimental measurements and simulation activities, in an attempt to reproduce and predict the performance of the real instrument.

As an example of the results of a simulation study, figure 1.11 reports the quantum-noise limited sensitivity estimated for the different interferometer configurations treated in this chapter. This simulation considers only the influence of shot and radiation pressure fundamental noises and their interaction with the test-masses suspension system. Results of more advanced studies, that also take into account other noise sources, are shown in figure 1.12. One can note that, in the studied configuration, the quantum noise contribution is mostly relevant above $\simeq$ 100 Hz, while at lower frequencies the most relevant noises are technical noises and thermal and seismic noises. Since some of the parameters necessary to perform a future interferometer's sensitivity estimates are subject to a certain degree of uncertainty, the predicted sensitivity curves are usually shown as "bands“, like in figure 1.13.

These estimates of detector sensitivity are a fundamental step in the design process of a GW interferometer and of its upgrades. However, many other studies are needed in order to ensure the operability of the instrument. The simulations and studies reported in the following chapters are indeed part of the design work involved in the upgrade of the Advanced Virgo interferometer.

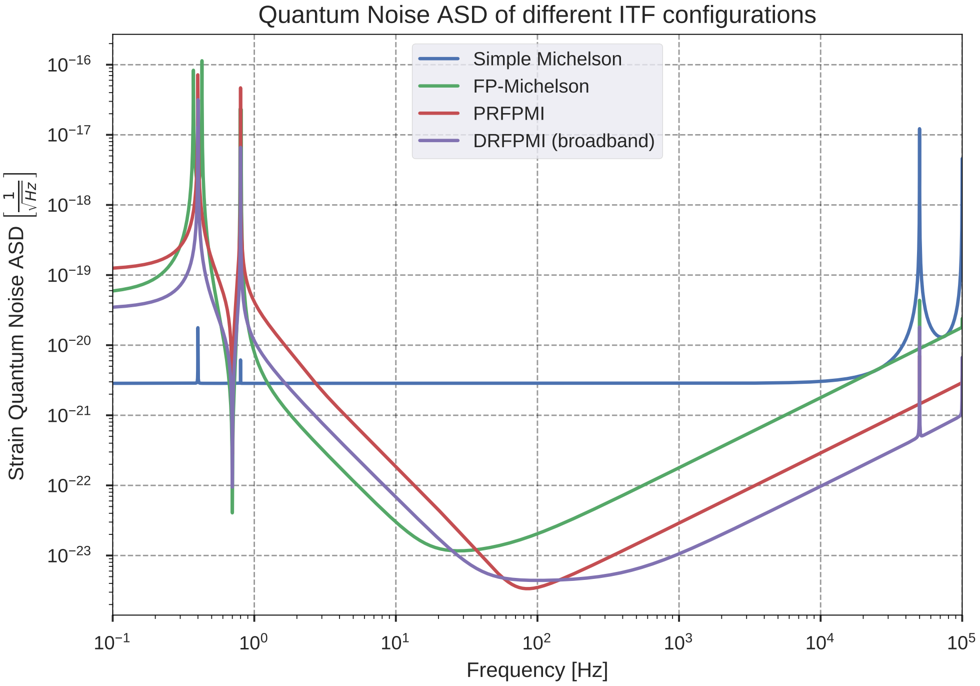

Figure 1.11: Simulated strain noise ASD for the different interferometer configurations mentioned in this chapter. All the simulated configurations are based on the Advanced Virgo Plus interferometer design parameters. Both shot-noise and radiation-pressure noise have been estimated without considering the quantum noise reduction effect generated by the Frequency-Dependent Squeezing (FDS) source that will also be implemented in Advanced Virgo Plus

1.4 The LIGO-Virgo-KAGRA collaboration

In the previous section, we showed that the instruments that since 2015 allowed the detection of gravitational waves are more than simple Michelson interferometers. We will conclude this chapter with an overview of the detection performances of these detectors in the past years, and on how the upgrade plans of these detectors will impact the search of gravitational waves in the near future.

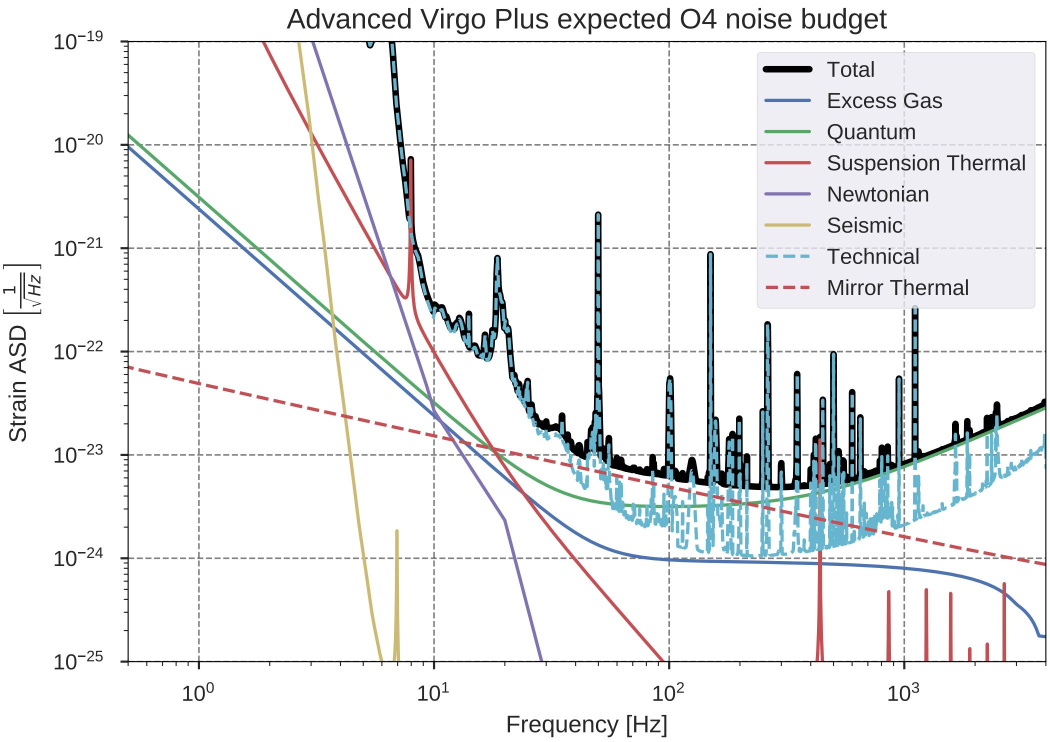

Figure 1.12: Expected noise contributions to the strain sensitivity during O4 computed with Advanced Virgo GW Interferometer Noise Calculator (AdVGWINC) ([17]). This plot, commonly called "noise budget" includes an estimate of the main contributions to the strain noise ASD. For simplicity, some contributions have been grouped and summed in a single contribution (dashed lines). For example, the "Mirror Thermal" contribution is mostly given by the mirror coating Brownian noise, but also includes contributions given by the coating's thermo-optic noise and by the substrate's Brownian and thermo-elastic noises. The "Technical" contribution is the sum of 17 different contributions given by the interferometer hardware, including the longitudinal and angular control noises.

1.4.1 A brief history of ground-based GW detectors

The history of the experimental attempts to observe gravitational waves started long before the first direct detection of gravitational waves (GW150914 [18]). The bar resonators built in the 1960s by Joseph Weber are milestones in this direction [19]. In the following years, these experiments gave origin to a series of other detectors based on the same principle, such as AURIGA, NAUTILUS, EXPLORER, NIOBE and ALLEGRO [20]. Their working principle was based on the use of a massive metallic bar (usually an aluminum alloy), with a high Q-factor mechanical resonance that amplifies and allows to measure the length variations originated by the GW.

A major breakthrough in the search for gravitational waves was achieved instead by the use of large scale interferometric detectors. The basic idea behind these instruments is to measure gravitational waves through the length variation between the two perpendicular arms of a Michelson-like interferometer. The first prototypes of meter-scale interferometric gravitational wave detectors were performed in the seventies [21].

It was soon apparent that one way to increase the sensitivity of these instruments was to increase the arm's length, allowing the gravitational wave strain to create overall more significant (and easier to measure) variations of length in the arm.

This led to the construction of larger interferometric detectors and prototypes, such as GEO600 (In Germany) and TAMA, and ultimately of the LIGO and Virgo interferometers, respectively having 4 km and 3 km long arms. The initial LIGO and Virgo interferometers construction concluded in the early 2000s and acquired data for several years without detecting gravitational waves. During this period, the interferometers were progressively upgraded in order to reach their design sensitivity. After this, in the 2010s the LIGO and Virgo interferometers were shut off for a comprehensive upgrade project, called Advanced LIGO and Advanced Virgo respectively. The upgrade of the Advanced LIGO interferometers concluded in 2015 while the upgrade of Advanced Virgo concluded in 2017.

1.4.2 The detector network and the Observing runs

There are currently four interferometers capable of reaching the extreme sensitivity required to detect gravitational waves, which are:

- The two LIGO detectors, located in Livingston (LA) and Hanford (WA), USA.
- The Virgo detector, located near Pisa, Italy
- the KAGRA detector, located in Kamioka, Japan.

Together they form the LIGO-Virgo-KAGRA (LVK) collaboration.

The joint operation of more than one detector is a fundamental requirement to consolidate the detection of gravitational wave signals. Indeed, detecting a gravitational wave with multiple detectors allows to significantly increase the confidence in the measurement (allowing to exclude the possibility of a fake gravitational-wave-like signal caused by one of the many noise sources affecting an interferometer) and to infer the astrophysical parameters of the source of gravitational-wave signal with higher precision. One of the parameters that largely depends on a multi-detector observation is the localization of the source of the signal. This dependence can be intuitively understood by considering a triangulation obtained from the delay between the signals detected by different observatories (thousands of kilometers away from each other), caused by the finite traveling speed (equal to c) of the gravitational wave.

Considering the advantages of a simultaneous operation of the interferometers, the activities of these interferometers are jointly planned and alternate between 'observing runs' and upgrade periods. The observing runs are periods in which the interferometer acquires data with minimal interventions on the detector in order to avoid disturbances on the detector and to maximize the amount of data collected.

They are alternated with periods in which the data acquisition is interrupted in order to allow upgrades of the instrument and commissioning of the new hardware. This road-map is advantageous since the technology behind the gravitational wave detectors is still in early and rapid development. Every upgrade allows a substantial increase in the sensitivity to gravitational wave signals and consequently, the rate of events detected, largely compensating for the time the detector was kept inactive due to the upgrade operations.

Since 2015, the Year in which the Advanced LIGO detectors started their first observing run and in which the first direct observation of gravitational waves GW150914 was achieved [18], three observing runs, denominated “O1”, “O2”, and “O3” respectively, have been concluded. Table 1.1 shows the periods corresponding to these observing runs and the average sensitivity of the involved detectors during the runs.

1.4.3 Current status and future prospects

Observing run	Period		Median BNS range [Mpc]			
	Begin	End	V1	H1	L1	K
O1	2015/09/18	2016/01/12	n.a.	80	80	n.a.
O2	2016/11/30	2017/08/25	30[8]	100	100	n.a.
O3a	2019/04/01	2019/10/01	45	108	135	n.a.
O3b	2019/11/01	2020/03/27	51	115	133	1 [9]
O4*	Late 2022	End of 2023	90-120	160-190	160-190	25-130
O5*	2025	2027	150-260	330	330	150+

Table 1.1: Past and future observing runs of the Advanced GW detectors and their average/estimated sensitivities during the runs. Data from [10], [4], [5], and [22].

Currently (as of late 2022), the LIGO and Virgo detectors are undergoing the commissioning of the latest upgrade phase, which started in spring 2020, after the conclusion of the O3 observing run. These upgrade projects are called “Advanced LIGO plus” (or “A+” in short) and “Advanced Virgo plus” (or “AdV+”) and will bring the detectors’ sensitivity above the design sensitivity that was initially planned for the “Advanced” project. The KAGRA detector is also performing commissioning and troubleshooting activities in order to get progressively closer to its design sensitivity[22].

The AdV+ upgrades: the AdV+ project is divided into two separate upgrade phases, the first of which is currently being implemented. In “phase one”, three major upgrades are being implemented on the Advanced Virgo detector [23]:

- Installation of the SR mirror;
- implementation of a Frequency-Dependent Squeezed FDS light source;
- increase of the power injected in the interferometer from 24 W (used in O3) to 40 W.

The joint effect of these three upgrades will reduce the shot noise affecting the interferometer at high frequencies without increasing the radiation pressure noise. In addition to these significant upgrades, the project also involves numerous interventions to reduce instrumental noises affecting the interferometer, such as stray scattered light couplings and control noises. Altogether, the upgrades will result in a net increase in the detector bandwidth and sensitivity, from the average of 50 Mpc during the O3 run to 90-120 Mpc of BNS range. An estimate of the impact of these upgrades on the detector’s strain ASD can be seen from figure 1.13, while table 1.1 shows the corresponding BNS ranges.

---

[8] Advanced Virgo joined the O2 run the first August 2017

[9] KAGRA joined the run the 25th February 2020 in a preliminary configuration [22]

The A+ upgrades: Both the LIGO detectors are undergoing ambitious upgrades, including the following key elements [24]:

- Replacement of Test Masses affected by point-absorbers on the mirror surfaces;
- increase of the injected laser power;
- implementation of a Frequency-Dependent Squeezed FDS light source;
- implementation of adaptive mode matching systems.

These upgrades focus primarily on increasing the power circulating in the arm cavities (from 200 to 400 kW) and minimizing power losses. The improvement, as shown in table 1.1 will allow an estimated increase of the BNS range from the previous 90-120 to 160-190 Mpc of BNS range.

Overall, the AdV+ and A+ upgrades will allow an estimated increase of the detected Binary Neutron Star BNS merger event rate by a factor of 10 and an increase of Binary Black Hole BBH merger events by a factor of 5 for the O4 observing run with respect to the previous observing run O3[10] [23]. Furthermore, such an improvement of the signal-to-noise ratio will allow more accuracy in the estimation of astrophysical parameters (such as the localization) of the observed sources of gravitational waves [10].

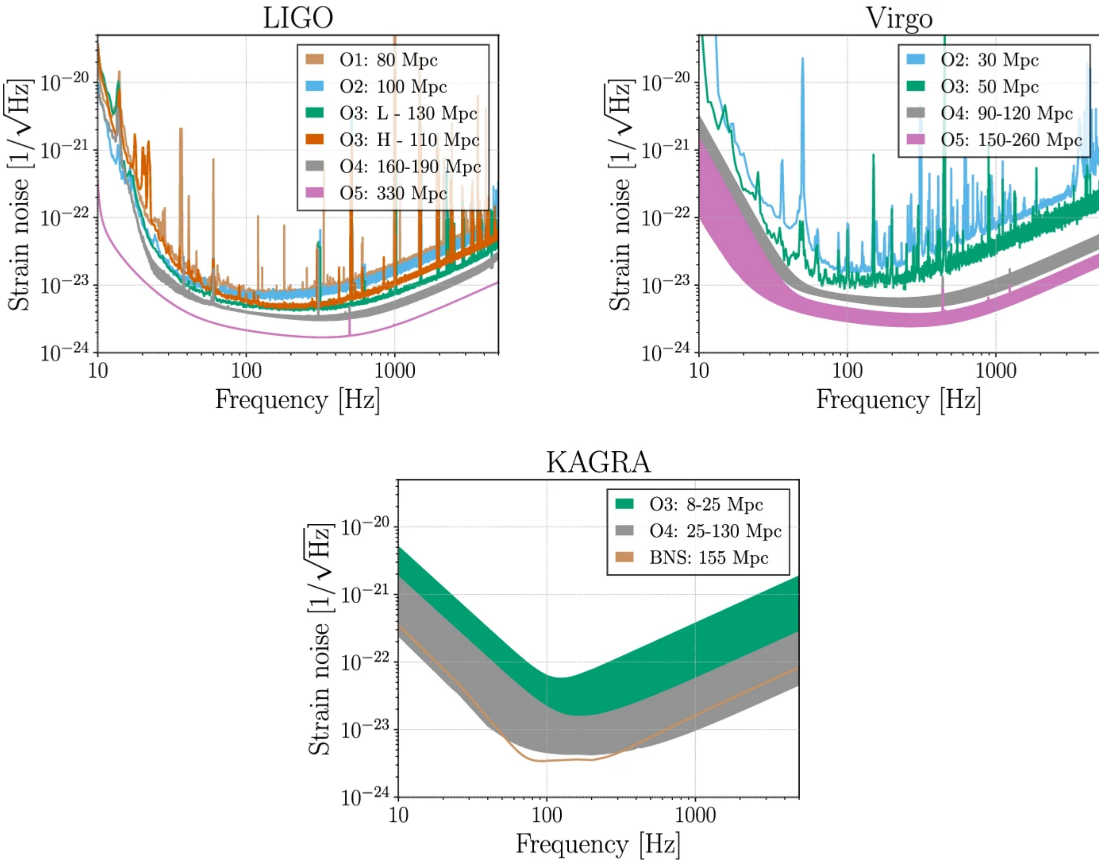

Figure 1.13: Strain sensitivity ASD curves of aLIGO (top left), AdV (top right) and KAGRA (bottom). O1 to O3 curves for AdV and aLIGO show the achieved performance in the past observing runs, while the other curves show the target sensitivities of the future runs. The legends show the BNS merger range corresponding to each curve, in Mpc. The image was created before KAGRA joined the latest part of O3 in a preliminary configuration with a sensitivty of 1 Mpc. The 'BNS' curve for Kagra corresponds to a possible detuned Signal Recycling configuration, aiming to optimize the sensitivity for BNS mergers. Image taken from From [10].

Chapter 2

Controlling a GW interferometer

The previous chapter gave an overview of the optical configuration of current ground-based GW interferometric detectors. Instead, this chapter will focus on the sensing and control systems that allow the interferometer to operate by maintaining its optical components at their optimal working point. This means controlling multiple degrees of freedom of the detector components with sufficient accuracy. A particular focus is given to the displacement and alignment of the main suspended optics that are named in figure 1.7 since the interferometer behavior is highly dependent on their motion. Indeed, despite the seismic isolation provided by complex inertial isolation systems (such as the superattenuators [25]), the suspended optics are subject to a non-negligible residual motion. This residual motion is a disturbance that hampers the correct operation of the interferometer and its capability to detect gravitational waves. Occasionally, the coupling of these disturbances with the GW strain signal can be straightforward (e.g., the differential motion of the test masses being virtually indistinguishable from the effect generated by GWs). However, most of the effects of residual motion are less obvious, and the estimation of their impact needs a deep understanding of the interferometer's optical response and the techniques used to acquire the relevant signals.

In order to suppress the residual motion and maintain the working point, several electromagnetic actuators are placed on the mirror itself and several key points of the suspensions and superattenuators. Multiple **"local"** detectors (accelerometers, Linear Variable Differential Transducerss (LVDTs), optical levers) monitor the motion of the suspension components, usually giving a measurement relative to the surrounding structure (LVDTs, optical levers). Their signals are blended and used by the "inertial damping" control system [26]. The mirror position itself is measured only by optical levers to avoid contact with other components. Local controls, however, do not allow for precisely estimating and compensating for the relative position between mirrors that are distant several kilometers from each other. The control of the relative position between mirrors on a microscopical level is essential in order to maintain the specific cavity resonance and michelson fringe conditions required for the interferometer to work. To achieve this, a **"global"** sensing system accurately measures the relative motion between the different suspended optics.

Section 2.1 will show the technique at the base of the global sensing system. This technique is an extension of the Pound-Drever-Hall (PDH) technique [27], and allows for measuring the relative displacement of the mirrors of optical resonators. We will initially show its primary usage, followed by a study of the signals produced by the double- and triple-demodulation variants. Understanding how this technique works will allow us to understand the limitations of the generated error signals, which have a linear behavior only in a very limited region.

The following section 2.2 will introduce the basics of control theory and how it is applied to design and optimize the interferometer's feedback systems.

Lastly, section 2.3 will go more into detail about the layout of the Advanced Virgo Plus detector. A particular focus will be dedicated to explaining the main interferometer longitudinal degrees of freedom since the main topic of this thesis revolves around the design and implementation of the sensing and control system for these DOFs.

One last note is that the techniques needed for the interferometer to ***reach*** its working point are as crucial and complex as the methods used to maintain it. The process of reaching the working point is commonly called **"Lock acquisition"** and will be explained in chapter 3.

2.1 Keeping an optical resonator locked

Chapter 1 showed that high-finesse FP cavities greatly enhance the response to length variations of a resonant optical field. We also observed that the linearity of their phase response rapidly decreases if the laser beam frequency deviates from the FWHM of the cavity resonance. In the general case, a deviation from resonance can be caused by a variation in the laser frequency, in the optical medium refractive index (e.g., due to temperature or pressure variations), or in the position of the cavity mirrors themselves. Most of the cavities used in GW detectors are composed of mirrors in high vacuum, so only the laser frequency noise and the residual mirror motion contribute significantly to the deviations from resonance. Actuating on either of the two allows suppressing these deviations as long as a reasonable error signal estimates the amount of correction needed.

The first step required to control an optical resonator is to obtain a reliable "*error signal*", which is a signal that allows estimating the deviation of the system from the wanted working point. In the case of a system involving a single cavity that needs to be *locked* to a laser (i.e., kept in resonance condition), the ideal error signal is proportional to the frequency difference between the laser beam and the cavity resonance.

2.1.1 Sensing the detuning of optical cavities

The PDH technique allows the generation of a signal that can be used to control the resonance of a laser beam with a single optical resonator. A generalization of this technique, involving multiple modulation and heterodyne demodulation frequencies and multiple detectors, is used to obtain error signals for the control of the multiple cavities of the interferometer[1]. Further extensions of this technique, involving the detection of high order Hermite-Gaussian modes, are also used to measure and control the alignment and mode mismatch of optical cavities[28] [15].

The generation of the error signal starts with a phase- or amplitude-modulation at radio frequency (usually from tens of kHz to tens of MHz) applied to the laser beam. The phase/amplitude modulation is, respectively, generated by either an Electro-Optic-Modulator (EOM) or an Acousto-Optic Modulator (AOM). Since the AdV+ main laser

---

[1] For simplicity, from now on we will use the "PDH-like" term to describe any signal or sideband obtained with the generalized modulation and heterodyne detection techniques used for the longitudinal controls of the interferometer.

is only modulated in phase, and since the treatment of amplitude-modulated fields would be similar, we will focus only on the treatment of phase-modulated fields. Despite the modulation being originated from a different physical phenomenon, the effect of an EOM's phase modulation is analogous to the modulation generated by the GW strain shown in equation 1.33. In particular, a phase-modulation of angular frequency ω_m has the effect of creating sideband fields shifted in frequency by a factor $\pm n\omega_m$ with respect to the original beam (commonly called "carrier"). Given a carrier field $E_0 = |E_0|e^{-i\omega_0 t}$, the modulated field can be expanded in Bessel functions, assuming the following form:

$$E_{mod} = E_{in} e^{-i\omega_0 t} \sum_{n=-\infty}^{\infty} i^n J_n[m] e^{-in\omega_m t} \tag{2.1}$$

Obviously, in this case, the modulation index m does not depend on the GW amplitude, but it depends instead on the specifics (type and size of non-linear crystal and electrodes, phase-matching, amplitude of the electric field applied by the modulation) of the EOM used to generate the sidebands. In many applications, the modulation index m is small enough so that the effect of sidebands of order $|n| > 1$ is negligible with respect to the first-order sidebands ($n = \pm 1$). However, it will be shown later that AdV+'s sensing and control systems use signals originating from second-order sidebands, especially during the lock-acquisition procedure. We will also see that, in these systems, the contributions given by third-order sidebands might not be negligible.

Extracting the error signal: In order to understand how the error signal is generated in the simple case of a single FP resonator locked to a laser, we expand equation 2.1 up to second-order sidebands:

$$E_{mod} \simeq E_{in} e^{-i\omega_0 t} \left[1 + iJ_1[m]\left(e^{-i\omega_m t} + e^{i\omega_m t}\right) - J_2[m]\left(e^{-2i\omega_m t} + e^{2i\omega_m t}\right) + O[3\omega_m]\right] \tag{2.2}$$

Where we used $J_{-n}[m] = (-1)^n J_n[m]$.

The actual sensing is performed by acquiring the field reflected by the cavity with a photodiode. Due to the different frequency of the sideband fields with respect to the carrier, the cavity reflects them with different phase and amplitude. This is represented by the term $r[\omega]$. Indeed he field reflected by the cavity assumes the form of:

$$\begin{aligned} E_{refl} = E_{in} e^{-i\omega_0 t} \Bigg[& r[\omega_0] + iJ_1[m]\left(r[\omega_0 + \omega_m] e^{-i\omega_m t + \phi_1} + r[\omega_0 - \omega_m] e^{i\omega_m t - \phi_1}\right) + \\ & - J_2[m]\left(r[\omega_0 + 2\omega_m] e^{-2i\omega_m t + \phi_2} + r[\omega_0 - 2\omega_m] e^{2i\omega_m t - \phi_2}\right)\Bigg] \end{aligned} \tag{2.3}$$

We added the generic phase therms ϕ_n to account for the different phases acquired along the propagation path by fields with different wave vectors.

The photodiode output depends on the field power P_{refl}, which is proportional to $|E_{refl}|^2$. By computing it in equation 2.4, one can notice that P_{refl} contains the products of all the different oscillating field components, having therefore beating-frequencies corresponding to the sum and differences of all the possible combinations of carrier and sideband fields. In our case therefore P_{refl} contains a $\boxed{DC}$ component, and components oscillating at $\boxed{\omega_m}$, $\boxed{2\omega_m}$, $\boxed{3\omega_m}$ and $\boxed{4\omega_m}$. Each row in the following equation (2.4) corresponds to the beating between two different components of 2.3.

$$
\begin{aligned}
\frac{P_{refl}}{P_{in}} = & \boxed{|r[\omega_0]|^2 + J_1^2\left(|r[\omega_0+\omega_m]|^2 + |r[\omega_0-\omega_m]|^2\right) + J_2^2\left(|r[\omega_0+2\omega_m]|^2 + |r[\omega_0-2\omega_m]|^2\right) +} \\
& \boxed{\begin{aligned} & + 2J_1\left(\cos[\omega_m t+\phi_1]\mathfrak{Im}[\chi_{01}] + \sin[\omega_m t+\phi_1]\mathfrak{Re}[\chi_{01}]\right) + \\ & + 2J_1J_2\left(\cos[\omega_m t+\phi_2-\phi_1]\mathfrak{Im}[\chi_{12}] + \sin[\omega_m t+\phi_2-\phi_1]\mathfrak{Re}[\chi_{12}]\right) + \end{aligned}} \\
& \boxed{\begin{aligned} & - 2J_2\left(\cos[2\omega_m t+\phi_2]\mathfrak{Re}[\chi_{02}] + \sin[2\omega_m t+\phi_2]\mathfrak{Im}[\chi_{02}]\right) + \\ & + 2J_1^2\left(\cos[2\omega_m t+2\phi_1]\mathfrak{Re}[\chi_{11}] - \sin[2\omega_m t+2\phi_1]\mathfrak{Im}[\chi_{11}]\right) + \end{aligned}} \\
& \boxed{+ 2J_1J_2\left(\cos[3\omega_m t+\phi_1+\phi_2]\mathfrak{Im}[\chi_{21}] - \sin[3\omega_m t+\phi_1+\phi_2]\mathfrak{Re}[\chi_{21}]\right) +} \\
& \boxed{+ 2J_2^2\left(\cos[4\omega_m t+2\phi_2]\mathfrak{Re}[\chi_{22}] - \sin[4\omega_m t+2\phi_2]\mathfrak{Im}[\chi_{22}]\right)}
\end{aligned}
\tag{2.4}
$$

Where we defined the χ cohefficients as the products of the FP cavity's reflection cohefficients corresponding to the involved field beatings:

$$
\begin{array}{ll}
\chi_{01} := r[\omega_0]r^*[\omega_0+\omega_m] - r^*[\omega_0]r[\omega_0-\omega_m] & \textbf{Carrier} \times \mathbf{1_{st}} \\
\chi_{11} := r[\omega_0-\omega_m]r^*[\omega_0+\omega_m] & \mathbf{1_{st}} \times \mathbf{1_{st}}(\textit{opposite sign}) \\
\chi_{02} = r[\omega_0]r^*[\omega_0+2\omega_m] - r^*[\omega_0]r[\omega_0-2\omega_m] & \textbf{Carrier} \times \mathbf{2_{nd}} \\
\chi_{12} := r[\omega_0+\omega_m]r^*[\omega_0+2\omega_m] - r^*[\omega_0-\omega_m]r[\omega_0-2\omega_m] & \mathbf{1_{st}} \times \mathbf{2_{nd}}(\textit{same sign}) \\
\chi_{21} := r[\omega_0-\omega_m]r^*[\omega_0+2\omega_m] - r^*[\omega_0+\omega_m]r[\omega_0-2\omega_m] & \mathbf{1_{st}} \times \mathbf{2_{nd}}(\textit{opposite sign}) \\
\chi_{22} := r[\omega_0-2\omega_m]r^*[\omega_0+2\omega_m] & \mathbf{2_{nd}} \times \mathbf{2_{nd}}(\textit{opposite sign})
\end{array}
\tag{2.5}
$$

These coefficients give us information on which sidebands are involved in each component of the oscillating power. For example, we can see that the ω_m oscillating components have contributions containing χ_{01} and χ_{12}, which correspond to the beating of the carrier with the first-order sidebands and of the first-order sidebands with the second-order sidebands of the same sign.

The output of the photodiode is then multiplied (using an RF mixer) with a sinusoidal signal and then low-pass filtered, demodulating the wanted frequency component. For example, by demodulating the photodiode signal at angular frequency ω_m and then filtering all the non-DC components, one would obtain a signal that depends only on the ω_m-oscillating components of P_{refl}. In other words, choosing the proper demodulation frequency allows "selecting" a specific beating frequency. The phase of the demodulating signals also has to be appropriately chosen to "select" either the real or the imaginary part of the wanted χ coefficient.

This can be graphically seen from the simulations in figure 2.1, in which we also included the third-order sideband contributions. In the first subplot (from the top), the fields of the carrier and of each sideband are represented with respect to the cavity detuning, supposing the carrier to be resonant in the origin of the plot. This allows checking the resonance points of each sideband. In the following three subplots instead, we represented the PhotoDiode (PD) signal demodulated at 1, 2, and 3 ω_m respectively (denoted as 1f, 2f, and 3f), with two different demodulation phases (I and Q) one shifted by 90°with respect to the other. Looking just at the "1f" plot, one could make a few interesting observations:

- The "I" component has three sharp and linear zero-crossings corresponding to the resonances of the carrier beam and of the 1st-order sidebands. These are a consequence of the χ_{01} coefficients in 2.4.

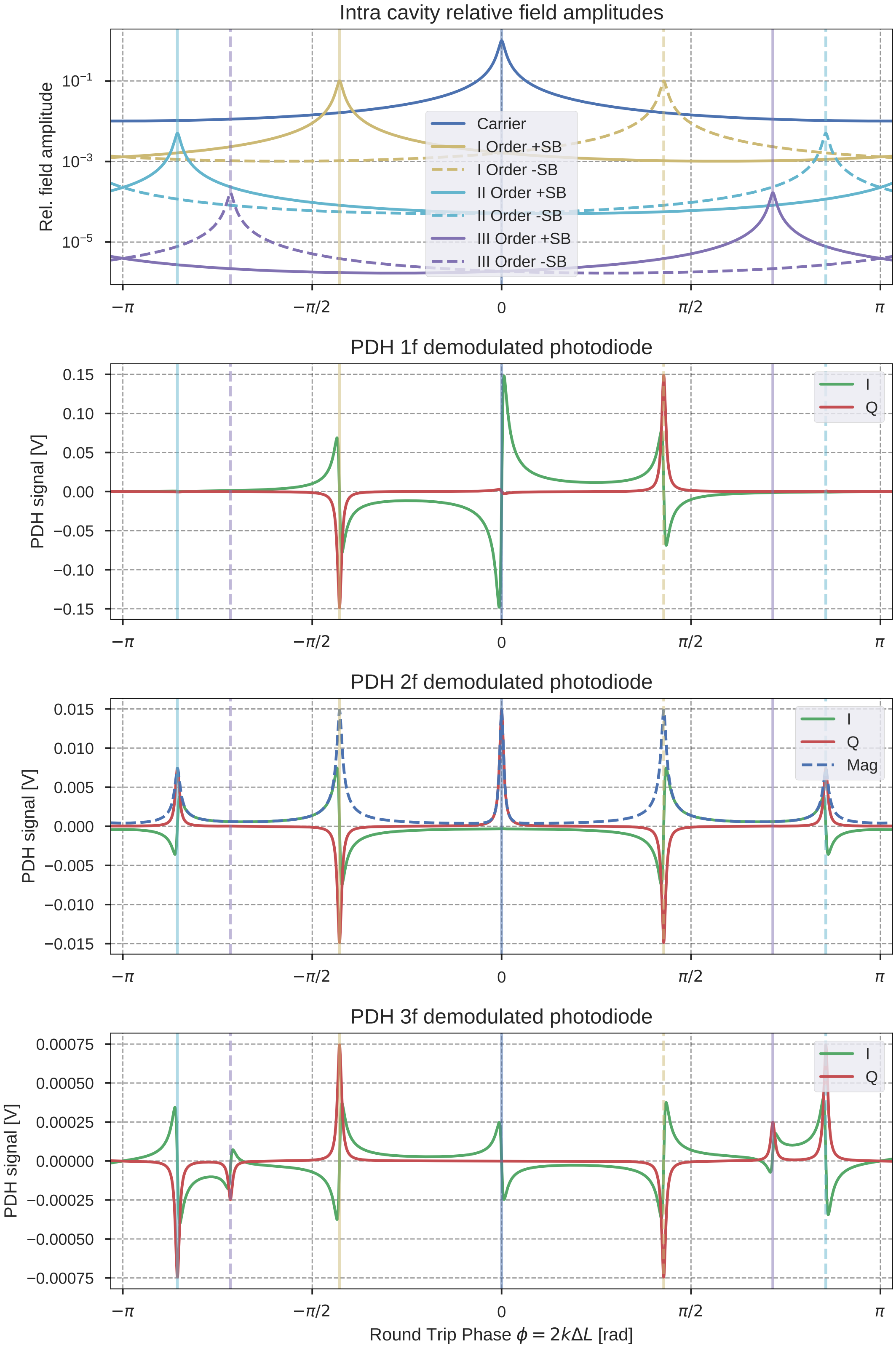

Figure 2.1: Simulated signals for the control of a generic FP cavity. The first plot (from the top) shows the intra-cavity field amplitudes of the Carrier and of the modulation sidebands up to the 3rd-order as a function of the cavity detuning. The other three plots show the corresponding I and Q demodulated signals, demodulated at one- ("1f"), two- ("2f"), or three-times ("3f") the modulation frequency, respectively.

- An additional “flat” zero-crossing is present in the anti-resonant point of the carrier (π).
- The contribution of the 2nd-order sidebands and of the χ_{12} coefficients is negligible and corresponds to a hardly noticeable step at the resonance frequency of the 2nd-order sideband. This is due to the fact that, for small modulation indices, $J_1[m] >> J_1[m]J_2[m]$. The main contribution is instead given by the beating of the carrier beam with the 1st-order sidebands, represented by the χ_{01} term.
- There should also be contributions arising from the beating of 3rd-order sidebands with the 2nd-order ones. However, they cannot be noticed in the plot due to how small the $J_3[m]$ components are with respect to the lower-order components.

Overall, one can see that very close to either the resonance of the carrier or one of the sidebands, the “1f” “I” signal can be used as an error signal to keep the cavity locked. Additionally, the width of the region in which the signal is linear is comparable with the cavity FWHM. A control system that uses these kinds of signals, therefore, can operate only when the system is close to the resonance of either the carrier or the control sidebands.

This requirement becomes even stricter in systems in which multiple coupled cavities need to be controlled, such as in gravitational interferometers. In these cases, all the DOFs need to simultaneously be near their respective working points in order for the control systems to be engaged. Therefore, a complex procedure called **“Lock acquisition”** is needed to reach the wanted working point and will be discussed in chapter 3.

2.1.2 Double (“2f”) and triple (“3f”) demodulations

We will now focus our attention of the use of the signals that can be obtained from demodulating the photodiode signals at twice or three times the modulation frequency.

“2f” signals: One of the main contributions to the “2f” signals, as shown in equation 2.4, is the beating between the first-order positive sideband with the negative one, represented by the χ_{11} cohefficient terms. Another, smaller, contribution is given by the beating of the second order sidebands with the carrier field (χ_{02} terms). These contributions create “transitions” in the “2f” signals in corrispondence to the Carrier, 1st order sideband and 2nd order sideband resonances (respectively, Blue, yellow and Cyan vertical lines in Figures 2.1and 2.2).

This behaviour is particularly useful in the case represented in figure 2.2, where the modulation frequency has been chosen as an integer multiple of the cavity FSR. In this case, all the sidebands are also resonant when the cavity is locked to the carrier resonance. This allows using the “2f” demodulated signal’s magnitude as a monitor of the sidebands resonance condition (expecially if the signal used is not the reflected field, but the intra-cavity field), which is often negatively influenced by factors such as the cavity misalignment or mismatch. Additionally, using the magnitude $\sqrt{I^2+Q^2}$ of the demodulated signals (dashed blue line in the “2f” plots of figure 2.2), allows a measurement that is independent on demodulation phase non-stationarities.

“3f” signals: As will be explained in detail in chapter 3, the “3f” demodulated signals are instead useful during the lock acquisition process. Due to their χ_{21} contribution, caused by the beating of 2nd-order sidebands with 1st-order sidebands, they show a linear transition with a sharp zero-crossing at the resonance of either the first-order (yellow vertical line) or second-order (cyan vertical lines) sidebands. In both cases of resonant and anti-resonant sidebands shown in Figures 2.2 and 2.3, these zero-crossings have a behavior similar to the “1f” signals. ‘3f” signals, therefore, allow locking the cavity, either in resonance or in anti-resonance with the carrier, even when the “1f” signals behave unpredictably. This is necessary when the phase of the carrier beam is influenced by external factors, such as during the “CARM offset reduction” phase of the lock acquisition procedure (see chapter 3). Since the signals demodulated at “3f” are mostly dependent on sideband-with-sideband beating, they are less influenced by the carrier phase-shifts and, therefore, more reliable.

One last critical observation about the “2f” and “3f” demodulated signals is that their amplitude is much smaller with respect to the “1f” signals. This means that, given a fixed amount of sensing noise (such as the shot-noise of the photodiode detecting the signal), their SNR is smaller than one of the “1f” signals. Therefore, they are sub-optimal signals in conditions in which the reintroduction of sensing noise in the control systems needs to be minimal.

2.2 Controlling Linear Time-Invariant systems

The steady-state controls of Advanced Virgo Plus are built with the assumption that, at the working point, the interferometer behaves as a Linear-Time-Invariant (LTI) system. Thanks to this, the Advanced Virgo Plus Longitudinal Sensing and Control (LSC) and Angular Sensing and Control (ASC) systems can be designed and studied in the frequency domain or s-domain, in accordance with the classical control-system theory notation. This allows representing the systems using rational transfer functions instead of differential equations.

Additionally, the coupling between the different interferometer’s DOFs is minimal, allowing a control scheme mainly based on multiple Single-Input-Single-Output (SISO) feedback loops working in parallel. Couplings between different DOFs are either minimized thanks to a ’hierarchical’ control structure or taken care of with a partial Multiple-Input-Multiple-Output (MIMO) approach. This approach, explained in section 4.3.2, involves an online subtraction of the most relevant couplings between “auxiliary” DOFs and the DARM DOF [29], which measures the GW strain. Additional subtractions of noise couplings that influence the GW strain channel are performed offline in the calibration and reconstruction process of the strain dataset [30]. This process uses measurements of the interferometer response to reconstruct the real shape of the measured GWs.

While the SISO approach partially oversimplifies the increasing complexity of a machine like Advanced Virgo, it allowed achieving a robust control of the interferometer in the past observing runs. The reliability of the lock and of the lock acquisition procedure allowed reaching 85% duty cycle during the O2 Run [31] and 75% during O3 [29]. However, the Advanced Virgo Plus upgrades introduced a significant complication to the sensing and control strategy. Indeed, the addition of the SR mirror not only introduced new angular and longitudinal DOFs that need to be controlled but also changed the couplings between other DOFs. The impact of this addition on the interferometer control scheme and lock-acquisition procedure and their re-design will be studied in

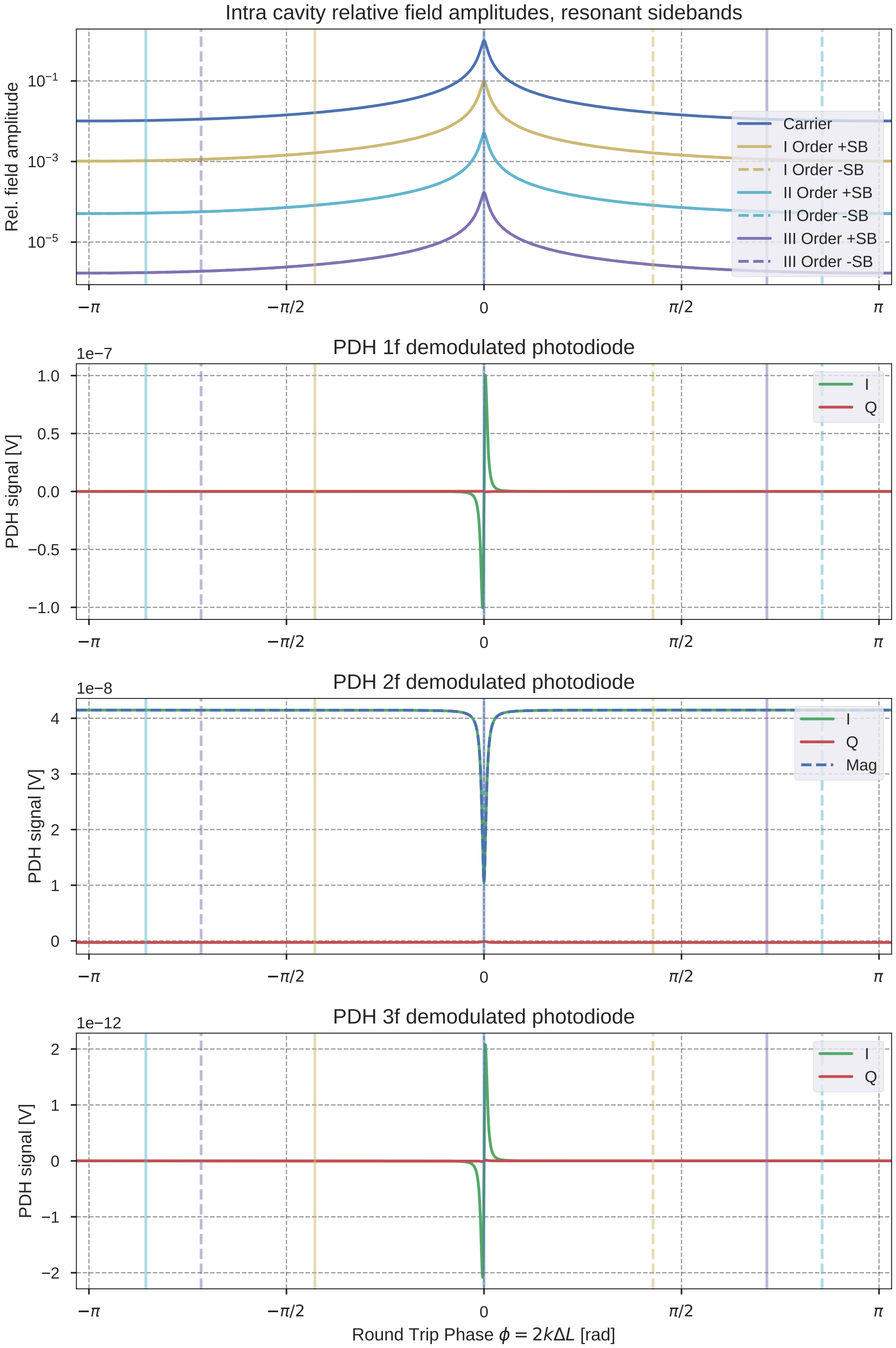

Figure 2.2: Simulated error signals for the control of a generic FP cavity with resonant odd-order sidebands. With respect to figure 2.1, the sideband frequency has been chosen to be an integer multiple of the cavity's FSR. The first plot (from the top) shows the intra-cavity field amplitudes of the Carrier and of the modulation sidebands up to the 3rd-order as a function of the cavity detuning. The other three plots show the corresponding I and Q demodulated signals, demodulated at one- ("1f"), two- ("2f"), or three-times ("3f") the modulation frequency, respectively.

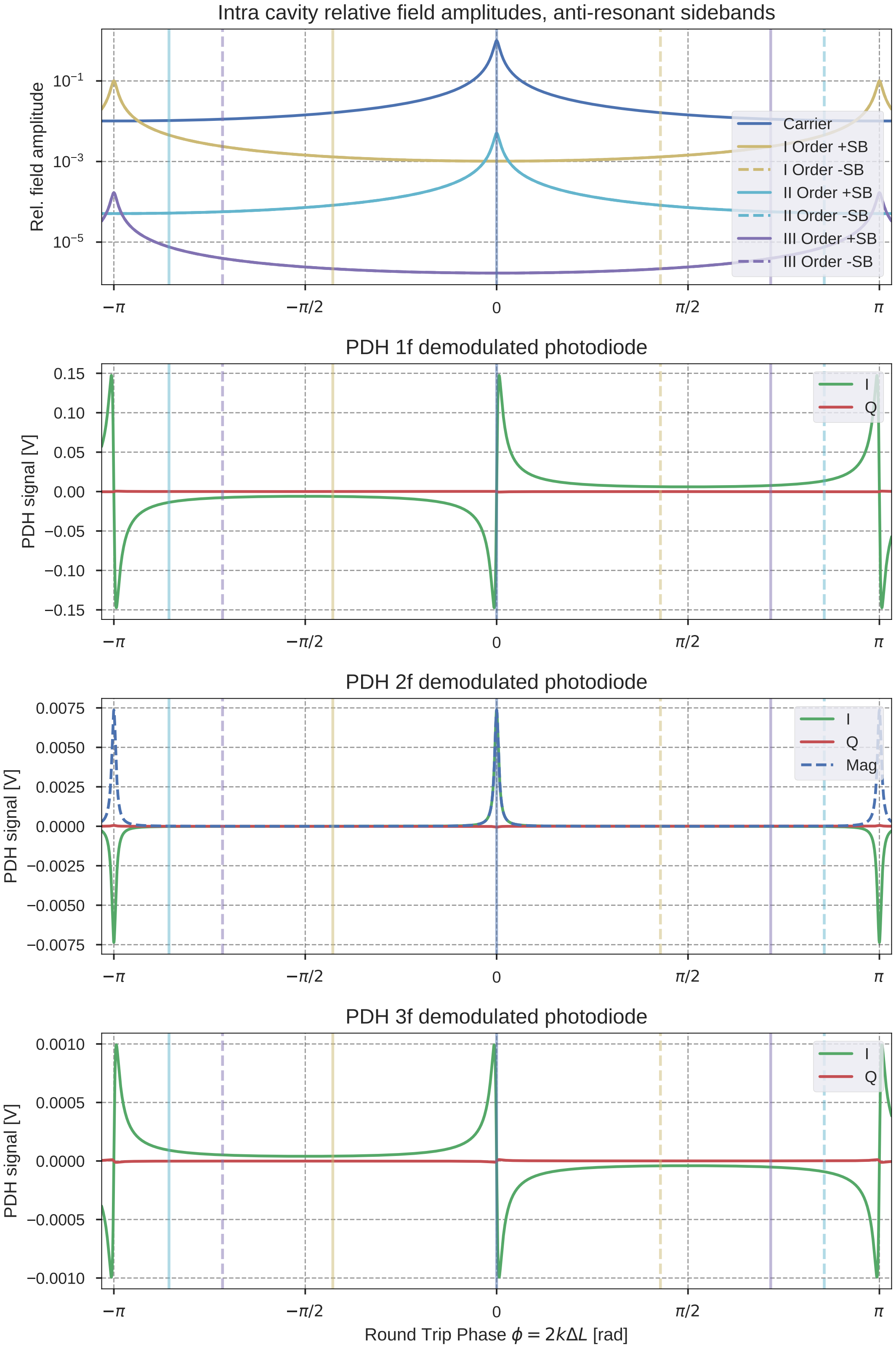

Figure 2.3: Simulated error signals for the control of a generic FP cavity with anti-resonant odd-order sidebands. With respect to figure 2.1, the sideband frequency has been chosen to be a semi-integer multiple of the cavity's FSR. The first plot (from the top) shows the intra-cavity field amplitudes of the Carrier and of the modulation sidebands up to the 3rd-order as a function of the cavity detuning. The other three plots show the corresponding I and Q demodulated signals, demodulated at one- ("1f"), two- ("2f"), or three-times ("3f") the modulation frequency, respectively.

detail in chapters 3 and 4.

While a "conservative" approach is preferred in the current upgrade plans of the Advanced Virgo Plus detector, studies on the optimization of the control systems and on the implementation of modern control theory techniques are constantly being carried on. For example, an extension of the control system design to a full MIMO state-space approach shows promising results in allowing a better estimate of the control noises affecting the interferometer strain signal [32] [33]. Alternative approaches in locking the interferometer cavities involving Time-Varying Kalman filtering ([34], [35]) and machine learning techniques [36] have also been tested on prototype setups and will be fundamental in the design of the next generation of GW interferometers, such as the Einstein Telescope and Cosmic Explorer.

In this section, we will explain the core concepts of the classical control theory, which will become helpful in the following chapters. A particular focus will be given to the challenges that are most often encountered in designing and optimizing the Advanced Virgo Plus sensing and control systems.

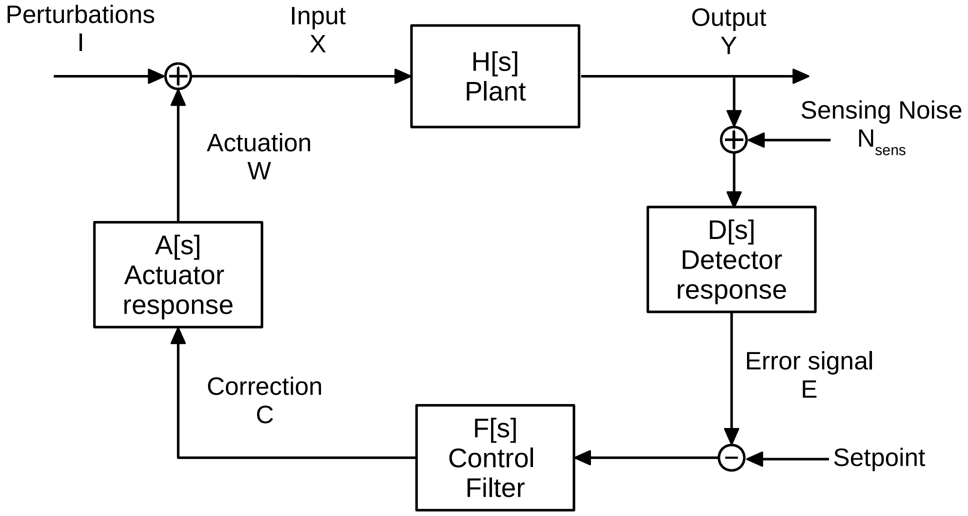

Figure 2.4: Block scheme of a generic SISO feedback loop. The plant H output state y is measured by a detector with response D and then fed-back to the plant system thanks to the actuator A. The control filter F compensates for the other components' response to obtain an overall stable plant that follows the wanted setpoint with the desired performance characteristics.

Some notes on the notation: We use lowercase letters for the signals in the time-domain and the impulse response of LTI systems. We use uppercase letters for the system's transfer functions (either in the s or in the frequency domain). Additionally, we indicate the ASD of the signal u with S_{uu}. Figure 2.4 shows the representation of a simple LTI SISO system with a feedback loop. The terminology used in this figure and in the following chapters is explained below:

- An external perturbation i. It can be a noise affecting the system, a signal, or a superposition of both.

- The system input $x = i + w$, given by the sum of the external perturbation with the actuation w.

- The Plant H, representing the physical system, with impulse response h, that has an output y linearly depending on its input x. In time domain this can be represented as $y[t] = h[t] * x[t] = \int_{-\infty}^{+\infty} h[\tau]x[t-\tau]d\tau$. In frequency domain their ASDs are therefore related by the transfer following transfer functions: $S_{yy}[\omega] = |H[\omega]|S_{xx}[\omega]$.

- The actuation w applied by the actuator A on the system input.

- The correction c, computed by applying the control filter to the error signal.

- the correction filter F, chosen according to performance, stability, and robustness criteria, to generate the correction c.

- The setpoint subtracted from the error signal to keep the system at the desired working point.

- The error signal e, which is a measurement of the status of the system performed by a detector D that measures the system output, giving $S_{ee} = |D|S_{yy}$.

Another important definition is the Open-Loop Transfer Function (OLTF) definition. Its usefulness is related to assessing the stability of the servo loop and will be clarified in the next paragraph. The OLTF is defined as follows:

$$OL := H \cdot D \cdot F \cdot A \tag{2.6}$$

Using the OLTF, it is also possible to define the Closed-Loop Transfer Function (CLTF). It is straightforward to check that, in the absence of additional noises, the CLTF gives the relation between the output of the system and the external input:

$$CL := \frac{Y}{I} = \frac{H}{1 - OL} \tag{2.7}$$

Stability Criterion: In the design of a servo loop, several figures of merit are taken into consideration, depending on the overall influence of the controlled DOF on the interferometer performance. Usual parameters considered in evaluating the **performance** of a servo loop are:

- The overall residual displacement with respect to a fixed setpoint;

- the actuation bandwidth of the loop;

- the capability of suppressing the motion in specific frequency bands, which are either particularly affected by external perturbations or highly coupled to the GW strain channel;

- the introduction of additional noises, for example, due to sensing noise affecting the error signal or to noises introduced by the actuators.

In addition to the **performance** characteristics, a major factor that needs to be taken into consideration is the **relative stability** and **robustness** of the loop. This means assessing the conditions under which the system is **stable**[2], taking into consideration the uncertainties given by disturbances affecting the system response and signals.

The first step is to model the system in ideal conditions, that is, with perfect linearity of all the system components and signals, no saturation of actuators or detectors, and perfect stationarity. Once the loop frequency response has been modeled, the stability of the ideal loop is evaluated in the s-domain according to the Nyquist stability criterion[37] [38]. Another helpful tool is the Bode plot of the OLTF. Using the Bode plots, one can intuitively visualize the **gain margin** and **phase margin** of the system, which are defined as follows:

- The Gain Margin (GM): It is defined as the amount of increase or decrease in gain that the system can withstand while remaining stable. It can be visualized on a Bode plot such as in figure 2.5 by looking at the OLTF magnitude at the **phase crossover frequency** ν_{-180}, where the phase is equal to -180°. If the OLTF magnitude in that point is < 1, the system is stable and $GM = 1/|OLTF[\nu_{-180}]|$.

- The Phase Margin (PM): Similarly, it can be estimated by looking at the OLTF phase at the frequency where the OLTF magnitude is equal to 1 (or 0 dB), called the **gain crossover frequency**, or the Unity Gain Frequency (UGF). It is defined as $PM = 180 + \phi[OLTF[UGF]]$, and the system is stable if it is positive.

The greater the gain and phase margins are, the more the system will be robust and capable of withstanding fluctuations in the plant transfer function without becoming unstable.

The Bode stability criterion becomes less straightforward to apply in cases where there are multiple phase crossover or gain crossover frequencies. It is preferable to use the more general Nyquist criterium in those cases instead. This is performed with the help of Nyquist or Nichols plots (figure 2.6), which also allow a better understanding of the system's behavior ([38, chapter 9.5]).

Real systems and noises: The loop's stability is just one of the factors that need to be considered in the design of a feedback system. The design of the controller also needs to take into consideration several other aspects of the system, which cannot be easily modeled in the frequency domain, such as the limitations of the actuators and detectors. Indeed, in an ideal LTI system, the actuators and detectors have an infinite dynamic range, which means that the actuators are capable of applying any amount of correction and that the detectors detect any state of the system while remaining linear. In a real system, instead, both the actuators and the detectors behave linearly only in a specific range, as shown in the examples in section 2.1 for the signals detected using PDH-like techniques. Therefore, these limitations need to be taken into consideration in the design process. For example, the amount of actuation required to satisfy specific performance requirements can be obtained by projecting an estimate of the noises

---

[2] This means satisfying a Bound-Input-Bound-Output (BIBO) stability condition, that is to say having a non-infinite output given any non-infinite input to the system.

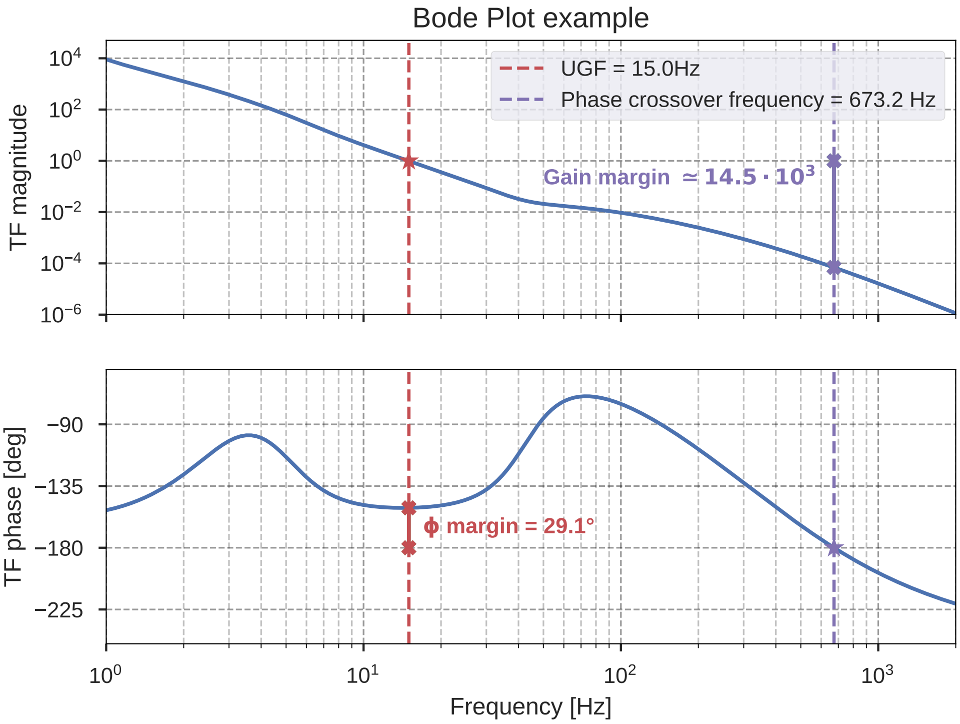

Figure 2.5: Example of Bode Plot of a stable system's OLTF. Stars and vertical dashed lines mark the UGF and the phase crossover frequency.

affecting the system given a particular controller. The input noise S_{ii} contribution to the actuation ASD is given by:

$$S^{i}_{ww} = |OL|S_{xx} = \left|\frac{OL}{1+OL}\right| S_{ii} \tag{2.8}$$

In frequency regions in which the loop gain is high, $(1 + OL) \simeq OL$. This means that $S_{ww} \simeq S_{ii}$ or, in more intuitive terms, that the actuation mirrors the input noise in order to cancel it. An estimate of the input noise Root Mean Square (RMS) in the actuation range $\sqrt{\int_{\omega_{min}}^{\omega_{max}} |S_{ii}[\omega]|^2 d\omega}$ allows, therefore, to predict the minimum required dynamics of an actuator that cancels that noise.

In the case of non-negligible sensing noises, those need to be considered. Their contribution can easily be estimated by

$$S^{n_s}_{aa} = |F \cdot A|S_{ee} = \left|\frac{D \cdot F \cdot A}{1+OL}\right| S_{n_s n_s} \tag{2.9}$$

One can also observe that in this case, the sensing noise contribution on the actuation $S^{n_s}_{aa}$ and on the input of the system $S^{n_s}_{xx}$ is exceptionally high when the gain of the plant H is small and is compensated by a relatively high gain on the feedback loop system $(D \cdot F \cdot A)$. This shows the importance of using error signals with the highest possible SNR. The error signals SNR will indeed be one of the prominent figures of merit used in choosing the error signals used in chapter 4.

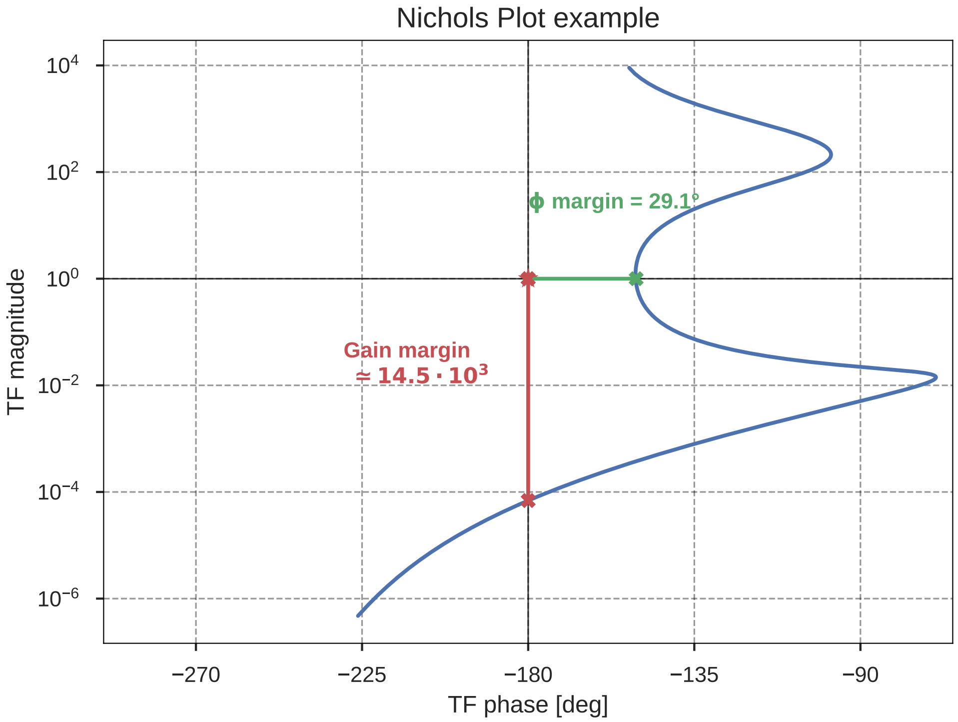

Figure 2.6: Example of Nichols Plot of the same system visualized in 2.5. Coloured lines show the gain and phase margins. An additional special grid can be added to also visualize the corresponding closed loop transfer function gains.

2.3 Advanced Virgo Plus Sensing and Control

We conclude this chapter with an overview of the longitudinal control scheme of Advanced Virgo Plus. By “Longitudinal” control, we mean controlling the interferometer’s suspended mirrors’ position in the direction orthogonal to the reflective surface (at the center of the mirror for curved mirrors). This direction is commonly referred to as the z-axis in the mirror’s reference system, while the x and y axes correspond to shifts in the transversal directions of the beam. The phase of the reflected beam depends much more on the longitudinal than on the transversal directions. Therefore, the latter are controlled with much broader accuracy requirements by local control systems which will not be treated in this thesis. Additionally, the LSC scheme involves the control of the main laser frequency since it is highly coupled with every longitudinal DOF.

While this thesis will focus mostly on the longitudinal DOFs, we should note that a full definition of the “interferometer working point” would require to take in consideration also the other DOFs. Indeed, to achieve an optimal sensitivity, the angular and transverse mode matching DOFs need also to be optimized. The first ones involve the control of the mirrors’ tilt and the consequent tilt and shift of the laser beam. They are controlled by the ASC system[29] [15].

The mode-matching DOFs are instead tuned statically, by telescopes, and dynamically, thanks to the Thermal Compensation System (TCS)[39] [40].

Before we go into the details of the LSC scheme, we introduce the main optical scheme of the interferometer, based on the DRFPMI configuration shown in figure 1.7.

2.3.1 The AdV+ Optical scheme

Figure 2.7 shows the main optical layout of the Advanced Virgo Plus interferometer. While still being a simplified representation, not showing the detailed layout of each optical bench, it shows most of the components that compose or directly interact with the LSC loops. Most of the additions to the DRFPMI optical layout (explained in chapter 1) are located before the symmetric or after the antisymmetric ports of the interferometer. These are part of the laser “injection system” or part of the “detection system” respectively.

Preparing the beam: Before entering the interferometer through the symmetric port, the laser beam must be generated and “prepared”. Indeed, to obtain optimal performance, the injected beam needs to satisfy stringent prerequisites, such as:

- High and stable continuous power (~ 40 W);
- Gaussian transverse beam profile and optimal mode-matching with the interferometer cavities;
- beam pointing stability;
- laser line-width and frequency stability;
- phase-modulation sidebands used for the control of the interferometer.

These requisites are satisfied thanks to the Laser and Injection systems.

Laser system: the main laser beam is generated by a Neodymium-doped Yttrium Aluminum Garnet (Nd:YAG) Non-Planar Ring Oscillator (NPRO) fibered seed, producing ~ 25 mW of continuous laser radiation at 1064 nm. The beam is then amplified thanks to two consecutive fiber amplifiers, up to a maximum power of ~ 100 W (currently, the planned interferometer input power is ~ 40 W). The beam is then injected into a 14cm-long Pre Mode Cleaner (PMC) cavity, which performs a preliminary cleaning of high order modes generated by the laser system and a reduction of the beam jitter.

In addition to this, the laser system contains a power stabilization system and three actuators that allow controlling the laser frequency. These three actuators work in three different frequency bands, allowing them to reach a bandwidth of a few hundred kHz:

- Thermal actuator: controls the temperature of the main laser crystal, allowing for high-dynamic, low-frequency (up to 50 mHz) corrections.
- Piezo actuator: a piezoelectric crystal directly bound to the seed laser crystal, allowing a mid-frequency (up to 30 kHz) range actuation.
- Electro-Optic-Modulator: the phase of the laser beam is modulated with the use of an EOM. This allows a high-frequency (up to 500 kHz) actuation on the main laser frequency.

As shown in more detail later, these actuators are also used by one of the most critical LSC control loops: the Second Stage Frequency Stabilization (SSFS) system.

Injection system: The injection system is the last step before the laser beam is injected at the symmetric port through the power recycling mirror. It ensures that

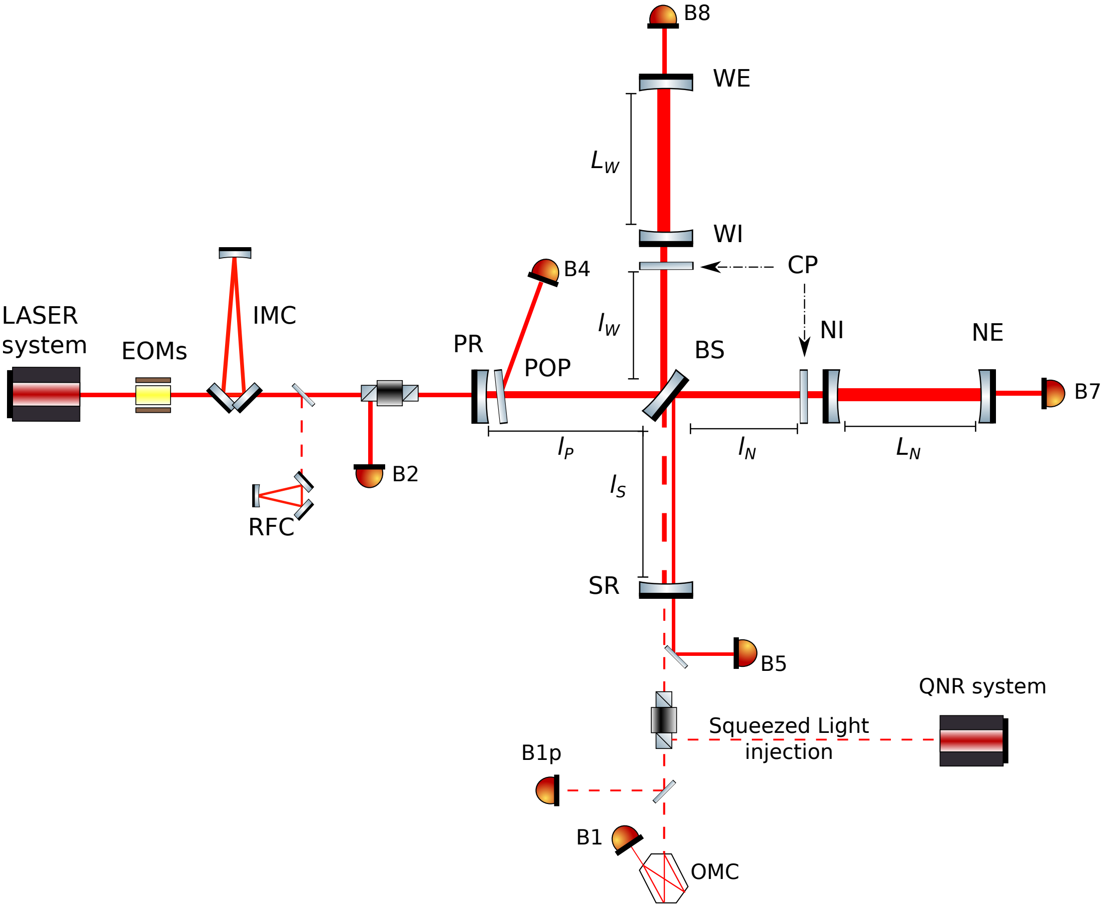

Figure 2.7: Advanced Virgo Plus main optical conceptual layout. The scheme shows the main suspended optics (PR, SR, BS, North Input (NI), West Input (WI), North End (NE), and West End (WE)) in a DRFPMI configuration, with the nomenclature of the relative longitudinal distances between them. All these optics have a diameter of 35 cm, except for the BS, which has a diameter of 55 cm instead. The position of the two Compensation Plates Compensation Plate (CP) and of the Pick-Off-Plate (POP) is also shown. In addition to the suspended optics, a simplified layout of the laser injection and of the detection systems is included. This allows to locate the main interferometer detected beams (B1, B1p B2, B4, B5, B7, B8), the control-sideband generating EOMs, the Input Mode Cleaner (IMC), the Output Mode Cleaner (OMC), and the ReFerence Cavity (RFC). The injection towards the antisymmetric port of the squeezed light generated by the Quantum Noise Reduction (QNR) system is also shown.

the beam is delivered to the interferometer with the correct geometrical shape (TEM_{00} mode, matched with the interferometer mode), power, frequency, and angular stability.

Three components of the injection system interact with the LSC system and are shown in figure 2.7:

- The IMC: It is a triangular cavity ($\simeq$ 140 m height, 8.65 cm base) with a suspended mirror, which main scope (as the name says) is to reflect the non-gaussian components of the beam. Additionally, it acts as a length reference for the preliminary laser frequency stabilization loop.

- The RFC: an additional $\sim$ 30 cm-long cavity with high seismic isolation and thermal stability characteristics, acting as an additional length reference for the frequency stabilization loops.

- The Control sideband EOMs: three different sidebands (see next paragraph) are used by the LSC system and the Angular Sensing and Control ASC system. Additional sidebands are used for the control of the IMC and PMC cavities. Two EOMs in the injection system generate them.

Another integral component of the injection system is the Beam Pointing Control (BPC) [41], aimed at monitoring and further suppressing the input beam jitter before the injection in the IMC. Without suppression, the beam jitter would spoil the functionality of the main interferometer angular control loops and, ultimately, the detector sensitivity. The jitter suppression is achieved thanks to two DC quadrant photodetectors which precisely monitor the beam jitter generating error signals for a jitter-suppression feedback loop. The loop actuates on the beam using two piezoelectric steering mirrors, reaching a control accuracy of 0.5 μrad RMS and 20 μm RMS for the beam tilt and shift, respectively [29].

Detection system: The gravitational-wave strain signal is obtained from the beam going out from the interferometer's antisymmetric port. However, before the photodiodes acquire it, the beam passes through an optical bench, which main components are the OMC, a mode-matching telescope, and a Faraday isolator that also allows the coupling of the interferometer beam with the squeezed-light arriving from the QNR system. The OMC is required to avoid the strain signal being affected by the control sidebands and the high-order Transverse ElectroMagnetic (TEM) modes of the field coming out of the interferometer. This signal is indeed acquired by low-noise DC photodiodes, which would otherwise not be able to reject those components.

The detection system also manages the acquisition of multiple other beams used to diagnose and measure the status of the interferometer components. These beams are shown in figure 2.7 and listed as follows:

- B1: Transmission from the OMC. Contains the GW strain signal.

- B1p: Pickoff before the OMC, used in the longitudinal and angular control of the interferometer.

- B2: Beam reflected by the interferometer at the Symmetric port. It is separated from the in-going beam by a Faraday insulator.

- B4: Beam circulating inside the PRC. It is acquired using a tilted PickOff Plate POP that reflects a small percentage of the circulating light.

- B5: Beam reflected by the antireflective surface of the interferometer beamsplitter. It is separated from the main interferometer beam (B1) in the detection bench.

- B7 and B8: Beam transmitted by the North arm and West arm end mirrors, respectively, which have a transmissivity of ∼ 4ppm.

PickOff and Compensation Plates: The last unmentioned components denoted in figure 2.7 are the PickOff Plate POP and the two Compensation Plates CP. The POP is a 3.5 cm-thick transparent plate inserted in the PR cavity, suspended together with the PR mirror. It has a tilted surface with a small reflectivity (∼ 200 ppm), which allows extracting a small part of the intra-cavity field, creating the B4 beam.

The CPs instead are completely anti-reflective 3.5 cm-thick plates placed behind the North and West arm input mirrors. These plates are heated by CO_2 lasers, generating a tunable thermal lens in the PR and SR cavities. These plates are part of the TCS [40] and help compensate for the thermal effects generated by the main laser beam, keeping an optimal mode-matching of these cavities with the arm-cavity field.

2.3.2 Longitudinal DOFs

Finally, we can define main longitudinal DOFs of Advanced Virgo Plus. Instead of focusing on the displacement of each mirror in a single-mirror basis, it is indeed much more convenient to refactor them according to the following basis:

$$DARM := L_N - L_W \tag{2.10}$$

$$MICH := l_n - l_w \tag{2.11}$$

$$CARM := \frac{L_N + L_W}{2} \tag{2.12}$$

$$PRCL := l_P + \frac{l_n + l_w}{2} \tag{2.13}$$

$$SRCL := l_S + \frac{l_n + l_w}{2} \tag{2.14}$$

Where we used the lengths defined in figure 2.7 and table 2.1.

In addition to these five, the frequency of the main laser is also included in the LSC DOFs, and its corresponding DOF is usually denominated SSFS, from the name of the Second Stage Frequency Stabilisation control loop controlling it. This basis is also helpful in relating the displacements of each DOF to the relevant optical cavities (DARM and CARM for the arm cavities, Signal Recycling Cavity Length (SRCL) for the SR cavity, Power Recycling Cavity Length (PRCL) for the PR cavity). Using the optical distances between components in table 2.1, one could indeed compute the lengths and FSR of the following cavities, obtaining an FSR of 49968.74 Hz for the arm cavities and of 12541554.00 Hz for the SR and PR cavities.

Additionally, as will be shown in detail in chapter 4, this basis allows a quasi-diagonal sensing matrix, with a few notable non-diagonal contributions.

A single SISO loop controls each of the LSC DOFs, but the actuation needs to be re-distributed between the single mirrors and the laser frequency actuators, according

Name	Length [m]
L_N	2999.8
L_W	2999.8
l_n	6.0152
l_w	5.7851
l_p	6.0518
l_s	6.0518

Table 2.1: Optical distances between the Advanced Virgo Plus's suspended optics

to the following Driving Matrix:

$$\begin{pmatrix} NE \\ WE \\ NI \\ WI \\ BS \\ PR \\ SR \\ \delta\nu \end{pmatrix} = \begin{pmatrix} 1^* & 0.5 & 0 & 0 & 0 \\ 1^* & -0.5 & 0 & 0 & 0 \\ 0 & 0 & 0 & 0 & 0 \\ 0 & 0 & 0 & 0 & 0 \\ 0 & 0 & \frac{1}{\sqrt{2}} & 0 & 0 \\ 0 & 0 & -0.5 & 1 & 0 \\ 0 & 0 & -0.5 & 0 & -1 \\ 1 & 0 & 0 & 0 & 0 \end{pmatrix} \begin{pmatrix} CARM/SSFS \\ DARM \\ MICH \\ PRCL \\ SRCL \end{pmatrix} \tag{2.15}$$

A few insightful observations can be made from the driving matrix 2.15:

- The CARM and SSFS DOFs have been put together since they are virtually degenerate. Chapter 4 will show that their error signal is equally affected by either a laser frequency change or by a common arm length variation.

- The contributions of CARM to the WE and NE mirror actuation are marked by a "*" to denote the fact that this actuation is not always active. In the steady-state, actuating only on the laser frequency is enough to compensate for most of the effects of a CARM displacement.

- The input mirrors (NI and WI) are not controlled by the LSC loops. Their motion is still mitigated by the local controls, and the residual motion is compensated by the other mirrors, leaving the LSC DOFs lengths unaffected.

- The differential small MICHelson length (MICH) is mainly compensated by the movement of the beam splitter. However, in order to compensate for the BS motion's effect on the length of the SR and PR cavities, the MICH DOF needs to actuate on the SR and PR mirrors too.

- The recycling mirrors' driving matrix terms have opposite signs due to a convention in the mirror motion directions. The convention defines a motion opposite to the beam propagation as a positive mirror motion. Since the beam enters the interferometer through the PR mirror, a positive PR motion means increasing l_p and PRCL. On the other hand, since the beam exits the interferometers through the SR mirror, a positive SR motion means decreasing l_s and SRCL, hence the negative sign in the driving matrix.

2.3.3 Control sidebands

As seen in section 2.3.1 and in figure 2.7, the AdV+ interferometer includes multiple output ports in which broadband photodiodes probe the laser beam.

To generate the heterodyne signals at these ports, the main laser is modulated by two EOMs at four different modulation frequencies. Three of these sidebands are transmitted by the input mode cleaner and are available for Interferometer Sensing and Control (ISC) purposes, the fourth one (22 MHz) is reflected by the IMC.

In order to provide helpful information, the modulation frequencies of these sidebands have been chosen carefully. In particular, the sidebands need to be fully transmitted by the Input Mode Cleaner IMC, be anti-resonant to the arm cavities, and are defined to follow these additional conditions, as schematized in figure 2.8:

- **f1 = 6 270 777 Hz:** resonates only in the PR cavity;
- **f2 = 9·f1 = 56 436 993 Hz:** resonates both in the PR and SR cavities;
- **f3 = 8 361 036 Hz:** not resonant in any cavity of the main interferometer.

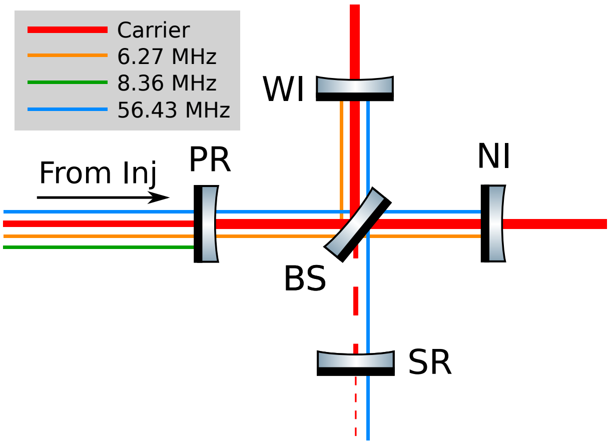

Figure 2.8: AdV + central interferometer layout. Colored lines indicate the resonance of the sidebands used by the LSC and ASC control loops.

2.4 Conclusions:

In this chapter, we established a common ground by giving the basics of the techniques used to sense and control the main interferometer optics. We also defined the AdV+ longitudinal degrees of freedom and their relation with the suspended optics.

Chapter 3 will overview the new lock acquisition technique implemented during 2021-2022 commissioning. This technique allows for the LSC DOFs to reach their operating point. Chapter 4 will report the studies concerning the accuracy requirements and the error signals for each LSC DOF in the Advanced Virgo Plus detector.

Chapter 3

Locking the detector

During the operation of a GW interferometer, external influences (e.g., earthquakes, storms, anthropic activity) or instrumental faults can disturb the operativity of the interferometer's control systems. The disturbances can reach the point of making the loops unable to keep one or more DOFs at their optimal working point. This usually creates a "chain reaction" that makes most of the ISC loops fail and causes what is commonly called a *"lock-loss"*. In order to recover the working point of the interferometer after a lock loss or to reach it in the first place at the beginning of the detector's operations, a procedure called **"lock acquisition"** needs to be executed. To avoid mistakes in the large number of operations involved in the procedure, the lock acquisition is, for the largest part, automated.

Due to the changes implemented during the AdV+ upgrade, the lock acquisition procedure used during the previous runs [42] [43] [15] is no longer applicable. We designed therefore a new lock acquisition technique [44][23], based on the one used in the Advanced LIGO detectors [45]. This work started a few years before the actual implementation of the upgrades and many members of the ISC and other commissioning teams were involved both in the design and in the commissioning activities.

This chapter will present the new lock acquisition procedure in detail. A particular focus will be given to the new problems studied with the ISC team during the design process and to the main challenges met during the implementation and commissioning of the procedure.

In particular:

Section 3.1 gives an overview of the main challenges of locking a DRFPMI and of the steps involved in the new AdV+ lock-acquisition technique.

Section 3.2 focuses on the lock of the arm FP cavities during the early stages of the lock acquisition procedure. It will also contain an overview of the new Auxiliary Laser System (ALS) used to lock the arm FP cavities independently from the main laser.

Section 3.3 draws attention to the procedure of locking the Central InTerFerometer (CITF), which consists of the DRMI given by the exclusion of the arm cavities from the complete DRFPMI. Most simulation studies concerning the lock acquisition focused on this critical step.

Section 3.4 focuses instead on the latest stages of the lock acquisition, in which the arm FP cavities are slowly being put back into resonance to achieve the final working point.

3.1 AdV+ lock acquisition procedure overview

Until all the global control loops are engaged, the local controls govern the motion of the various interferometer DOFs. Since their accuracy is limited, the residual mirror motion causes the DOFs to travel unpredictably in and out of their respective working points. At the same time, the corresponding cavities go in and out of the resonance condition. Furthermore, for most DOFs, the average residual motion amplitude (when unlocked) is much larger than the region in which the global controls can be engaged. This means that each control loop can be engaged with success only during very brief and unpredictable time windows. For example, plot 3.1 shows the North Arm cavity transmission just before a lock (at second 18). The moments in which a loop can be engaged with success are defined by a boolean "trigger" signal, which is different from zero only when certain conditions are satisfied. Trigger signals are usually obtained by putting a minimum threshold in the transmitted or inner circulating power of the relevant cavities. In the case shown in figure 3.1, the trigger signal becomes positive when the transmitted power is above 0.1 mW. This happens an average of once per second, and the trigger has a duty cycle of $\simeq 1.5\%$. More complex trigger signals can be obtained from the "2f" sideband signals or the combination of multiple signals. Combining different signals is needed when multiple resonance conditions have to be satisfied as will be shown later in this chapter for the lock of the CITF.

An additional issue is that the various DOFs are not completely independent one from another and, therefore, it is not possible to lock them in any order. For example, the carrier field inside the CITF is highly affected by the reflection of the arm FP cavities. As shown in figure 1.6, every time an arm cavity passes through its resonance peak, the phase of the reflected field shifts by π, completely changing the overall round trip phase shift of the recycling cavities. Keeping the recycling cavities locked on the carrier field while the arm cavities are still unlocked is therefore problematic. At the same time, locking the CITF with the arms locked on the main laser would not be possible due to the large power and phase transients in the carrier beam caused by the PRCL lock.

Locking all the DOFs at the same time is equally unpractical due to the unpredictability of every single DOF's motion, making the simultaneous triggering of all the loops extremely unlikely. Additionally, the dynamical effects that (as will be explained in section 3.2.1) make the lock of the arm FP cavities particularly challenging would be severely magnified in case of a simultaneous lock with the PR cavity due to the higher power involved.

The consequence of these limitations is that building a lock acquisition procedure means finding ways to temporarily decouple the various DOFs, allowing for locking them independently. This decoupling, however, often means that the interferometer configuration is changed during the lock acquisition, either by turning mirrors or by bringing cavities off-resonance. Another challenge of the procedure is, therefore, to bring the interferometer to the default configuration while maintaining the lock.

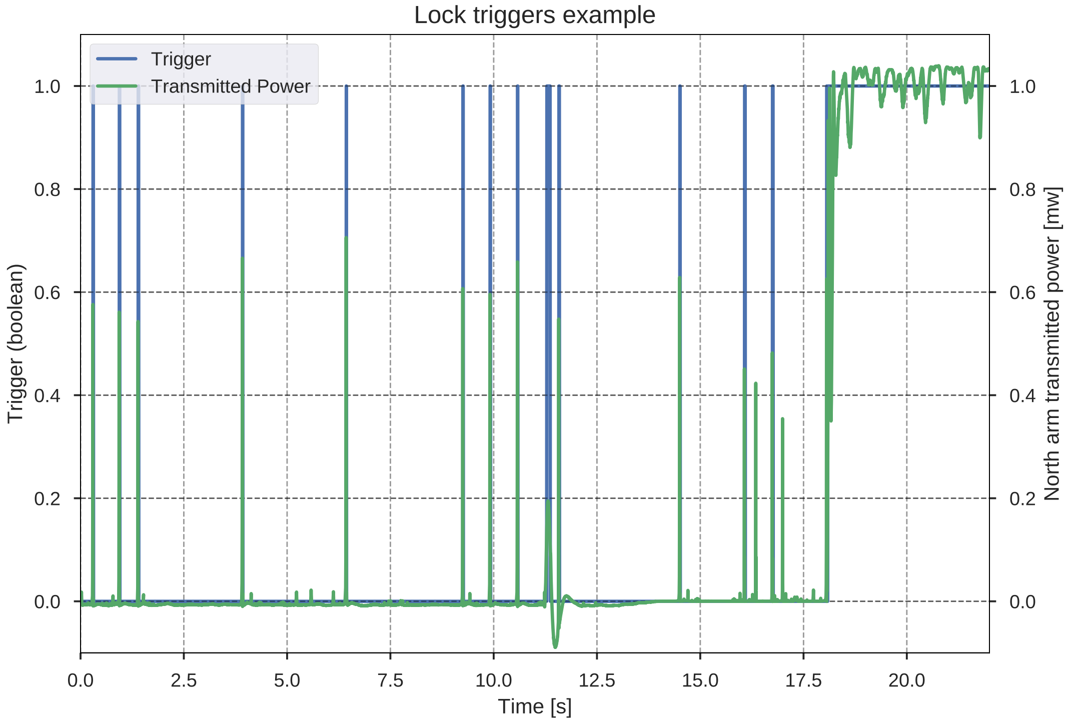

Figure 3.1: Example of the behavior of an FP cavity before and just after the lock. Before the lock, we can notice the random power spikes in the transmitted power, corresponding to the resonance peaks. A simple boolean trigger signal determines the moments when the lock can be engaged by setting a threshold on the transmitted power.

3.1.1 Main steps

The lock acquisition of AdV+ can be summarized by the following steps:

- Independent lock of the arm cavities on the IR beam;
- Lock of the arm cavities with the ALS and addition of CARM offset;
- lock of the CITF;
- progressive reduction of the CARM offset;
- engagement of the SSFS loop and of the steady-state controls at CARM offset zero;
- addition of the DARM DC offset and lock of the OMC;
- engagement of low-noise controls and injection of squeezed vacuum.

The following sections will explain the operations corresponding to each of these steps.

3.1.2 Starting conditions

Due to the reliability and relative simplicity (compared with the full interferometer's complexity) of the laser pre-stabilization and injection system, the lock of these systems is usually not considered part of the main lock acquisition procedure. It is separately automated and considered a prerequisite to check before the beginning of the lock of the main interferometer. This prerequisite includes the following sub-conditions:

- Operativity of the main laser seed and amplification chain;
- lock of the PMC;
- operativity of the laser Power STABilization (PSTAB) system;
- lock of the laser pre-stabilization system, including the IMC and RFC cavities (as shown in Figure 3.3).;
- operativity of the BPC systems;
- operativity of the EOMs used for the generation of the control sidebands and optimal transmission of the sidebands through the IMC.

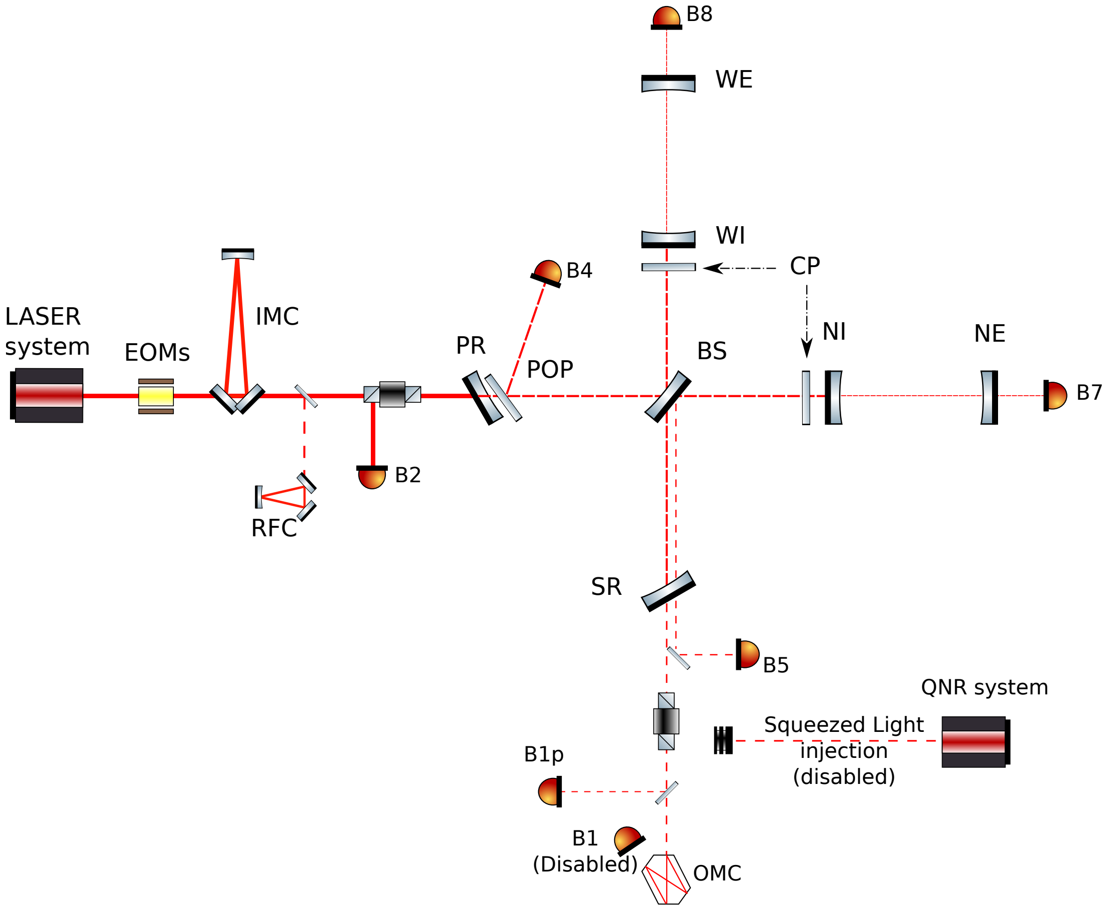

Figure 3.2: Scheme of AdV+ in an unlocked state, ready for the start of the lock acquisition procedure.

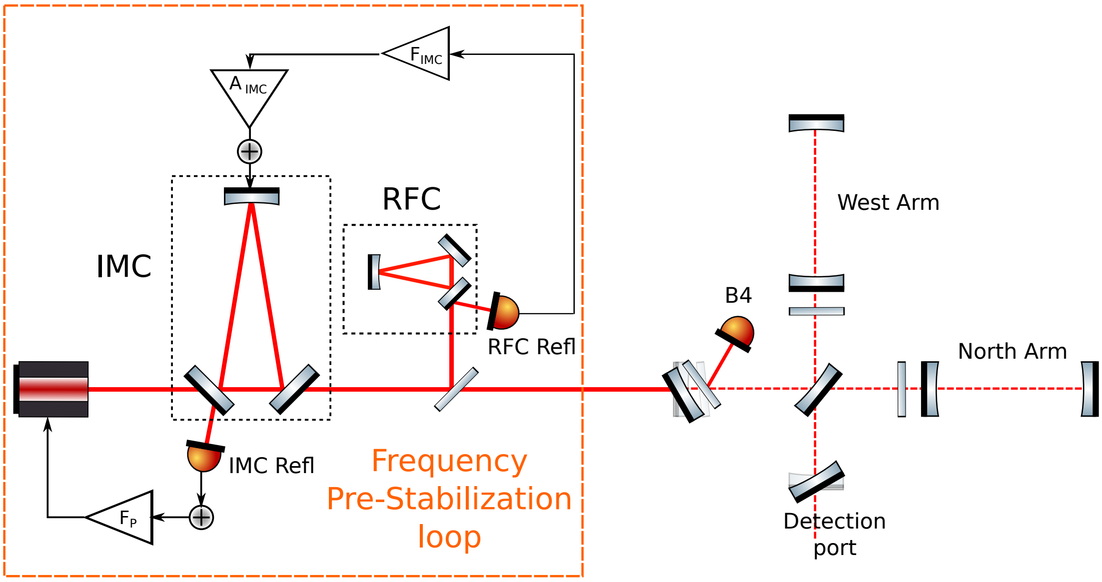

Figure 3.3: Scheme of the AdV+ frequency stabilization loop with the main interferometer in an unlocked state. Only the pre-stabilization loop is enabled, controlling the laser frequency with the IMC error signal, and controlling the IMC length with the RFC (acting as stable length reference) error signal. The interferometer is ready for the start of the lock acquisition procedure.

Additional systems, such as the TCS central heating and ring heaters, are also active before the start of the lock acquisition in order to keep the optical cavities ready for the lock.

The LSC and the ASC systems are disabled, and the main interferometer suspended mirrors and optical benches are controlled only by local controls.

Most detection systems and the QNR systems are also disabled at the beginning of the lock acquisition.

Lastly, to allow the lock of the arm cavities, the PR and SR mirrors are tilted by 25 and 460 μrad, respectively. This decouples their corresponding cavities to avoid sudden phase and amplitude changes in the laser beam caused by the free-swinging recycling cavities passing through a resonance peak. An additional effect of having the PR cavity unlocked and decoupled is that the PR mirror reflects $\simeq 95\%$[1] of the input power into a beam dump. This means that the actual power entering the interferometer during the early stages of the lock acquisition is only $\simeq 2$ W instead of 40 W.

The initial state of the interferometer is represented in figure 3.2.

3.2 Arm cavities lock and the Auxiliary Laser System

Once all the prerequisites are satisfied, the lock acquisition procedure can start. The first step is the independent lock of the two arm FP cavities on the infrared main laser.

---

[1] The transmissivity of the PR mirror is indeed $\simeq 5\%$

3.2.1 Independent arm cavity lock

The lock of the arm cavities is performed independently one from each other, using their corresponding transmitted beams (B7 and B8 for the North and West arm cavities, respectively as shown in figure 3.5a) as triggers and error signals. The DC power is used as a trigger since it peaks when the cavity crosses the resonance. The error signal is instead generated by demodulating the beam at the frequency of the 6.27 MHz sideband.

Due to the high finesse ($\simeq 400$ [16]) of the arm FP cavities, several physical limitations can complicate the engagement of their lock. In particular, when the mirror crosses the resonance peak, and the feedback is engaged, several dynamical effects might not allow the mirror to be stopped before exiting the peak:

- bandwidth/response-time of the feedback loop;
- maximum force applied by the actuators;
- optical power buildup and cavity ringdown effects distorting the error signal.

In order to solve these issues, a particular algorithm called "Guided lock algorithm"[46] [43] has been developed and used in the previous Virgo configurations.

This algorithm is based on estimating the speed of the mirror while it crosses a resonance peak and sending pulses to the actuator coils to invert its speed and slow it down sufficiently for the lock to be engaged. Since the arm FP cavities were not affected by the AdV+ upgrade, this step was left unchanged.

While the arm cavities are locked on the InfraRed (IR) beam, an automatic alignment system based on the dithering technique [47] [48] is activated to optimize the alignment of the input and end mirrors.

Once both arm cavities have been locked on the main IR beam (figure 3.5a), the lock of the green ALS can be engaged.

3.2.2 The auxiliary laser system

The ALS is a brand new system in the Virgo detector, installed and commissioned during the AdV+ upgrade between 2020 and 2021. The design of this system is based on the design tested and installed on the Advanced LIGO detectors [49] [50], with differences primarily in how the green laser is generated (using Second Harmonic Generations (SHGs) instead of LIGO's separate green laser sources) and in how the beating signals are acquired (using digital demodulation instead of analog Phase-Locked Loops (PLLs)). As with the other interferometer subsystems, we will focus mainly on the longitudinal control of the ALS and its role in the AdV+ lock-acquisition procedure.

The primary purpose of the ALS is to control the arm FP cavities independently from the main laser, allowing their lock to be maintained during the lock of the CITF. In particular, having the arm cavities locked on a different laser allows them to be kept out of resonance with respect to the main laser. At the same time, the ALS lock needs to be stable enough for the arm cavities not to move and cross the main laser resonance peaks as it would happen if the arms were unlocked.

A scheme of the ALS main components is shown in figure 3.4. The system is based on three green laser sources [51]. One of them is located near the main laser injection system, and we'll call it the *"central green laser"* from now on. The other two sources are located one at the end of each arm (*"arm green laser"*). For simplicity, the scheme

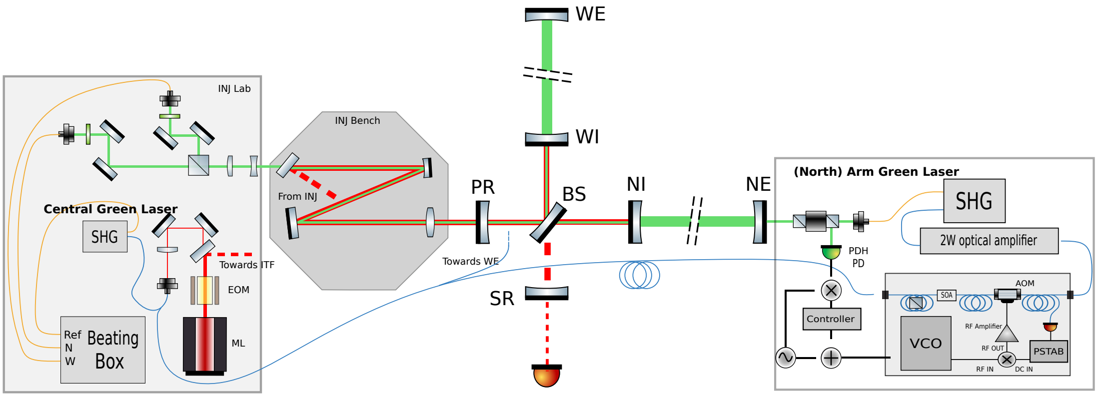

Figure 3.4: Simplified scheme of the ALS. The components located near the main laser are in the **grey square on the left side**. These include the main laser pickoff, the "central green laser" SHG, the fiber collimators collecting the arm transmitted beams, and the "beating box" where these beams interfere with the "central green laser" before being acquired by photodiodes. **On the right side:** generation and injection of the North arm green laser. We also included the "fast" control system that allows the green beam to lock on the North arm cavity. The main components of this system are the Voltage-Controlled Oscillator (VCO) controlling the AOM used to generate control sidebands and to shift the laser frequency, and the demodulated photodiode acquiring the beam reflected by the cavity.
For simplicity, we omitted an identical setup located at the West arm's end. (*Picture courtesy: Matthieu Gosselin and the ALS team.*)

in figure 3.4 does not show the source at the end of the West arm since it is identical to the one at the end of the North arm. They have two different (linear) polarizations and are injected into the arm cavities through the end mirrors. The three laser sources generate 532 nm green laser light, starting from a pickoff of the 1064 nm main infrared laser and doubling its frequency with an SHG crystal. This setup has the following functional properties:

- Relatively high reflection coefficient for the arm mirror coatings at 532 nm, allowing the green beam to resonate inside the cavities with finesse between $\simeq 150$ and $\simeq 190$ [51].
- Easily separates the green ALS beams from the main infrared ones using dichroic mirrors.
- Easily separates the beams coming from the two arms using polarizing beam-splitters.
- The generation using the SHG allows to loosely maintain the relative phase with the main laser, without the need for additional PLLs.

Before being doubled in frequency and injected into the arm cavities, each arm green beam passes through an AOM, which has the double role of shifting its frequency and generating control sidebands for the lock on the arm cavities. The reflected beam of each cavity is acquired and demodulated, generating two error signals that measure the detuning between the green beam frequency and the cavity.

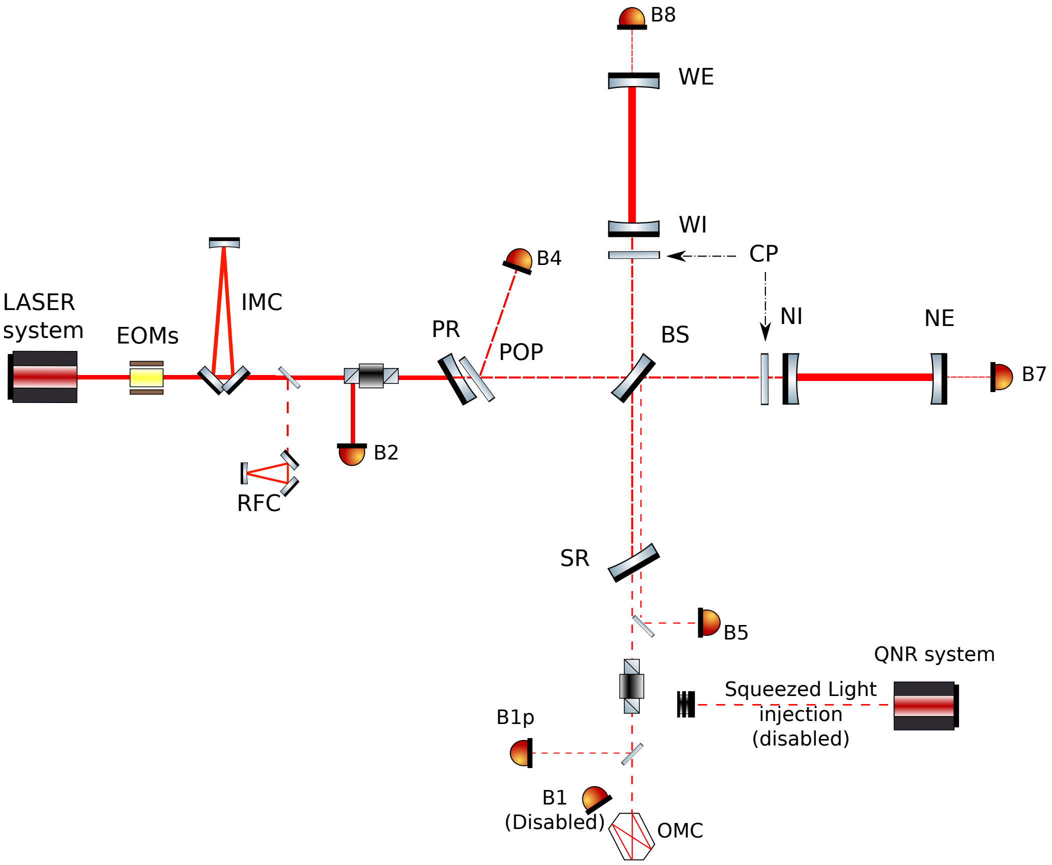

(a) Scheme of AdV+ after the independent lock of the arm FP cavities on the main IR laser. The CITF is still unlocked, and the PR and SR mirrors are misaligned.

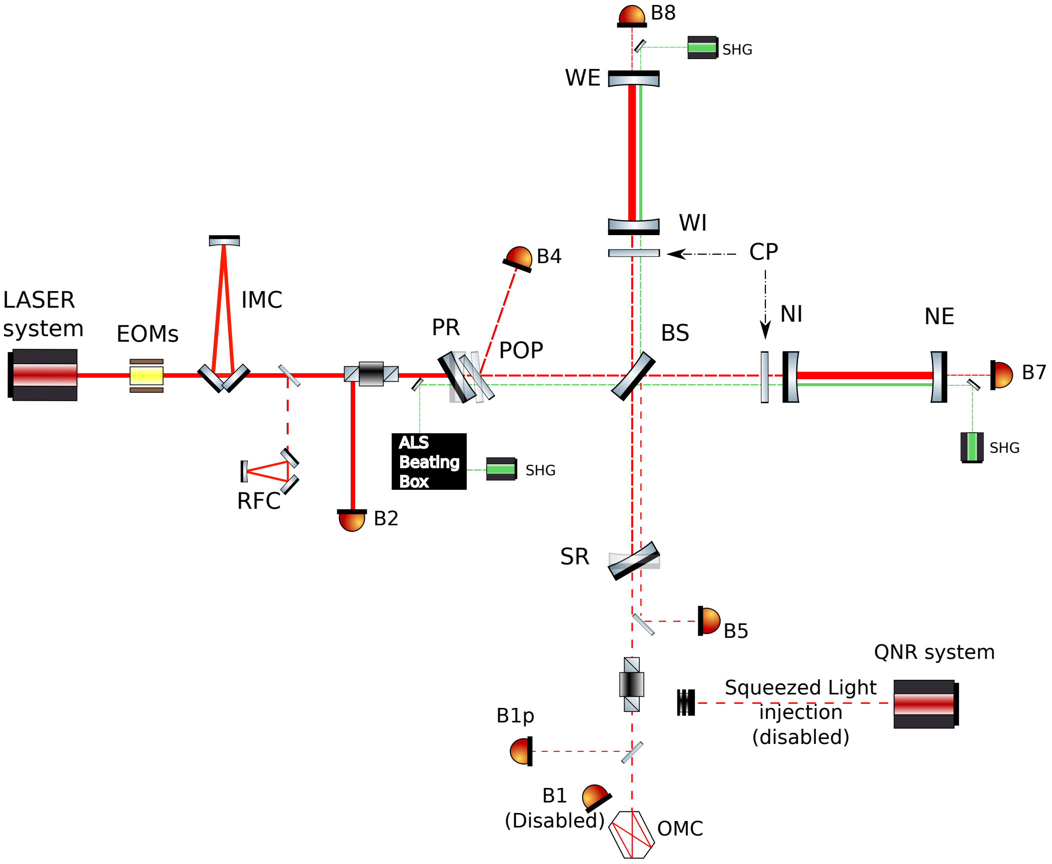

(b) Scheme of AdV+ after the lock of the ALS lasers on the arm cavities. The length of the arm cavities is still controlled by the main IR laser.

Figure 3.5

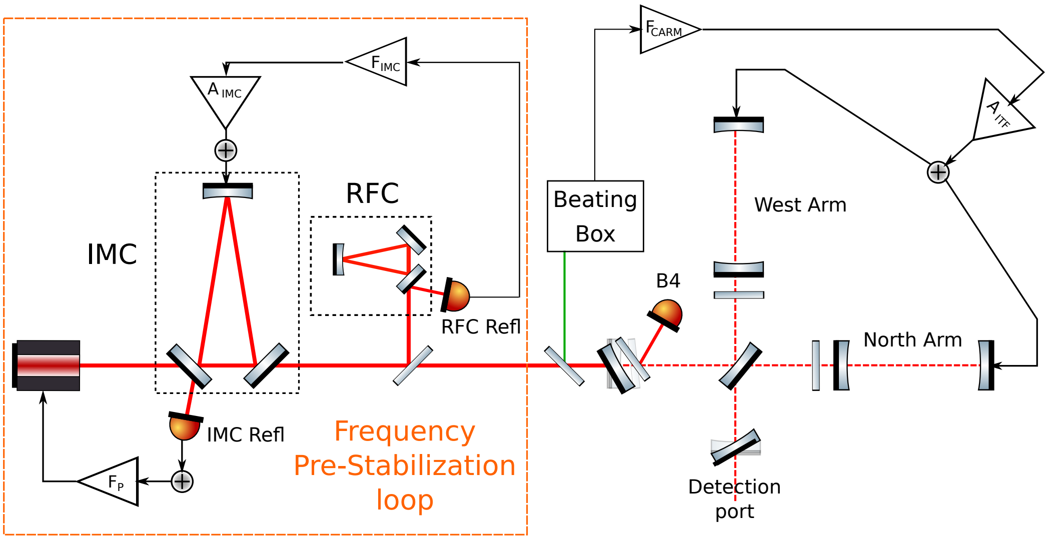

(a) Scheme of the AdV+ frequency stabilization loop when CARM is controlled by the ALS. The differential arm length DARM is analogously controlled by the beating signals. The laser frequency is still controlled by the pre-stabilization loop, using as length reference the RFC.

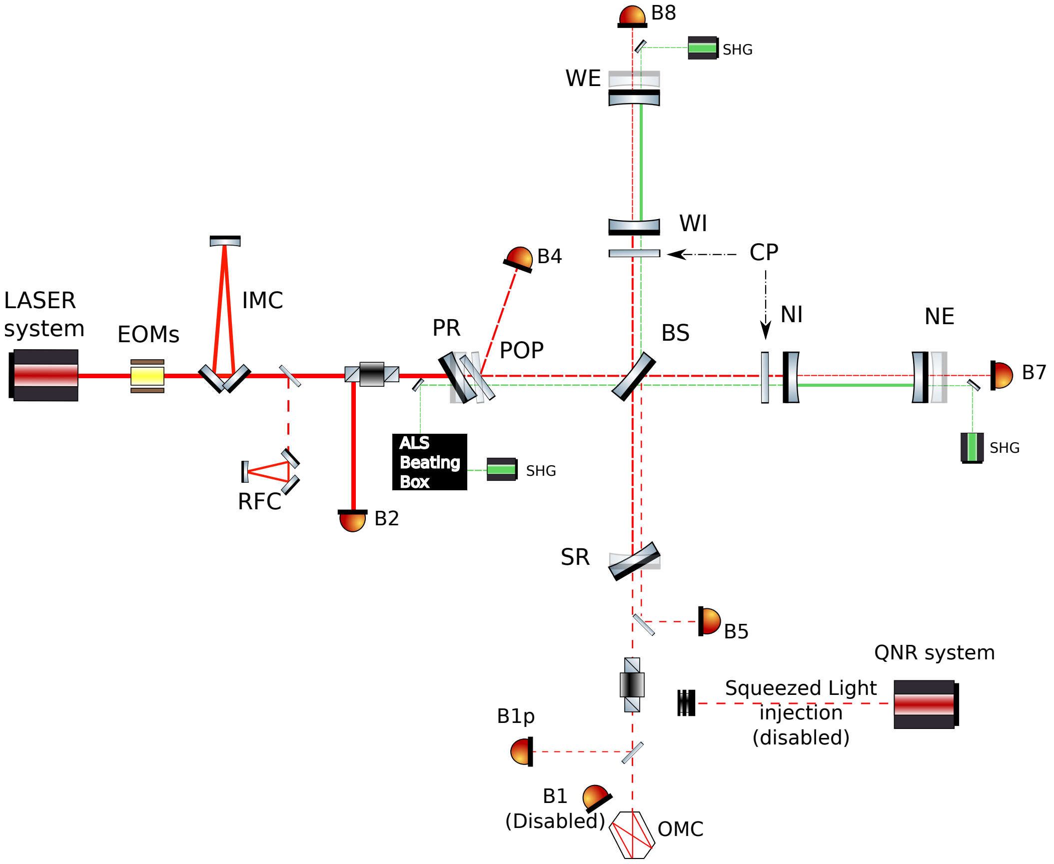

(b) Scheme of AdV+ after the addition of the CARM offset. The arm cavities are now under the control of the ALS, and they are off-resonance with the IR main laser.

Figure 3.6

In the “beating box” of figure 3.4, the central green beam is split in two, and each of the resulting beams is summed with one of the transmitted arm cavity green beams. The resulting beatings allow measuring the frequency difference between each arm green laser and the central green laser. The measured beating signals are $\Delta\nu_N = \nu_N - \nu_C$ and $\Delta\nu_W = \nu_W - \nu_C$, where ν_N , ν_W, and ν_C the frequencies of the North arm, West arm and central green lasers respectively.

The use of these signals will be clarified in the next section 3.2.3.

3.2.3 Arms lock with the ALS

The ALS is engaged once the arm cavities are independently locked on the main IR beam. The ALS lock can be divided into three main steps, explained in the following paragraphs.

Independent lock of the arm green lasers: using the reflection demodulated error signals, each arm green beam is locked on its arm FP cavity. The feedbacks actuate on the laser beams’ frequency using the AOMs to keep them resonant with their corresponding cavity. These two loops, called *“fast green loops”*, will remain engaged until the end of the lock acquisition procedure when the ALS arm beams stop being injected to avoid any possible interference with the main laser signals. The state of the interferometer after the lock of the arm green lasers is shown in figure 3.5b.

Handoff of the arms control to the green beating signals: Once the fast green loops are engaged, the $\Delta\nu_N$ and $\Delta\nu_W$ signals obtained from the beating of the transmitted arm green beams with the central green laser can be used to control the length arm cavities.

Indeed, since the arm green beam lasers are locked on the arm cavities, their frequency is tied to the corresponding arm cavity length by being an integer multiple n of their FSR:

$$\nu_{N/W} = n_{N/W} \cdot \frac{c}{2L_{N/W}} \tag{3.1}$$

Due to the way it is generated, the central green beam’s frequency ν_c is twice the frequency of the main IR laser ν_{ml}. Indeed, when the cavities are resonant with the main laser, we have:

$$\nu_c = 2\nu_{ml} = 2n_{Nml} \cdot \frac{c}{2L_N} = 2n_{Wml} \cdot \frac{c}{2L_W} \tag{3.2}$$

We should note that at this point of the lock acquisition, depending on which resonance peak (n_{Wml}, n_{Nml}) the initial arm cavity lock is locked on, the arm lengths L_N and L_W can be different.

When the arm cavities are locked on the main laser, and the green arm lasers are locked on the arm cavities, $\Delta\nu_N$ and $\Delta\nu_W$ are integer multiples of the respective arms’ FSRs. Indeed

$$\Delta\nu_{N/W} = \left(n_{N/W} - 2n_{Nml/Wml}\right) \frac{c}{2L_{N/W}} \tag{3.3}$$

The arm cavity lock on the IR is then disabled, and the cavity can change length while the main laser and the central green laser frequency remain the same (since the main laser is locked on the RFC).

The arm green lasers instead change frequency to remain locked on the arm cavities. For small arm length variations around the initial length $\overline{L}_{N/W}$, their frequency can be approximated with a first order expansion:

$$\nu_{N/W}[\overline{L}_{N/W} + \delta L_{N/W}] \simeq \overline{\nu}_{N/W} \left(1 - \frac{\delta L_{N/W}}{\overline{L}_{N/W}} \right) \tag{3.4}$$

Where $\overline{\nu}_{N/W} := n_{N/W} \frac{c}{2\overline{L}_{N/W}}$ is the initial North/West arm green laser frequency. Considering that ν_C remains instead constant, once the initial offset is subtracted, the beating signals $\Delta\nu_N = \nu_N - \nu_C$ and $\Delta\nu_W = \nu_W - \nu_C$ are proportional to $\delta L_{N/W}$ and can be used as error signals for the arm cavities lengths. In particular, these error signals allow the choice of the "distance" of each arm cavity's resonance from the resonance of the main laser. Since $\overline{L}_{N/W} \simeq 3$ km, for any reasonable detuning $\delta L_{N/W}$, we have $\frac{\delta L_{N/W}}{\overline{L}_{N/W}} \ll 1$ and therefore we maintain the linearity of the error signal. An additional limitation on the linearity of the error signal comes, however, from the method of measuring $\Delta\nu_{N/W}$ from the beating of the two lasers. Indeed, the digital demodulation used to estimate the frequency difference between the two beams gives a meaningful output only in a range of $\simeq 4 \cdot 10^5$ Hz, corresponding to a CARM length of $\simeq 4$ μm. This range allows detuning the cavity from the main laser by any amount between two resonance peaks (we remind that the arm cavities' FSR is $\simeq 50$ kHz).

As shown in figure 3.6a, the arm cavity control is handed off to the beating signals, recombined in a green CARM/DARM basis for convenience:

$$\begin{aligned} gDARM &:= \frac{\Delta\nu_N - \Delta\nu_W}{2} = \frac{\nu_N - \nu_W}{2} \\ gCARM &:= \frac{\Delta\nu_N + \Delta\nu_W}{2} = \frac{\nu_N + \nu_W}{2} - \nu_C \end{aligned} \tag{3.5}$$

Addition of the CARM offset: The last step of the ALS lock procedure is the addition of a gCARM offset to bring them out of the main IR laser's resonance (figure 3.5b). gDARM is instead kept at zero to maintain an equal distance of the main laser frequency from the cavity resonance peaks.

We choose the gCARM offset according to the following criteria:

- Sufficient distance from the leading laser carrier, sidebands, and Higher Order Modes (HOMs) resonance peaks
- Being close enough to the carrier resonance peak to allow reaching it during the carm offset reduction without crossing other peaks that would influence the 3f error signals used to keep the DRMI locked.

These criteria have been first checked by running CARM offset reduction simulations (see figure 3.7), and then CARM offset scans during the commissioning. The tests showed that a gCARM offset of 3 kHz, corresponding to a 1.5 kHz of detuning of the main laser with respect to the cavity resonance peak, is a good point to allow a reliable lock of the CITF (see the following subsection) and a stable CARM offset reduction.

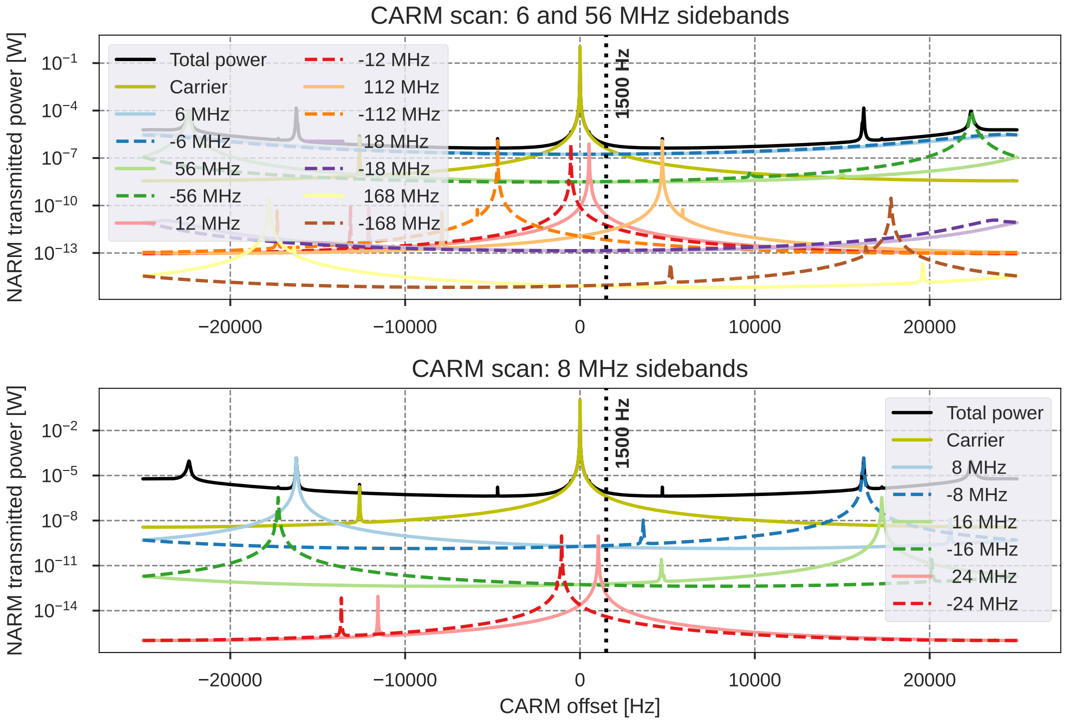

Figure 3.7: Simulated North-arm transmitted power during CARM offset scans. The plots show the carrier and sideband resonances in the North arm cavity. Positive and negative sidebands up to third order of Bessel expansion and fourth order Hermite-Gauss TEM mode have been simulated and plotted. The top plot shows the 6 and 56 MHz sidebands contributions, while the bottom plot shows the 8 MHz sidebands contributions (which are not used during the lock-acquisition). One can notice that between the 1.5 kHz offset (choosen as starting point of the CARM offset reduction) and the Carrier beam resonance, only the 12 and 24 MHz sidebands' resonances are crossed. Further checks showed that the '3f' error signals used to lock the DRMI are not affected by this crossing.

3.3 Lock of the Central Interferometer

Once the arms are locked on the ALS beating signals and the gCARM offset has been added, the procedure to lock the CITF can start.

The three CITF DOFs (PRCL, SRCL, and MICH) are locked simultaneously.

In order to obtain the lock, we need to remember that phase of the carrier beam inside the CITF cavities is shifted by 90° due to the arm cavities being off-resonance. Therefore, the initial lock of the PR cavity needs to be engaged with an anti-resonant carrier condition. In this way, when the arm cavities are brought back to resonance in the later steps of the lock acquisition, the carrier beam automatically becomes resonant in the PR cavity. At the same time, the CARM offset makes the carrier resonant in the SR cavity while it is anti-resonant at the end. Since the MICH dof depends on the relative phase between the arm-reflected beams at the beam-splitter level, it is not affected by the CARM offset, and the carrier beam is kept in the dark-fringe condition through all the reduction.

The first step before locking them is to realign the PR and SR mirrors. Otherwise, it would not be possible to lock their respective cavities.

3.3.1 Alignment of the CITF mirrors

Locking the CITF is particularly sensitive to a good alignment of the PRCL cavity. This is due to its strong influence on the circulation of the control sidebands in the CITF.

Considering that the arm input mirrors' alignment has already been optimized with a dithering control [47] in the previous step of the lock acquisition, a particular focus is given instead to the alignment of the PR and BS mirrors.

Since no automatic-alignment loop can be engaged before the lock, their alignment is managed by local controls. Their working point, however, often needs to be re-optimized from lock to lock. The optimization of the initial alignment uses the "2f" signals (explained in section 2.1.2) to check the powers of the 6 and 56 MHz sidebands circulating in the PR cavity. The procedure aims to maximize the peaks of the "2f" signals (acquired from the intra-cavity pickoff beam B4) in correspondence with the sideband resonances (crossed several times per minute since the longitudinal controls are not engaged yet). At the same time, the anti-resonance of the carrier beam inside the PR cavity is also checked by minimizing the intra-cavity DC power. A macro to pre-align automatically the PR mirror based on a simple bang-bang control ([52]) has been recently implemented, allowing to automatize this procedure.

In case manual intervention is required (due to exceedingly misaligned mirrors), additional figures of merit can be obtained from the cameras monitoring the various interferometer beams (B1, B2, and B4).

Extensive simulation studies were also performed to check the CITF lock's robustness (after its engagement) against subsequent misalignments. The methodology and the results of the studies are summarized in [53] and reported in detail in appendix A, while we will sum up here the most relevant outcomes for the lock acquisition procedure.

Figure 3.8 shows the effect of the PR, NI, and SR mirrors' misalignment on the CITF error signals' optical gains (see section 4.4.2 for a definition of "optical gain"). More results can be found in appendix A. This figure of merit resulted in being the most heavily affected by the misalignments and was used to determine maximum misalignment thresholds for each mirror. The thresholds were fixed at the angle corresponding to a 50% optical gain loss of any of the CITF error signals. As explained in A, the 50% threshold is based on empirical experience on the previous behavior of the CITF longitudinal loops since complete modeling of their gain margin and robustness was not yet possible at the moment of preparation of the studies.

As expected, the most restrictive threshold is on the misalignment of the PR mirror, which causes the PRCL error signal to lose 50% of its optical gain at a misalignment of $\simeq 0.6 \cdot 10^{-7}$ rad. We investigated, therefore, the possibility of engaging high-bandwidth (a few Hz) angular controls for the PR alignment, based on the Ward technique ([54]), as soon as the CITF lock is achieved. The error signals reported in the resulting studies ([55]) allowed to engage the auto-alignment loop immediately after the CITF lock reliably, substantially increasing the robustness of the lock during the rest of the AdV+ lock-acquisition [56].

The low effect of the SR mirror misalignments on the error signals showed no necessity of engaging high-performance angular controls at this stage of the lock.

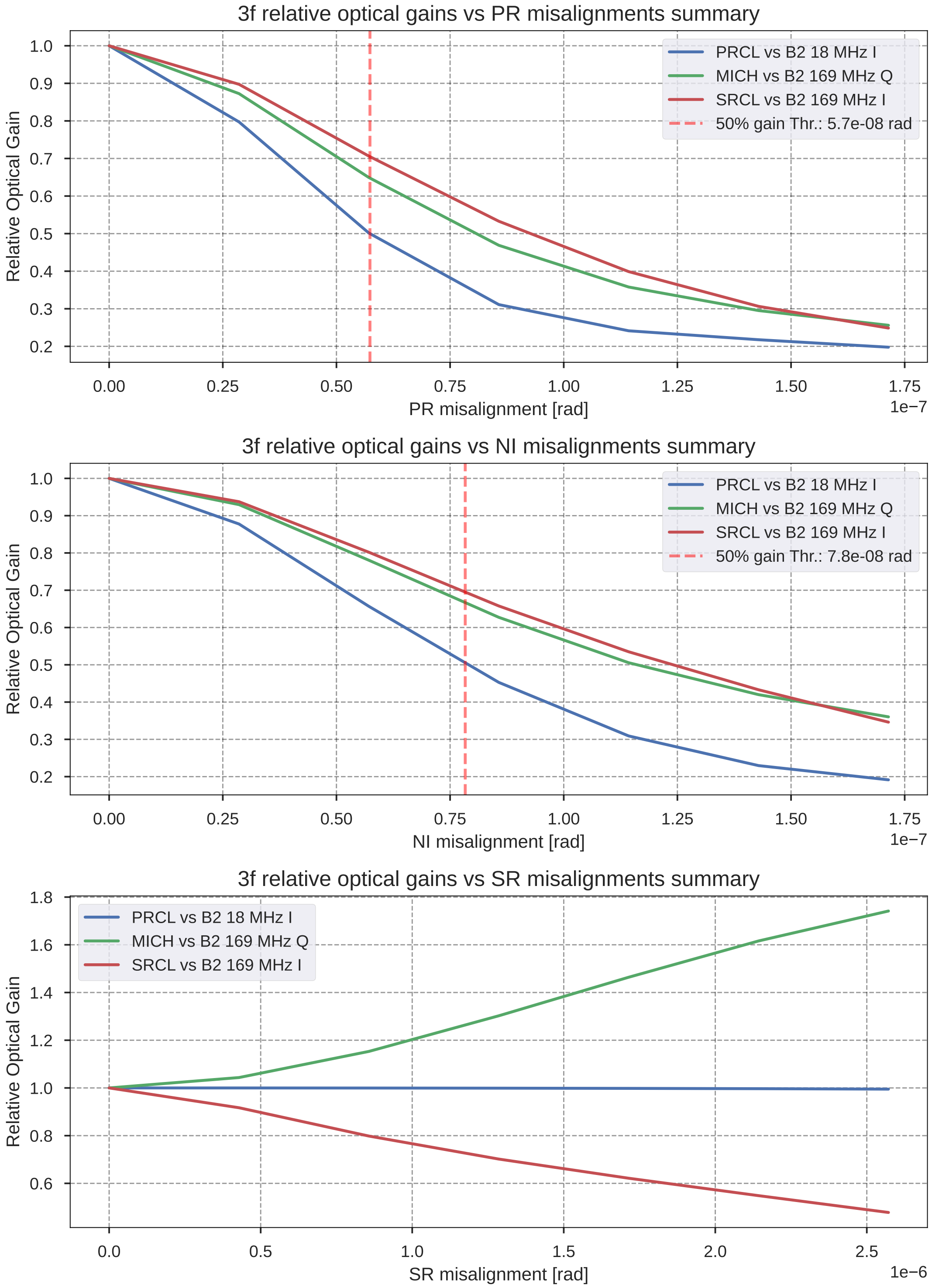

Figure 3.8: CITF error signals Optical Gain (OG) variation vs misalignments of the PR (first plot), NI (second plot) and SR (third plot) mirrors. Each line corresponds to the relative optical gain of a "3f" error signal used for the control of the CITF. The OGs are relative to the gains in a fully aligned condition. The vertical line marks the lowest angle at which one of the error signals has lost 50% of its OG, if present. Note the much different scale of the third plot, since SR misalignments affect the error signals much less than the other two mirrors.

3.3.2 Trigger logic and engagement of the CITF lock

The lock of three coupled DOFs at the same time poses two main challenges: choosing an appropriate trigger logic to determine the right moment to engage the feedback loops and finding good decoupled error signals.

CITF lock triggers: In order to find the optimal trigger signals for the engagement of the CITF lock, we studied the behavior of many available signals using both modal (Finesse) and time-domain (E2E [57]) simulations. The necessity of using time-domain simulations was due to the possibility of cavity dynamical effects spoiling the behavior of the studied signals. These effects would not be visible using simpler frequency-domain simulations, which have anyway been used as a cross-check.

The results of these studies are reported in detail in [53]. The resulting trigger logic is based on the intersection of four different trigger signals. As shown in table 3.1, two of them have a positive logic, which means that they are not zero only when their relative signal is above a certain threshold, while the remaining two have a negative logic, meaning the opposite.

Signal	Threshold	Corresponding Condition
B4 12 MHz Magnitude	Positive	Resonance of 6 Mhz sidebands in the PR cavity.
B4 112 MHz Magnitude	Positive	Resonance of 56 Mhz sidebands in the PR cavity.
B4 DC	Negative	Anti-resonance of the carrier in the PR cavity.
B1p DC	Negative	Small Michelson (MICH) in dark fringe.

Table 3.1: Chosen triggers for the lock of the CITF. The intersection of these four triggers determines the moment when the longitudinal feedback loops are engaged.

CITF error signals: Three different sets of error signals are used for the longitudinal control of the CITF DOFs, corresponding to three different phases of the lock acquisition. All three sets of error signals are summarized in table 3.2.

Lock acq. step	PRCL	MICH	SRCL
Initial lock	B2 6 MHz	B2 56 MHz I	B2 56 MHz Q
CARM offset reduction	B2 18 MHz	B2 169 MHz I	B2 169 MHz Q
Steady-state	B2 8 MHz	B2 56 MHz I	B2 56 MHz Q

Table 3.2: Planned error signals for the longitudinal control of the CITF DOFs.

The first set used for the initial CITF lock acquisition is based on high-snr "1f" signals to reduce the possibility to saturate the longitudinal actuators. These signals, however, are influenced by the carrier beam phase shift happening when the arm FP cavities are brought back to resonance as a consequence of the CARM offset reduction. After the initial lock, therefore, the control is handed off to a second set, based on the "3f" demodulation error signal. These signals's gain is a factor $\simeq 100$ lower (see table A.1), resulting in a higher sensing noise, as seen in figure 3.9. Nevertheless, they are robust enough to maintain a low-bandwidth lock until the latest stages of the lock acquisition.

Both the first and the second set of error signals have been identified by modal Finesse simulations reported in [44]. The behavior of the final set of error signals, used for the low-noise controls at the end of the lock acquisition, is studied in chapter 4.4 and, in more detail, in appendix B.

Figure 3.10 shows the status of the interferometer after the lock of the CITF.

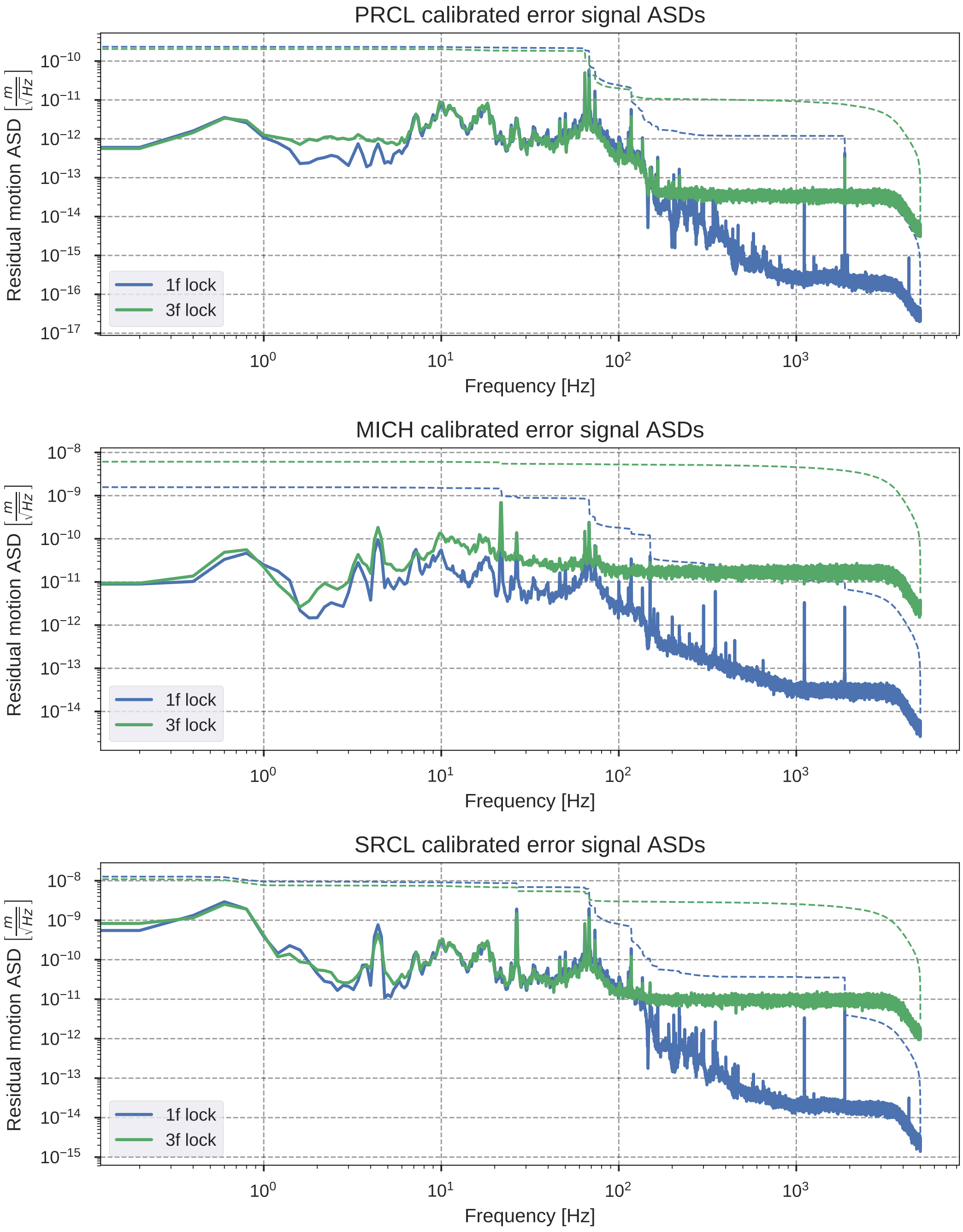

Figure 3.9: Comparison between “1f” and “3f” error signals used to lock the CITF. In particular, the comparison is between B2 6 MHz and B2 18 MHz for PRCL, and between B2 56 MHz and B2 169 MHz for SRCL and MICH. One can easily note that in all three cases, a flat shot noise dominates the spectrum above $\simeq 100$ Hz in the “3f” signals. The dashed lines are the cumulative RMS of the ASD, computed starting from the maximum frequency bin.

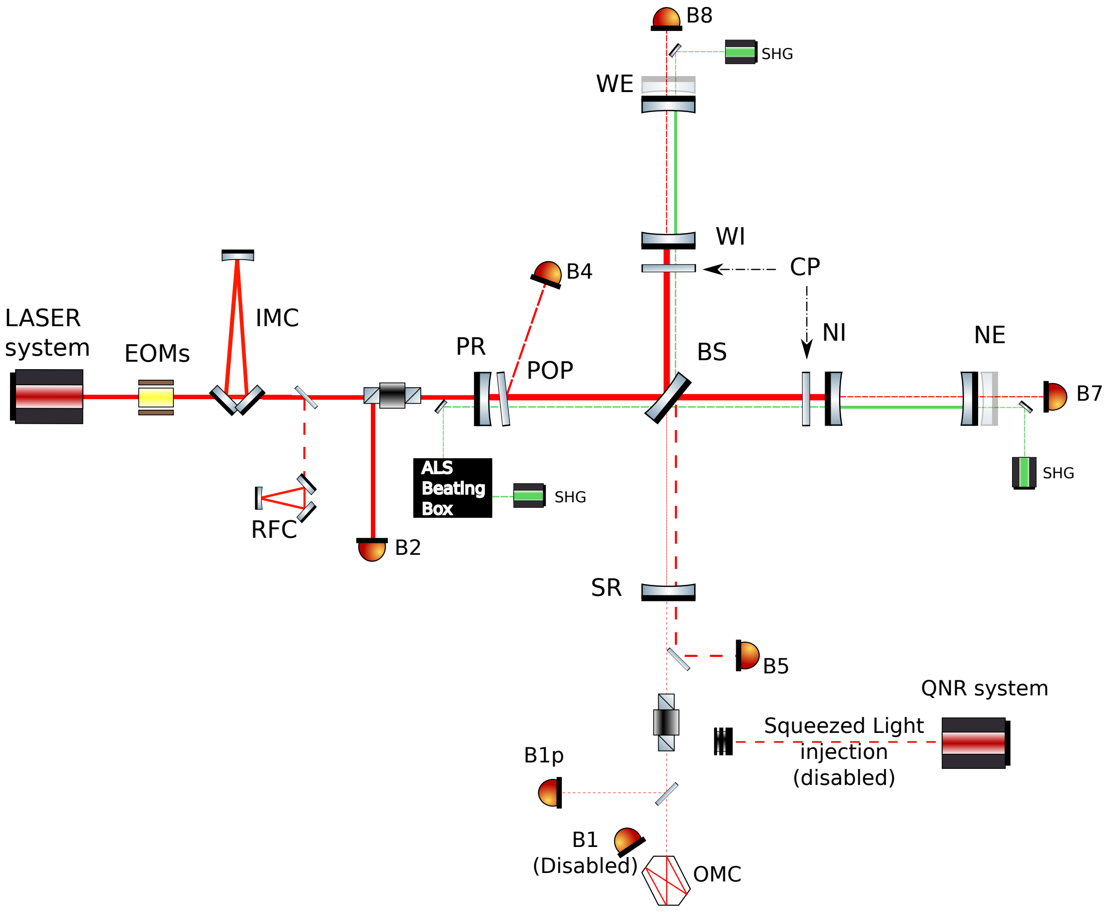

Figure 3.10: Scheme of AdV+ after the realignment and lock of the CITF. The arm cavities are still under the control of the ALS, and off-resonance with the IR laser.

3.4 CARM offset reduction and final working point

Once the CITF is locked, and its control is handed off to the “3f” error signals, the reduction of the CARM offset can begin.

Despite the relatively low influence of the CARM offset on the “3f” CITF error signals, several complications make it so that this procedure cannot be done in a single quick step. The main steps of the carm offset reduction are listed below:

- **Reduction of the CARM offset from 1.5 kHz to 75 Hz**: This step is a straightforward reduction of the setpoint of the gCARM loop setpoint and only takes a few seconds. At this point, the power circulating in the arm FP cavities is still extremely low due to the narrowness ($\simeq 1$ Hz) of the CARM resonance for the carrier beam. The circulating power is monitored by measuring the corresponding arm transmitted power, shown in figure 3.11. At 1.5 kHz of offset it is $< 1\ \mu$W and it reaches $\simeq 0.15$ mW at 75 Hz of offset. At the end of the CARM offset reduction, when the arm cavities are fully resonant with the IR beam, the transmitted power by each arm is above 600 mW.

- **Handoff of the CARM control and actuation:** At 75 Hz of offset, CARM control is handed off from the ALS signals to IR DC signals obtained from the arm

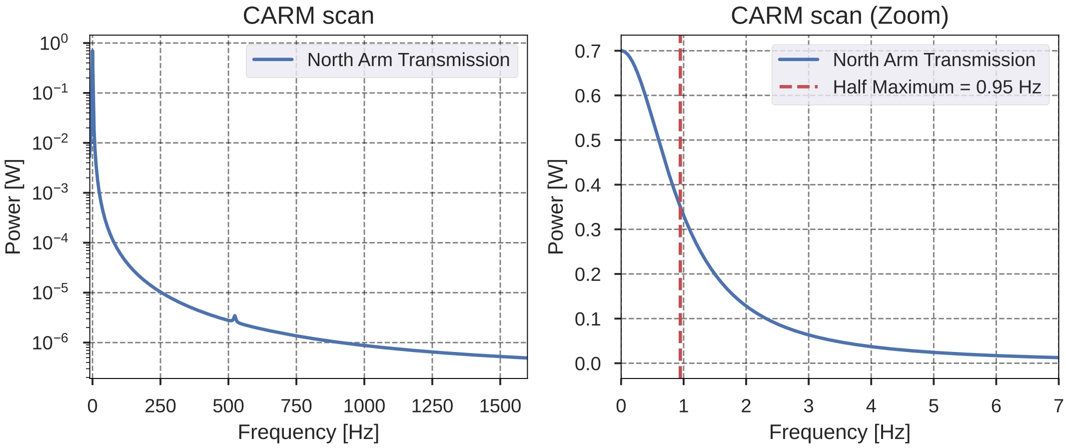

Figure 3.11: Simulated scans of the CARM offset. On the left, a 1500 Hz scan with power in logarithmic scale, corresponding to the full width of the CARM offset reduction. On the right, a scan focused on the transmission peak with linear scales.

transmitted power. At the same time, the CARM loop switches from actuating on the arm lengths to actuating on the main IR laser frequency. The necessity of this crucial step is explained in detail in section 3.4.1. After the CARM handoff, there is no longer a way to precisely measure the CARM offset in Hz, since the transmission peak is often influenced by alignment, mismatch and thermal effects which are not always reproducible at this point of the lock acquisition.

- **DARM handoff:** The offset is further reduced, allowing to reach 40 mW of arm transmitted power corresponding to approximately $\simeq 5$ Hz. At this point the DARM loop is also handed off from the ALS beating signals to a RF-demodulated signal based on the IR beam, as detailed in 3.4.1. From this point of the lock acquisition onwards, the ALS system is no longer used.
- **Further reduction steps:** Once both the CARM and DARM loops are handed off to IR signals, the rest of the reduction can proceed without major changes to the control systems' structure. Nevertheless the control loops need gain, demodulation phase and filter adjustments in order to remain stable until CARM offset zero is reached. The adjustments are performed at additional steps at 100, 200 and 480 mW of arm transmitted power.
- **Reaching CARM offset zero**: Once 480 mW step is reached, the half-maximum of the CARM resonance peak is reached, meaning that the offset is $\simeq 1$ Hz. At this point, the CARM IR RF-demodulated error signal (B4 6 MHz) can be used. The handoff is carried out removing any offset. Therefore, the CARM peak is reached simultaneously with the handoff. At this point, the interferometer is fully locked and in dark fringe (as shown in Figure 3.12) and the operations to bring the interferometer to the final steady-state Working Point (WP) can begin (see section 3.4.2).

The most impacting factors that require the CARM offset reduction to be performed in multiple steps are discussed in the following subsection.

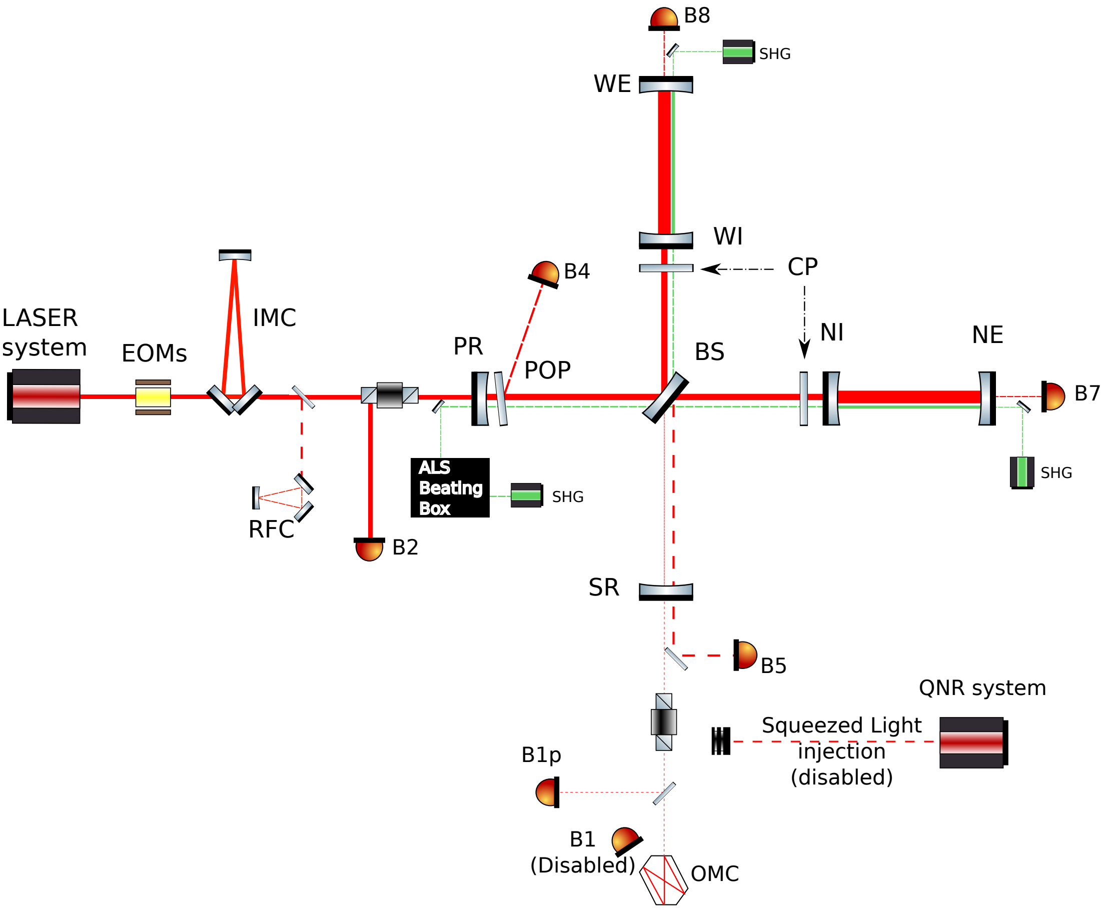

Figure 3.12: Scheme of AdV+ in the dark fringe state after the completion of the CARM offset reduction. All the LSC DOFs are now locked on the IR main laser. The green lasers are still locked on the arm cavities but are no longer used.

3.4.1 Main obstacles in reducing the CARM offset

Green laser frequency noise: One of the first obstacles that prevent reaching CARM offset zero in a simple way is the frequency noise affecting the gCARM and gDARM ALS error signals. When the arm cavities are controlled by these signals, the green lasers' frequency noise is transduced into cavity length noise. Preliminary studies [44], based on the results achieved in the past by LIGO's analogous ALS, estimated a resulting frequency noise of $\simeq 5 - 10$ Hz rms. During the commissioning, however, it was noticed that the gCARM and gDARM signals are affected by unexpected additional noise. Noise-hunting investigations discovered that this additional noise originates from the acoustic coupling of the ALS beams when they pass through optical fibers before reaching the beating box (see figure 3.4). This noise is added downstream the arm green fast loops and therefore cannot be mitigated by them. Despite several coupling mitigation attempts, the resulting frequency noise (shown in figure 3.13) could not be lowered below $\simeq 100$ Hz rms [58]. Since most of the noise was in the frequency between 20 and 100 Hz, reducing the bandwidth of the gCARM and gDARM loops below 10 Hz helped in avoiding the reintroduction of this noise in the loops, allowing in optimal conditions to reach a residual frequency noise < 10 Hz rms [59]. Despite this improvement, the additional noise on the green beating signals severely impacted the stability of the lock during the CARM offset reduction, requiring considerable adjustments in the overall procedure. In particular the higher noise required to anticipate the handoff of CARM to IR-based error signals. The reason of this necessity and its consequences will be clairfied in the following paragraphs.

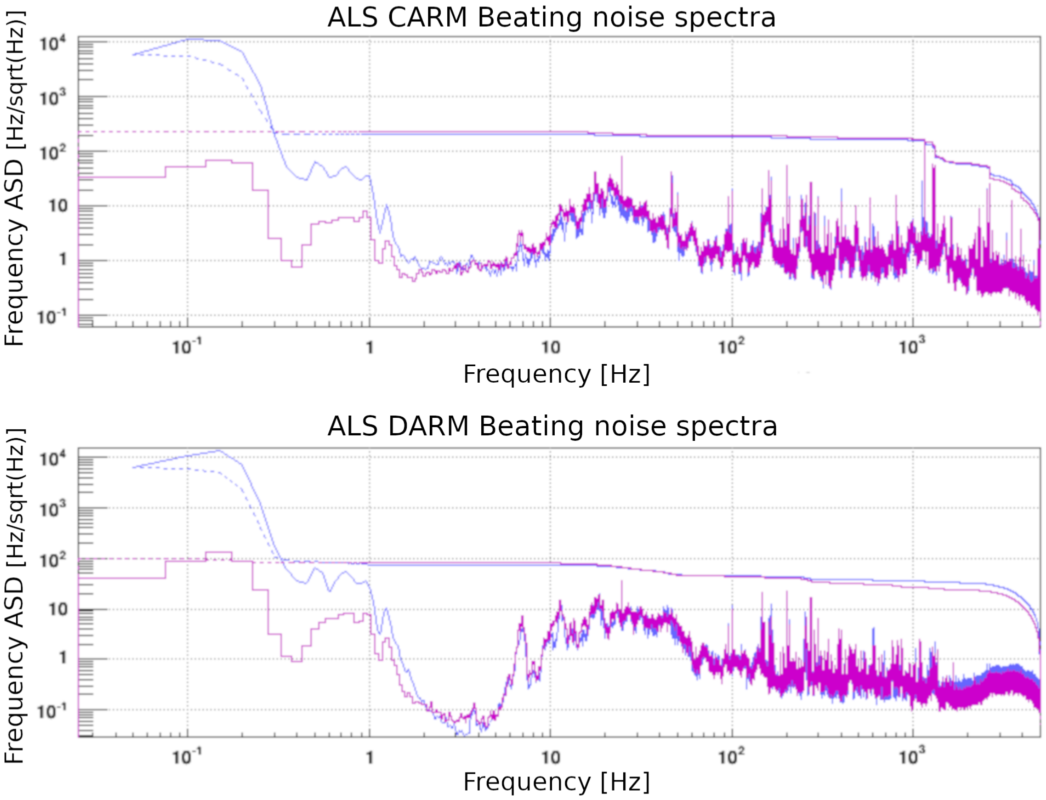

Figure 3.13: gCARM and gDARM beating signals frequency noises. The blue line corresponds to an initial measurement, the purple line corresponds to the noise after noise-mitigation and control filter optimization. The wideband acoustic noise “bump” between 10 and 100 Hz is still present and a major contribution in the overall noise.

To fully understand the impact of the noise, we need to remind that the CARM linewidth for the main IR laser is $\simeq 1$ Hz, thanks to the coupled cavity interaction with the locked PR cavity. This means that keeping the arm cavities locked with the ALS signals at CARM offsets smaller than the green reintroduced frequency noise would mean continuously crossing the IR CARM resonance. Despite the robustness of the “3f” error signals used to control the CITF during the CARM offset reduction, if the arm cavities cross the CARM resonance too quickly, the CITF immediately loses the lock. The main reasons for this are the high-power flashes caused by the arm cavities' transient effects. Additionally, the effects of a too noisy CARM control hamper the possibility of using the CARM IR RF-demodulated signal, which is linear only at very small (< 1 Hz) CARM offsets.

To successfully bring the CARM offset to zero and handoff the arm cavities control to the final IR signals, an intermediate error signal for CARM is therefore necessary.

The intermediate error signal chosen for CARM is the square root of the sum of the arm transmitted powers: $\sqrt{\mathrm{B7\_DC} + \mathrm{B8\_DC}}$.

CARM transfer function instability and actuation handoff: Simultaneously to the change of error signal, we also change actuation in the CARM feedback loop. Indeed, in order to enhance the loop bandwidth, the actuation switches from the common arm length to the IR laser frequency by means of actuating on the IMC length, as shown in figure 3.14. The drastic reduction in the loop and cavity-power noise corresponding to this handoff can be seen in figure 3.15b.

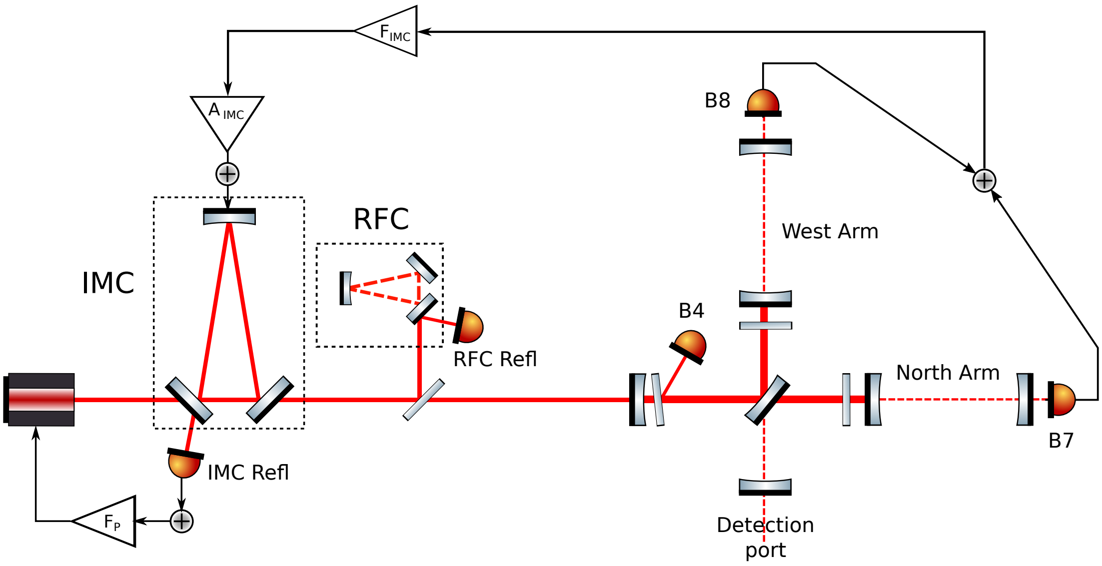

Figure 3.14: Scheme of the AdV+ frequency stabilization loop after the handoff of CARM to the IR DC signals. The laser frequency is now controlled by the CARM error signal through actuation on the IMC, while the CARM length itself is uncontrolled.

Up to this stage of the lock acquisition, the IMC length was controlled by the RFC error signal, acting as a stable length reference. Handing off the IMC control to the CARM error signal means that the IMC length (followed by the frequency of the main laser, locked on the IMC error signal) is changed according to the frequency difference between the current CARM setpoint and the laser frequency. The increase of bandwidth of the loop is required for two different reasons:

- A larger bandwidth means a higher noise suppression and an overall reduced residual frequency noise, necessary to maintain the lock and ultimately hand off the control to the CARM final error signal.
- The optomechanical transfer function of CARM vs. any IR-based error signal has a pole corresponding to the CARM offset frequency, as shown in figure 3.15a. If not compensated by a proper actuation, this pole creates instability in the feedback loop.

  Due to the higher-than expected residual noise on the beating signals, the handoff from the ALS to the IR DC signals needs to be performed before reaching $\simeq 50$ Hz of offset, a higher than 50 Hz bandwidth is immediately necessary upon the engagement of the IR signals.

An additional consequence of the early IR handoff and engagement of the CARM-IMC loop is that, to properly compensate the change of frequency of the moving pole during the offset reduction, the IMC control filter needs to be progressively changed.

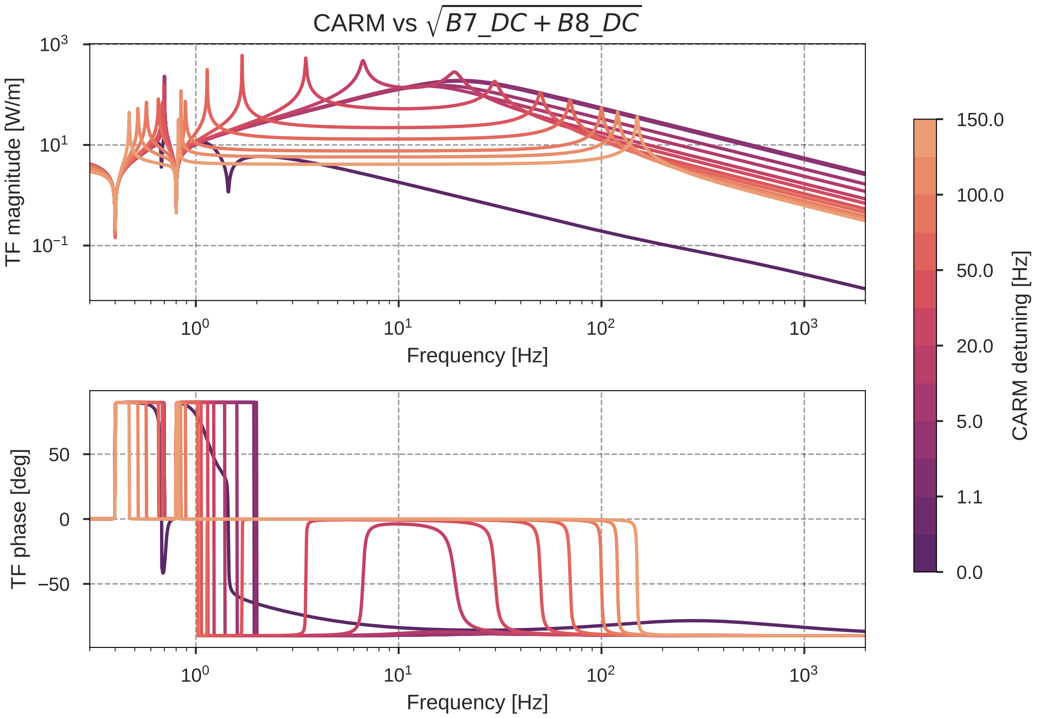

(a) CARM displacement to transmission DC signals transfer function for different levels of CARM offset. One could notice that for offsets above ≃ 10 Hz, a pole at the offset frequency is clearly visible.

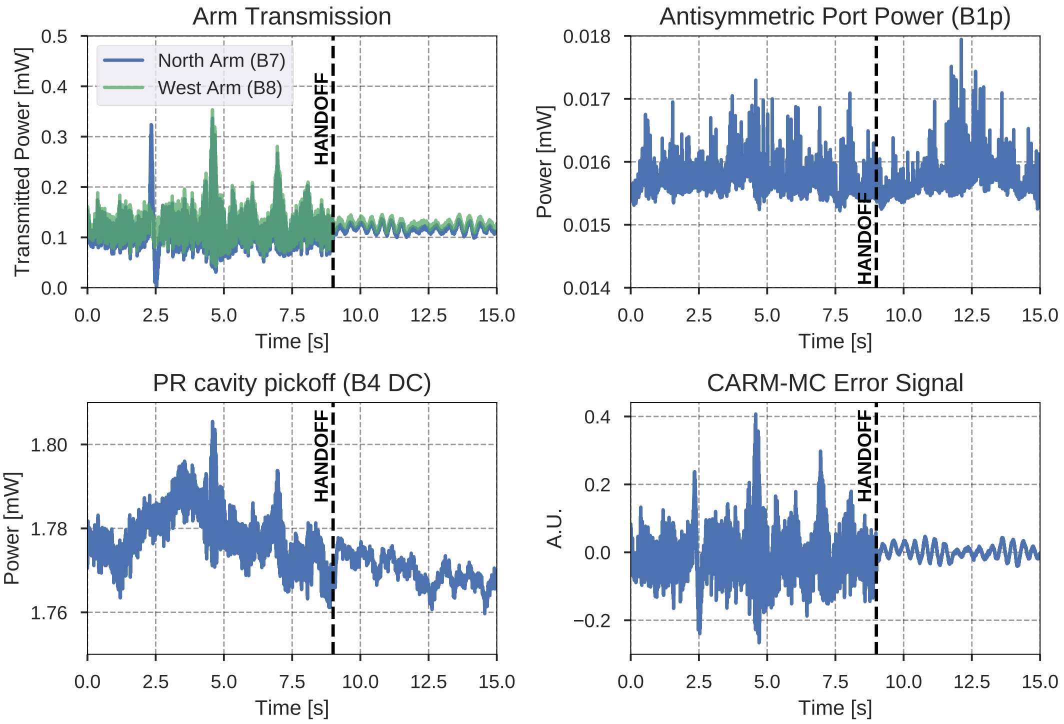

(b) Interferometer powers at the CARM handoff from the ALS beating signal to the IR DC signal ($\sqrt{\mathrm{B7\_DC} + \mathrm{B8\_DC}}$). The plots show the sudden reduction of noise both in the cavity DC powers (left plots) and in the in-loop error signal (bottom-right plot) at the engagement of the CARM-IMC loop, replacing the ALS CARM loop. The dark fringe power (top-right plot) is instead unaffected since it depends on the differential lengths.

Figure 3.15

DARM sign change and handoff to IR-based error signals: Differently from CARM, the linewidth of DARM is not reduced by the PR cavity coupling, and its RF-demodulated error signal can be engaged at an earlier stage. A limitation on the usage of this signal is however given by an error signal sign-change during the CARM offset reduction. Early studies [44] estimated the sign-change to take place at $\simeq 7$ Hz of CARM offset. Follow-up simulations (in figure 3.16) and experimental measures (figure 3.17a) during the commissioning showed instead that the sign-change happens at an earlier stage corresponding to $\simeq 15 - 20$ Hz of CARM offset [60]. Therefore, the DARM IR RF-demodulated error signal (B1p 56 MHz) can replace the ALS gDARM signal early enough in the CARM offset reduction (at $\simeq 10$ Hz) not to require an intermediate signal. The reduction in the loop and cavity-power noise during this handoff can be seen in figure 3.17b.

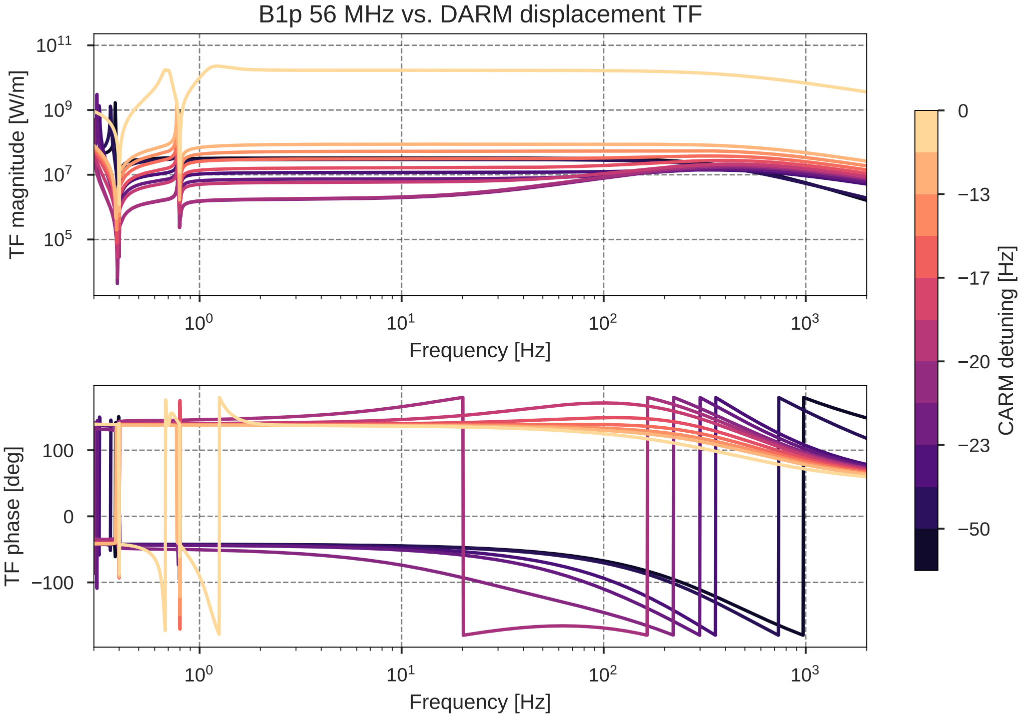

Figure 3.16: DARM displacement to its IR RF error signal transfer function for different levels of CARM offset. A wideband 180° phase shift happens when crossing $\simeq 20$ Hz of CARM offset, indicating a sign-change in the error signal.

Additional complications: While the arm cavities are the most influenced by the CARM offset reduction, the CITF feedback loops also need some adjustments during the procedure. In particular, the optical gains and the optimal demodulation phases of the error signals change during the CARM offset reduction. These changes are particularly rapid in the latest stages of the reduction, when the power circulating in the arm and PRCL cavities increases abruptly.

Therefore, the gains, the demodulation phase and the filters of the DRMI control loops must be adjusted to maintain the loops stable until the CARM offset reduction is complete. Additionally, at the end of the CARM offset reduction, automated servo

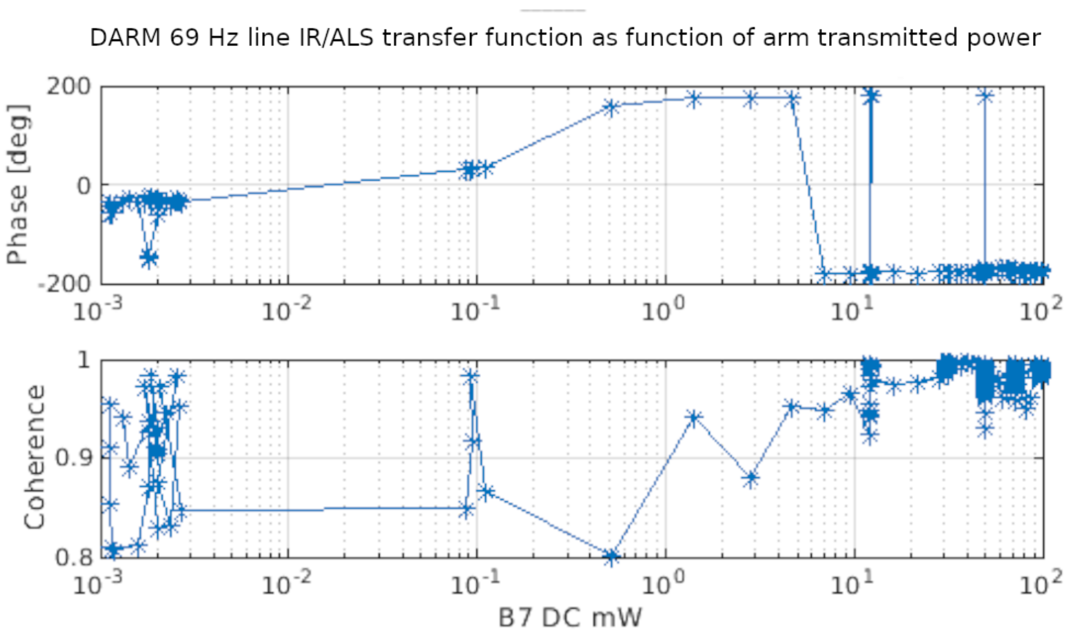

(a) Measurement of the phase difference between the ALS and IR RF-demodulated error signals for DARM as function of the arm transmitted power during the CARM offset reduction. The phase has been measured by estimating the transfer function between the two error signals at 69 Hz. At the same frequency, the DARM motion was excited by a noise line, in order to maximize the coherence of the error signals. One can notice a 180 °change happening between 0.1 and 1 mW of transmitted power.

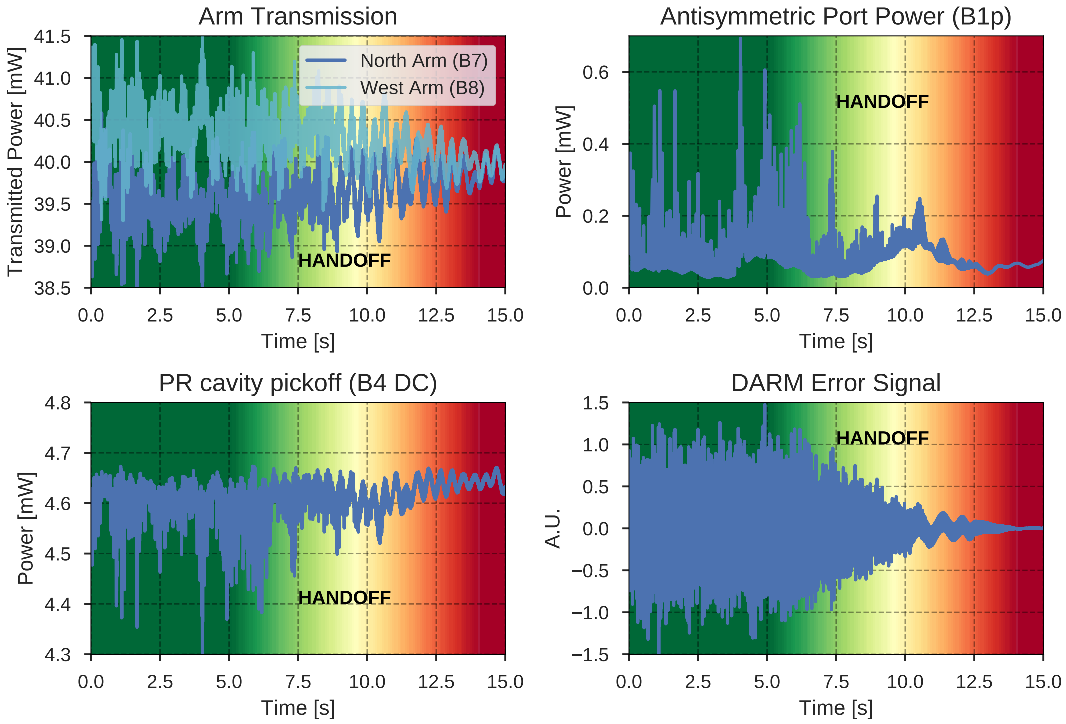

(b) Interferometer powers at the DARM handoff from the ALS error signal to the IR RF-demodulated signal (B1p 56 MHz). The plots show a gradual reduction of noise in the DC cavity powers (left plots), in the dark-fringe power (top-right plot), and in the in-loop error signal (bottom-right plot) during the change of error signal.

Figure 3.17

loops constantly monitor the UGF of all the LSC loops, and correct their gains to optimize their behaviour. Since the response time of the UGF monitors is too slow (usually a few seconds), they are not effective during the CARM offset reduction but only once the steady-state is reached.

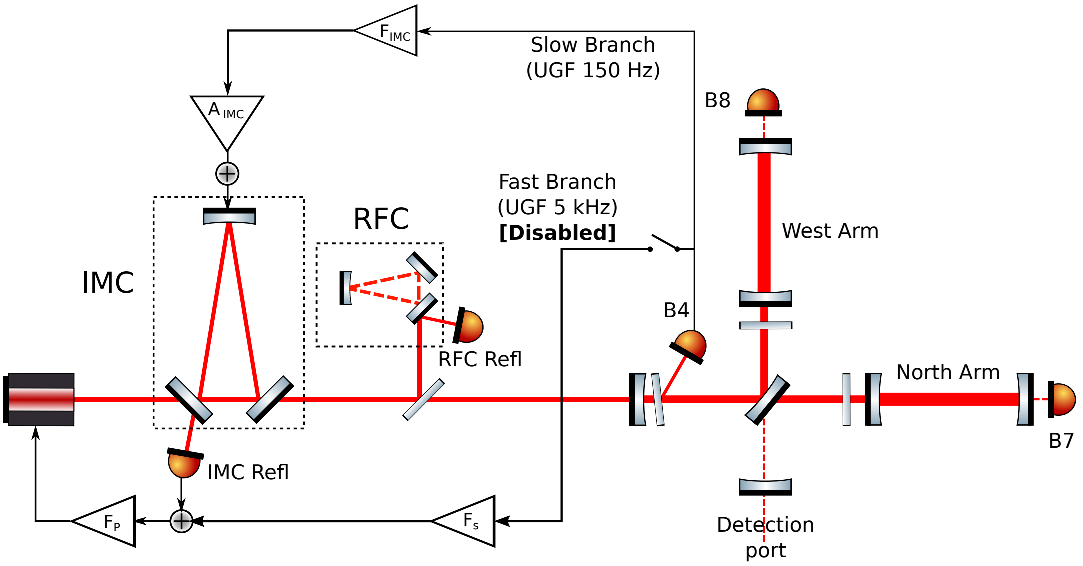

Figure 3.18: Scheme of the AdV+ frequency stabilization loop after the handoff of CARM to the IR RF signals. The laser frequency is now controlled by the CARM error signal through actuation on the IMC, while the CARM length itself is uncontrolled. The SSFS (fast branch) is still disabled.

3.4.2 Reaching Low-Noise operation

After the CARM offset zero point is reached, the interferometer (shown in figures 3.12 and 3.18) is ready for the final operations that will bring it to its final working point. The most relevant of these are the following:

- **Full engagement of the SSFS loop:** up to this point, the laser frequency control uses only the IMC error signal (see figure 3.18). At the same time, the IMC length is controlled by the CARM error signal. Therefore, the laser frequency is indirectly controlled by the interferometer. With the engagement of the SSFS loop, the high-frequency components of the CARM error signal are instead sent directly to the laser system, as shown in figure 3.19a. This allows to partially bypass the IMC loop, which has limited bandwidth ($\simeq 150$ Hz) due to the limitations of actuating on a suspended mirror. Thanks to the SSFS, the bandwidth of the frequency stabilization control loop can instead reach several kHz of UGF [61], greatly enhancing the frequency noise suppression. At the same time, since the low frequency (< 100 Hz) part of the error signal is still managed by the IMC loop, the IMC cavity remains locked, allowing the transmission of the laser to the interferometer.

- **Handoff of CITF error signals to the final "1f" low-noise signals:** Once the SSFS loop is engaged and the phase of the carrier in the CITF is stable enough, the PRCL, SRCL, and MICH loops control can be handed off to the final steady state signals, which have a much higher SNR. The PR Automatic Alignment (AA) loop's control, which is also enabled since the initial CITF lock, is also handed off from the "3f"' to the "1f"signals.

- **Engagement of the automatic alignment systems:** Most of the angular DOFs are uncontrolled during the lock-acquisition, relying on the local control systems until CARM offset zero is reached.

- **Thermal compensation:** Reaching CARM offset zero with the CITF locked dramatically increases the power circulating in the arm cavities, up to several hundreds of kilowatts. While the TCS system has been partially engaged since the start of the lock acquisition (mostly to compensate for the cold defects), the compensation needs to be changed at high power to compensate for the thermal effects caused by the high circulating power.

- **Low noise operation:** During most of the lock-acquisition, the feedback loops' control filters are optimized for robustness due to the necessity of keeping the lock during the transients. To achieve maximum sensitivity to GWs, many filters are changed at the end of the lock acquisition. The new filters aim to optimize noise suppression while maintaining reasonable robustness. Noise subtraction filters are also engaged (see section 4.3.2), and the arm mirror actuator electronics are switched from a high-dynamic actuation mode to a low-noise actuation with less maximum applicable force.

- **Engagement of RFC-CARM loop**: While most of the effects of a CARM displacement can be compensated by actuating on the main laser frequency, to achieve optimal conditions the CARM length drifts need also to be compensated. Indeed, suppressing CARM displacements allows to maintain a more stable laser frequency, simplifyng the lock of other cavities (such as the OMC) that would otherwise need to follow its changes. As shown in figure 3.20, the CARM stabilization is obtained by locking it on the RFC error signal, since the RFC is a more stable length reference at low frequency. In order to avoid injecting additional sensing noise, the CARM-RFC loop is maintained at a very low bandwidth of a few Hz.

- **Darm Offset and OMC lock:** A small offset ($\simeq 1 - 2 \cdot 10^{-12}$ m) is then added to the DARM loop in order to allow the engagement of the DC detection. The OMC is then locked on the beam from the antisymmetric port to transmit the carrier TEM 00 mode to the GW detection photodiodes on the B1 beam. Once this is done, the DARM control is handed off from the RF-demodulated signal B1p 56 MHz to the B1 DC signal.

- **Injection of squeezed light:** The last step before entering the "observation mode" (the state in which the detector is acquiring data for GW detection purposes) is the engagement of the squeezed light injection. Thanks to the FDS technology, the squeezed light injection allows reducing the effect of shot noise and radiation pressure noise on the DARM (and consequently on the GW strain) signal.

The final state of the interferometer, at the end of the lock acquisition, is shown in figure 3.19b.

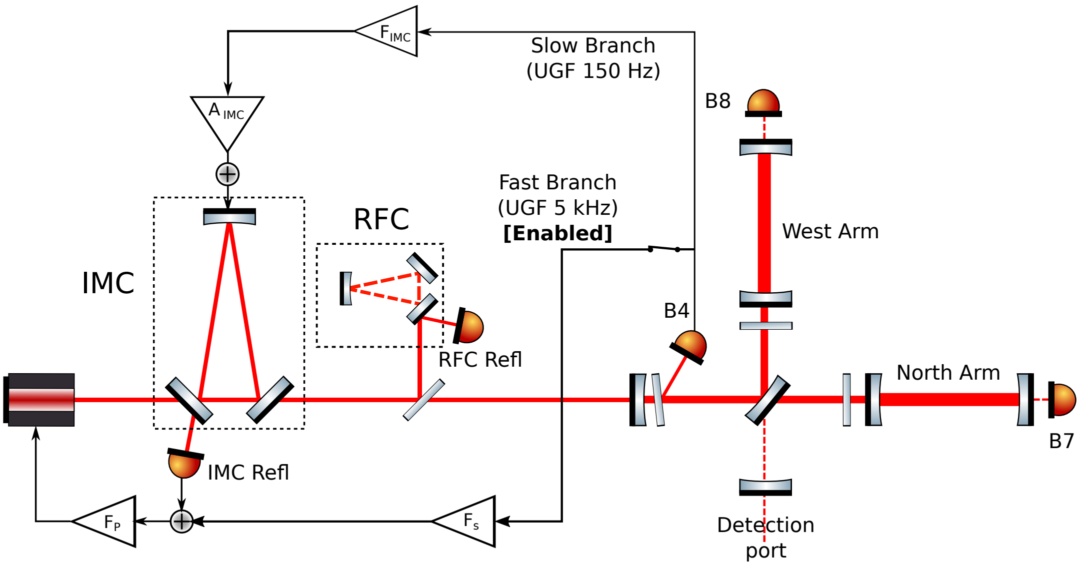

(a) Scheme of the AdV+ frequency stabilization loop after the angagement of the SSFS loop. The laser frequency is still controlled by the CARM RF-demodulated error signal through actuation on the IMC, while the CARM length itself is uncontrolled. The SSFS is now enabled, enhancing the frequency noise suppression up to the levels required for the detection og GWs.

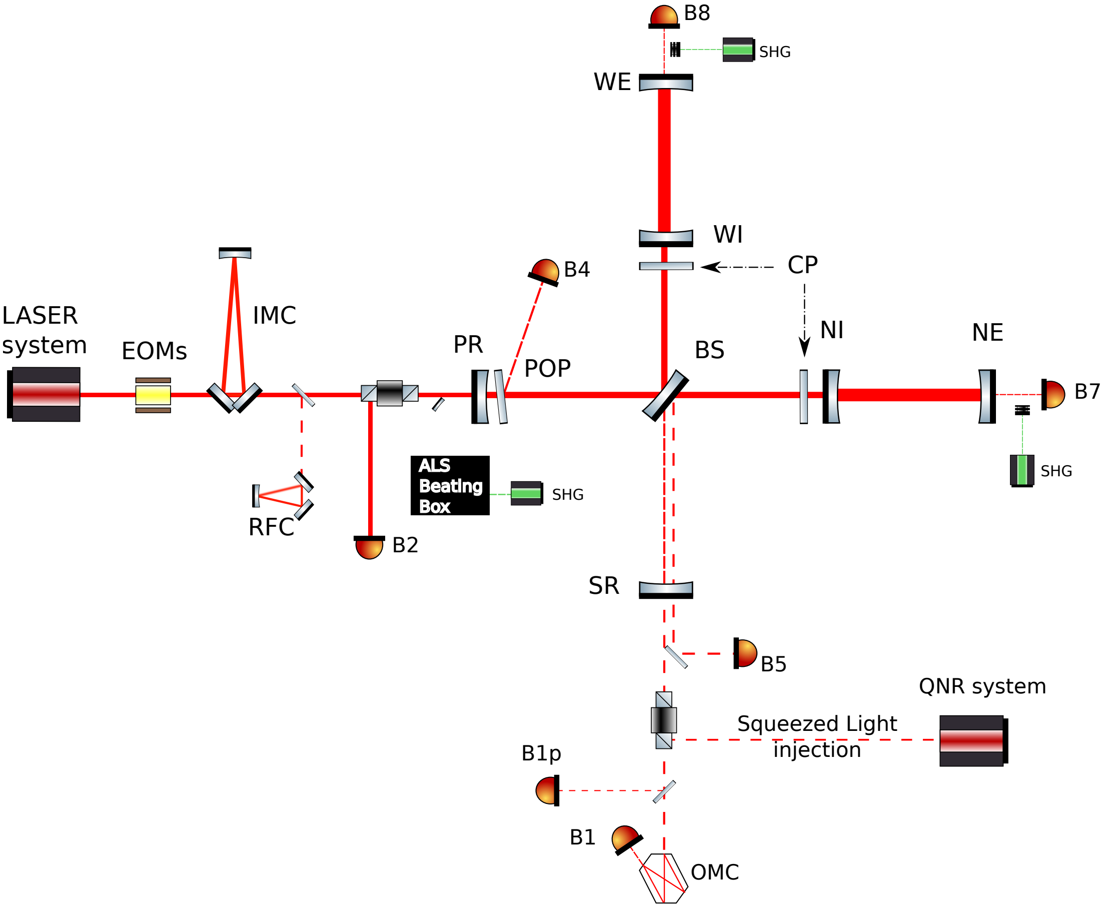

(b) Scheme of AdV+ in the final state, after the addition of the DC offset and the lock of the OMC. The ALS injection has been disabled, and the squeezed vacuum injection has been enabled.

Figure 3.19

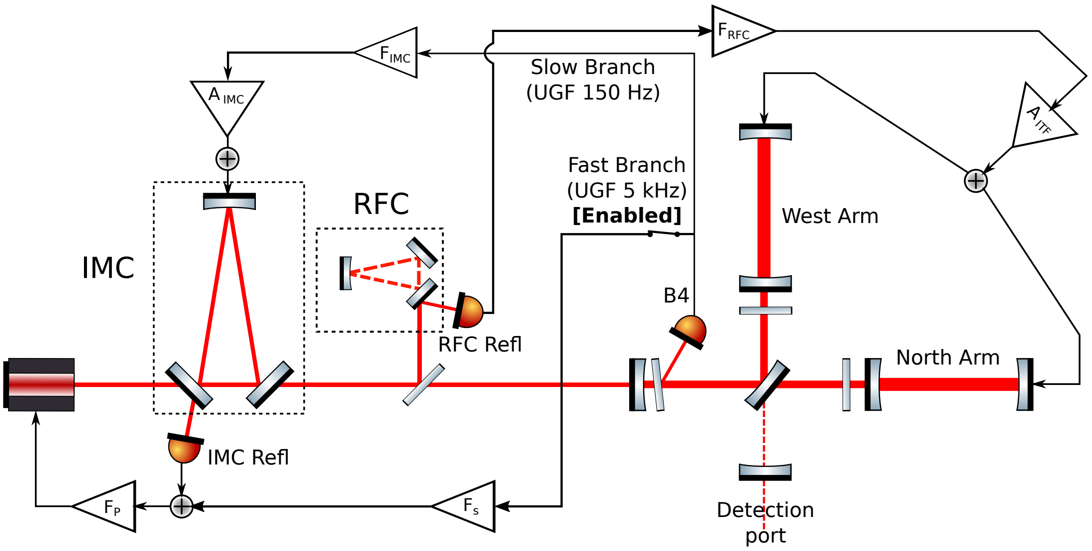

Figure 3.20: Scheme of the AdV+ frequency stabilization loop after the angagement of the RFC-CARM loop. The laser frequency is still controlled by the CARM RF-demodulated error signal through actuation on the IMC, while the CARM length is controlled by the RFC error signal. The SSFS is enabled, enhancing the frequency noise suppression up to the levels required for the detection og GWs.

3.5 Conclusions

Despite the unforeseen issues during the commissioning, the new AdV+ lock acquisition technique reliably allows the interferometer to reach the dark-fringe condition. Figure 3.21 shows an example of lock acquisition, highlighting the main locking steps described in the previous sections.

The first successful attempt at reaching CARM offset zero was achieved on 15 July 2021 [62], with an arm cavity circulating power of $\simeq$ 120 kW, after many months of efforts by the ISC team and the other commissioning groups. While initially, the procedure was lengthy and repeatable only a few times per day in optimal conditions, progress in its automation and the understanding of the interferometer behavior dramatically increased its reliability in the following months.

Unfortunately, the behavior of the interferometer in the dark-fringe state proved to be unstable and subject to transients that end up in an unlock after a variable amount of time (a few seconds up to tens of minutes). Since then, most of the commissioning work has been dedicated to better understanding the issues affecting the steady-state condition of the interferometer. The efforts allowed to obtain locks lasting up to a few hours, with the most extended lock (achieved in January 2022 [63]) lasting more than nine hours. However, the conditions leading to long-lasting locks proved to be non-systematically repeatable yet, and the corresponding working points feature sub-optimal strain sensitivity. The importance of maintaining an optimal steady-state working point and the studies related to it are treated in the next chapter 4.

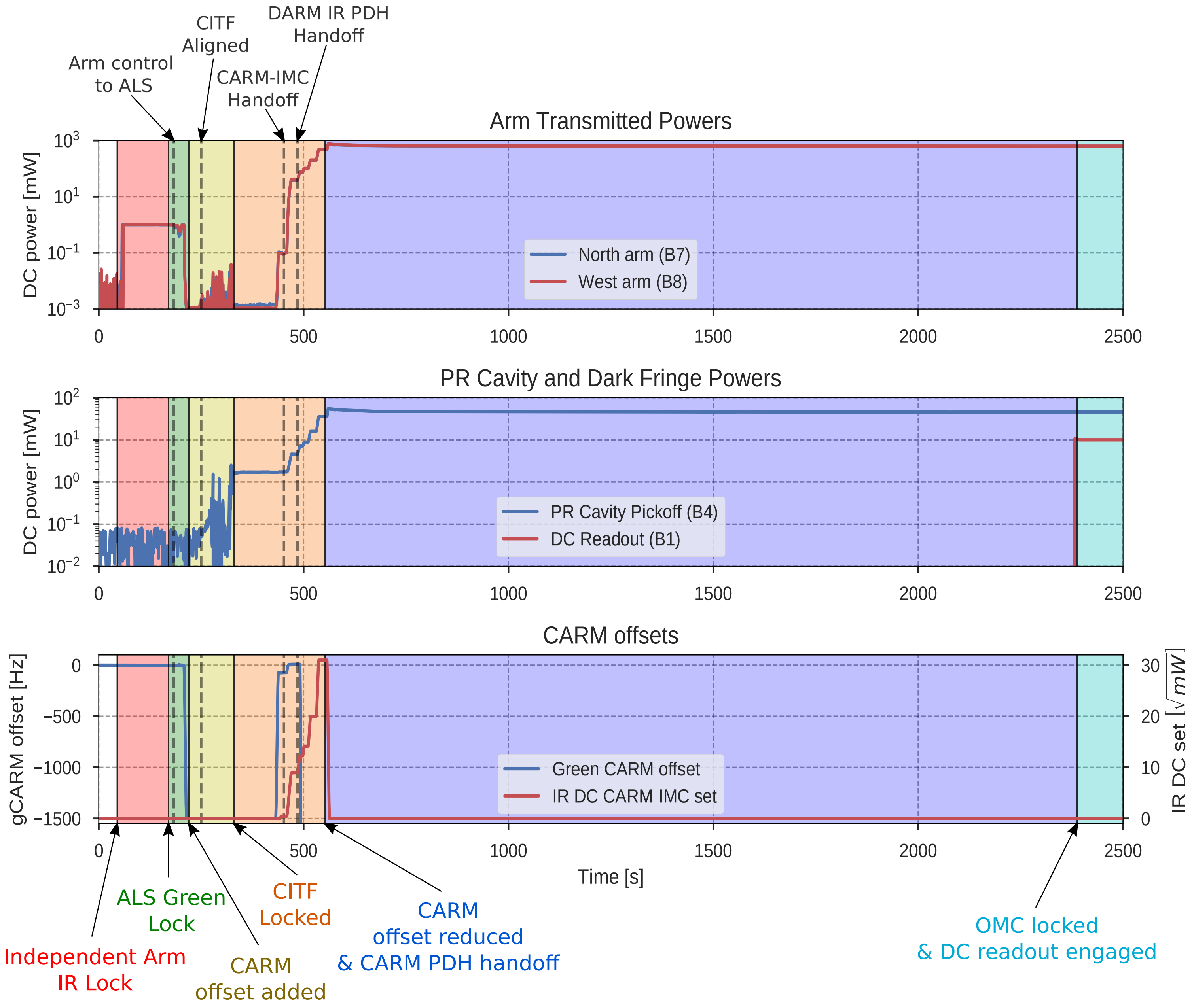

Figure 3.21: Behaviour of the cavity powers and of other interferometer signals during the lock-acquisition. The different background colors indicate the main steps of the lock-acquisition: IR arm lock (red), ALS lock (green), DRMI lock (yellow), CARM offset reduction (orange), CARM offset zero (blue), DC readout (cyan).

Chapter 4

Steady-state longitudinal control of Advanced Virgo Plus

This chapter reports the studies on the steady-state configuration of Advanced Virgo Plus. We refer to "steady-state" to indicate the final working point of the interferometer at the end of the lock acquisition procedure. In this point, no transient effects or optical configuration changes are expected. Most of these studies were performed prior to the commissioning of the AdV+ upgrades (started in January 2021). The overall purpose was to refine and finalize the design of the new control strategy before its implementation. Indeed, before the upgrades, the Advanced Virgo interferometer used a PRFPMI configuration. As mentioned in the previous chapters, the addition of the SR mirror required an overhaul of both the lock acquisition procedure and the final steady-state control strategy.

We carried out the studies with the help of the modal frequency-domain simulation tool Finesse 2 [48] [64].

At the end of the chapter we will give a preliminary comparison of the simulations results with the outcomes of the new control strategy's implementation. Since the steady-state commissioning of AdV+ is not yet complete, the comparison will focus on highlighting the main discrepancies encountered up to now.

4.0.1 Chapter Summary

Section 4.1 overviews how we modeled the AdV+ optical layout in Finesse for the simulations treated in this chapter. In this section, we also discuss the limitations of this model and possible improvements.

Section 4.2 updates the LSC loops accuracy requirements for the Advanced Virgo Plus configuration. These requirements define the maximum allowable RMS displacement for each DOF to ensure the controllability of the system.

Section 4.3 contains a more comprehensive study of the couplings of each LSC DOF to the strain channel as a function of frequency. This allows estimating the influence of their residual motion (and of the noises causing it) on the detector's sensitivity. This work is part of what is commonly called "Noise Budget". Preliminarily it involves a mix of theoretical modeling (of the noise sources) and simulations of the optical couplings.

However, to have a definitive estimate, both the couplings and the actual residual motion of each DOF can be measured experimentally once the detector is operative.

Section 4.4 studies the error signals for the longitudinal controls in the steady-state configuration. Simulations of the possible error signals have been used to compare the signals RMS and the coupling between the different DOFs to build a complete sensing matrix and choose the best candidates for the interferometer control. The results of the simulations are then compared with the outcome of the commissioning period on the real interferometer.

4.1 AdV+ configuration highlights and its Finesse representation

The first step of a simulation study is to model the interferometer in a way that resembles as much as possible the real setup. When available, we used the actual measured parameters of the interferometer components; otherwise, we used the design parameters. Fortunately, not every single component of the detector needs to be perfectly modeled, but particular attention is due to any component and parameter that might influence the results of the planned simulations. On the other hand, an as complete as possible model can be shared between different simulations with minimal changes, allowing multiple users to cross-check for possible discrepancies or errors. For this reason, a standard baseline configuration is maintained and kept up to date with the most recent measurements performed on the interferometer [65].

In preparing the model used in this chapter, we dedicated particular attention to ensuring that the interferometer is simulated in a ”tuned” and matched condition. This means that these simulations do not always represent the condition of the real interferometer, especially during the commissioning period, in which the optimal working point for all the DOFs is yet to be found. It is possible, however, from a perfectly matched and tuned configuration to incrementally add non-idealities and to study their effect while getting closer to the state of the real interferometer. This is currently being performed in parallel with the commissioning activities of AdV+.

The version used in this chapter’s simulations is one of the first iterations of this common configuration file after its update from the previous PRFPMI configuration to the new DRFPMI configuration. For the sake of ISC simulations, the most important updates with respect to the old model are the addition of the SR mirror and the increase of input power to 40 W (from the 25 W injected in O3).

In particular, the addition of the SR mirror and the corresponding cavity posed a challenge that can be understood by looking at the cavity parameters listed in table 4.1.

Indeed, from the above parameters, one may notice that the SRCL cavity is very close to a marginal stability condition. The same goes for the PRCL cavity, which shares the same curvature and length parameters. The low mode separation of such cavities makes the cavity resonant not only with the TEM00 mode but with many higher-order modes. This means that the presence of HOMs generated by non ideally matched or aligned interferometer can easily spoil the interferometer sensitivity and the quality of the error signals used by the control systems.

Additionally, the behavior of marginally stable cavities is difficult to reproduce in the simulations accurately, particularly in the presence of non-idealities. The limitations

Parameter	Value
SR cavities length	11.952 m
SR mirror High Reflectivity (HR) surface Radius Of Curvature (ROC)	1439* m
SR mirror HR surface Transmissivity	0.6
Input mirror HR surface ROC	1420 m
Cavity mode separation	7 kHz
Cavity TEM_{00} Round Trip (RT) Gouy ϕ	3.7 mrad

Table 4.1: SR mirror and SRCL cavity main parameters. Data were taken from [16] and [66]. *The ROC value of 1439 m corresponds to the measured ROC of the cold mirror. The value used in the simulations, however, is 1430 m, as explained in section 4.1.1.

given by this issue and by other simplifications of the simulated model are discussed in the following subsection.

4.1.1 Simulation model simplifications and limitations

In this section, we treat the most relevant issues met while building the simulated configuration for Finesse (also known as "kat" script), and the possible discrepancies between the simulated and the real interferometer.

Systems included in the simulated setup: The simulated layout includes only the main interferometer (starting from the PR mirror) and a simplified version of the detection system, including a mode-matching telescope and two OMCs.

The laser and injection systems and all the auxiliary benches are therefore not included in the simulated setup since they are not relevant for the sake of the studies reported in this document.

The old AdV design OMC setup (two cascaded OMCs) has been used instead of the new single-OMC since the latter was not complete when this study was performed. Conveniently, the influence of the OMC layout on the studied error signals is minimal. For similar reasons, the squeezed light source has been excluded from the simulated setup.

Length tunings: "Tuned" means that the microscopic position of the main interferometer optical components has been chosen in order to achieve the optimal interferometer working point. In practice, in the simulated setup, this means:

- Tuning the arm and power recycling cavities lengths in order to maximize the carrier power inside them;
- tuning the MICH DOF in order to minimize the carrier power on the antisymmetric port, reaching the dak fringe condition;
- tuning the SRCL in order to maximize the 56 MHz side-bands power in a position anti-resonant with the carrier field;
- (Not performed in all the studies) adding a small offset to DARM in order to have 4 mW of TEM_{00} DC power at the output of the OMCs.

Recycling cavities matching: A particular effort was required to study the mode-matching of the recycling cavities with the arm cavities. Indeed, in order for the SR and PR cavities to be matched with the arm ones, they both result marginally stable. The nominal design Radius of Curvature (RoC) of the PR and SR mirror is 1430 m[16].

However, the cold RoCs of the PR and of the future SR mirror substrates have been measured to be 1477 m and 1439 m, respectively [66] [67]. Using these measured values in the simulations raises several issues. Indeed, with these values and without considering any additional compensation or thermal effect, the PR and SR cavities are not matched with the arm cavities modes. This issue cannot be solved by just tuning the focal length of the two compensation plates as long as the PR and SR mirror RoCs are different.

While, in the real interferometer, the interplay of thermal effects caused by the main laser on the input and PR mirrors and the actuation of the TCS actuators (Ring heaters, Central-Heating, and Double-axicon heating) can solve these issues, a simplified approach has been chosen for the simulations. As mentioned above, this approach is based on the assumption of a well-matched and aligned interferometer, allowing to solve the aforementioned issues without limiting the representativeness of the study. In practice, this means that:

- the RoC of the SR and PR mirrors fixed to 1430 m (design value);
- the WI and NI Compensation Plates focal length chosen in order to match the SR and PR cavities with the arm cavities and to have a 3.7 mrad RT Gouy Phase shift for the TEM_{00} mode;
- the value of the two meniscus lenses before the OMCs have been tuned in order to minimize the matching losses with the Arm cavities eigenmodes.

4.2 Accuracy requirements

Accuracy requirements define which is the maximum RMS allowable displacement that a particular DOF control has to provide in order not to spoil the overall interferometer performance. In particular, most of the requirements in this section are defined by taking into consideration the controllability and the linearity of the control loop signals. The full impact of each DOF residual motion on the detector sensitivity is instead studied in the frequency domain with linear noise projection techniques, as treated in the next section 4.3.

The results and the methodology of this section's study have been initially reported in [68] [23]. The aim of this study was to update the residual accuracy requirements for the mirror longitudinal Degrees Of Freedom DOFs of the Advanced Virgo + detector. Indeed, the main intention of this study was to check the impact of the new optical configuration on the requirements computed and obtained for the previous configurations. Therefore, the used methodology was the same used in the previous version of this study, based on a different interferometer configuration, and reported in [69].

The main difference with respect to the above-mentioned reports is that the DARM and MICH requirements have been reconsidered in light of the accuracies obtained during the O2 and O3 runs. These differences and the principle followed to set the requirements for each DOF are summarised in the following paragraphs.

4.2.1 DARM and MICH

In the previous studies, the most restrictive requirement on the DARM and MICH DOF was estimated considering the quadratic nature of the dependence on DARM and MICH of its readout signal (B1 DC). This non-linearity indeed leads to a possible up-conversion of low-frequency residual displacement noise modulated by high-frequency oscillations given by the "violin modes", which are high-Q resonances of the silica suspension fibers holding the test masses [70]. Following this reasoning, requirements of $6 \cdot 10^{-16}$ m and of $2 \cdot 10^{-13}$ m were found, respectively, for DARM and MICH, in the PRFPMI configuration used in O2 and O3 [69]. Similar requirements ($2 \cdot 10^{-16}$ m and $6 \cdot 10^{-14}$ m respectively) resulted in applying the same approach to the new configuration [68]. However, these requirements were never completely satisfied during the previous observing runs. Indeed, during O3, an estimated residual motion of $3.2 \cdot 10^{-11}$ m was estimated for MICH [71], which is more than a factor 100 above the planned requirement. Despite this, no particular influence of up-conversion noise was observed on the detector sensitivity during the AdV observing runs.

This led to a change of approach. An alternative requirement for DARM can be defined by considering the linewidth of the arm FP cavities, which is $\simeq 1$ nm. To ensure the linearity of the phase response, we defined a conservative requirement of 1000 times below the cavity linewidth, resulting in $\mathbf{1 \cdot 10^{-12}}$ m.

The MICH DOF is not affected by the arm FP cavities, but the behavior of its error signals is, nevertheless, only monotonic in a limited region (as seen, e.g., in Figure B.7). A requirement based on the linearity of the error signal can therefore be obtained by scaling the DARM requirement by the FP cavity OG ($\simeq 290$). The resulting MICH requirement is $\mathbf{3 \cdot 10^{-10}}$ m.

4.2.2 PRCL

The main constraint on the PRCL DOF residual motion requirement is given by its controllability. This means that in order for the PRCL control loop to work properly, its length cannot deviate too much from the working point. Requiring the residual motion to be at least 1000 times smaller than the resonance peak FWHM of the Power Recycling cavity ($\simeq 5$ nm, as shown in Figure 4.1) leads to a requirement of $\mathbf{5 \cdot 10^{-12}}$ m.

4.2.3 CARM and frequency stabilization loop

Most of the effects of a CARM length variation can be compensated by an appropriate main laser frequency shift. Indeed, the CARM length error signal is used by the Second Stage Frequency Stabilisation SSFS control loop [72] [23]. However, this frequency shift will have to be followed by the other common-mode DOFs (PRCL and SRCL) and the OMC cavity. In order to suppress low-frequency drifts, the CARM length will also be controlled thanks to the use of a Reference Cavity acting as a frequency reference for the main laser (see scheme in B.3).

SSFS loop requirements: The most significant effect of a residual laser frequency shift will be a phase shift of the arm cavities reflected beam, which will directly affect the field inside the PR and SR cavities and can be mistaken for a length variation of such cavities. Due to the PRC's higher finesse than the SRC, the first one will be the most affected cavity. We can obtain the CARM accuracy requirement by re-scaling the

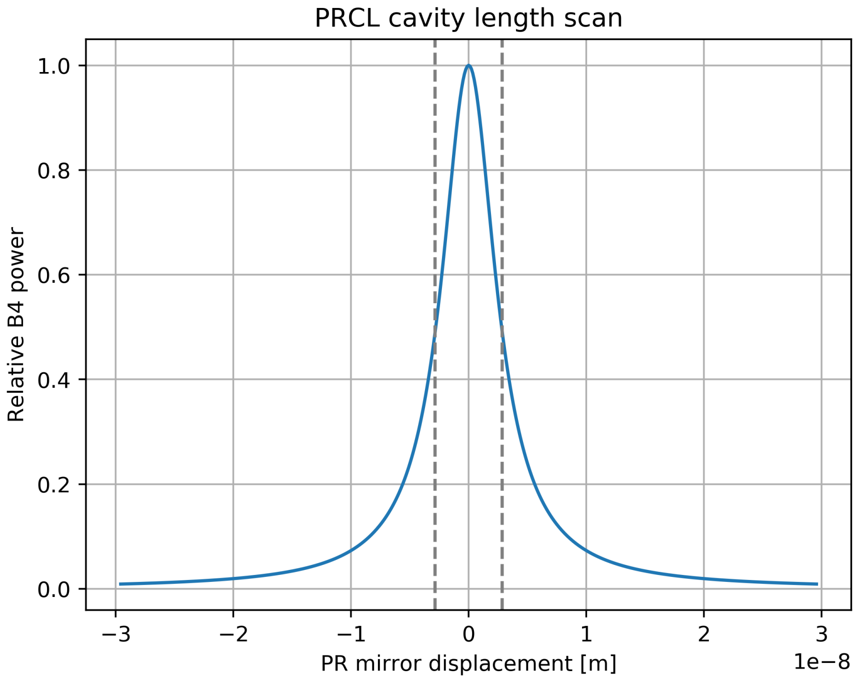

Figure 4.1: Finesse simulation of a PRCL cavity length scan. It was used to estimate the FWHM of the PR cavities. The resulting FWHM is ≃ 5 nm

PRCL accuracy requirement by dividing it by the arms Fabry-Perot cavities optical gain. This displacement can then be converted into a residual laser frequency shift accuracy requirement as follows:

$$\delta z_{\text{CARM}\rightarrow\text{SSFS}} = \frac{\delta z_{\text{PRCL}}}{OG_{arms}} \tag{4.1}$$

The result of this computation is a CARM residual motion of $2 \cdot 10^{-14}$ m, which is a stricter requirement than the one that can be estimated considering the CARM resonance linewidth. This requirement can then be converted to an SSFS residual frequency variation requirement of 10^{-3} Hz.

$$\frac{\delta f_{\text{SSFS}}}{FSR_{\text{CARM}}} = \frac{\delta z_{\text{CARM}\rightarrow\text{SSFS}}}{\lambda_0} \tag{4.2}$$

CARM requirement: As mentioned above, even if the SSFS loop follows a CARM length variation perfectly, the OMC cavity control loop does not have enough bandwidth to follow the frequency change. Therefore, a CARM displacement is converted into an effective OMC length variation. One could then compute a CARM requirement as follows:

$$\delta z_{\text{CARM}} = \frac{L_{\text{arm}}}{L_{\text{OMC}}} \cdot \delta z_{\text{OMC}} \tag{4.3}$$

Considering an OMC residual motion requirement of $\delta z_{\text{OMC}} = 6 \cdot 10^{-13}$ m as computed in [73], the CARM requirement is then $\delta z_{\text{CARM}} = 1 \cdot 10^{-8}$ m

4.2.4 SRCL

The main effect of a length displacement of the SRCL cavity is a variation of the interferometer response to DARM motion and, therefore, to gravitational wave signals.

The accuracy requirement for the SRCL is therefore set by requiring an absolute relative change of the interferometer DARM frequency response lower than 1% at any frequency in the detection band (≃10 to 5000 Hz).

In order to achieve this, the DARM optical transfer function has been simulated for various values of displacement of the Signal Recycling Mirror (SRM). A DARM offset of 4.5 pm, corresponding to 8 mW of power on the B1 photodiodes, has been used in the simulations. Results of the simulation are shown in Figure 4.2, showing the resulting accuracy requirement $2 \cdot 10^{-9}$ m. Due to the dependence of the DARM response to the DC offset, this requirement must be recomputed in case a much different DC offset is used.

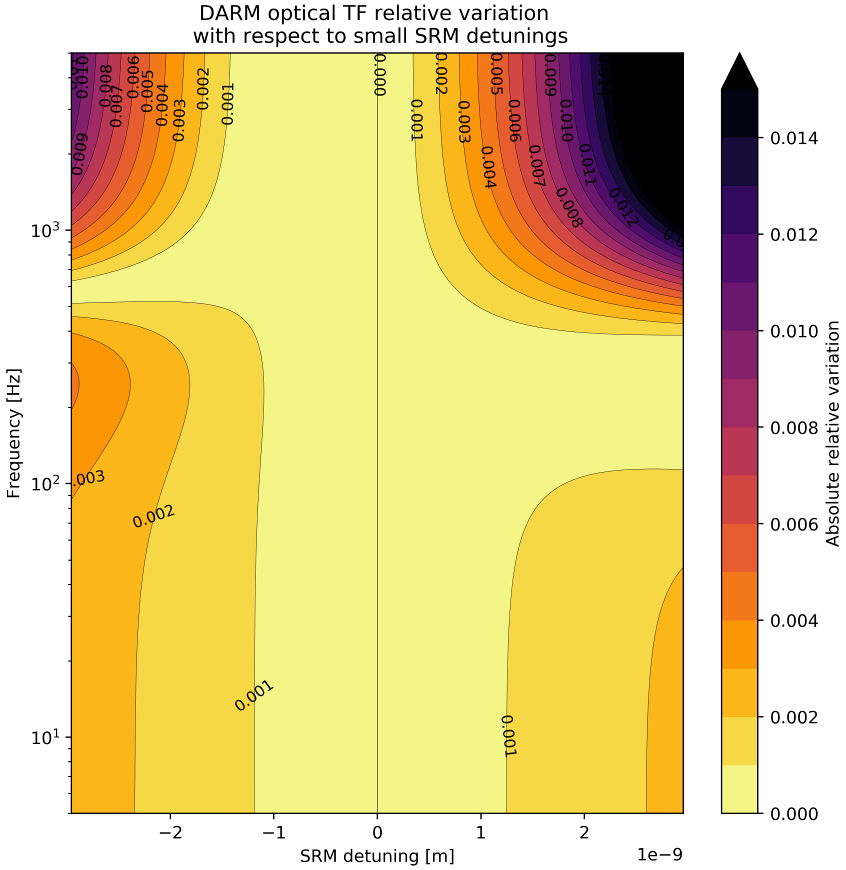

Figure 4.2: Results of the SRM detuning simulations. The plot shows the absolute value of the relative variation of the DARM transfer function as a function of frequency and SRM displacement in the detection band of the interferometer. It can be noticed that the variation of the DARM TF is well below 1% for displacements lower than 1.75 nm.

The effect of the SR cavity tuning on the DARM DOF transfer function can also impact its controllability and performance. Additional studies concerning this matter have been performed for an ideally matched interferometer ([74]) and are currently being updated to represent better the related issues met in the real interferometer during the commissioning [75].

4.2.5 Accuracy requirements results:

DOF	Requirement [rms]
DARM	$1 \cdot 10^{-12}$ m
MICH	$3 \cdot 10^{-10}$ m
CARM	$1 \cdot 10^{-8}$ m
SSFS	$1 \cdot 10^{-3}$ Hz
PRCL	$5 \cdot 10^{-12}$ m
SRCL	$2 \cdot 10^{-9}$ m

Table 4.2: Summary of the updated LSC requirements for AdV+ phase I.

Table 4.2 represents a summary of the updated accuracy requirements. As expected, the largest differences with respect to the requirements computed in [69] are the ones for the DARM, MICH, and SRCL DOFs. While the DARM and MICH requirements differences are mainly due to the different approaches taken in their estimate, the SRCL difference originates from the different tuning and reflectivity of this mirror with respect to the values initially planned for the Advanced Virgo detector.

4.3 LSC residual noise projections

In order to obtain a more advanced estimate of the impact of LSC DOF residual motion on the interferometer sensitivity, we computed a preliminary linear noise projection of the longitudinal displacement noises [76], based on the simulations of the new AdV+ configuration. More advanced studies have been carried out in the past months, using results from the commissioning of the real instrument and abandoning some of the simplifications used in this initial study. The refinement of these studies is part of the continuous effort to understand and mitigate the noises and the couplings affecting the interferometer. While the current status of these studies will be mentioned at the end of this section, the main focus will be on the methodology and results of the initial baseline study.

We will therefore focus on the estimate of the LSC noise projections (excluding the SSFS/CARM DOFs, which require a separate treatment), performed under the following assumptions:

1. The coupling of the ground motion with the mirror motion was the same as during the O3 run. SRCL is an exception to this assumption since it was not present during O3.
2. The coupling of the ground motion with the SRCL DOF is comparable with the coupling with the PRCL DOF.
3. The cross-couplings between different DOFs (excluding the couplings to DARM) are negligible.

Assumption 1 is based on the fact that the superattenuator system has not been meaningfully changed between the O3 and O4 runs. Assumption 2 considers that, out of the five suspended optics involved in the SRCL and PRCL DOFs, three are in common (NI, WI, and BS), while the two remaining ones (PR and SR) are very similar one to the other. Assumption 3 greatly simplified the preliminary estimate, but, ultimately, a complete study without this assumption ([77]) was required to verify the effects of cross-couplings.

4.3.1 Methodology

These assumptions allowed us to estimate the LSC residual- and sensing-noise procedure using the following procedure:

1. Estimate the DOFs input displacement noise using the error signals measured and calibrated during O3.
2. Compute the new OLTFs by replacing the old optical response with the new simulated one. Use it to estimate the new residual DOF displacement given by the input displacement noise.
3. Estimate the new detector shot noise and the corresponding residual displacement introduced by the feedback loop.
4. Simulate the couplings between the residual motion of each DOF and the DARM error signal. Use them to project the residual motion estimate on DARM and h[t].

Displacement noise estimate: Either the error signal or the feedback loop correction signal can be used to estimate the input DOF displacement noise [78]. Since we built this preliminary estimate before the commissioning of the AdV+ upgrade, we used measurements taken during the O3 run, shown in figure 4.3. Indeed, since the superattenuator system was unchanged with the upgrade, we assumed that the input seismic noise would remain the same in O4.

Thanks to the multi-stage pendulum superattenuator response, which sharply decreases at frequencies above 1 Hz, and to the natural spectral composition of ground seismic vibration [25], the seismic contributions to the residual mirror motion become indeed very small above a few Hz. Another major source of mirror displacement is the suspension thermal noise, which ASD decreases with a "$\sim \frac{1}{f^{\frac{5}{2}}}$" rate [79]. However, the error signal is also affected by sensing noise, which major contributor is the photodiode shot noise [80]. Therefore, since the shot noise does not decrease with the increase of frequency, the actual mirror displacement becomes negligible with respect to the sensing noise above 20 Hz. A low-pass filter has then been applied to the error signal in order to isolate only the frequency band in which the contributions given from the real mirror displacement are predominant. The shot noise contributions have instead been re-estimated and added as separate contributions in a later step.

Given S_{ee} the estimated ASD of the error signal, we estimated the residual DOF motion given by mirror displacement by lowpass-filtering and dividing S_{ee} by the DOF optical response H and the detector response D. Since, for most LSC DOFs, both $H[\omega]$

and $D[\omega]$ are flat at low frequency, they were replaced by a constant calibration factor G, measured during the O3 run [71].

$$S^i_{xx} \simeq S_{ee}\frac{|H_{lp}|}{|D \cdot H|} \simeq S_{ee}\frac{|H_{lp}|}{G} \tag{4.4}$$

Where H_{lp} is the transfer function of the low-pass filter applied to the error signal.

After this step, the residual motion has been divided by $\frac{1}{1-OL^{O3}}$, using an OLTF representing the O3 configuration, in order to obtain the corresponding input noise.

$$S_{ii} = S^i_{xx}[O3]|1 - OL[O3]| \tag{4.5}$$

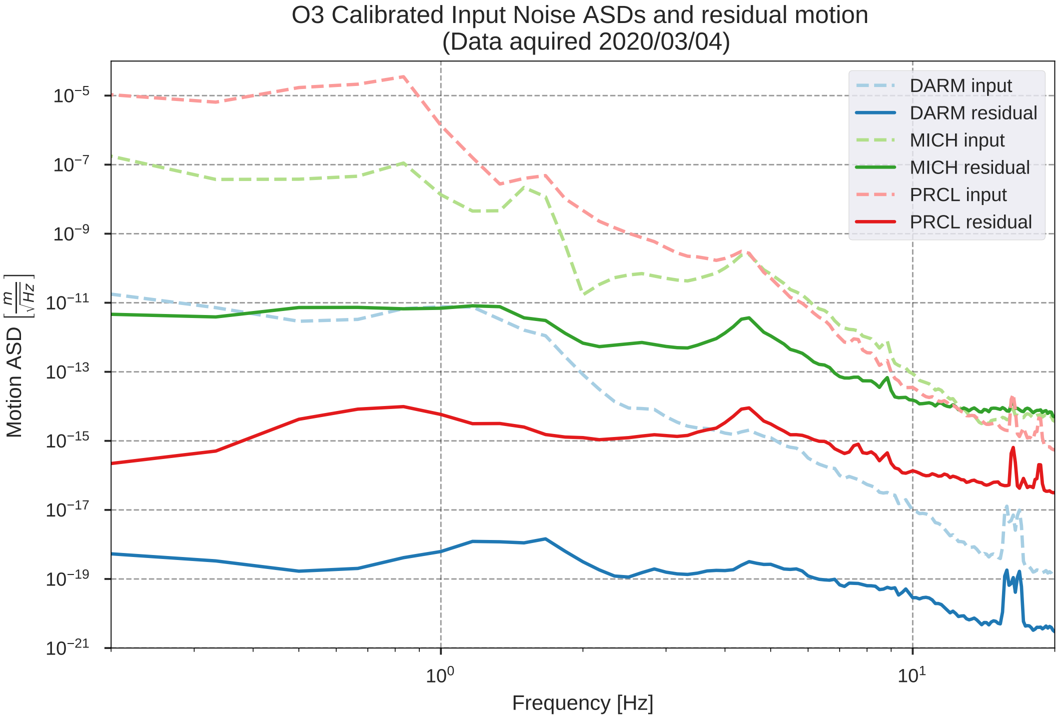

Figure 4.3: LSC DOFs estimated input displacement and residual motion ASDs measured during the O3 run. The residual motion estimate was performed using O3b data, and its corresponding input noise (dashed lines) has been used for the O4 noise projections.

New OLTF and residual displacement estimate The next step is to estimate the OLTF of the new configuration. Considering the performed upgrades, the following blocks constituting the OLTF will be different:

- Optomechanical plant (H): the new optomechanical plants were simulated with Finesse.
- Detector gain (D): the photodetectors and their electronics have been built in order to have a flat response in the detection bandwidth. However, the impinging light intensity and their gain are different in O4. We compensated for this gain

change by tuning the overall OLTF gain in order to follow stability, robustness, and performance criteria.

- Control filter (F): in order to optimize the feedback loop's robustness and performance, the control filters required a re-design. However, in these preliminary estimates, the old control filters (used during O3) were used since a control filter optimization procedure based only on the simulated plant would be premature. The final, MIMO-comprehensive projections [77] instead, have been performed with the current control filters and will be kept up-to-date with any changes.

The actuator response (A) will instead remain the same, since no changes in the actuators are planned for O4. The estimated OLTFs are shown in figure 4.4.

The new residual DOF displacement noise can be estimated using the new OLTF as follows:

$$S_{xx}^{i}[O4] = \frac{S_{ii}}{|1 - OL[O4]|} \tag{4.6}$$

New sensing (shot) noise estimate: The main noise contributor to the sensing noise is the laser shot noise on the photodiodes used to detect the error signals. A new shot noise estimate $S_{n_s n_s}$ has been obtained starting from the predicted impinging power on each of the involved detection photodiodes [81]. In these preliminary estimates, we did not account for squeezing effects given by the Quantum Noise Reduction systems. Additional sensing noise sources can be added and treated in the same way as the shot noise. The effective displacement noise given by the reintroduction of the sensing noise is obtained with:

$$S_{xx}^{n_s} = S_{n_s n_s} \left| \frac{D \cdot F \cdot A}{1 - OL[O4]} \right| \tag{4.7}$$

Projection on DARM photodiode: Once the noise source contributions to the residual motion of each DOF have been estimated, it is finally possible to project them to DARM. The cross-coupling transfer function of each LSC DOF to the DARM error signal $H_{\mathrm{DOF} \to \mathrm{DARM}}$ has also been estimated using Finesse. The contribution of each DOF's residual motion can then be computed and treated as an additional noise n_{coupl}^{DOF}added to the DARM error signal. Each contribution can be represented in the frequency domain by its ASD $S_{ee}^{\mathrm{DOF} \to \mathrm{DARM}}$:

$$S_{ee}^{\mathrm{DOF} \to \mathrm{DARM}} = S_{xx}^{\mathrm{DOF}} \left| \frac{H_{\mathrm{DOF} \to \mathrm{DARM}}}{OL_{\mathrm{DARM}}} \right| \tag{4.8}$$

Projection on the strain channel h[t]: Once the contributions to the DARM error signal have been computed, they can be compared between each other. Additionally, by converting them into strain units ($h[t]$), they can be compared with the overall planned or measured detector sensitivity curve. In order to do this, one has to first convert them into their equivalent DARM input displacement and then divide them by 3000 (the common arm length).

$$S_{hh}^{\mathrm{DOF} \to \mathrm{DARM}} = S_{ee}^{\mathrm{DOF} \to \mathrm{DARM}} \left| \frac{1}{3000 \cdot CL_{\mathrm{DARM}}} \right| \tag{4.9}$$

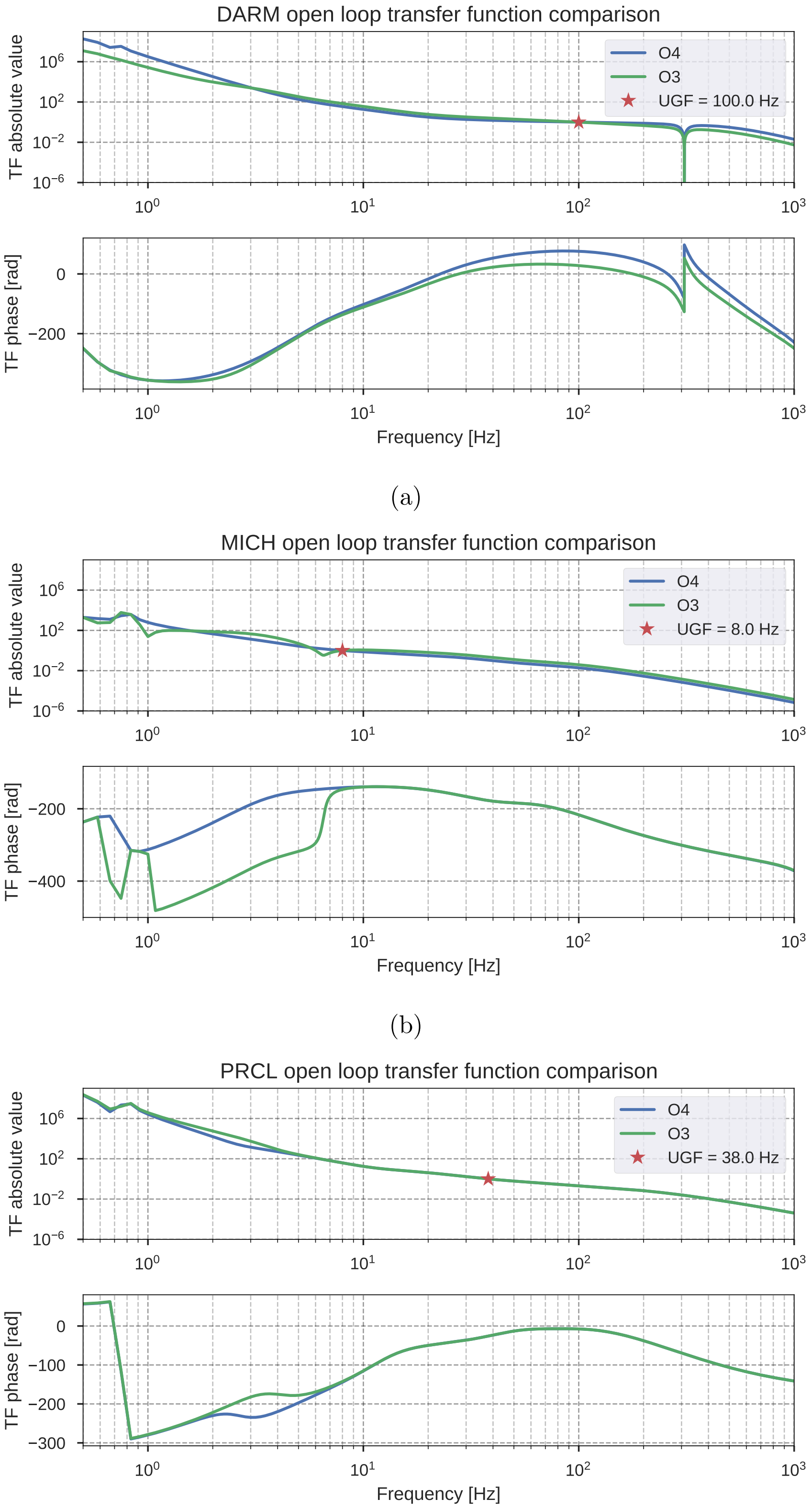

(a)

(b)

(c)

Figure 4.4: Comparison between O3 and O4 DARM, MICH, and PRCL (plot a, b, and c respectively) open-loop transfer functions. The same control filter, detector, and actuator TF as in O3 have been used, with the only difference between the O3 and O4 TFs being the interferometer's optomechanical response. The gains of the TFs have been tuned to obtain UGFs of $\simeq 100$, $\simeq 8$, and $\simeq 38$ Hz respectively, as was measured during O3.

Where we remind that $CL_{\text{DARM}} := \frac{H_{\text{DARM}}}{1-OL_{\text{DARM}}}$ is the closed-loop transfer function of DARM.

Additionally, if the contributions are independent of each other, they can be summed to estimate the total contribution of LSC noises to the detector sensitivity.

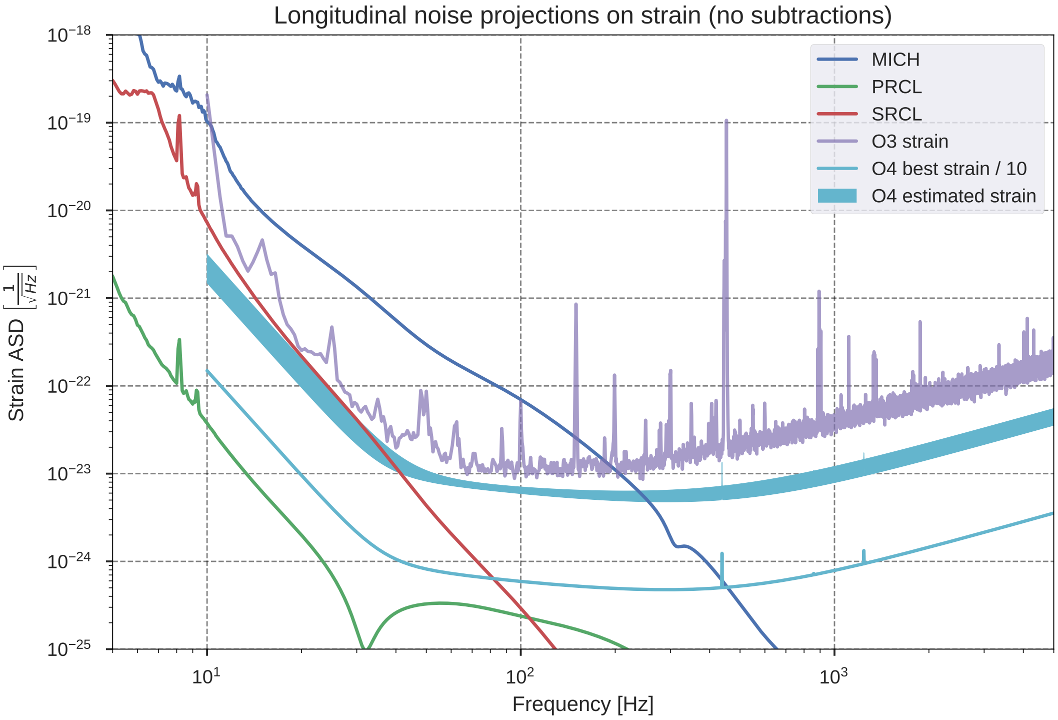

Figure 4.5: Results of the preliminary LSC noise projections on the detector strain sensitivity. The contributions of the MICH, PRCL and SRCL DOFs to the strain are compared with the strain sensitivity measured during the O3 run, with the planned sensitivity for the O4 run, and with the requirement of the noise being ten times below the lowest planned sensitivity curve. One could notice that both the MICH and SRCL noises do not fit below the threshold and will require the use of a noise subtraction technique.

4.3.2 Resulting projections and further studies

Figure 4.5 shows the resulting noise projections for PRCL, SRCL, and MICH, compared with the O3 and with the planned O4 sensitivity curves. The planned target for the control noise contributions to the strain signal is for them to be at least ten times below the planned sensitivity.

One could quickly notice that the resulting contribution of MICH is largely above the planned sensitivity curve. The SRCL contribution is also above the “10 times lower” threshold. Such large contributions cannot be meaningfully mitigated by simply optimizing the control filters. Indeed, during the previous observing runs of Virgo+ and Advanced Virgo, the issue was solved with the implementation of cross-coupling noise subtraction loops [82].

The noise subtraction technique is based on estimating a DOF’s residual motion using its feedback loop's correction C_{DOF}. Then, this correction is passed through a filter F_{sub}^{DOF} and then added to the DARM correction channel.

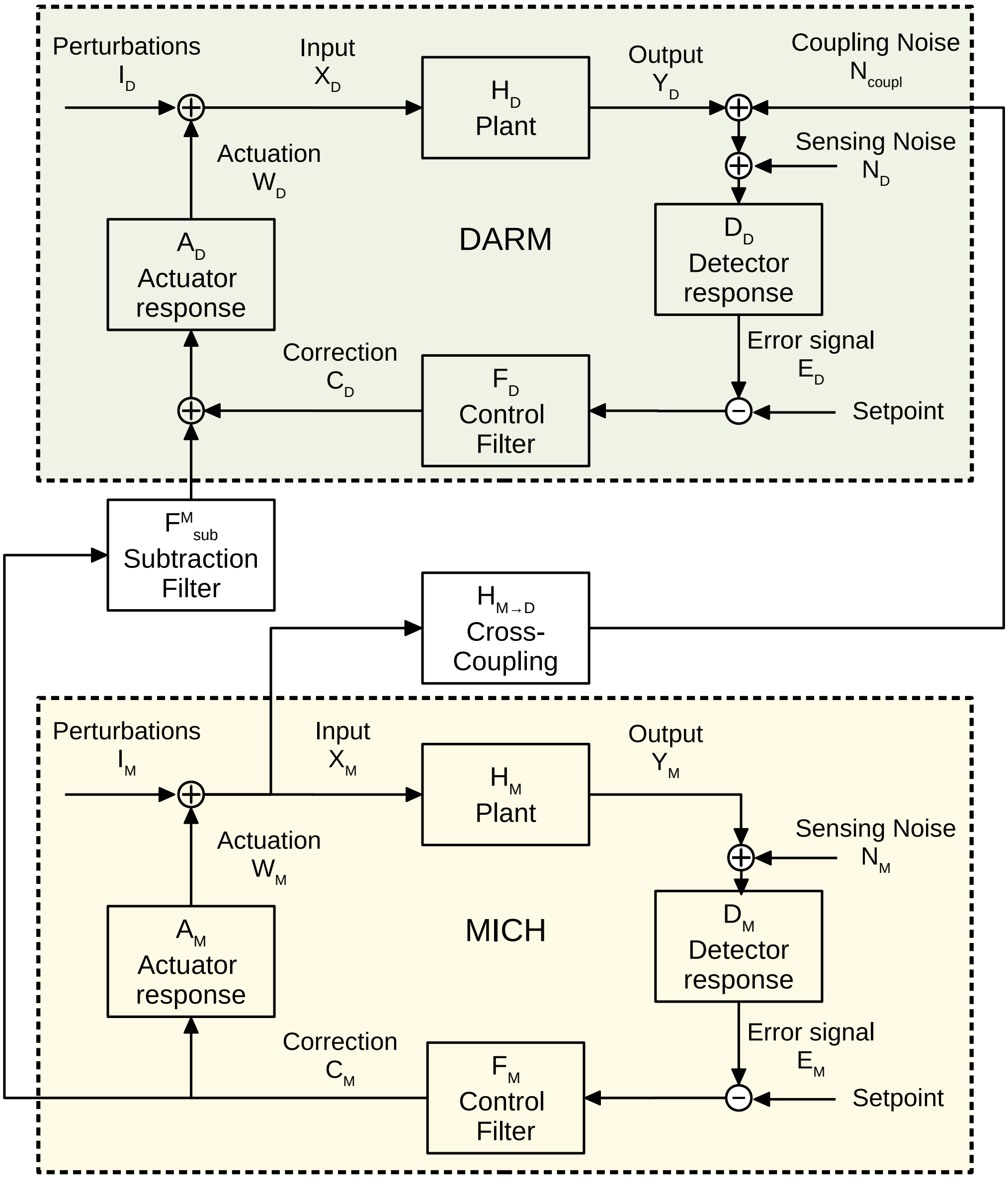

Figure 4.6: Example of the coupling mechanism between two DOFs and of its corresponding noise subtraction. In this example, the MICH cross-coupling contribution ($H_{M\rightarrow D}$) to the DARM error signal is suppressed by adding the MICH correction to the DARM correction signal after appropriate filtering with F_{sub}^{M}.

The filter is designed using an estimate of the cross-coupling of that DOF to DARM and allows the loop to ultimately suppress it.

For example, let's consider the MICH coupling to DARM. The two loops and their interactions are represented in figure 4.8. For readability purposes, in this example, we shortened their names to $_M$ and $_D$ respectively. Given $\mathbf{X}_M$ the MICH residual motion, and $H_{M\rightarrow D}$ its coupling transfer function to the DARM error signal, one has, without subtraction:

$$\mathbf{E}_D = (\mathbf{Y}_D + \mathbf{X}_M \cdot H_{M\to D}) \cdot D_D \tag{4.10}$$

The MICH residual motion X_M can have contributions from different noises added at different points of the feedback's path. Following the scheme in 4.6, we can consider as the main contribution the sensing noise n_{sens} added by the detector and an input displacement perturbation i given, for example, by seismic or thermal noise. We remind therefore that the residual MICH displacement can be written as $\mathbf{X}_M = \frac{1}{1-OL_M}(\mathbf{I}_M + \mathbf{N}_M \cdot D_M \cdot F_M \cdot A_M)$. The correction, used by the noise subtraction loop, can therefore be written as

$$\mathbf{C}_M = \frac{\mathbf{X}_M - \mathbf{I}_M}{A_M} \tag{4.11}$$

Adding the noise subtraction loop to equation 4.10 as in figure 4.6 gives therefore:

$$\begin{aligned}
\mathbf{E}_D &= (\mathbf{Y}_D + \mathbf{X}_M \cdot H_{M\to D}) \cdot D_D && (4.12)\\
&= \left[H_D A_D \left(\mathbf{E}_D F_D + \mathbf{C}_M F^M_{sub}\right) + \mathbf{X}_M \cdot H_{M\to D}\right] \cdot D_D && (4.13)\\
&= \left[H_D A_D \left(\mathbf{E}_D F_D + \frac{\mathbf{X}_M - \mathbf{I}_M}{A_M} F^M_{sub}\right) + \mathbf{X}_M \cdot H_{M\to D}\right] \cdot D_D && (4.14)\\
&= \frac{D_D}{1 - OL_D}\left(H_D A_D \frac{\mathbf{X}_M - \mathbf{I}_M}{A_M} F^M_{sub} + \mathbf{X}_M \cdot H_{M\to D}\right) && (4.15)
\end{aligned}$$

One can see that the contribution of MICH cannot be canceled entirely. This is due to the slightly different paths followed by the subtraction loop and the optical coupling. In the case the input noises $\mathbf{I}_M$ are small, one could, however, decide to tune the subtraction filter to cancel the $\mathbf{X}_M$ contribution:

$$F^M_{sub} := -\frac{H_{M\to D} A_M}{H_D A_D} \tag{4.16}$$

This will result in an overall contribution of MICH to the DARM error signal given by

$$\mathbf{E}_D = \frac{D_D}{1 - OL_D} \mathbf{I}_M H_{M\to D} \tag{4.17}$$

This approach was used since the early Virgo science runs, during which the MICH contribution to DARM was suppressed by a factor of ≃ 1000 between 10 and 200 Hz [83].

During the O3 run, this approach was extended to couplings between PRCL and SSFS DOFs. Additionally, a similar technique was used to subtract from DARM the effect of noises that are not originated from the coupling with a different DOF but from external noise sources, such as the 50 Hz noise coming from the electrical mains [29].

For O4, the implementation of an additional subtraction filter for the SRCL loop is currently under study.

4.4 Optimal error signals for the O4 run

An in-depth study of the error signals and control strategy used for Advanced Virgo (AdV) in the O2 and O3 run is in [15] and [84]. The results of its implementation during the O2 and O3 scientific runs are explained in [31] and [29], respectively. However, the difference between the AdV and Advanced Virgo plus (AdV+) configuration required an update on multiple aspects of those studies.

This section summarizes the study on the error signals that have been chosen for the control of the longitudinal DOFs in the steady-state configuration of the AdV+ phase one interferometer. This study has been performed using the modal frequency-domain simulation tool Finesse with Pykat [64] and is also reported (with some additional details) in [85].

Despite the commissioning of the new configuration not being complete at the time of writing this thesis, this section contains a comparison of the simulations with preliminary observations of the behavior of the error signals in the real interferometer.

In particular, the following topics will be treated:

- AdV+ available error signals;
- proposed error signal choices and corresponding sensing matrix;
- study of preeminent error signals for each DOF;
- comparison with the real interferometer.

4.4.1 Control side-bands, ports, and available error signals

We remind that the AdV+ interferometer includes multiple output ports in which broadband photodiodes probe the laser beam. The photodiode's location and the denomination of the acquired beams are listed in section 2.3.1. They are also displayed in the interferometer's layout in figure 2.7.

In particular, beams measured at the following ports have been simulated and studied:

- Antisymmetric port, pick-off before the OMC (B1p).
- Symmetric port or interferometer reflection (B2).
- Power recycling cavity pick-off port (B4), extracted using the POP.
- Beam Splitter antireflective surface pick-off (B5).

DOF	Error Signal	Loop UGF [Hz]	Sampling Freq. [Hz]
PRCL	B2 8 MHz	40	10^4
MICH	B4 56 MHz (Q)	18	10^4
CARM	B4 56 MHz (I)	10000	$5 \cdot 10^5$
DARM	B1p 56 MHz	70	10^4

Table 4.3: Overview of the LSC error signals and control loop main characteristics during the previous O3 run. Note that the SRCL loop was not present at the time and now also has 10^4 Hz of sampling frequency and a low UGF of ($\simeq$ 7Hz).

Table 4.3 lists the LSC error signals that were used in the Advanced Virgo Power Recycled InTerFerometer (PRITF) steady-state configuration during O2 and O3. Note that, in this configuration, the 6.27 MHz sideband (f1) was not used. Indeed, due to photodiode saturation issues, the corresponding EOM modulation depth was significantly decreased (-29 dB) in the last stages of the locking sequence, as explained in [31].

This issue was solved in the new AdV+ configuration. Nevertheless, in addition to the main sidebands listed in 2.3.3, alternative higher modulation frequencies of 31 353 885 Hz (5·f1), and 43 895 439 Hz (7·f1) have also been simulated to address any possible limitations. The reason behind studying higher possible modulation frequencies is that, as shown in chapter 3 for the central interferometer lock, high modulation frequency error signals are moderately less affected by misalignments in the marginally stable recycling cavities. This is due to the lower finesse of the recycling cavities for sidebands at higher frequencies, caused by the Schnupp asymmetry.

However, since the observed robustness improvement was not substantial and higher frequency signals also have an overall lower optical gain, these signals have been considered to be valid but sub-optimal alternatives to the 6.27 MHz signal. Therefore, the study focused on the behavior of the 6.27, 56.4 and 8.36 MHz sidebands, with the assumption that no issues will prevent the usage of error signals based on the 6.27 MHz sidebands. Indeed, the AdV+ commissioning showed no particular issues in the use of these sidebands up to now.

4.4.2 Study overview

The controllability of a system can be evaluated by modeling the sensitivity of the error signals with respect to the DOFs displacements. One of the requirements needed to ensure the accuracy and stability of the control loop design is, in simple terms, that the motion of other DOFs does not influence the chosen error signal for a specific DOF. The most straightforward way of estimating whether this requirement is met is by studying the **optical gain** of the error signals relative to the displacement of each DOF.

The optical gain: The optical gain is the derivative of an error signal with respect to the displacement of a specific DOF in units of [W/m]. In order to compare different error signals, their optical gains can be normalized with respect to the maximum power measured by their corresponding photodiodes. We will call this **power-normalized optical gain**.

Error signal SNR: To estimate the shot noise SNR, we computed the optical gain divided by $\sqrt{h\nu P}$, where P is the total beam power arriving on the photodiode and ν is its frequency [86]. This quantity is not independent of the DC power impinging on the photodiode. Therefore an estimate of the powers foreseen on each photodiode [81] has been used to compute it.

The sensing matrix: The optical gains of multiple error signals with respect to each interferometer DOF can be used to build the “sensing matrix”. In this matrix, each element G_{ij} is the power-normalized optical gain of the error signal ‘i’ with respect to the DOF ‘j’. The previously mentioned requirement for the controllability of the interferometer control loops can therefore lead to the requirement of having an *as diagonal as possible* sensing matrix. The normalized sensing matrices resulting from this study, such as table 4.4, are reported at the end of this section. The demodulation phase used in the error signals reported in these matrixes has been chosen to maximize the optical gain for the diagonal element.

Working point and Optical Gain dependence on the demodulation phase In the real interferometer, several issues can result in a sub-optimal demodulation phase tuning for an error signal. A sub-optimal demodulation phase can deteriorate the error signal in the following ways:

- Lowering the Optical Gain of the controlled DOF;
- shifting the Working Point;
- increasing the coupling with other DOFs.

In a good error signal, as long as the demodulation phase is tuned properly (within a precision of $\simeq 10^\circ$), these effects are small enough to not hamper the controllability of the system. However, certain error signals show a particularly high working point dependence on small demodulation phase variations, as in the example in figure 4.7b. This is due to the non-zero contribution of other DOFs to the error signals ([15], sec. 5.2). Therefore, for each error signal, the amount of working point displacement corresponding to a demodulation phase variation of 10° has been checked against the accuracy requirement of the controlled DOF (defined in section 4.2). As shown in tables B.1, B.2, B.3, B.4, and B.5, all the error signals have a working point displacement within the accuracy requirements.

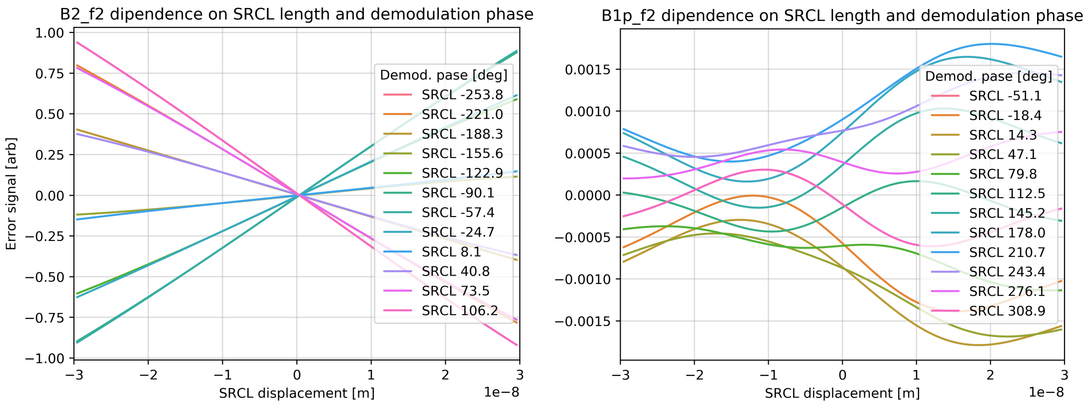

(a) Robust (b) Not Robust

Figure 4.7: Example of error signals with different robustness against demodulation phase variations.

Additional aspects of the error signals: A deeper study of the error signals behavior shows that the optical gain and, therefore, the sensing matrix is an incomplete figure of merit of the quality of an error signal. Indeed we will show that alone it can lead to the exclusion of good error signals or to the choice of sub-optimal ones. Other important parameters that have to be considered in the choice of an error signal are:

1. The width of the linear region, that is, the maximum displacement that a DOF can be subjected to without the error signal losing linearity;

2. the ‘peak-to-peak’ value that each error signal reaches within the linear response region of each DOF;
3. the error signal working point, that is, the point of zero-crossing, with respect to the controlled DOF working point;
4. the robustness of the error signal working point and optical gain with respect to demodulation phase variations and noise;
5. the error signal SNR with respect to the sensing noise, considering, in particular, the shot noise contribution, which depends on the total power measured by the sensing photodiode;

These factors have been considered in the choice of the error signals, and the most relevant insights obtained are explained in detail for each DOF in appendix B.

4.4.3 Sensing matrices

Table 4.4 shows the sensing matrix for the primary error signal choice for each LSC DOF. These error signals and their corresponding loops (with the exception of CARM/SSFS) are also represented in figure 4.8.

In the table, the CARM column values have all been divided by a factor of 10^8. This is done to emulate the behavior of the SSFS loop, which hierarchically suppresses the effect of CARM displacement on the error signals [72].

Several issues can be immediately spotted by giving a quick look at it and by noticing that it is not diagonal:

- The error signal designed for PRCL (B2 8 MHz) shows a relatively high optical gain for both PRCL and DARM;
- the error signals chosen for MICH and SRCL (B2 56 MHz I and Q) both show a relatively high optical gain for PRCL and DARM too.

These issues, respectively, to each DOF, are treated in detail in appendix B, along with additional clarifications and alternative error signals proposals, summarised in the alternative sensing matrices 4.5 and 4.6.

One last note is that the primary choice of error signals, listed in 4.4, is similar to the one that was used in the PRITF configuration, with the following differences:

- CARM/SSFS and MICH error signals are moved from B4 to B2 photodiode;
- CARM/SSFS error signal uses now the 6 MHz sidebands instead of the 56 MHz one, since, during O3, the 6 MHz sideband was disabled due to photodiode saturation issues;
- SRCL error signal has been added, using the in-quadrature component of the signal used to control of MICH.

	PRCL	MICH	CARM·10^{-8}	DARM	SRCL
B2 8 MHz I	**2.7e+08**	6.4e+05	7.3e+02	1.3e+08	2.0e+04
B2 56 MHz Q	**2.3e+07**	**6.0e+06**	5.9e+01	1.1e+07	2.1e-01
B2 6 MHz I	3.1e+07	8.4e+04	**1.0e+11***	1.8e+08	1.0e+05
B1p 56 MHz I	3.8e+04	1.4e+08	1.9e+00	**4.2e+10**	5.4e+04
B2 56 MHz I	**9.8e+06**	1.4e+05	5.1e+2	9.3e+07	**3.1e+06**

Table 4.4: Primary sensing matrix. Note that the error signals are listed in the same order with respect to the DOF that they are designed to control so that the diagonal elements (bold) correspond to the relative-power optical gain of the DOF controlled by each error signal. Red values highlight off-diagonal elements that have higher optical gain than the corresponding diagonal element. Red values in the PRCL column are in bold since they have a larger overall influence on the error signal than the DARM ones, as discussed in the MICH B.3 and SRCL B.5 subsections. Values are in units of [1/m]. *All the CARM column values except for the diagonal elements are multiplied by 10^{-8}, as explained in section 4.4.3.

	PRCL	MICH	CARM·10^{-8}	DARM	SRCL
B2 8 MHz I	**2.7e+08**	6.4e+05	7.3e+02	1.3e+08	2.0e+04
B4 56 MHz Q	**9.9e+06**	**2.2e+06**	2.7e+01	4.7e+06	2.2e+03
B4 6 MHz I	3.0e+07	6.3e+04	**2.5e+10***	4.7e+07	3.4e+04
B1p 6 MHz I	8.5e+04	2.7e+07	3.3e-01	**7.7e+09**	7.7e+03
B4 56 MHz I	**6.3e+06**	8.0e+04	-1.5e+2	2.7e+07	**1.1e+06**

Table 4.5: Alternative sensing matrix. This solution uses B4 signals for CARM MICH and SRCL instead of the B2 signals. It also shows the alternative signal B1p 6 MHz for DARM. Note that the error signals are listed in the same order with respect to the DOF that they are designed to control so that the diagonal elements (bold) correspond to the relative-power optical gain of the DOF controlled by each error signal. Red values highlight off-diagonal elements that have higher optical gain than the corresponding diagonal element. Red values in the PRCL column are in bold since they have a larger overall influence on the error signal than the DARM ones, as discussed in the MICH B.3 and SRCL B.5 subsections. Values are in units of [1/m]. *All the CARM column values except for the diagonal element are multiplied by 10^{-8}, as explained in section 4.4.3.

	PRCL	MICH	CARM·10^{-8}	DARM	SRCL
B2 8 MHz I	**2.7e+08**	6.4e+05	7.3e+02	1.3e+08	2.0e+04
B4 56 MHz Q	**9.9e+06**	**2.2e+06**	2.7e+01	4.7e+06	2.2e+03
B2 56 MHz I	6.7e+06	3.7e+06	**3.6e+10***	6.6e+07	2.4e+06
B1p 56 MHz I	3.8e+04	1.4e+08	1.9e+00	**4.2e+10**	5.4e+04
B4 56 MHz I	**6.3e+06**	8.0e+04	-1.5e+2	2.7e+07	**1.1e+06**

Table 4.6: Another alternative sensing matrix, this one with a focus on not using 6 MHz signals. Note that the error signals are listed in the same order with respect to the DOF that they are designed to control so that the diagonal elements (bold) correspond to the relative-power optical gain of the DOF controlled by each error signal. Red values highlight off-diagonal elements that have higher optical gain than the corresponding diagonal element. Red values in the PRCL column are in bold since they have a larger overall influence on the error signal than the DARM ones, as discussed in the MICH B.3 and SRCL B.5 subsections. Values are in units of [1/m]. *All the CARM column values except for the diagonal elements are multiplied by 10^{-8}, as explained in section 4.4.3.

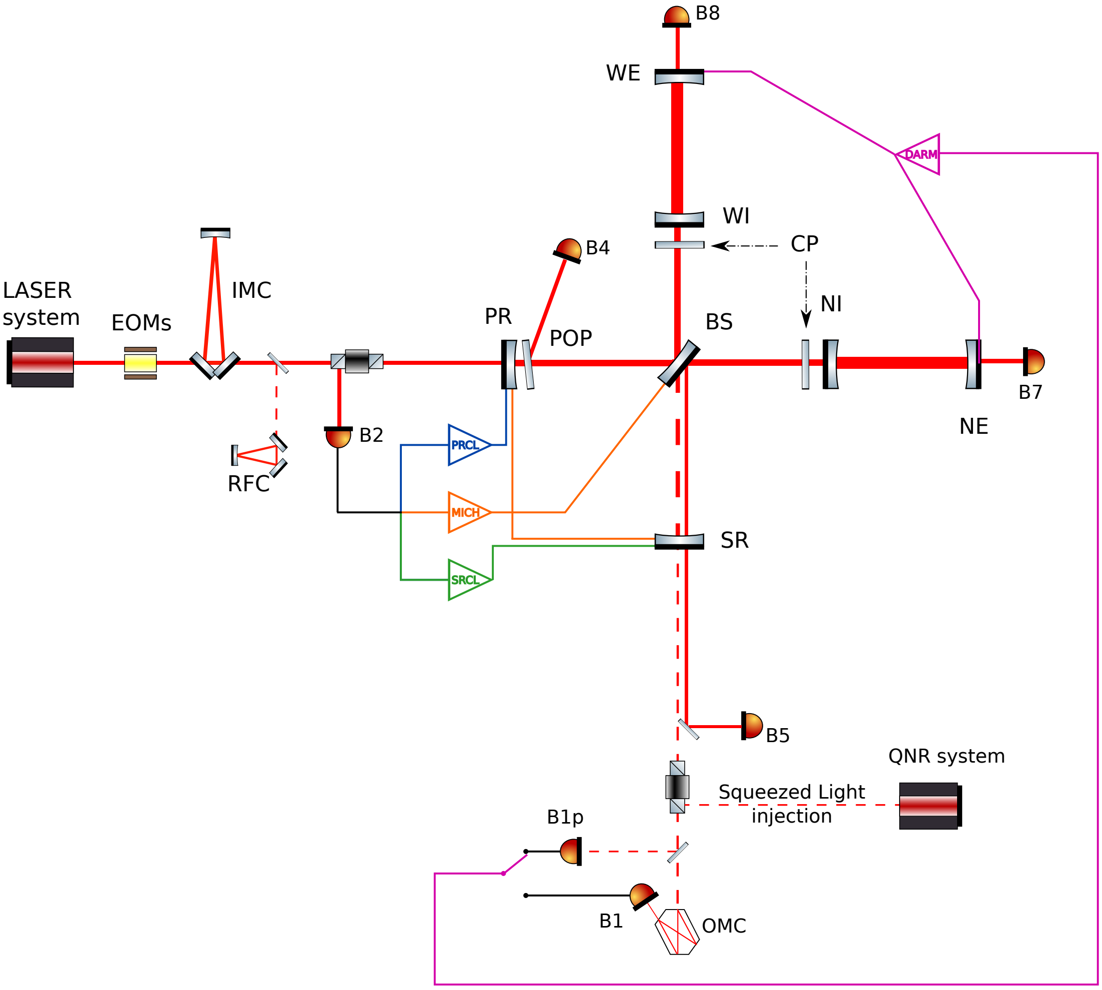

Figure 4.8: AdV+ optical layout with LSC error signals and actuation. The corresponding scheme for the CARM/SSFS loop can be found in figure B.3 in section B.2.

4.5 Conclusions and commissioning results

In this chapter, we presented the main aspects of the steady-state longitudinal controls for the new Advanced Virgo Plus configuration. Not all the studies performed to obtain an in-depth characterization of the AdV+ control strategy have been reported in this chapter since the focus was on the author's contributions to the design of the steady-state control strategy. Other studies relevant to the steady-state controls are listed below:

- Influence on the error signal of Relative Amplitude Modulation Noise Residual Amplitude Modulation (RAM) caused by non-ideal phase modulation of the laser [87] [88].
- Behaviour of the control sidebands and of the error signals in different phases of the interferometer locking sequence. [84]
- Effects of the SR working point on the DARM optomechanical transfer function [74].
- Complete study of the optomechanical plants and of the couplings between each DOF in the frequency domain and of the corresponding noise projections (work still in progress [77] [89]).

The studies did not find obstacles precluding the usage of the new steady-state control strategy, which was indeed implemented during the 2020 and 2021 commissioning of Advanced Virgo Plus.

4.5.1 Commissioning results

At the time of writing this thesis, the AdV+ interferometer commissioning and noise hunting are not yet finished, and a quantitaive evaluation of the performance of the LSC control loops would be extremely premature. However, a few discrepancies between the design [23] and the real interferometer have already been encountered during their implementation. The most interesting and pertinent ones are treated in this section.

Error signals choice: Looking at the relative optical gain and at the predicted shot-noise SNR, the best error signals for CARM, MICH, PRCL and SRCL are all taken from the B2 beam. Since signals from B2 are also used during the lock acquisition (see chapter 3), three different photodiodes with different dynamic ranges and bandwidths have been placed on acquiring this beam. This was needed due to the need for high demodulation frequencies for the 3f signals (in particular for the 169 MHz signals) and due to the reflected power changes happening during the lock acquisition procedure.

The resulting signals work indeed well for the lock acquisition. However, once the CARM offset zero point is reached, and the interferometer is fully locked and ready to switch to the steady-state error signals, the B2 signals show unexpected issues. The B2 error signals based on the 6 and 56 MHz sidebands show low coherence during noise injections ([90], [91]), as shown in figure 4.9 for the MICH error signal. Furthermore, their ASD shows that they are affected by additional noise [92]. This hampers the performance of the related control loops when using these signals to the point of making them unusable.

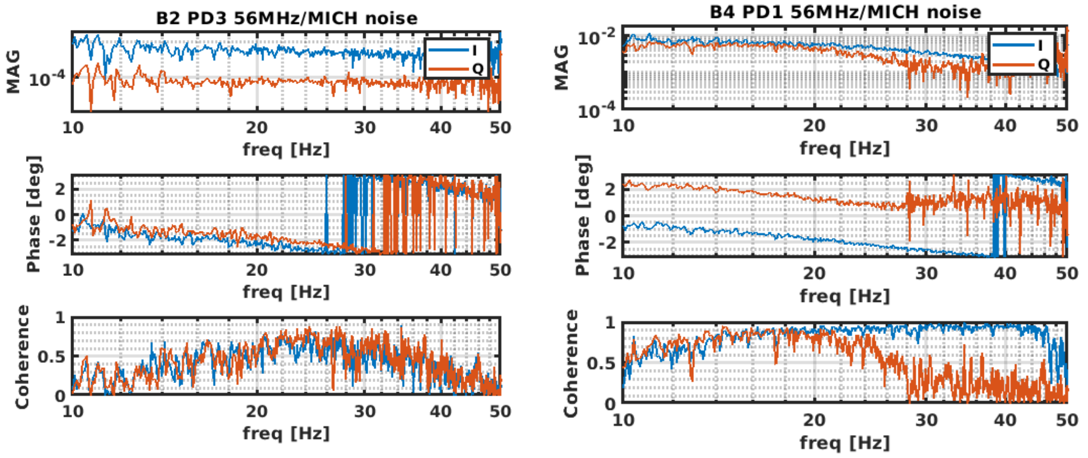

(a) (b)

Figure 4.9: Transfer function and magnitude square coherence estimates between MICH displacement and different error signals. The estimate has been obtained from broadband noise injection measurements. Blue and orange lines correspond to different demodulation quadratures. In all the plots the demodulation phase has been tuned to maximize the coherence with the "I" quadrature. **Left** plots show the TF and coherence of the B2 photodiode signal, while **right** plots refer to the B4 photodiode signal. The coherence of the B4 photodiode "I" signal is close to one in all the displacement-noise injection banddiwth (15-45 Hz), while the coherence of the B2 signals is lower, indicating that they are affected by additional noise uncorrelated with the MICH displacement. (Plots taken from [91]).

The origins of this noise are not completely understood, but some investigations observed correlations of this noise with PR mirror angular motion and with a sharp change of HOM content in the B2 beam happening when the resonance of the arm cavities is achieved. For this reason, the steady-state control for MICH, SRCL, and SSFS was handed off to the alternative error signals on B4, shown in the alternative sensing matrix 4.5 (DARM remained on B1p 56 MHz, however). These error signals have been proven to reliably allow reaching the dark fringe state of the interferometer.

Input and photodiode power changes Most of the simulations have been performed with the assumption of having 40 W of input power, as planned in [23]. However, during the commissioning, several issues in obtaining stable locks with this amount of power appeared, and therefore it was reduced to 33 W for the time. This can impact the radiation pressure effects affecting the optomechanical transfer functions at low frequency (< 10 Hz).

Additionally, to avoid RF saturation issues, the powers on some of the photodiodes used in the LSC steady-state have also been reduced with respect to the expected values used in the simulations. In particular, the power on B4 is a factor $\simeq 2$ lower, on B1p is a factor $\simeq 10$ lower, and on B2 is a factor $\simeq 30$ lower.

While this does not affect the relative-power optical gain estimates, the SNR estimates of the affected error signals need to be divided by the square root of these factors.

Couplings and other non-idealities. As mentioned above, a completely stable steady state has not yet been achieved during the commissioning. Most of the issues related to this are currently under investigation, and treating each is outside this thesis's scope. A common factor connecting many of these issues is the unexpected presence of higher-order modes that originate from a non-ideal working point of the interferometer. In particular, investigations on the non-idealities affecting the interferometer and on how to simulate them (e.g., [75] [93] [94]) showed as main culprit the mode-mismatch between the SR and PR cavities.

This process, performed in parallel with the commissioning operations, is fundamental for better understanding the interferometer's current behavior and for reaching a stable and optimally sensitive working point.

Chapter 5

An alternative lock acquisition procedure: *"Twin Variable Finesse"*

In chapter 3, we presented the ALS-based lock acquisition procedure. We successfully implemented this procedure to lock the AdV+ detector, and a similar approach has been used to lock the Advanced LIGO detectors since their first observing run O1 [45]. However, this procedure is not exempt from problems, most of which can be divided into three main categories:

- Cost and complexity of all the ALS apparatus (which required several months of work of a dedicated team to be designed, installed, and commissioned).
- Proneness to issues (discussed in 3.4.1) of the CARM offset reduction phase, revealed to be the most complex to commission and time-consuming phase of the lock acquisition.
- Impossibility of independent commissioning of the PR cavity in a single-recycled configuration, due to the necessity of coincident lock of the DRMI.

To overcome these issues, we studied the possibility of exploiting the peculiarities of the AdV+ detector to design a new lock-acquisition procedure based on an extension of the old “Variable Finesse” technique [42]. This technique was previously used to lock the Virgo and Advanced Virgo [15] detectors in the PRFPMI configuration. Due to the similarity, the new technique will be called Twin Variable Finesse (TWF). As described in more detail in section 5.1, this technique revolves around the idea of keeping the arm FP cavities locked on the resonance of the main IR laser since the beginning of the lock acquisition, completely avoiding the necessity of an ALS. The lock of the CITF DOFs is not engaged simultaneously as in the current procedure, but one DOF at a time, starting from MICH. The PRCL and SRCL DOFs are subsequently locked one at a time by keeping their respective mirrors misaligned until their engagement.

In principle, this technique can also be adapted for future upgrades of the Advanced Virgo detector and 2.5 and third-generation DRFPMI interferometers, such as Kagra and Einstein Telescope. In-depth simulation studies using the layout of these interferometers need to be completed to verify the applicability of the TWF on these setups. Furthermore, the mirror suspension system needs to allow a sufficient misalignment (tens of μrad) of the PR and SR mirrors.

Section 5.1 explains the main steps of the TWF lock acquisition procedure.

Section 5.2 will focus on the studies of the impact of misaligning and realigning the SR mirror during the lock acquisition on the longitudinal error signals.

5.1 The *Twin Variable Finesse* lock acquisition

As already mentioned, the TWF is an extension of the "Variable Finesse" technique. The name of this technique originates from tuning the power-recycling cavity's finesse during the lock-acquisition by changing the MICH offset. Indeed, this technique allowed to lock of the PR cavity with the interferometer in half-fringe condition. In this condition, half of the power circulating in the PR cavity is lost through the antisymmetric port. Due to this loss and to the effective lower finesse of the cavity, the impact of aligning and locking the PR cavity is reduced, allowing to preserve the arm cavities' lock during the process.

The TWF main addition to this procedure is the independent lock of the SR cavity. This lock will not need a particular tuning of the MICH offset and will be performed in dark fringe condition after the PR cavity lock and the MICH offset reduction.

In this section, we will outline the main steps of the TWF lock acquisition, including an overview of the steps which are shared with the old "variable finesse" technique.

5.1.1 Independent arm lock

In complete analogy with the ALS-based lock acquisition described in chapter 3, the first step of the procedure is the independent lock of the arm FP cavities. The lock is engaged using the arm transmission IR RF-demodulated signals (B7 and B8 6 MHz). Since the initial conditions of the lock are also the same (engagement of the frequency pre-stabilization system, misalignment of the PR and SR mirrors, etc.), we will not repeat the details of this step. Figure 5.1 shows the interferometer's status after the arm cavities lock.

5.1.2 Small Michelson lock

The next step is the lock of the MICH DOF in half-fringe condition. No reliable RF-demodulated signal is available for the lock at this working point. Therefore, a DC error signal is built from the B1p and the B4 DC signals. With suitable calibration α, these signals respectively measure the power transmitted through the antisymmetric port and the power reflected towards the symmetric port. The resulting error signal is:

$$Err_{MICH} = \frac{B1p - \alpha B4}{B1p + \alpha B4} \tag{5.1}$$

5.1.3 Arm control basis change

After the lock of MICH, the arm control changes following a series of smaller sub-steps. First, the control loop changes basis passing from single-arm control to CARM and DARM basis, using combinations of the B7 and B8 RF-demodulated signals as error signals.

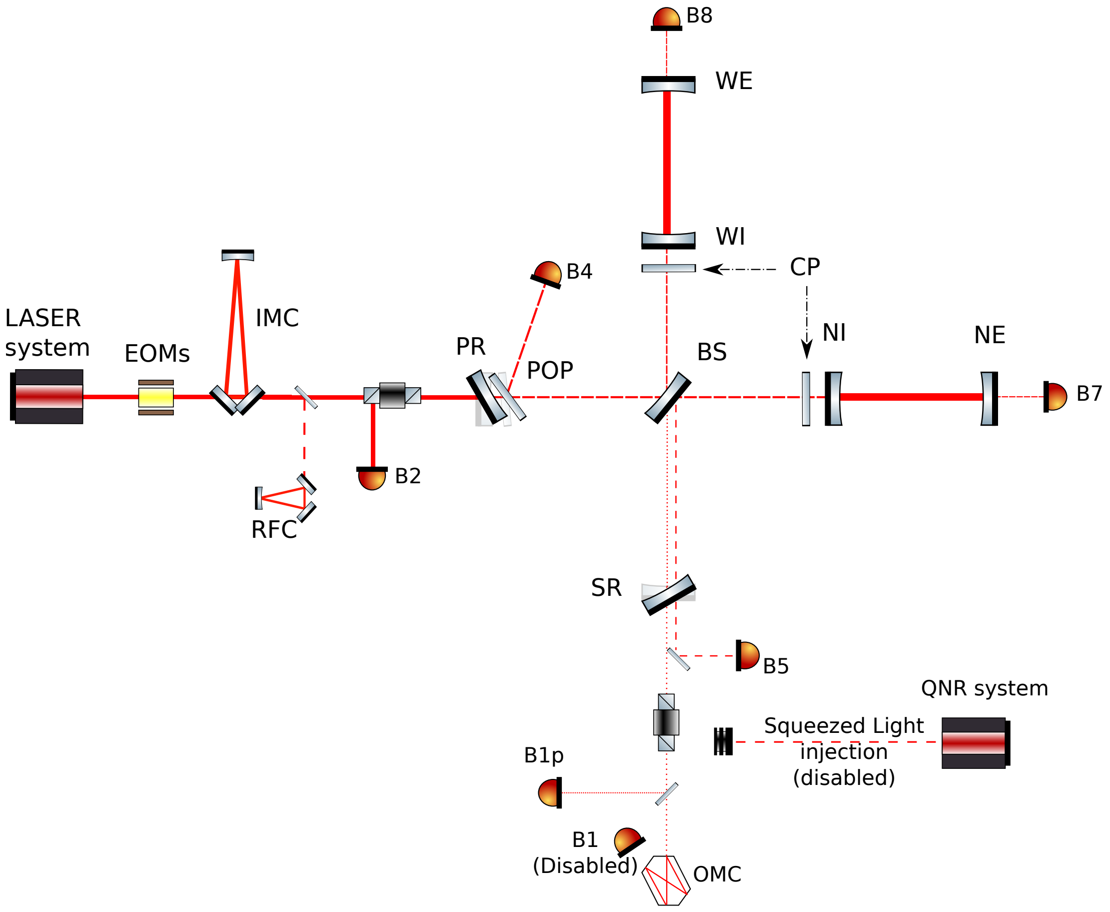

Figure 5.1: The first step of the TWF lock acquisition: Lock of the arm FP cavities on the IR laser. The SR and PR mirrors are misaligned, and all the CITF DOFs are uncontrolled.

Then, the CARM error signal is switched to a B4- or B2-based RF error signal[1]. At the same time, (similarly to what is done during the CARM offset reduction described in 3.4.1), the actuation of CARM is handed-off to the IMC length instead, allowing for a larger bandwidth actuation.

Lastly, the SSFS loop is engaged to allow an even greater suppression of the laser frequency noise. The status of the interferometer at the end of this step is represented in figure 5.2a.

5.1.4 Lock of the PR cavity

The PR mirror is realigned at this point, and the PRCL control loop is engaged, locking the PR cavity using the B2 8 MHz error signal. During this step, the power circulating in the interferometer increases by a factor $\simeq 10$. The interferometer can maintain the lock thanks to the use of power-normalized error signals for all the locked DOFs. Figure 5.2b shows the interferometer's status after the PR cavity's lock.

---

[1] since the 6 MHz sidebands were not available in O3, B4 56MHz was used in the past, but in AdV+ B4 6 MHz should be the best choice instead.

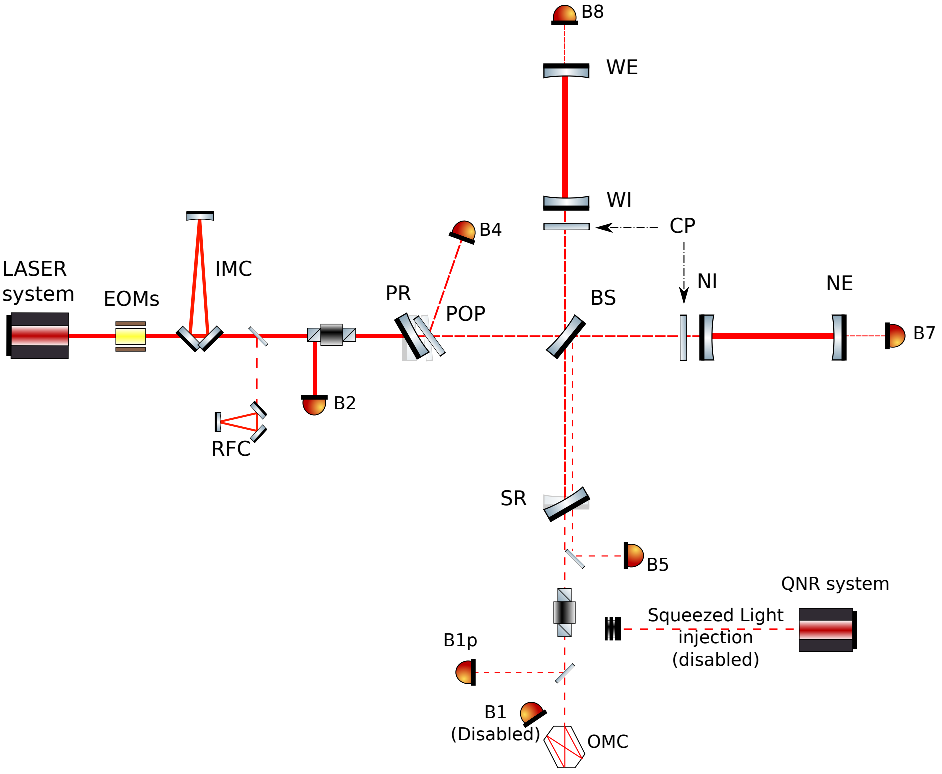

(a)

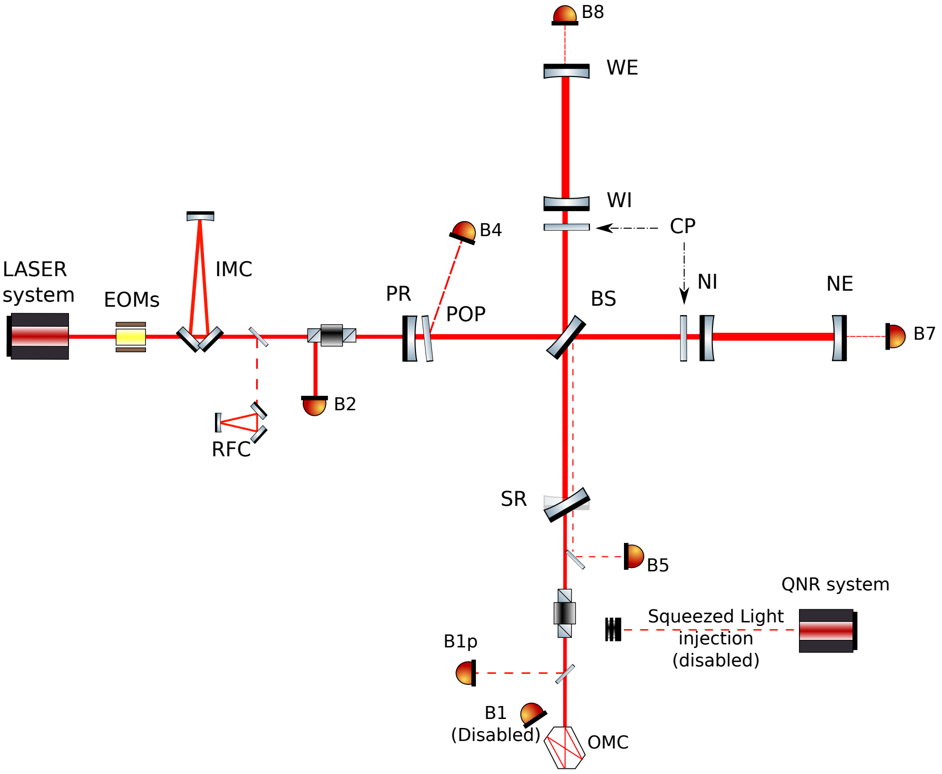

(b)

Figure 5.2: Further steps of the TWF lock acquisition. 5.2a: MICH in half-fringe and SSFS engaged. The SR and PR mirrors are still misaligned, and MICH is locked in half-fringe on a DC signal. Additionally, the DARM and SSFS DOFs replace the independent control of the arm cavities.
5.2b: The PR mirror is realigned, and the PRCL dof is locked. MICH is still in half-fringe. The SR mirror is still misaligned.

5.1.5 MICH offset reduction and dark fringe

In this step, the MICH offset is progressively reduced until the dark fringe is reached. This operation increases the effective finesse of the PR cavity by reducing the losses through the antisymmetric port. Therefore, the power circulating in the PR and arm cavities further increases, roughly by a factor of 100.

Once dark-fringe is reached, the control of MICH and DARM is handed off to the B4 56 MHz and B1p 56 MHz error signals, respectively. The resulting state is represented in figure 5.3.

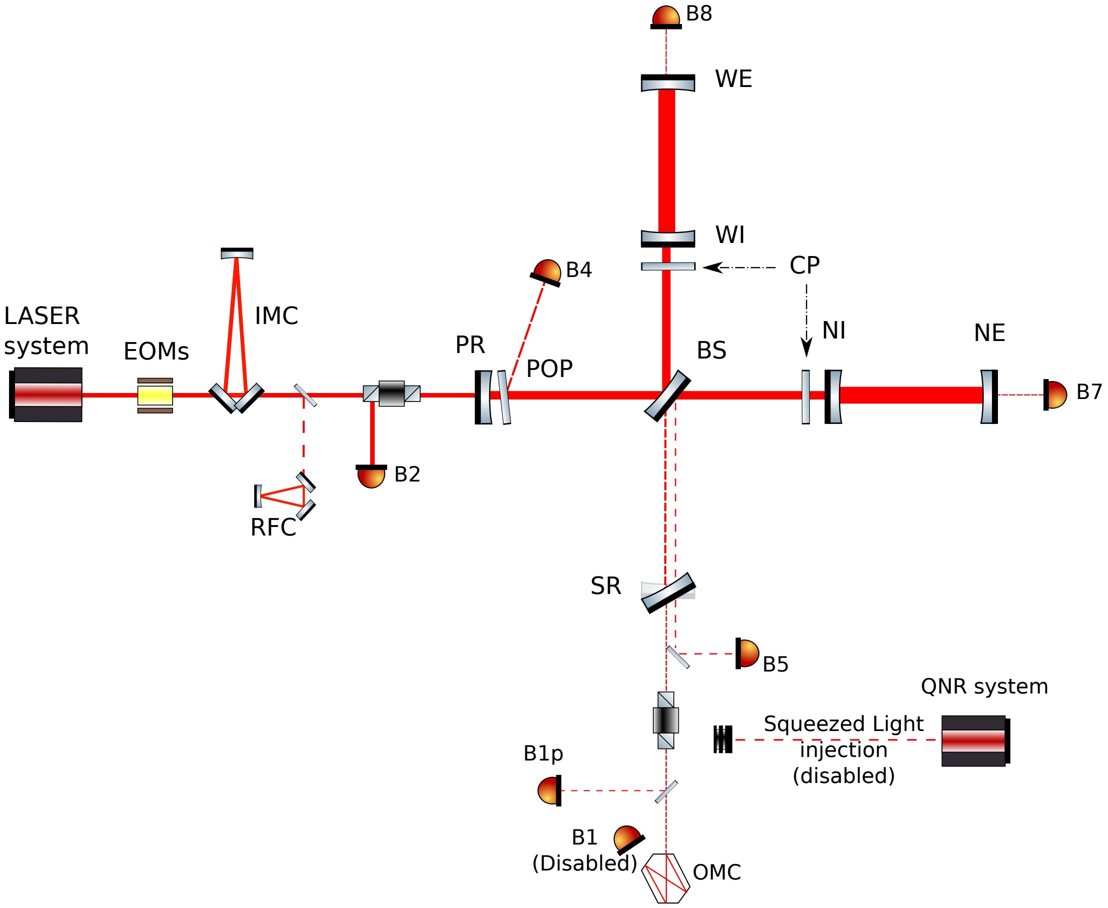

Figure 5.3: MICH is brought from half-fringe to dark-fringe while the SR mirror is still misaligned.

5.1.6 Lock of SRCL

Finally, the SR mirror can be realigned, allowing for locking its corresponding cavity. This step is the main novelty with respect to the old variable finesse technique. Since the interferometer is in dark fringe condition and the SR cavity is locked in anti-resonant condition, the impact of this step on the carrier beam and phase is negligible compared to the impact of locking the PR cavity. The highest impact of locking the SR cavity is on the 56 MHz sidebands and its derived error signals. The overall impact of aligning and locking the SR cavity on the LSC error signals is the main subject of the study reported in section 5.2.

The status of the interferometer after this step is shown in figure 5.4.

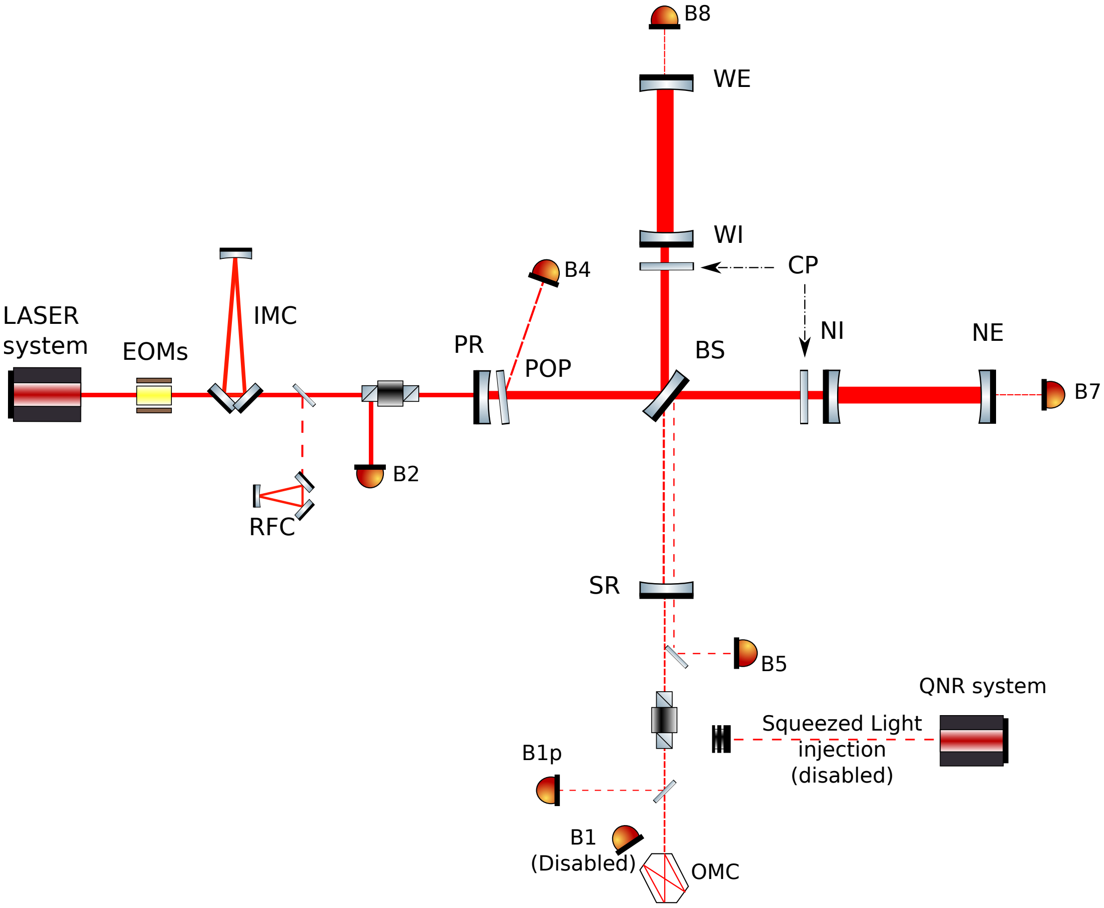

Figure 5.4: Lock of SRCL. The SR mirror is realigned, and SRCL is locked. The interferometer is still on the dark fringe.

5.1.7 DC readout and low-noise operation

After the lock of SRCL, the interferometer is almost in the same condition as it would be after the completion of the CARM offset reduction in the ALS-based lock-acquisition. The main differences are that the CITF is already locked on the “1f” signals since no “3f” error signals are used in the TWF procedure and that the SSFS loop is also already engaged. The remaining steps, which are adding a DARM offset to engage the DC readout, engaging the injection of squeezed light and engaging low-noise controls and actuation, are shared with what is described in 3.4.2. The final state of the TWF lock acquisition is shown in figure 5.5.

5.2 Validation of the “twin variable finesse” lock acquisition

Until the dark-fringe state (fig 5.3), the TWF procedure is identical to the variable finesse technique used to lock the old PRFPMI configuration, with as only difference the presence of the misaligned SR mirror at the antisymmetric port. As long as the

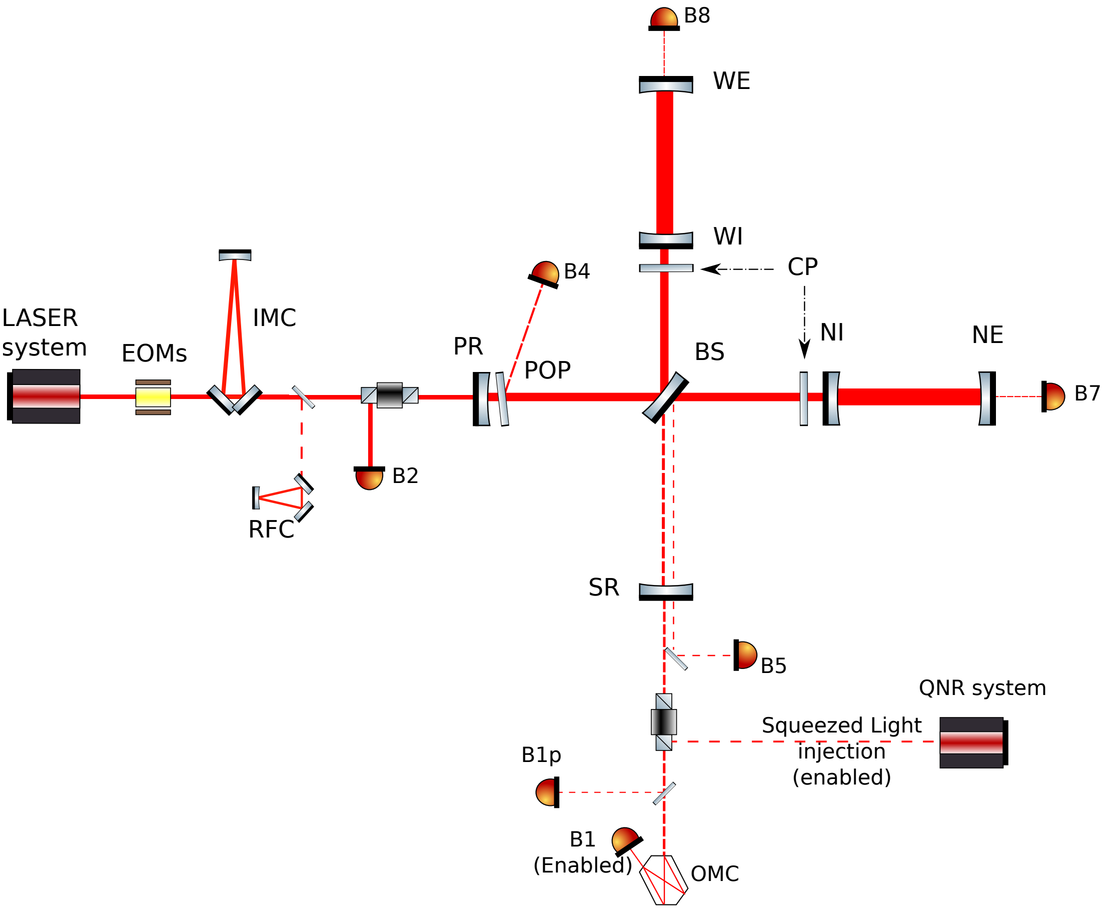

Figure 5.5: The final state of the TWF lock acquisition: DC readout and squeezed light injection. A DC offset is added to DARM, and then the OMC is locked in order to enable the DC readout. Low noise controls are enabled, and the squeezed light is injected into the interferometer.

reflected light is beam-dumped and does not couple with the other beams, its only effect at this stage is a loss of power (40% for AdV+) on the B1p beam used to control DARM. The latest steps of the lock acquisition (after the lock of the SR mirror) also share the same procedure with another technique, this time being the ALS-based lock acquisition currently used on AdV+.

The studies on the validation of the TWF lock acquisition, therefore, focused on two main points:

- Finding a “parking position” for the misaligned SR mirror, which allows to correctly dump the reflected light. These studies have been performed using the ray-tracing software “Optocad” and have also been used for the initial step of the ALS-based lock acquisition procedure, in which both recycling mirrors are also misaligned (see chapter 3).

- Studying the effects of progressively realigning the SR mirror on the other DOFs’ error signals to assess the lock’s robustness to this procedure. These studies have been performed with the modal frequency-domain simulation software Finesse 2 [95] and are the main focus of this chapter.

5.2.1 Study overview

In the dark fringe condition and before the lock of the SR cavity, all the LSC DOFs except for SRCL (which is still unlocked) are locked using the error signals studied in chapter 4.4 and appendix B. For convenience, we listed them again in table 5.1

DOF	Error Signal
CARM/SSFS	B2/B4 6 MHz I
DARM	B1p 56 MHz I
PRCL	B2 8 MHz I
MICH	B2/B4 56 MHz Q
SRCL*	B2/B4 56 MHz I

Table 5.1: Summary of the LSC error signals in dark-fringe. *: SRCL is initially unlocked during the alignment of the SR mirror.

As mentioned above, the impact of the SR mirror realignment during the lock of the SR cavity is a major concern regarding the applicability of the TWF lock-acquisition procedure. Finesse simulations were carried out with the aim of investigating this crucial step. A similar approach to the one used in the study of the impact of misalignments in the CITF lock (see appendix A) has been used, focusing on the following figures of merit:

- Variations of optical gain;
- couplings between different DOFs, with particular focus on the impact of SRCL displacements since it is unlocked during the initial part of the procedure;
- variations in the optimal demodulation phases;

These simulations assume that no significant dynamical effect will occur during the SR mirror's alignment and lock. This assumption allows subdividing this process into a series of stationary steps, which can be simulated with frequency-domain simulation methods. This assumption is justified by the low finesse of the SR cavity for both the carrier and the sidebands but might need further verification with time-domain simulations.

The main differences with respect to the studies reported in appendix A are:

- The simulation of larger misalignments, which are required to evaluate the full impact of misaligning the SR cavity until it is completely de-coupled.
- The different status of the interferometer, with no CARM offset and all the LSC DOFs locked, including CARM and DARM. For the same reason, the simulations included the study of the CARM and DARM error signals.

5.2.2 Extent of the simulated misalignment

The TWF technique starts with a largely misaligned SR mirror ($\geq 50\ \mu$rad). The misalignment is needed to have the signal recycling cavity completely de-coupled and to minimize the impact of SRCL displacements until this DOF is locked too.

However, simulating such a large misalignment is impossible with Finesse due to the limitations of using the paraxial approximation. First, the cavity's misalignment should not be above the beam's diffraction angle Θ. The diffraction angle is defined as

$$\Theta := \arctan\left(\frac{\lambda}{\pi w_0}\right) \tag{5.2}$$

Where w_0 is the waist size of the beam. In the AdV+ interferometer, the waist size of the beam is $\simeq 10$ mm, therefore giving an upper limit to the misalignment of $\Theta \simeq 35\ \mu$rad, well above the simulated angles.

In addition to this limit, simulating optical setups containing misaligned (or mismatched) cavities often requires using a large number of HOMs to reproduce the physical behaviour of the system correctly. The number of used HOMs is determined by Finesse's 'maxtem' value, which indicates the maximum order of the simulated Hermite-Gauss modes. The larger the misalignment, the higher the impact of HOMs on the simulations' results. We evaluated this impact by studying the “convergence” of the simulations. The convergence has been checked by comparing specific figures of merit resulting from simulations with an increasingly higher number of HOMs.

The most basic figure of merit used to make this comparison is given by the LSC DOF working points found by Finesse's lock algorithm. This algorithm emulates the effect of the interferometer control loops by displacing the LSC DOFs in order to minimize their corresponding error signals. To simplify the process, most simulations start from a fully aligned condition (which is simpler to simulate) and then progressively increase the misalignment. The order of this procedure is vice-versa with respect to what happens during the TWF lock-acquisition, in which the SR mirror is initially misaligned and then realigned and locked. Tests to simulate the lock in the opposite (correct) order showed no difference in the resulting working points.

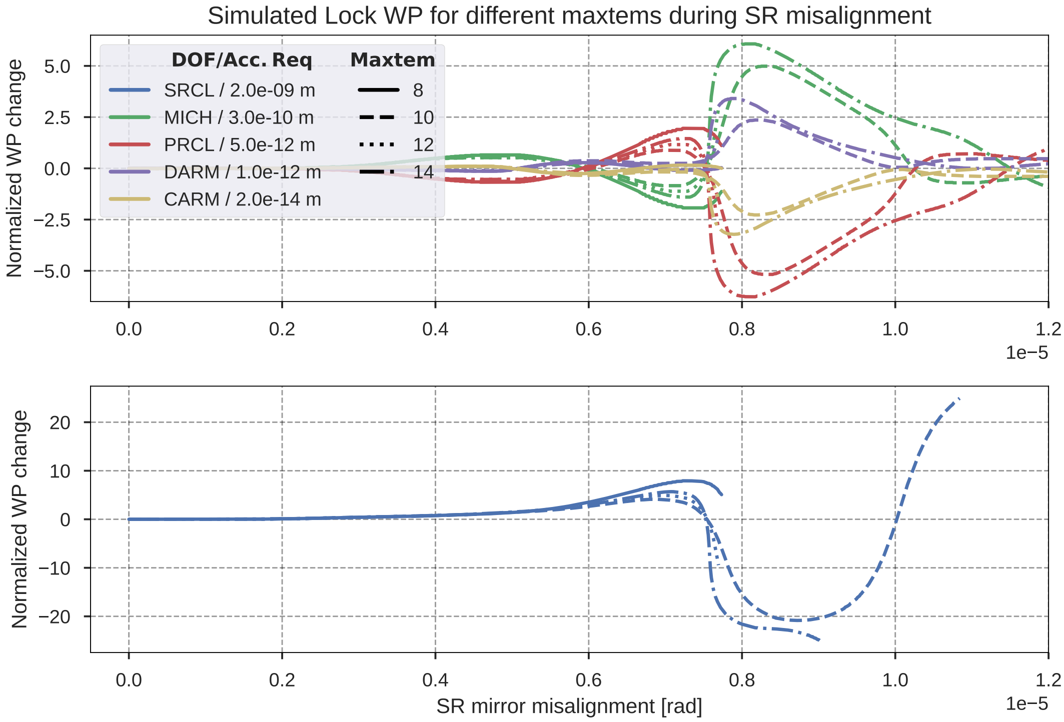

(a) LSC DOFs' simulated WPs during the misalignment of the SR mirror for different 'maxtem' values. The DOFs are 'locked' using the error signals in table 5.1. The 'maxtem' parameter indicates the highest Hermite-Gauss mode order used in the simulation. The SRCL dof is in a separate plot due to having much larger deviations than the other DOFs. The lines that end before $1.5 \cdot 10^{-5}$rad are interrupted at the point where the simulation lock algorithm failed.

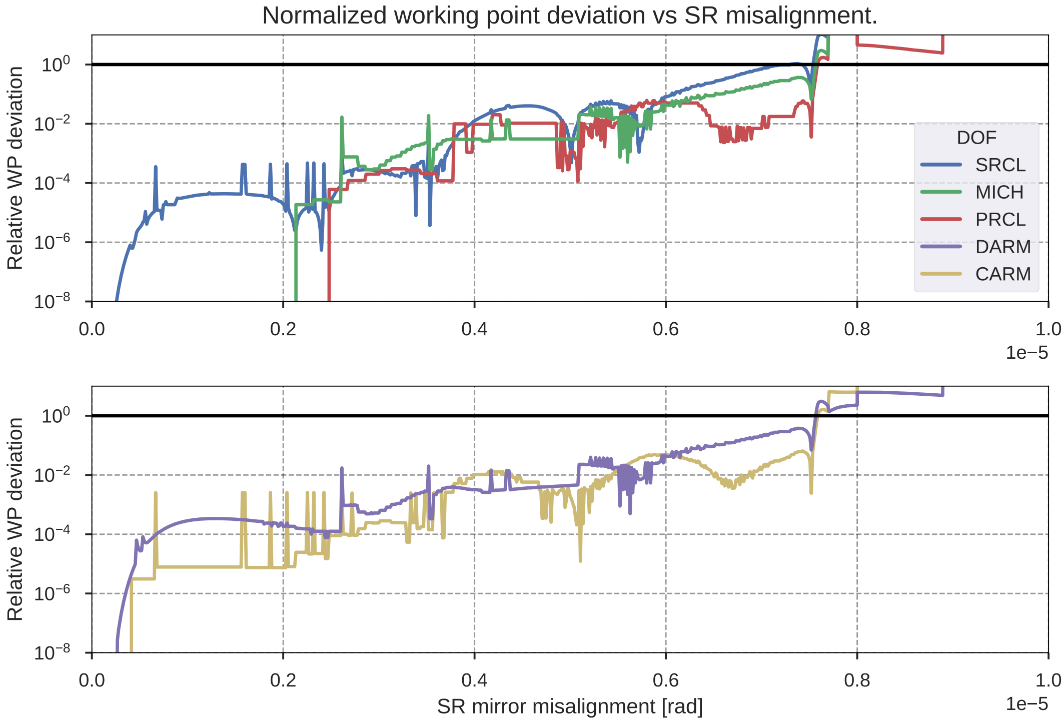

(b) Normalized WP differences for SR misalignments. The lines indicate the difference in the WPs simulated with 'maxtem' 14 and 'maxtem' 12, normalized by the respective DOF accuracy requirements. Discontinuities in the line before 7.5 μrad are caused by the finite tolerance of the lock algorithm.

Figure 5.6

Figure 5.6a shows the resulting WPs computed for various maxtem values. To simplify the plotting the WP values of each DOF have been normalized by its corresponding accuracy requirement (defined in chapter 4.2).While these accuracy values were defined for the interferometer in the steady-state condition and can be more relaxed during the lock acquisition, they are still a good reference value to compare displacements of different DOFs. Most of the simulations were not able to maintain the lock up to the maximum simulated angle (12 μrad), and are indeed interrupted earlier. Due to computational resources limitations, our simulations could not exceed 14 as the highest simulated HOMs order. In the highest maxtem simulation (14), despite the SRCL DOF losing lock at $\simeq$ 9 μrad, the lock algorithm for the other DOFs keeps working properly. A first look shows that the separation between different 'maxtem' simulations quickly increases for SR misalignments above $\simeq$ 5 μrad. This means that the influence of higher order Hermite-Gauss modes on the error signals becomes higher.

Another figure of merit to evaluate the convergence is the relative WP variation between a simulation including up to a certain 'maxtem' value and the subsequent one, e.g., the difference between the WP estimated with 'maxtem' 12 and with 'maxtem' 14. This variation is also compared with the accuracy requirements values discussed in chapter 4.2.

From the results, shown in figure 5.6b, one could see that the difference between the maxtem 14 and maxtem 12 simulations is relatively low and below the accuracy requirements until the point where the maxtem 12 simulation loses lock, which is $\simeq$ 7.5 μrad. We can therefore conclude that, according to these figure of merit, the simulations with maxtem 12 and 14 are a good representation of the interferometer's behaviour up to a misalignment of $\simeq$ 7.5 μrad. As a conservative choice, all the subsequent simulations have been performed with 'maxtem' 14. It is possible that maxtem 14 simulations have validity above this angle but we have no data that allows to confirm this.

Most other convergence studies, based on looking at the optical gain and optimal demodulation phase variations between different 'maxtem' simulations, resulted in less restrictive misalignment thresholds. An exception to this is the behaviour of the "2f" demodulated error signals. As explained in the next subsection (5.2.3), their behaviour also suggest to remain below the $\simeq$ 7.5 μrad threshold.

In addition to the convergence studies, a simulation with an aligned but non-reflective SR mirror has also been carried out. In this simulation, the transmissivity of the mirror has been left to 0.4, changing the 0.6 reflection coefficient to a loss in order to recreate the effect of a completely misaligned mirror, whose reflected light is dumped. Since no misalignments are present in this simulation, it is not subject to convergence issues, and its results have been used for additional comparisons.

5.2.3 Sideband recycling

The SR mirror misalignment does not only impact the error signals' optical gains but also the recycling and the transmission of the sideband fields too. A large change in the sideband field powers has an impact on the detection photodiodes and needs to be considered in their design to avoid the triggering of saturations.

The behaviour of the sidebands can be seen in figure 5.7, where the relative amplitude of the sideband fields is represented by the '2f' demodulated signals. The '2f' signals have been probed both inside the power recycling cavity (B4) and in transmission at the antisymmetric port (B1p). The results show that the only signal that goes above the fully aligned value (1.0) is B1p 12 MHz, coherently with the fact that the SR cavity is anti-resonant with it, and its alignment increases its reflection towards the symmetric port. Its sudden change of behaviour at $\simeq 7.5\mu$rad, matched by a change of slope in the other "2f" signals, is not completely understood yet. Since the reliability of the simulated quantities above $\simeq 7.5\mu$rad is uncertain (see previous subsection) this does not impact the rest of the study, but in the case of larger range simulation, a study dedicated to clarify this behavior will be needed.

Another noteworthy impact of the misalignment is the recycling gain of the 56 MHz sidebands inside the PR cavity, which is greatly enhanced by the presence of an aligned SR cavity. Indeed, the dotted line shows that in the absence of signal recycling (dashed line), the sideband magnitude is a factor of $\simeq 4$ lower.

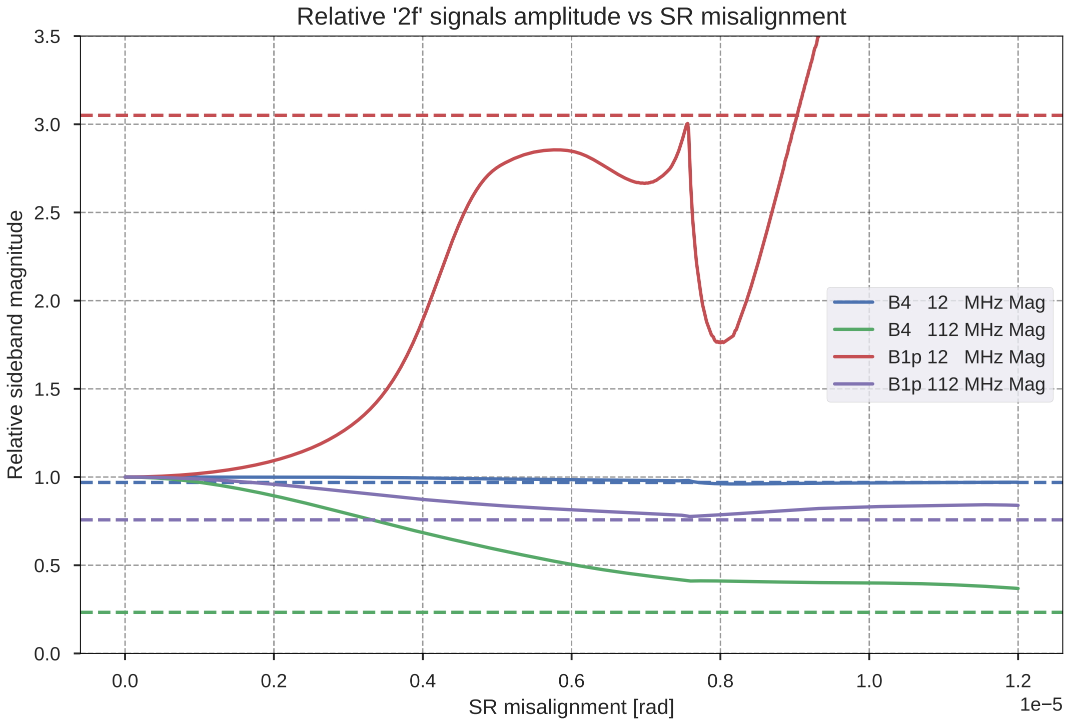

Figure 5.7: Normalized "2f" demodulated signal magnitude. The signals represent the evolution in the 6 and 56 MHz sideband amplitude inside the PR cavity (B4) and at the antisymmetric port (B1p). The plotted results are normalized by the respective values in the aligned condition. The dashed lines represent the simulation with a non-reflective SR mirror to emulate the completely misaligned behaviour.

5.2.4 Optical gains

One of the main effects of the misalignment is a progressive variation of optical gain on the longitudinal error signals. The extent of this effect depends on which error signal is taken into consideration. Figure 5.8 shows the overall impact of misaligning the SR mirror on the LSC error signals, keeping each demodulation phase fixed to the optimal values for no misalignment.

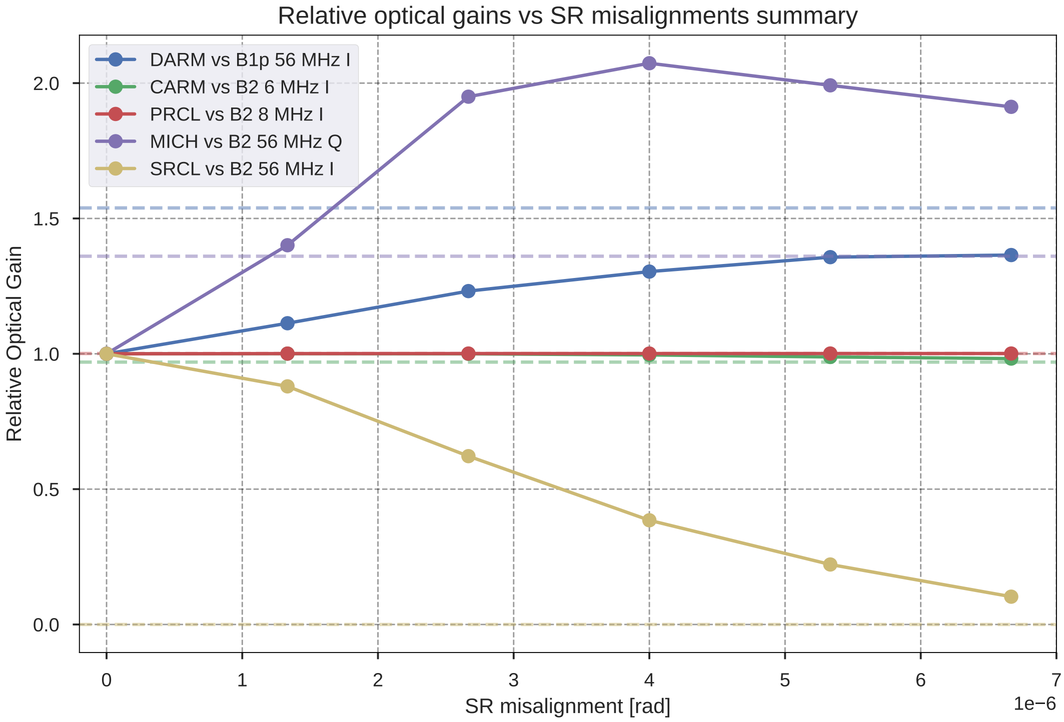

Figure 5.8: Normalized OGs of the LSC error signals for the simulated SR misalignments. The optical gains are normalized by the fully aligned value. The horizontal lines represent the values obtained with a non-reflective SR mirror, simulating a completely de-coupled condition.

As expected, the CARM and PRCL error signals, which are not based on the 56 MHz sidebands, are minimally affected by the SR misalignment.

The SRCL error signal’s (B2 56 MHz I) optical gain quickly decreases, going below 0.5 at $\simeq 3.5$ μrad of misalignment. This confirms that the SRCL loop can be engaged only once the mirror is sufficiently aligned. The DARM and MICH error signals increase in optical gain with the SR misalignment. The magnitude of the increase is low enough for this not to be considered an obstacle in the implementation of the technique, since it can be compensated by an appropriate loop-gain decrease needs during the realignment. A comparison with the ’no sr’ values (horizontal lines) shows a discrepancy with the latest simulated angle. This discrepancy suggests that, while a large part of the effects of the misalignment are encompassed within the simulated range, the range might need to be encreased to characterize them fully.

A preliminary measurement of the effects of misaligning the SR mirror on the Advanced Virgo Plus interferometer has been carried out recently. In particular, the optical gains of the LSC loops have been monitored by measuring the open-loop gains of an injected displacement-noise line for each DOF. These lines are used by the “UGF servos” to constantly monitor and adjust the loop gains. These monitors do not allow to measure the DC gains but instead the gains at specific frequencies above the loops’ UGFs. However, the results shown in figure 5.9 show an overall accordance with the simulated DC gains in figure 5.8. The main difference with respect to the simulations is that a larger misalignment was needed to obtain a comparable amount of gain-loss.

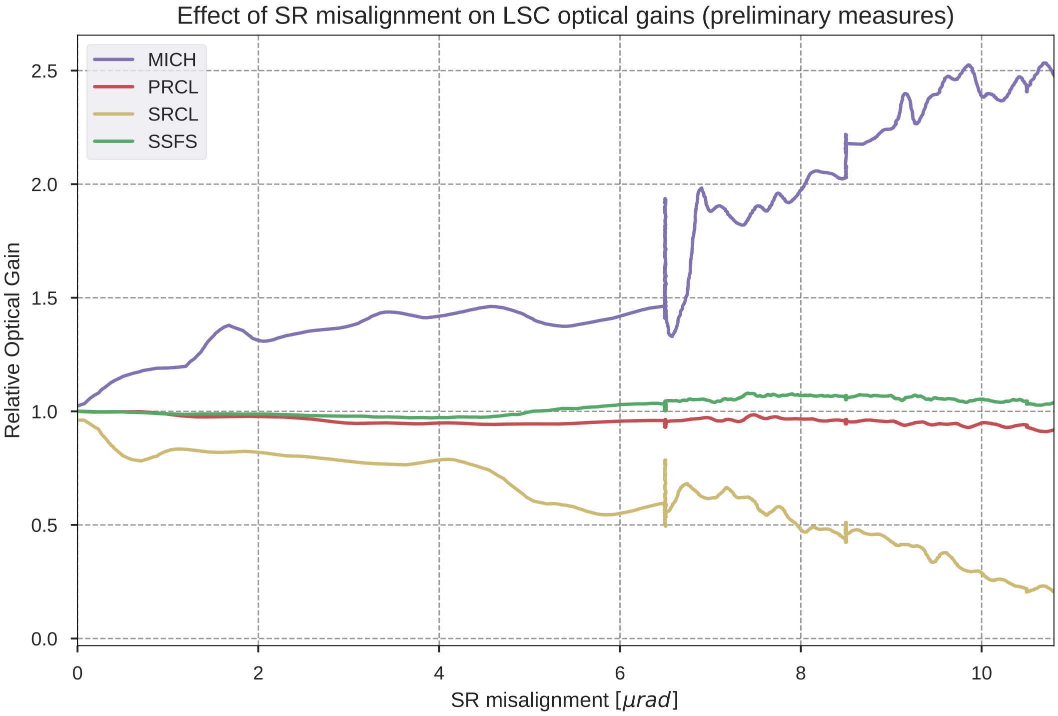

Figure 5.9: Preliminary measurement of the impact of the SR misalignment on the LSC error signals' gains. The measures have been obtained by monitoring the open-loop gain of displacement-noise lines injected at specific frequencies (above the loops' UGFs). The DARM dof is missing since its TF was strongly affected by other angular loops drifts at the time of the measurement.

This allowed the SRCL loop to remain engaged for misalignments up to $\simeq 11\ \mu$rad, which would be impossible if the gain would follow the simulated behaviour. This discrepancy is most likely due to the overall lower finesse of the recycling cavities caused by the mismatch losses in the real interferometer and should be investigated with further measurements. Nevertheless, the feasibility of introducing large misalignments without the interferometer losing lock gives a promising outlook on the feasibility of the TWF procedure.

5.2.5 Demodulation phases and cross-couplings

Each error signal is demodulated at the phase that maximizes the optical gain against the displacement of the respective DOF. Misalignments can affect the relative phase between the carrier and the sideband fields, changing the optimal demodulation phase for the error signal. Significant variations ($> 90°$) will change the sign of the error signal immediately, causing an unlock, but even relatively small changes can affect the cross-couplings between different DOFs to the point of disrupting the lock.

Figure 5.10 shows the variations in optimal demodulation phase for each LSC error signal. As expected, the only meaningfully impacted optimal demodulation phases are the ones relative to the 56 MHz error signals. In particular, the MICH error signal is subject to a $\simeq 10°$ change for large SR misalignments. This amount of change can be easily compensated and is minimal compared to the changes of demodulation phase

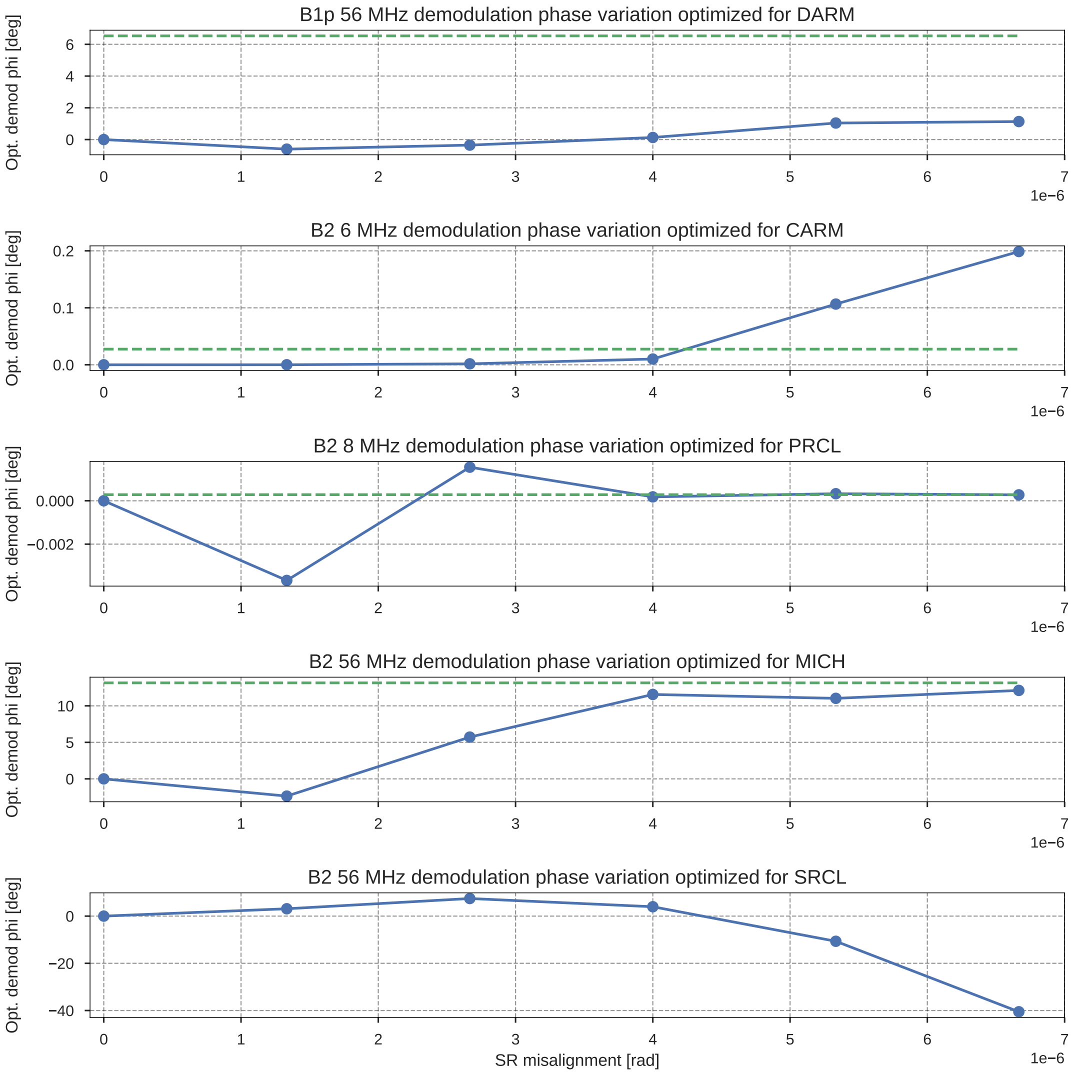

Figure 5.10: Variation of optimal demodulation phases for the LSC error signals. In blue, for each misalignment angle of the SR mirror, the demodulation phase that would maximize the optical gain has been compared with the optimal demodulation phase at no misalignment. The green dashed lines show the values computed with a non-reflective SR mirror, to emulate the fully misaligned condition. The discrepancy between the misaligned simulation and the non-reflective simulation for the DARM error signal (first plot) is not completely clear, but its low magnitude does not raise concerns regarding the stability of the lock.

observed during the CARM offset reduction in the ALS lock-acquisition procedure.

The SRCL error signal is subject to a dramatic optimal demodulation phase change. However, the largest part of the change happens at misalignments in which the longitudinal loop is not yet engaged.

Additionally, the cross-couplings between different DOF error signals have been checked for relevant variations. The results are shown in figure 5.11.

The impact of SRCL displacement on the other DOF’s error signals is already negligible and becomes less with the misalignment. Due to the reduction in SRCL

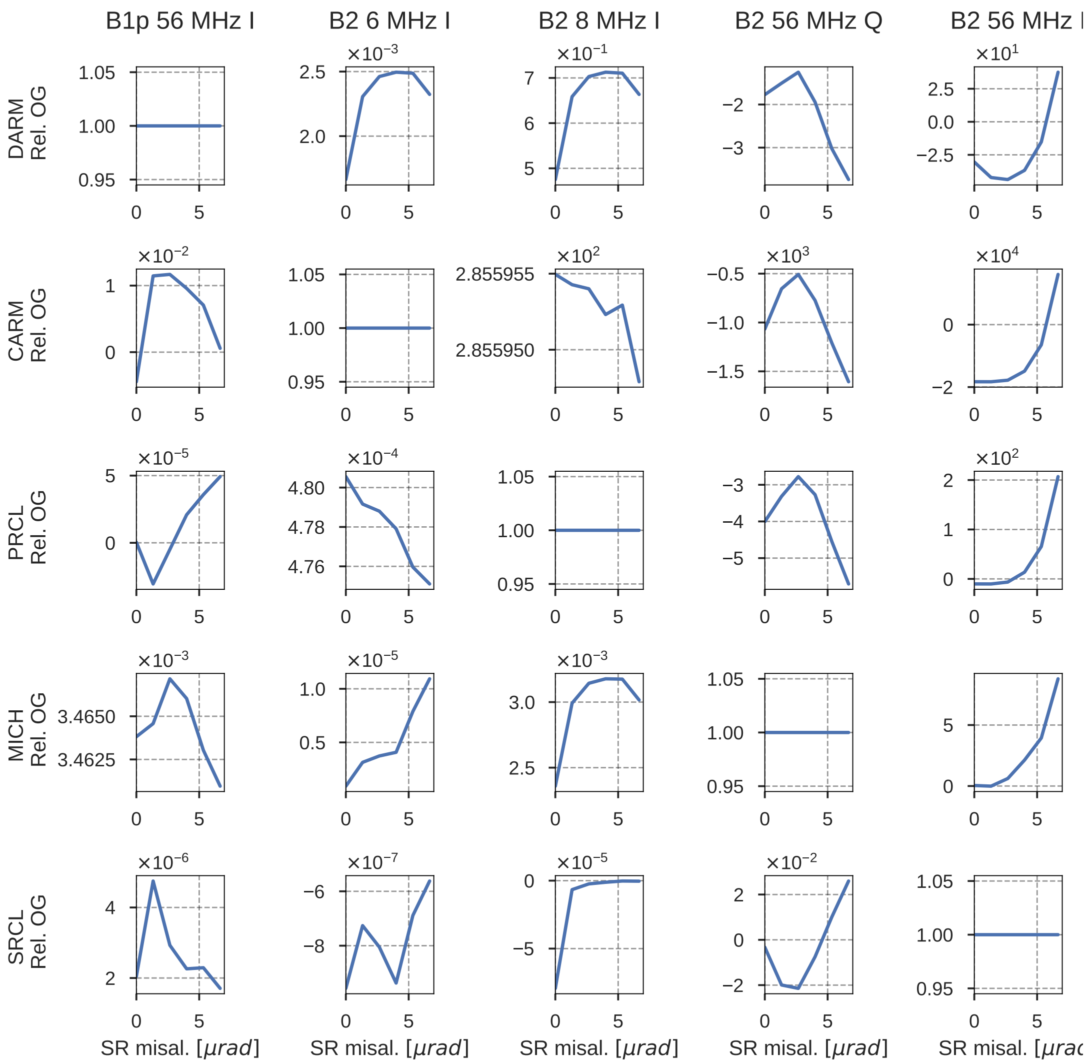

Figure 5.11: Evolution of cross-couplings between LSC DOFs for misalignments of the SR mirror. Each column corresponds to a different error signal, each row to a different DOF. Each plot shows the relative OG of the respective error signal against displacements of the respective DOF. The OGs are divided by the OG of the diagonal elements, corresponding to the OG of the signals used in the feedback loops.

optical gain, the relative impact of other DOFs on the SRCL error signal (B2 56 MHz I) increases. However, for angles in which the SRCL loop can be engaged ($< 3\ \mu$rad), the change is minimal. Other potentially impacting cross-couplings, such as the DARM to the MICH error signal (B2 56 MHz Q), do not show significant change within the simulated range.

5.2.6 Impact on the DARM transfer function

During the commissioning of AdV+, we observed that unintended misalignments of the SR mirror have a noticeable impact on the DARM transfer function, spoiling the detector sensitivity and stability of the lock. This effect was also recreated by specific simulations presented in [96]. Since this effect will also affect the interferometer during the realignment of the SRC mirror, we included in our simulations the impact of the misalignments on the optomechanical longitudinal transfer functions. A change of DARM filter during the misalignment/realignment might be necessary to compensate the plant function change and mantain the loop stability.

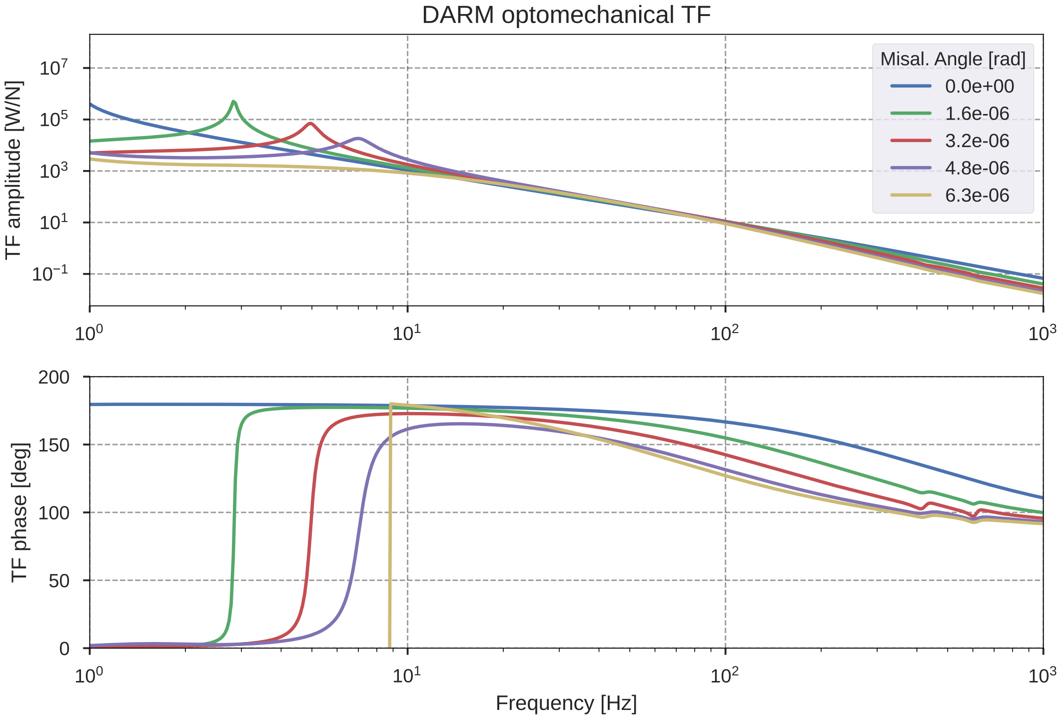

Figure 5.12: The optomechanical transfer function of DARM for different SR mirror misalignments.

Figure 5.12 shows, in particular, the DARM transfer function since it resulted in being the most affected DOF. The results show an optical-spring effect (originating from radiation pressure) with a pole with a frequency proportional to the misalignment. As long as the frequency is within the actuation range of the DARM loop, the effect can be compensated by choosing appropriate control filters. A more in-depth study is suggested, evaluating the stability of the closed feedback loops and the design of ad-hoc filters to mitigate the impact of misalignments.

5.3 Limits of the simulations

We used a variation of the simulation setup described in chapter 4.1. The limits and the observations discussed in 4.1 regarding the capability of that configuration to represent the real interferometer are still applicable to these simulations.

5.3.1 Ideal interferometer

Consistently to the studies reported in chapter 4, the simulated interferometer configuration is optimally mode-matched. This is not completely true in the real interferometer, especially during the lock-acquisition, in which, despite the best efforts in optimizing the mode-matching, the interferometer optics are subject to aberrations called “cold defects” [97] and other not fully compensated thermal aberrations.

Simulating an interferometer with all the defects however is very computationally demanding and will not necessarily provide insightful information. Indeed, in many cases optimally matched cavities are subject to a higher impact of misalignments with respect to mismatched cavities, and the preliminary measurements shown in figure 5.9 seem to confirm this behaviour. Moreover, obtaining a reliable representation of the exact combination of interferometer defects affecting the error signals is no simple task and it is still a work in progress. Furthermore, the any defect estimate will inevitably be subject to changes following the mode-match optimization operations during the commissioning.

5.3.2 Misalignment range

Due to the limitations in the simulated misalignment (see section 5.2.2), the behaviour of the interferometer for misalignments larger than 7.5 μrad remains unexplored.

However, the simulation results suggest that the highest impact of misaligning and displacing the SR mirror happens for misalignments within the simulated range. For large angles (> 5 μrad), at which the optical gain of SRCL is too low to maintain the lock, the overall impact of the SR mirror displacement on the other error signals is negligible. This is also in accordance with the experience accumulated when working with Advanced Virgo’s PRMI configuration and the realignment of the PR mirror.

Further optimization of the simulations and better hardware allows for simulating a higher number of Hermite-Gauss TEM modes and, therefore, simulating larger angles within the limitations given by the paraxial approximation. The necessity of this should be evaluated after the outcomes of experimental misalignment tests actuated on the AdV+ interferometer are available (see conclusions 5.4).

5.4 Conclusions

The simulation studies reported in this chapter showed an overall limited impact of SR misalignment and SRCL disengagement on the other LSC error signals. This prospects the feasibility of locking SRCL subsequently to the lock of the rest of the interferometer, or to disengage the SRCL lock and decouple the SRCL cavity for commissioning purposes (for example to tune the TCS systems and to mode-match the PR cavity without influence from the SR cavity on the figures of merit used for the tuning).

Before any attempt of implementation, the TWF lock-acquisition needs, however, further efforts to be thoroughly validated. From the simulation standpoint, the following studies can help in obtaining a broader picture of the effects of misaligning and realigning the SR mirror:

- An evaluation of the stability of the control loops at various misalignment angles using the simulated transfer function, possibly within a MIMO approach.

- A complete check of all the error signals shapes at various misalignments to avoid the presence of distortions (multiple zero-crossings, heavy nonlinearities) near the working point.

- A comparison with the impact of misaligning the PR mirror in half fringe, as used in the Variable Finesse technique.
- The simulation of larger misalignments within the limitations of the paraxial approximation.
- The simulation of SR misalignment in a closer representation of the real interferometer, including mirror surface maps and a non-ideal mode-matching of the recycling cavities.

While some of those points can be solved with relatively small amounts of effort, the last two points (larger misalignments and realistic interferometer) would require a large amount of computational power and trial-and-error attempts.

More insightful information could be instead obtained from further experimental tests on the AdV+ interferometer. In addition to simple misalignment tests, it should be possible to completely disengage the SRCL loop once a sufficient SR mirror misalignment is reached, and to check the stability of the other LSC DOFs feedback loops in this condition. To help with this, their gains and demodulation phases should be adjusted according to the simulation results. This adjustment will allow compensating for the changes caused by the misalignment and, therefore, minimize the chance of unlocking.

Chapter 6

Conclusions

The commissioning of the Advanced Virgo Plus upgrades is still ongoing, but the majority of the lock-acquisition procedure was successfully implemented and tested in 2021.

The commissioning activities started with the integration of the (completely new) ALS subsystem in the global ISC infrastructure, allowing for locking the arm FP cavities on both the IR and green lasers.

The main challenges encountered during this step were related to maintaining or recovering the alignment of the green beams in 3 km long arm cavities and the fiber collimators collecting the transmitted beams. Slow relative drifts between the arm cavities and the suspended optical benches from which the green beams are injected would initially degrade the quality of the ALS signals over a few hours or days, depending on the environmental conditions. These issues were progressively mitigated over the following months with interventions on the suspended benches and green beam collimators, drastically increasing the uptime and stability of the ALS lock. A few weeks of commissioning were also necessary to achieve a quick, reliable and automated handoff of the arm cavities length control from the IR signals to the ALS beating signals.

From this step on, the implementation proceeded roughly following the steps of the lock-acquisition procedure explained in chapter 3.1. The DRMI was initially locked with the end mirrors of the arm cavities misaligned to avoid the need for a CARM offset and consequently a fully functional ALS system. This step showed the importance and validity of the simulation activities carried out in the previous years during the planning phase. Their results, also published in [53], allowed us to determine the best trigger and error signals and to predict the criticality of an optimal PR alignment for the engagement and stability of the DRMI lock. Achieving a stable DRMI lock required less than one month of commissioning, during which the main difficulty was determining a reliable mirror pre-alignment procedure. Once the ALS system was stable enough, it was possible to seamlessly proceed with locking the DRMI with aligned arm cavities, locked on the green lasers, and with a CARM offset to keep them out of the main IR laser resonance.

The commissioning of the CARM offset reduction was instead less straightforward. As mentioned in section 3.4.1, the higher-than-expected noise on the ALS beating signals required significant adjustments in the reduction procedure. Additionally, the “3f” error signals resulted less stable than expected during the CARM offset reduction, requiring further adjustments and tuning of the DRMI loops. Due to the complexity of diagnosticating the transient states of the CARM offset reduction, this process required strong commissioning efforts.

The complexity of troubleshooting the ALS subsystem and the overall interferometer behavior during the CARM offset reduction remarked the importance of studying alternative lock-acquisition procedures. Indeed, the “twin variable finesse” lock acquisition procedure studied in chapter 5 showed a promising alternative that would allow circumventing these issues without needing extra hardware.

As mentioned in the conclusions (3.5) of chapter 3, despite the complications encountered in the CARM offset reduction, the project’s biggest stumbling block was achieving a stable steady-state at the end of the lock-acquisition process. The difficulties in mode-matching both recycling cavities simultaneously had a particularly detrimental impact on the stability of the longitudinal and angular control loops once high power operation was reached. On the one hand, these issues showed the limitations of a simulation approach based only on a fully mode-matched interferometer representation. On the other hand, they showed that, even with large non-idealities and an overall sub-optimal working point, the longitudinal error signals resulting from the steady-state studies in chapter 4 and appendix B are nevertheless the best choice and are still in use. Thanks to the joint efforts of the commissioning, optical characterization, and simulation teams, recent progress (autumn 2022) in solving the mismatch issues allows for a sufficiently stable steady-state configuration and for engaging the DC readout. Further optimization activities are ongoing, allowing us to proceed toward the stability and sensitivity goals of the O4 observing run starting in 2023.

Overall, the commissioning results showed the validity of the simulation methods presented in this thesis, allowing us to design a robust control strategy and predict most of the problematic steps. Together with the knowledge accumulated on the new DRFPMI configuration during the commissioning, they will allow us to be prepared for the future upgrades of the Advanced Virgo experiment. Having robust methodologies that allow for accurately predicting the interferometer behavior is even more critical for the increased complexity of the third generation of gravitational wave interferometers, of which the design process is taking off these years.

Acknowledgements

With great pleasure, I thank the following people for the support shown during the years of work on the PhD project and the writing of this thesis.

My supervisor, prof. Antonio Perreca has been very supportive throughout my doctoral journey, and I am grateful to him for his teachings, patience and encouragement.

This work could not have been completed without the supervision and insightful ideas of Maddalena Mantovani, who guided us through the design process and the implementation phase of the AdV+ upgrades.

Many thanks to Rosario de Rosa and Andreas Freise for reviewing the manuscript in its final stages and suggesting valuable improvements.

A particular thank goes to professor Giovanni Andrea Prodi, head of Trento's experimental gravitation group, for his wisdom and advice.

I acknowledge the University of Trento, the European Gravitational Observatory (EGO) and the Istituto Nazionale di Fisica Nucleare (INFN) for funding my studies and the permanence at the Virgo experiment site.

Thank you to all the young researchers with whom I shared the joys and struggles of the 2021 commissioning period in Cascina: Marco, Julia, Diego, Manuel, Enzo, Yuefan, Eleonora, Riccardo, Priyanka, Camilla, Matthieu, Suzanne and Piernicola. Special thanks and a warm hug to Mattia Boldrini, who has been not only an amazing flatmate and scientist/genius but also a good friend during these years.

And also, thanks to the EGO personnel and everyone else sharing their expertise with us during the commissioning, particularly Paolo Ruggi, Matteo Tacca, and Jean-Pierre Zendri.

Thanks to Andrea Grimaldi, Andrea Miani, and Damiano Avi, who put up with me during my permanence in Trento's physics department.

Finally, I would not have completed my PhD without the patience and support of my family and friends. In particular, Martino, Chiara, and Alice, who always welcomed me back in Trento and supported me even in the darkest moments, and Lorenzo, always willing to waste time on video games with me.

The optical configuration layouts in this thesis have been illustrated using ComponentLibrary.

Impossible n'est pas français.

Appendix A

Effects of misalignments on the CITF longitudinal error signals

During the acquisition of the DRMI lock, the mirror alignment is controlled by limited-bandwidth local controls, resulting in a residual angular motion of the order of magnitude of 0.05 μrad. The main problem is that the local controls error signals do not have information about the beam/mirror misalignment, but they are only a ground-based reference. This means that, even if the accuracy control is enough to maintain the lock, a pre-alignment strategy could be needed. Moreover, this amount of residual motion is incompatible with the accuracy required for the detection of gravitational waves, and, for this purpose, higher performance angular controls need to be enabled at the end of the lock acquisition [29]. A study of the error signals in the previous PRMI configuration evaluated the impact of misalignments of the PR mirror during the lock acquisition [84], crucial for the Variable Finesse technique [42].

In the new DRMI configuration, however, the lock of the CITF DOFs is radically different from before. The structure of the new lock acquisition procedure (explained in chapter 3) raised concerns regarding the feasibility of achieving and then maintaining the CITF lock for the full duration of the CARM offset reduction procedure, which lasts several minutes. During this period, a recycling cavity's alignment drift affecting the longitudinal error signals could ultimately spoil the stability of the lock.

Therefore, we simulated the influence of misalignments of the arm input mirrors, PR, and SR mirrors on the DRMI longitudinal error signals. Particular focus was given to finding a maximum allowable misalignment for each mirror, above which the stability of the lock cannot be guaranteed. The results of the simulations are also reported in [98] and summarized in [53]. Simulating both the “1f” and “3f” error signals allowed us to respectively evaluate the possibility of engaging the lock and its robustness during the CARM offset reduction. The maximum allowable misalignment thresholds were then used to choose the alignment strategy during the CARM offset reduction phase.

A.1 Simulation details and limits

The simulations have been carried out using the modal simulation software Finesse 2 [95]. Like in chapter 5, we used a variation of the simulation setup described in 4.1. The limits and the observations discussed in 4.1 regarding the capability of that configuration to represent the real interferometer are still applicable to these simulations. The main difference in the setup used in this study is the addition of a 1.5 kHz CARM offset. Since during these steps, the arm cavities are off-resonance and controlled by the ALS, the influence of small CARM and DARM displacements on the IR beam is minimal, and the simulations focused on studying the CITF DOFs. Additionally, the study of misaligned components added the necessity of simulating a larger number of Hermite-Gauss modes to correctly represent the laser field in the interferometer.

To optimize the simulation process, the procedure was divided into the following steps explained in detail in sections A.1.2-A.1.4.:

- Base simulation of misaligned interferometer and convergence check;
- simulation of the longitudinal DOFs sweeps;
- optimization and study of the error signals.

A.1.1 Optimally matched interferometer

Consistently to the studies reported in chapter 4 and 5, the simulated interferometer configuration is optimally mode-matched. The choice of simulating an optimally mode-matched interferometer was given for the following reasons:

- Impossibility of having a representative estimate of the non-idealities affecting the CITF error signals before the installation and commissioning of the upgrades, currently ongoing.
- The overall impact of misalignments is maximum in the ideally matched configuration. A likely explanation is that in the ideal configuration, the studied misalignments are the only source of HOMs contributing to the error signals' degradation. An additional presence of losses toward HOMs given by mismatch and other cold defects mitigates the impact of the misalignment by preemptively lowering the finesse of the cavity for the gaussian components. Therefore, the simulated setup corresponds to the "worst case scenario" regarding the impact of misalignments, making it an ideal choice for this study.

A.1.2 Base simulation of misaligned interferometer and convergence check

To accurately study the behaviour of the interferometer when subject to misalignments, the correct working points of the LSC DOFs need to be found for each angle of each misaligned mirror. This is accomplished by minimizing the '3f' error signals using the built-in 'lock' command of Finesse. This procedure simulates the action of the CITF LSC loops, which are indeed engaged during the simulated scenario. The found working points are then saved and used for further simulations.

During this step, the convergence of the simulations is also tested. This means estimating whether the amount of TEM HOMs used in the simulation is sufficient to give realistic results. We used a procedure equivalent to the one described in section 5.2.2 to check the convergence.

The working points at different 'maxtems' are reported in the top plots of figures A.1, A.2, and A.3 for the misalignment of the PR, NI and SR mirrors, respectively. One can notice that in most cases, the larger the misalignment becomes, the more significant the impact of adding additional HOMs.

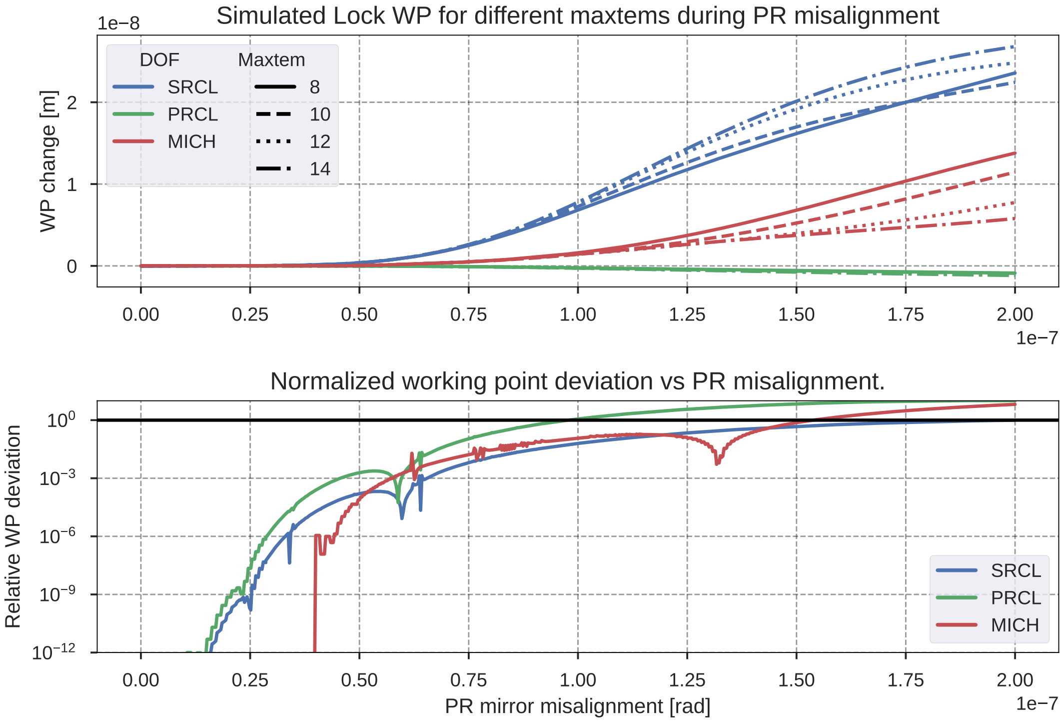

Figure A.1: **Top:** CITF DOFs' simulated WPs during the misalignment of the PR mirror for different 'maxtem' values. The DOFs are 'locked' using the '3f' signals. The 'maxtem' parameter indicates the highest Hermite-Gauss mode order used.
Bottom: Normalized WP differences for misalignments of the PR mirror. The lines indicate the difference between the WPs simulated with 'maxtem' 14 and 'maxtem' 12, normalized by the respective DOF accuracy requirements. Discontinuities in the line are caused by the finite tolerance of the lock algorithm.

As also mentioned in 5.2.2, an interesting figure of merit to evaluate the convergence is the relative WP variation between a simulation including up to a certain 'maxtem' value and the subsequent one, e.g., the difference between the WP estimated with 'maxtem' 12 and with 'maxtem' 14. This variation is compared with the accuracy requirements values discussed in chapter 4.2. The results, shown in the bottom plots of figures A.1, A.2, and A.3 (respectively for PR, NI and SR misalignments), show that using maxtem 14, the PR and NI misalignment simulations converge up to $\simeq 9.5 \cdot 10^{-8}$ rad and $\simeq 1.25 \cdot 10^{-7}$ rad respectively. For the misalignment of SR, the simulations converged in all the simulated ranges, up to $\simeq 3{\cdot}10^{-6}$ rad. The results of the simulations (in section A.2) show that these ranges are sufficient to study the necessity of a high-bandwidth (and gain) automatic alignment control.

Additionally, the optical gain of the error signals and their optimal demodulation phases have also been simulated for multiple maxtems. The results showed, between maxtem 12 and maxtem 14 and up to the angles mentioned above, differences lower than 1% for optical gains and lower than 5° for the optimal demodulation phases, thus not giving additional restrictions in the simulations.

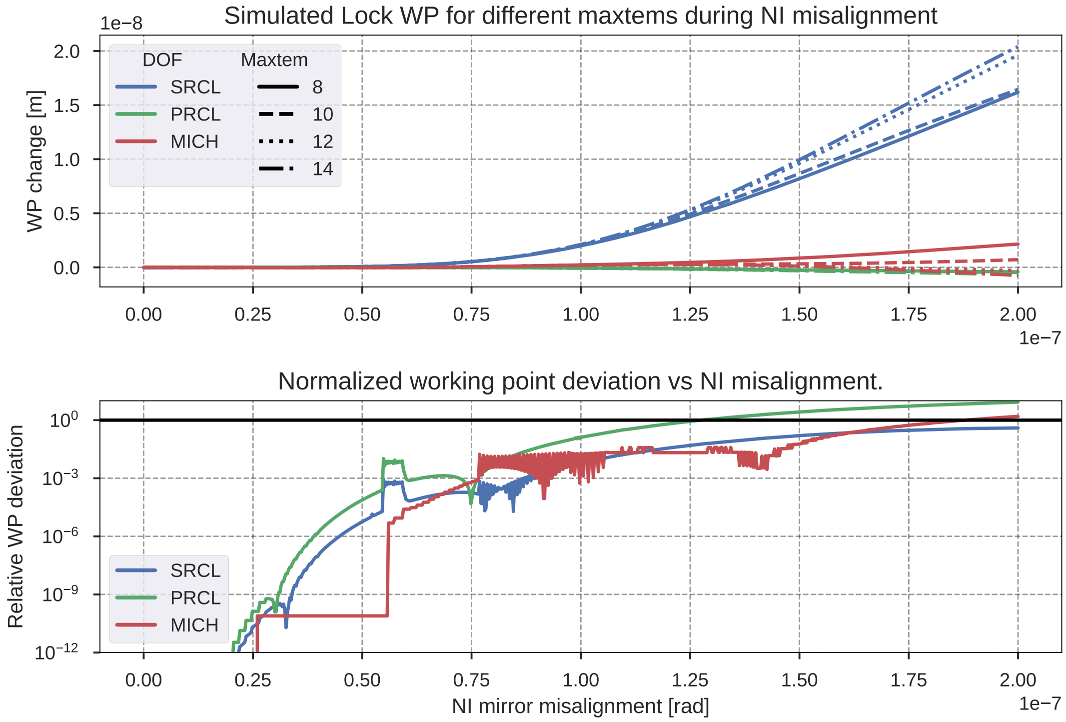

Figure A.2: **Top:** CITF DOFs' simulated WPs during the misalignment of the NI mirror for different 'maxtem' values. The DOFs are 'locked' using the '3f' signals. The 'maxtem' parameter indicates the highest Hermite-Gauss mode order used.
Bottom: Normalized WP differences for misalignments of the NI mirror. The lines indicate the difference between the WPs simulated with 'maxtem' 14 and 'maxtem' 12, normalized by the respective DOF accuracy requirements. Discontinuities in the line are caused by the finite tolerance of the lock algorithm.

A.1.3 Simulation of the longitudinal DOFs sweeps

. The initial simulations (described in section A.1.2) allow to study the error signals at their working point and to estimate their optical gain, optimal demodulation phase, and cross-couplings. However, further simulations are required to check how the misalignment of the mirror affects the error signals in a region around the working points. These simulations use the required 'maxtem' values and WP found in the initial simulation. Therefore, we simulated longitudinal sweeps of one CITF LSC DOF at a time for a limited number of misalignment angles.

Simulating these sweeps allows checking the shape and linearity of the error signals around the working point, including checking for multiple zero-crossings. Additionally, the zero-crossing of the error signals can be compared with the resonance peaks of the carrier and (more importantly for this step of the lock acquisition) of the control sideband fields.

The longitudinal sweeps are simulated by displacing the mirrors corresponding to the studied DOF while keeping the others at the WP. During this step, the behaviour of the laser beam in the main interferometer ports is monitored in detail by virtual photodiodes and field amplitude detectors. Both I and Q quadrature of each error signal is acquired, allowing to emulate the demodulation at any wanted phase ϕ as

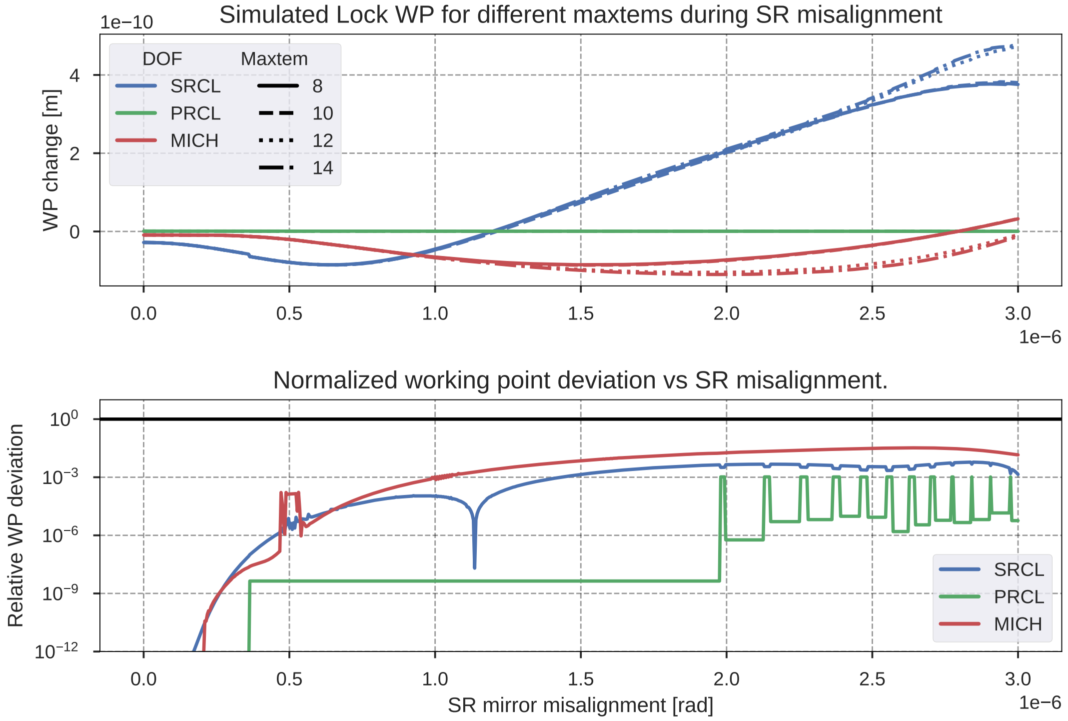

Figure A.3: **Top:** CITF DOFs' simulated WPs during the misalignment of the SR mirror for different 'maxtem' values. The DOFs are 'locked' using the '3f' signals. The 'maxtem' parameter indicates the highest Hermite-Gauss mode order used.
Bottom: Normalized WP differences for misalignments of the SR mirror. The lines indicate the difference between the WPs simulated with 'maxtem' 14 and 'maxtem' 12, normalized by the respective DOF accuracy requirements. Discontinuities in the line are caused by the finite tolerance of the lock algorithm.

follows:

$$Err[\phi] = \Re[(Err_I + iErr_Q)e^{-i\phi}] \tag{A.1}$$

A.1.4 Optimization and study of the error signals

This last step involves using the results of the simulations performed in the previous steps to study the behaviour of the error signals at different values of misalignment of the interferometer.

By setting the demodulation phase to the one used in the perfectly aligned condition, we studied the variation of multiple figures of merit against the misalignment of the CITF optics.

- Optical gains;
- working point;
- shape of the error signal (multiple zero crossings etc.).

As discussed in detail in the following section, the study of these quantities allows estimating a "threshold angle" beyond which the error signal cannot be used to keep the CITF locked.

Additionally, we studied how the optimal demodulation phases of each error signal changes with the misalignment, allowing us to estimate the increase of cross-couplings between the different DOFs.

A.2 Results

The error signals for the control of the CITF are listed in table A.1, together with their respective optical gain in an optimally aligned configuration.

DOF	Signal	"1f" Rel. OG [1/m]	"3f" Rel. OG [1/m]
PRCL	B2 6/18 MHz	$3.2 \cdot 10^{1}$	$2.6 \cdot 10^{-1}$
MICH	B2 56/169 MHz Q	$8.9 \cdot 10^{-1}$	$8.2 \cdot 10^{-3}$
SRCL	B2 56/169 MHz I	$4.5 \cdot 10^{-1}$	$5.7 \cdot 10^{-3}$

Table A.1: CITF lock acquisition error error signals and relative optical gains. The optical gains of the error signal have been normalized by the power on the relative photodiode.

A.2.1 Optical Gain variation

One of the main effects of the misalignment is a progressive variation of optical gain on the longitudinal error signals. The extent of this effect depends both on the error signal and on which mirror is misaligned. As expected, the simulations show that higher-frequency demodulated signals are overall less impacted by the misalignment than the lower frequency ones. This is due to the higher finesse of the latter ones, less impacted by the Schnupp asymmetry losses towards the antisymmetric port.

A loss of gain impact both the capability of engaging the lock and of maintaining it. The amount of gain loss that can affect a loop before it loses lock depends on several factors, in particular on the "gain margin" of the involved control loop and on the SNR of the error signal used. Automatic loop gain tuning processes based on a real-time estimate of the loop UGF help in maintaining the loop stable, as long as they "react" quickly enough. Even if compensated, a gain loss means a loss of SNR and an increase of re-injected sensing noise. Empirical experience shows that an optical gain loss above a factor of 50% often leads to loss of control. For this reason, the misalignment angle at which this threshold is reached is an important figure of merit subject of this study. Figure A.4 shows the relative effect of PR, NI and SR mirror misalignments on the planned error signals' optical gains. The optical gains are normalized by the corresponding values in the aligned condition.

From the results, summarized in table A.2, one can see that the most restrictive condition is given by the behaviour of the B2 6 and 18 MHz signals (used to control PRCL) for PR mirror misalignments. This error signal loses 50% of its optical gain at $5.7 \cdot 10^{-8}$ rad of PR misalignment (see figures A.4b and A.4a).

These error signals are also the most affected by NI mirror misalignments, with a half-gain threshold of $7.8 \cdot 10^{-8}$ rad, as seen in figure A.4d and A.4c.

SR misalignments instead have a much lower overall impact on the error signals (see figure A.4f), and, as expected, have more effect on the 56 MHz sidebands signals than on the 6 MHz ones due to the 56 MHz sidebands being resonant in the SR cavity. Additionally, the MICH error signal gain increases with the SR mirror misalignment.

DOF	Signal	PR thr. [rad]	NI thr. [rad]	SR thr. [rad]
PRCL	B2 6 MHz I	$5.7 \cdot 10^{-8}$	$7.8 \cdot 10^{-8}$	N.A.
	B2 18 MHz I	$5.7 \cdot 10^{-8}$	$7.8 \cdot 10^{-8}$	N.A.
MICH	B2 56 MHz I	$6.9 \cdot 10^{-8}$	$1.0 \cdot 10^{-7}$	N.A.
	B2 169 MHz I	$8.0 \cdot 10^{-8}$	$1.2 \cdot 10^{-7}$	N.A.
SRCL	B2 56 MHz Q	$7.0 \cdot 10^{-8}$	$9.6 \cdot 10^{-8}$	N.A.
	B2 169 MHz Q	$9.2 \cdot 10^{-8}$	$1.2 \cdot 10^{-7}$	$2.4 \cdot 10^{-6}$

Table A.2: 50 % OG loss thresholds for each error signal. Each column shows the respective mirror misalignment at which the error signal loses 50 % of its optical gain. For SR misalignments (last column), most of the error signals do not reach the 50 % threshold in the simulated range (up to $3.0 \cdot 10^{-6}$ rad).

No maximum threshold has been found for the simulated misalignments. Increasing the simulation range will eventually find a threshold given by the gain drop of SRCL itself. However, this is not of interest for this study since the simulated misalignment is already well above the residual angular motion with the mirror under the control of the local controls alone ($\simeq 0.05$ μrad).

A.2.2 Error signal shapes and zero-crossing

The simulated DOF sweeps allowed to check for abnormalities in the error-signal shape and the correspondence of their zero-crossings with the control sideband peaks. The results for the error signals used to control the DRMI are represented in figures A.5 to A.10.

No particular concerns arise from the shapes of the error signals. At the simulated angles, the shape and the linear region of all the error signals are minimally affected, with the loss of optical gain as the noticeable main effect. The most noteworthy zero-crossing deviation is the SRCL error signal (B2 169MHz I), which, at the maximum simulated SR mirror misalignment, deviates $\simeq 1.7$ nm from the 56 MHz sideband peak observed by the B2 112 MHz magnitude signal. However, as mentioned above, the maximum simulated SR misalignment ($\simeq 3$ μrad) represents an unlikely scenario, even with the alignment controlled by local controls. Lower SR misalignments or large PR and NI misalignments also introduce a similar deviation but of negligible magnitude (≤ 0.5 nm).

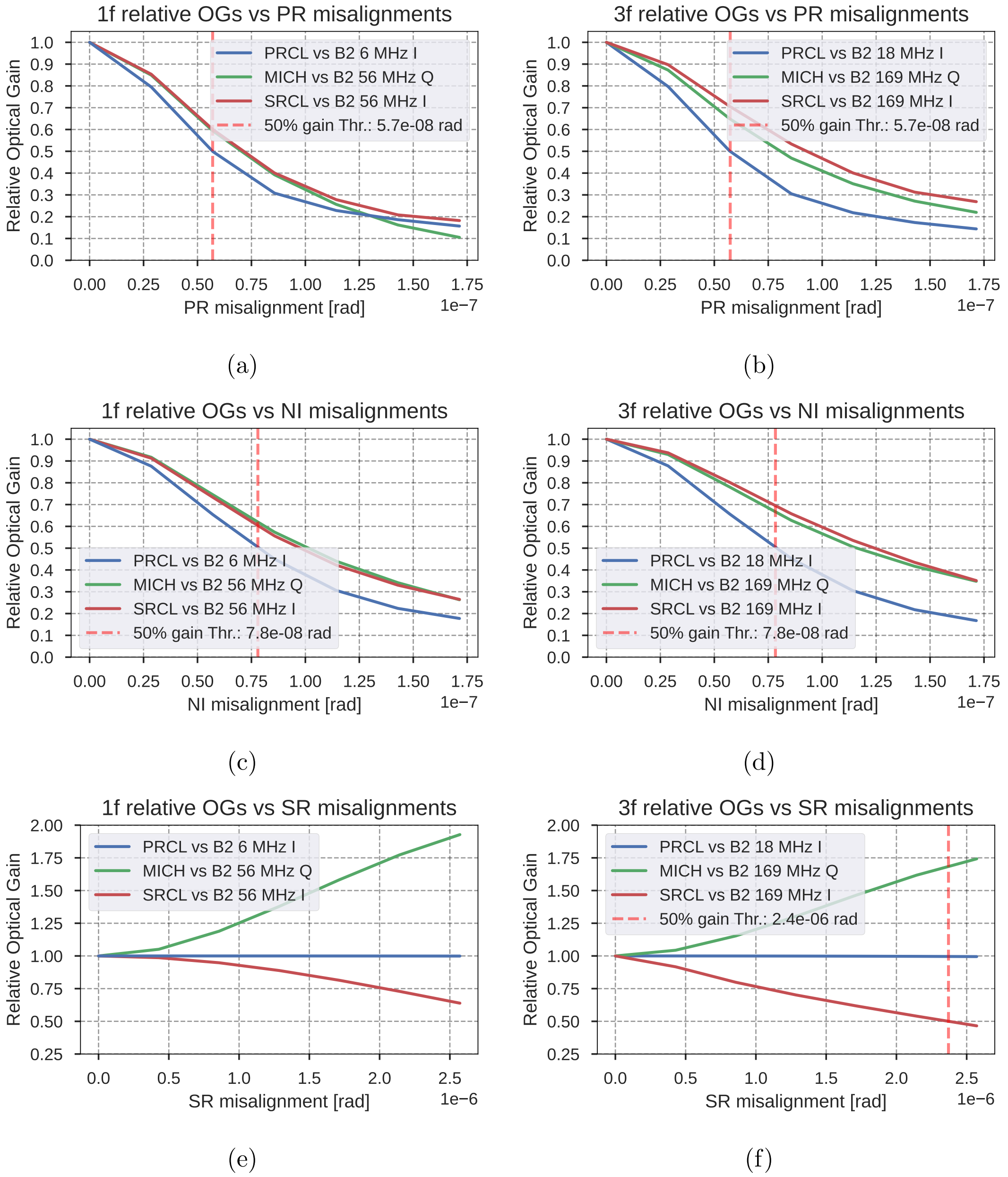

(a) (b)

(c) (d)

(e) (f)

Figure A.4: CITF error signals OG variation vs misalignments of the PR, NI, and SR mirror (first, second, and third row respectively). Each line corresponds to the relative optical gain of an error signal used for the control of the CITF. The first column (plots a, c, e) shows the values for the “1f” error signals, while the second column (plots b, d, f) shows the values for the “3f” ones. The OGs are relative to the gains in a fully aligned condition. The vertical dashed line marks, when present, the lowest angle at which one of the error signals has lost 50% of its OG.

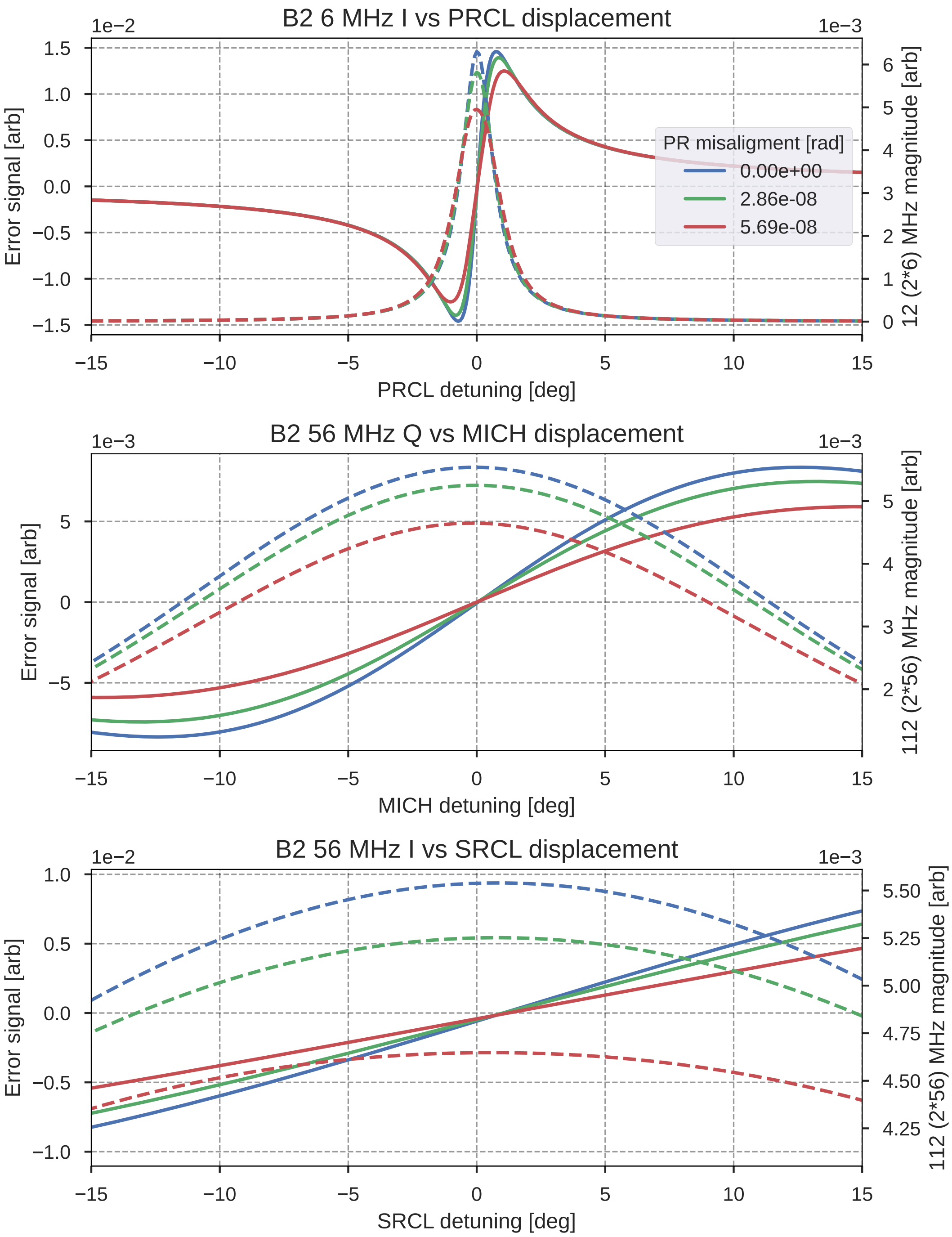

Figure A.5: CITF error signals scans for various PR misalignments. Each plot shows the scan of a different CITF dof and its corresponding “1f” error signal (continuous lines). The dashed lines show the “2f” signal magnitude corresponding to either the 6 MHz (first plot) or 56 MHz (second and third plot) resonances. Each color represents a different misalignment of the PR mirror.

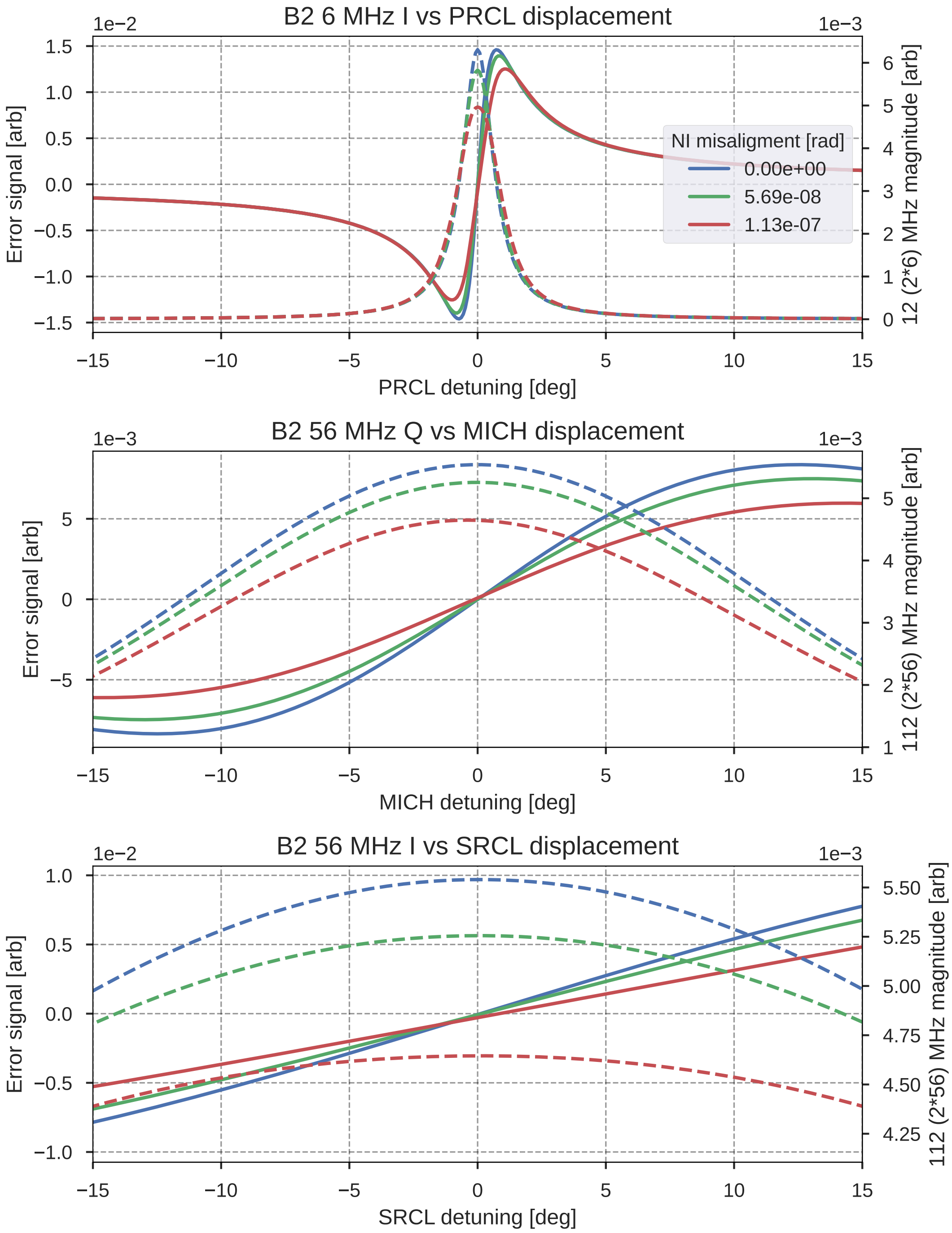

Figure A.6: CITF error signals scans for various NI misalignments. Each plot shows the scan of a different CITF dof and its corresponding “1f” error signal (continuous lines). The dashed lines show the “2f” signal magnitude corresponding to either the 6 MHz (first plot) or 56 MHz (second and third plot) resonances. Each color represents a different misalignment of the NI mirror.

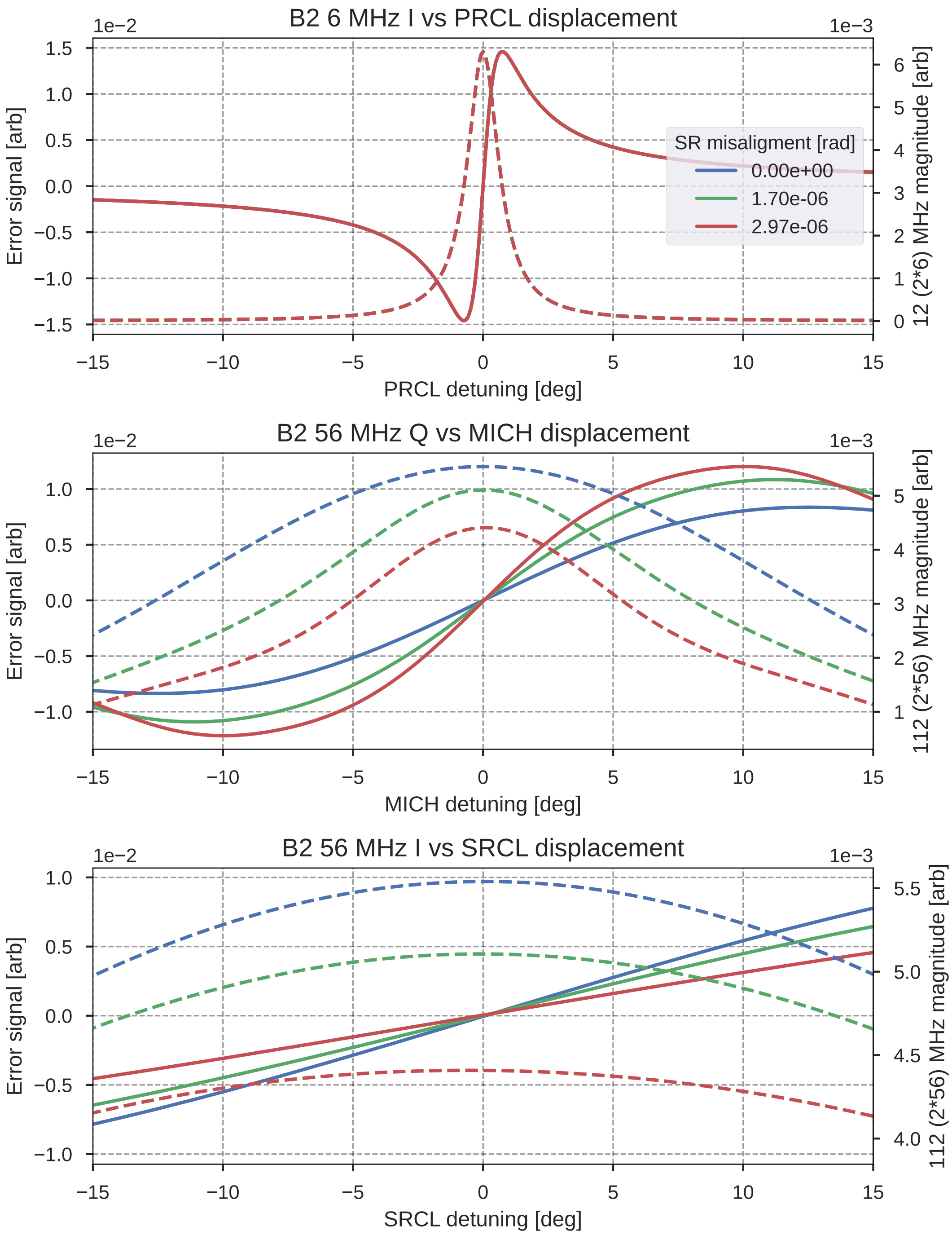

Figure A.7: CITF error signals scans for various SR misalignments. Each plot shows the scan of a different CITF dof and its corresponding “1f” error signal (continuous lines). The dashed lines show the “2f” signal magnitude corresponding to either the 6 MHz (first plot) or 56 MHz (second and third plot) resonances. Each color represents a different misalignment of the SR mirror.

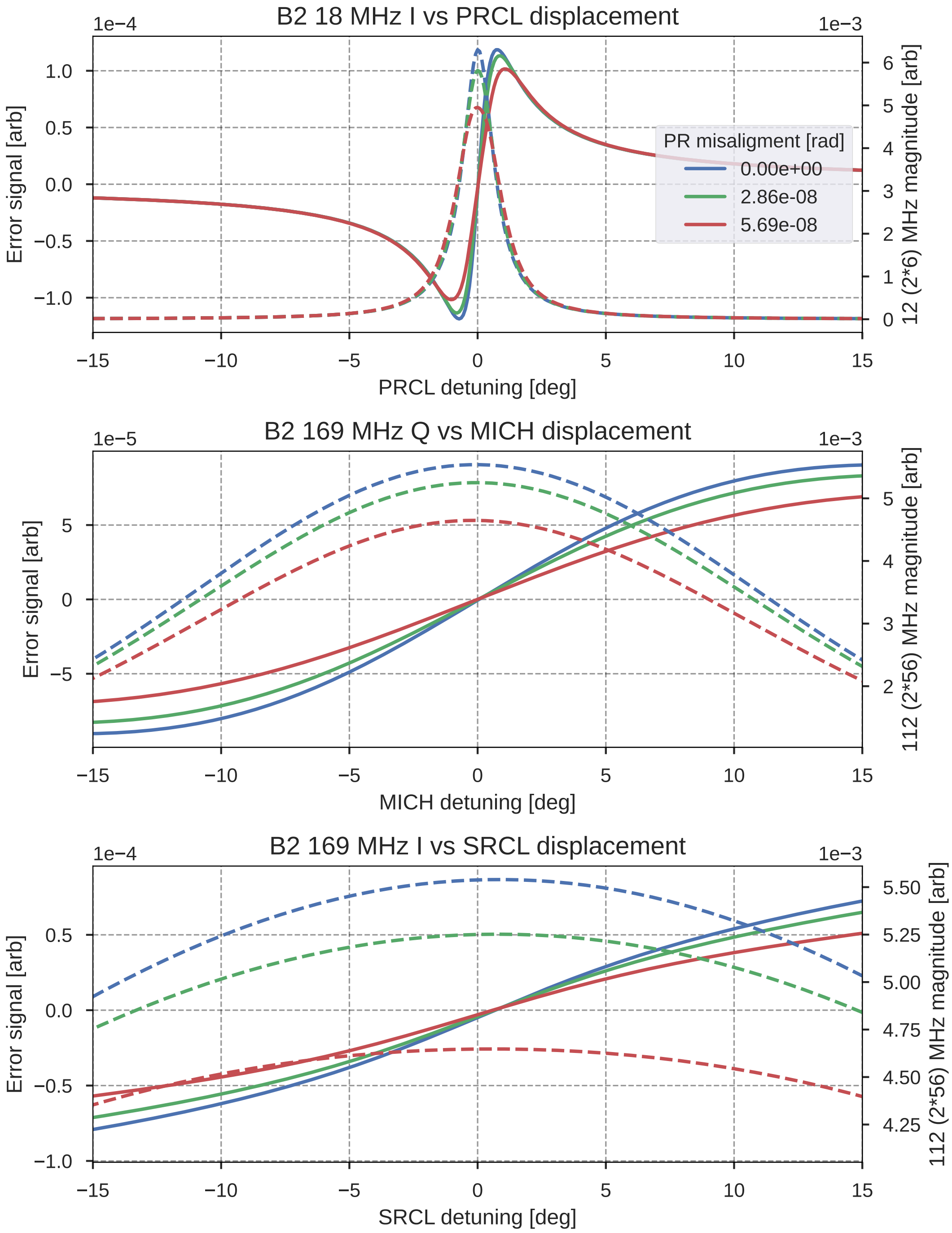

Figure A.8: CITF error signals scans for various PR misalignments. Each plot shows the scan of a different CITF dof and its corresponding "3f" error signal (continuous lines). The dashed lines show the "2f" signal magnitude corresponding to either the 6 MHz (first plot) or 56 MHz (second and third plot) resonances. Each color represents a different misalignment of the PR mirror.

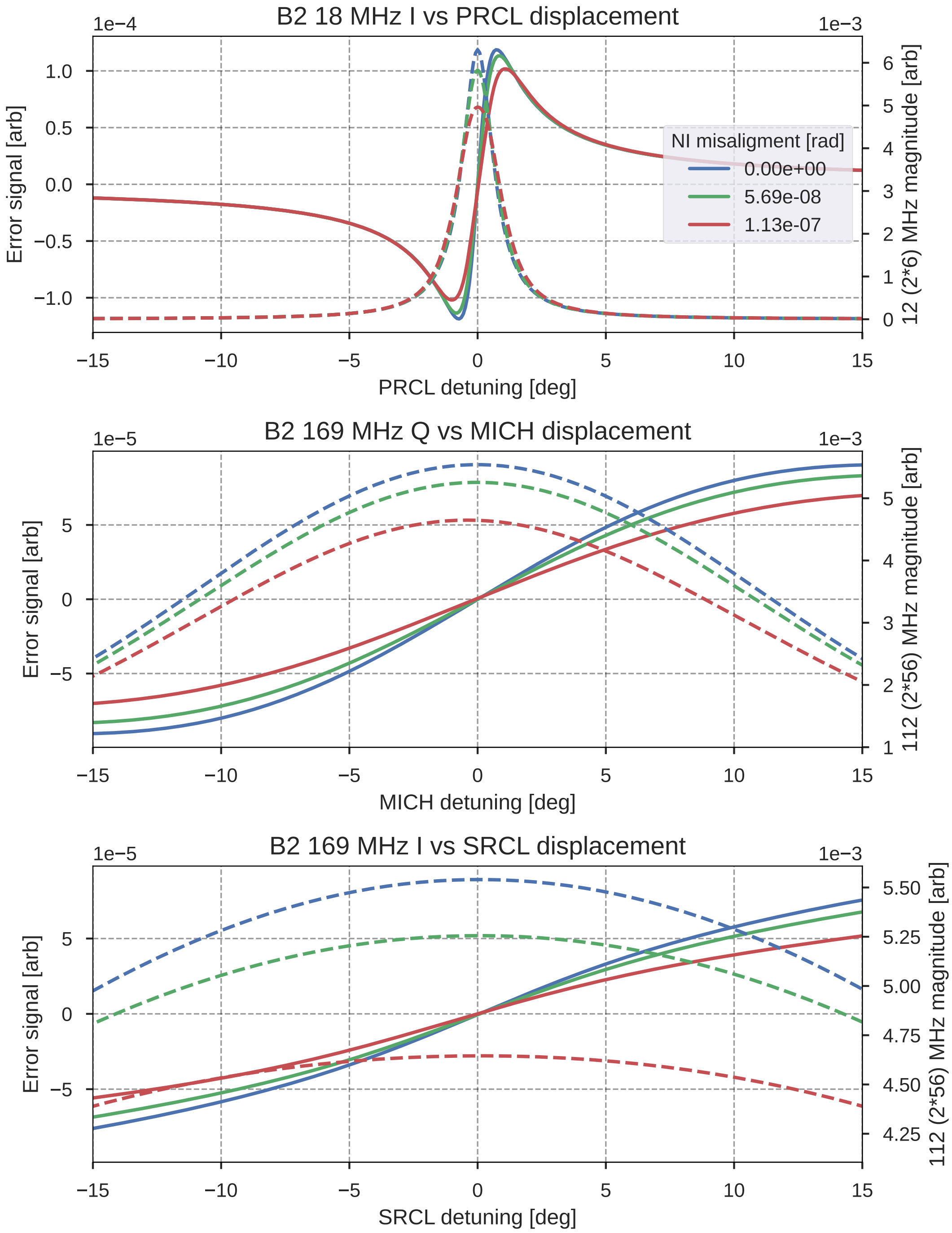

Figure A.9: CITF error signals scans for various NI misalignments. Each plot shows the scan of a different CITF dof and its corresponding "3f" error signal (continuous lines). The dashed lines show the "2f" signal magnitude corresponding to either the 6 MHz (first plot) or 56 MHz (second and third plot) resonances. Each color represents a different misalignment of the NI mirror.

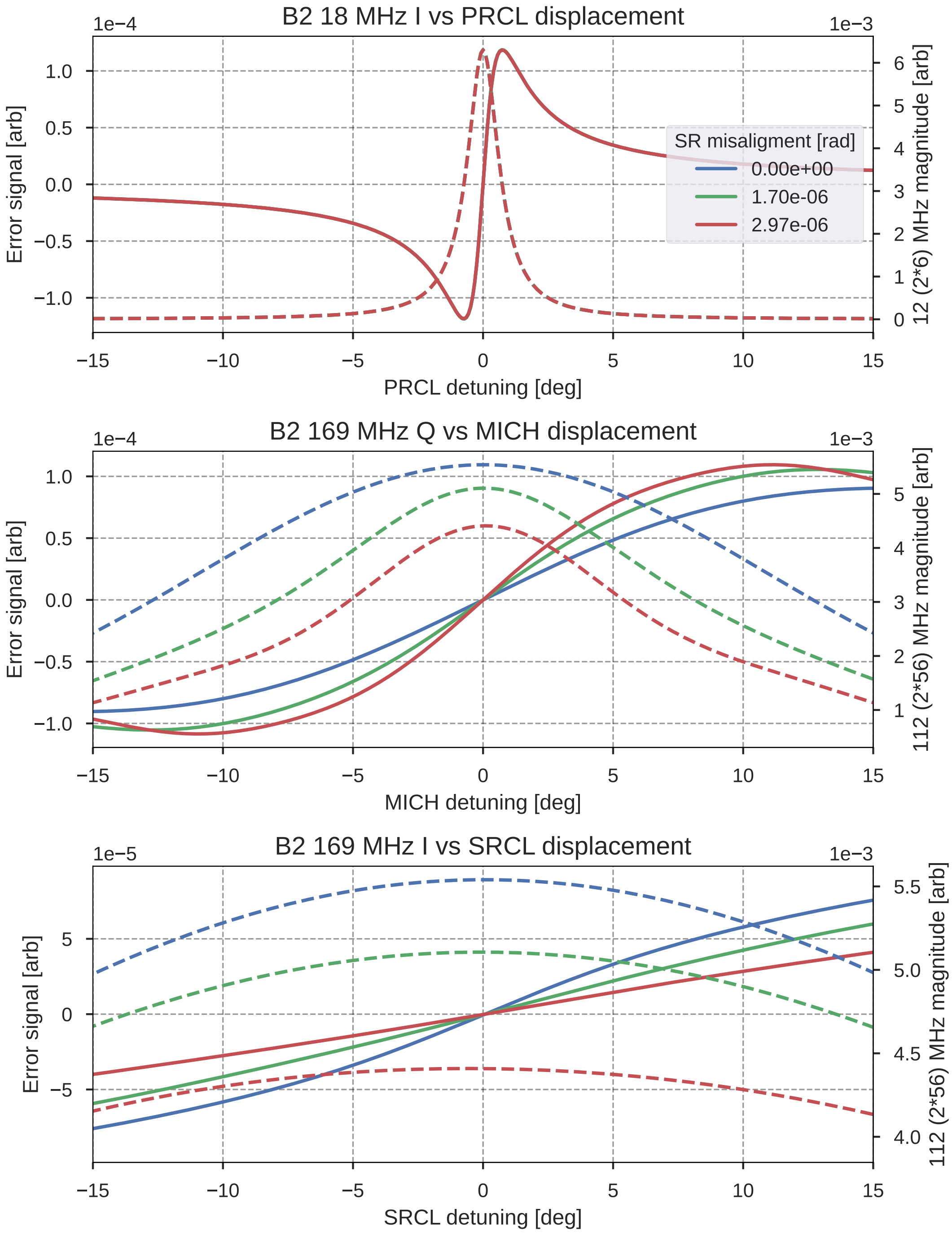

Figure A.10: CITF error signals scans for various SR misalignments. Each plot shows the scan of a different CITF dof and its corresponding “3f” error signal (continuous lines). The dashed lines show the “2f” signal magnitude corresponding to either the 6 MHz (first plot) or 56 MHz (second and third plot) resonances. Each color represents a different misalignment of the SR mirror.

A.2.3 Optimal demodulation phase variations

Each error signal is demodulated at the phase that maximizes the optical gain against the displacement of the respective DOF. A mirror misalignment can change the optimal demodulation phases and, consequently, introduce cross-couplings between different DOFs and reduce the overall SNR. A variation of optimal demodulation phase larger than 90° means a change of sign of the error signal, but usually, the lock fails much before reaching this point. Changes larger than $20 - 30^\circ$ usually are enough to cause an unlock.

Figure A.11a to A.12c show the change in the demodulation phase of the main error signals for misalignments of the PR, NI and SR mirrors, for the “1f” and “3f” error signals. From the results, one can see that the change in the optimal demodulation phase is always lower than 12° for misalignments lower than the thresholds determined by the optical gain variations (table A.2). Therefore, the change in the demodulation phase is not the limiting factor in the allowed misalignment.

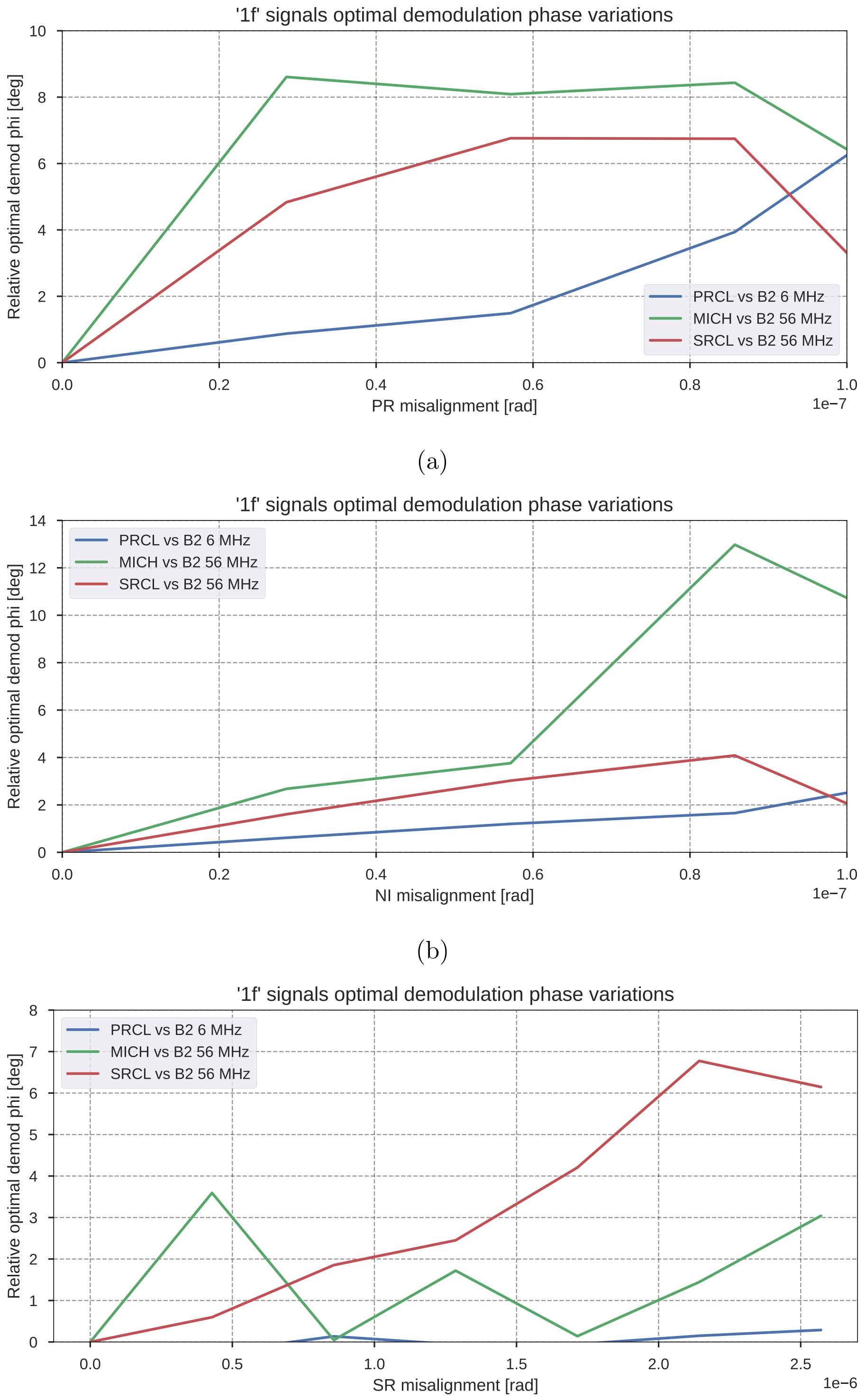

(a)

(b)

(c)

Figure A.11: Variation of the optimal demodulation phase for the main “1f” error signals against misalignments of the PR, NI and SR mirror respectively for plots A.11a A.11b and A.11c.

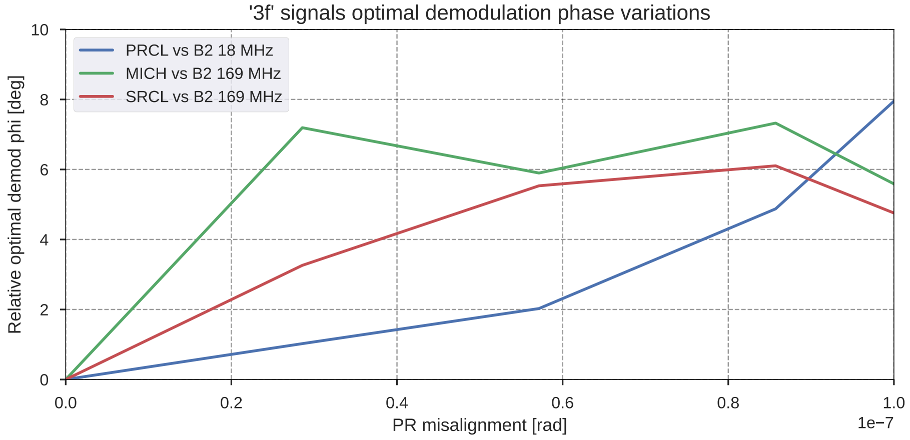

(a)

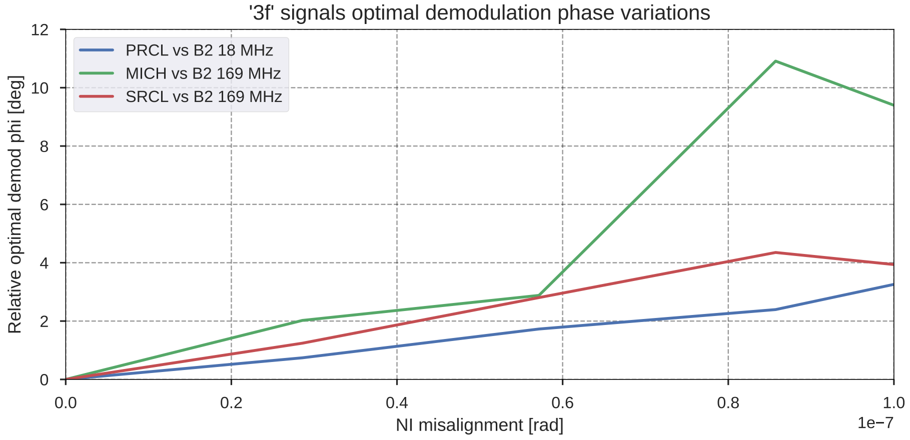

(b)

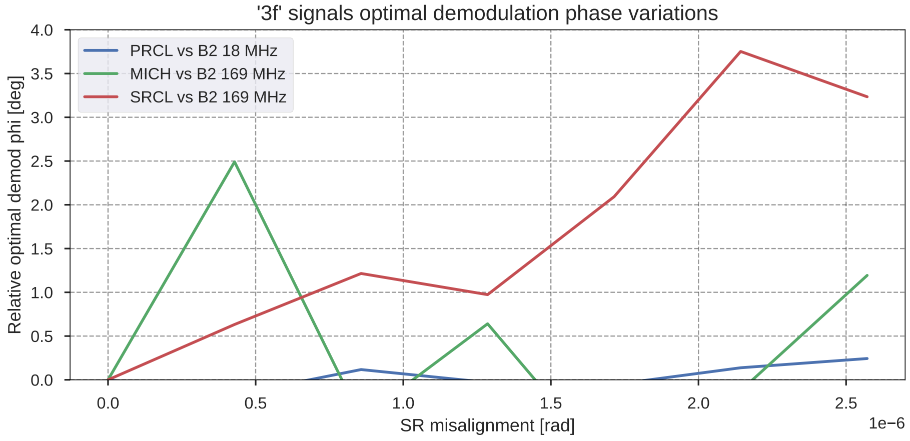

(c)

Figure A.12: Variation of the optimal demodulation phase for the main “3f” error signals against misalignments of the PR, NI and SR mirror respectively for plots A.12a A.12b and A.12c.

A.2.4 Cross couplings

Another effect that has been studied is the influence of the misalignment in the couplings between different DOFs.

Figure A.13 to A.18 compare, at each studied misalignment, the optical gain of each error signal against the three different CITF DOFs. The optical gains of each signal (each column) have been divided by the optical gains of the corresponding controlled DOF[1].

Results: The results show that PRCL has a large impact on all the error signals, and its error signals (B2 6/18 MHz) are minimally influenced by MICH and SRCL displacements, even at high misalignments. Nevertheless, due to its high optical gain (see table A.1), the PRCL loop can be closed with a much higher gain and bandwidth than the MICH and SRCL ones. This allows suppressing PRCL residual motion at the level of having little impact on MICH and SRCL.

Indeed, experimental results confirmed that the PRCL loop is stable up to an UGF of $\simeq 70$ Hz, while SRCL and MICH are respectively kept at UGF of $\simeq 5$ Hz and $\simeq 15$ Hz during the lock acquisition. Additionally, the phase of the MICH error signal (B2 56/169 MHz Q) is maintained as orthogonal as possible to the optimal PRCL phase, minimizing the influence of its displacement. This has the downside of maximizing the impact of PRCL displacements on the SRCL loop, but since this loop has the lowest bandwidth and the largest linear region, its robustness is not affected by this cross-coupling.

SRCL detuning has a low impact on all error signals for any misalignment angle, not raising particular concerns.

The MICH displacement impact on the PRCL error signal remains negligible. Its impact on the SRCL error signals (B2 56/169 MHz I) instead increases by a factor of $\simeq 2$ for PR and NI misalignments above $0.5 \cdot 10^{-7}$ rad (figure A.13, A.14, A.16, A.17). Considering that the MICH impact remains a factor 2 below the SRCL gain and considering the high robustness and low UGF of the SRCL loop, the main limiting factor to the NI and PR misalignment remains the loss of optical gains discussed in section A.2.1.

---

[1] e.g., plots in the first column (corresponding to the B2 6/18 MHz I signal) have been divided by the OG of B2 6/18 MHz I for PRCL

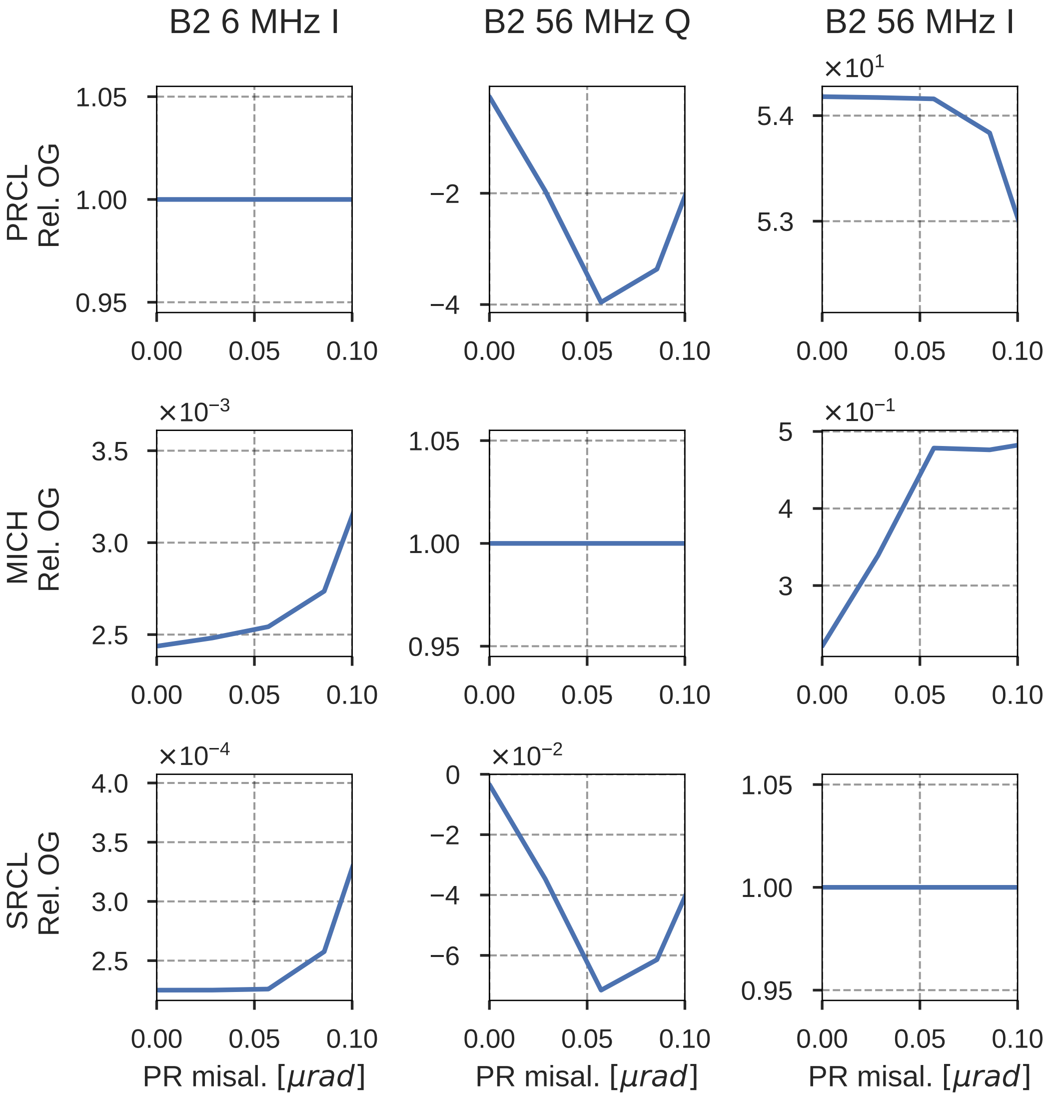

Figure A.13: Evolution of "1f" signals' cross-couplings between CITF DOFs for misalignments of the PR mirror. Each column corresponds to a different error signal, each row to a different DOF. Each plot shows the relative OG of the respective error signal against displacements of the respective DOF. The OGs are divided by the OG of the diagonal elements, corresponding to the OG of the signals used in the feedback loops.

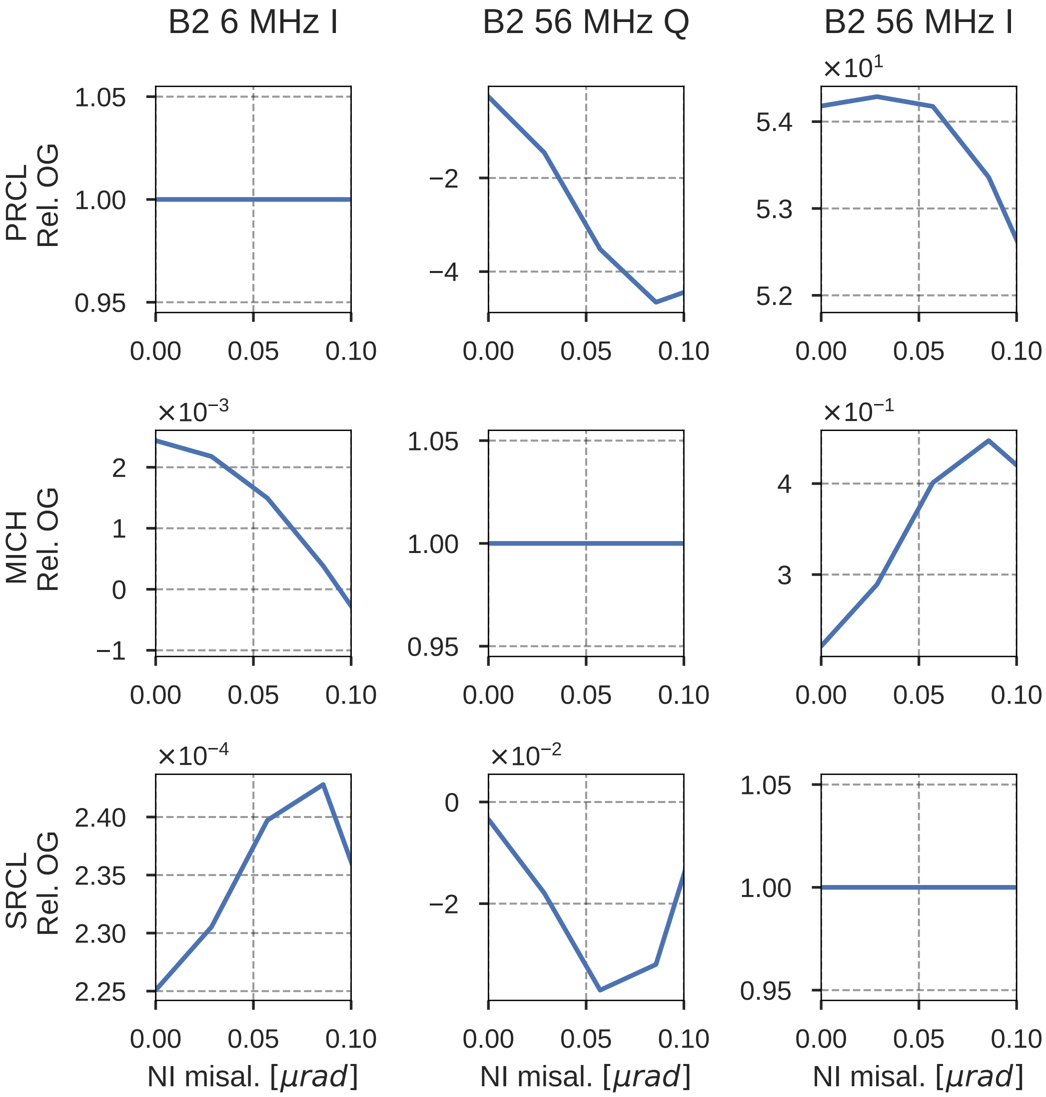

Figure A.14: Evolution of "1f" signals' cross-couplings between CITF DOFs for misalignments of the NI mirror. Each column corresponds to a different error signal, each row to a different DOF. Each plot shows the relative OG of the respective error signal against displacements of the respective DOF. The OGs are divided by the OG of the diagonal elements, corresponding to the OG of the signals used in the feedback loops.

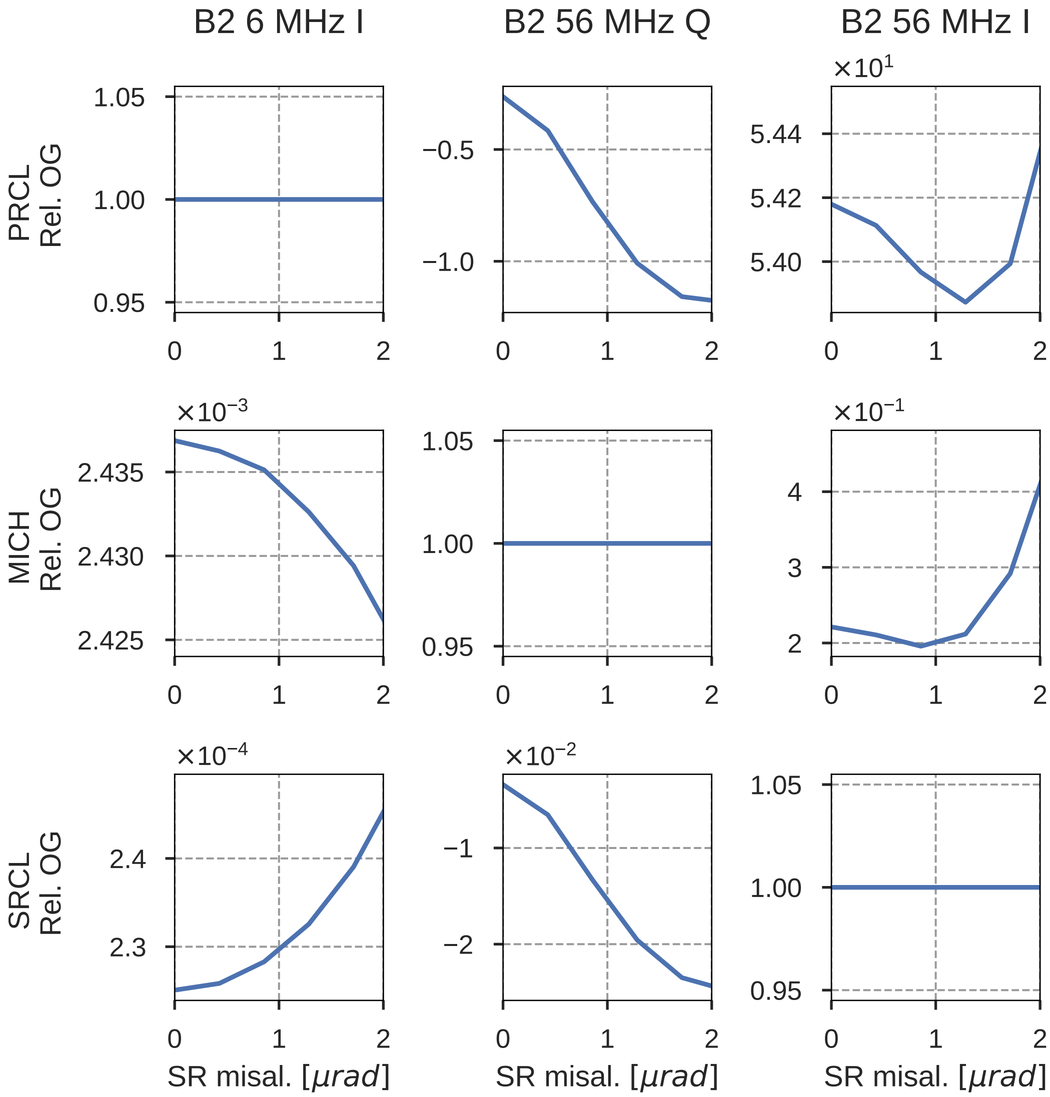

Figure A.15: Evolution of "1f" signals' cross-couplings between CITF DOFs for misalignments of the SR mirror. Each column corresponds to a different error signal, each row to a different DOF. Each plot shows the relative OG of the respective error signal against displacements of the respective DOF. The OGs are divided by the OG of the diagonal elements, corresponding to the OG of the signals used in the feedback loops.

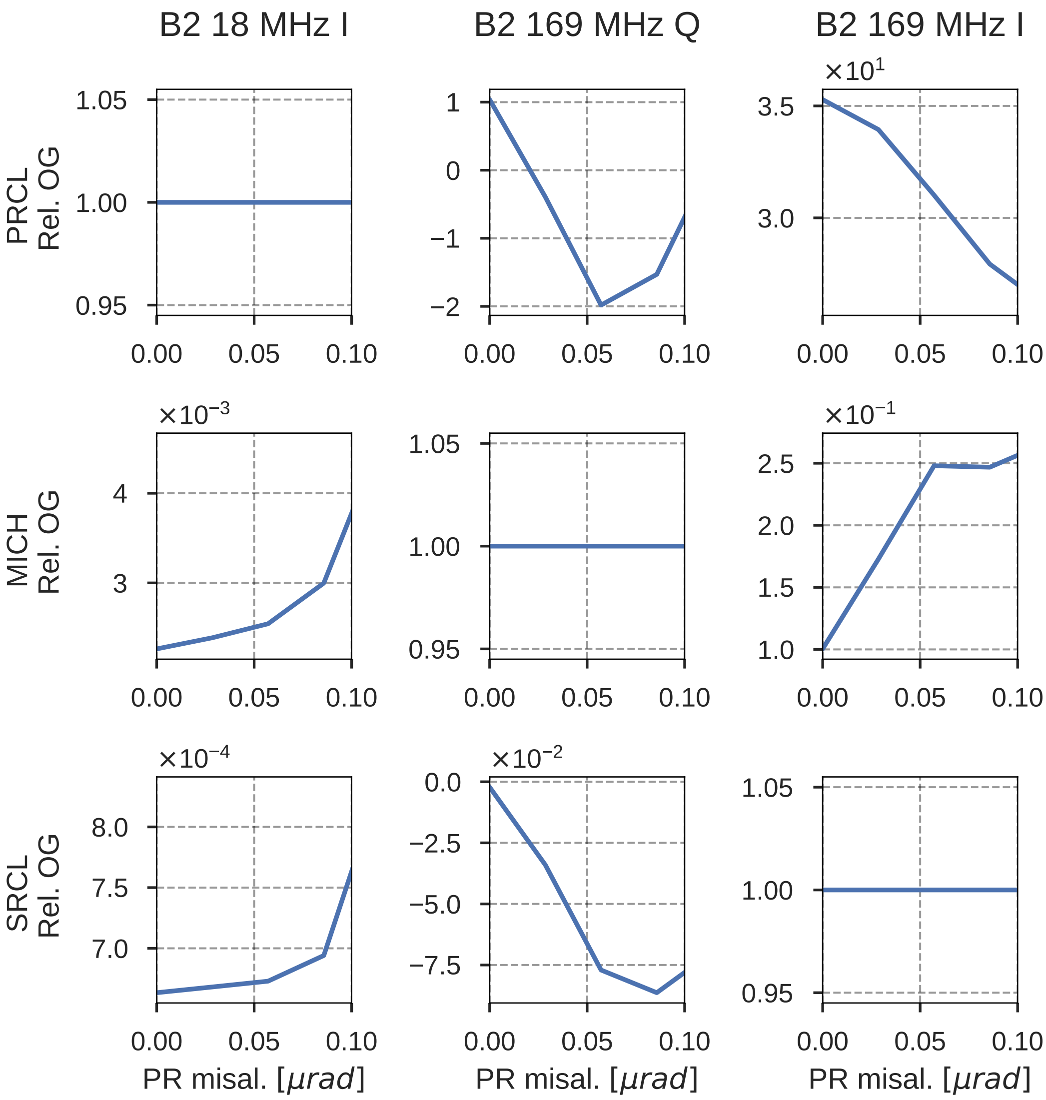

Figure A.16: Evolution of "3f" signals' cross-couplings between CITF DOFs for misalignments of the PR mirror. Each column corresponds to a different error signal, each row to a different DOF. Each plot shows the relative OG of the respective error signal against displacements of the respective DOF. The OGs are divided by the OG of the diagonal elements, corresponding to the OG of the signals used in the feedback loops.

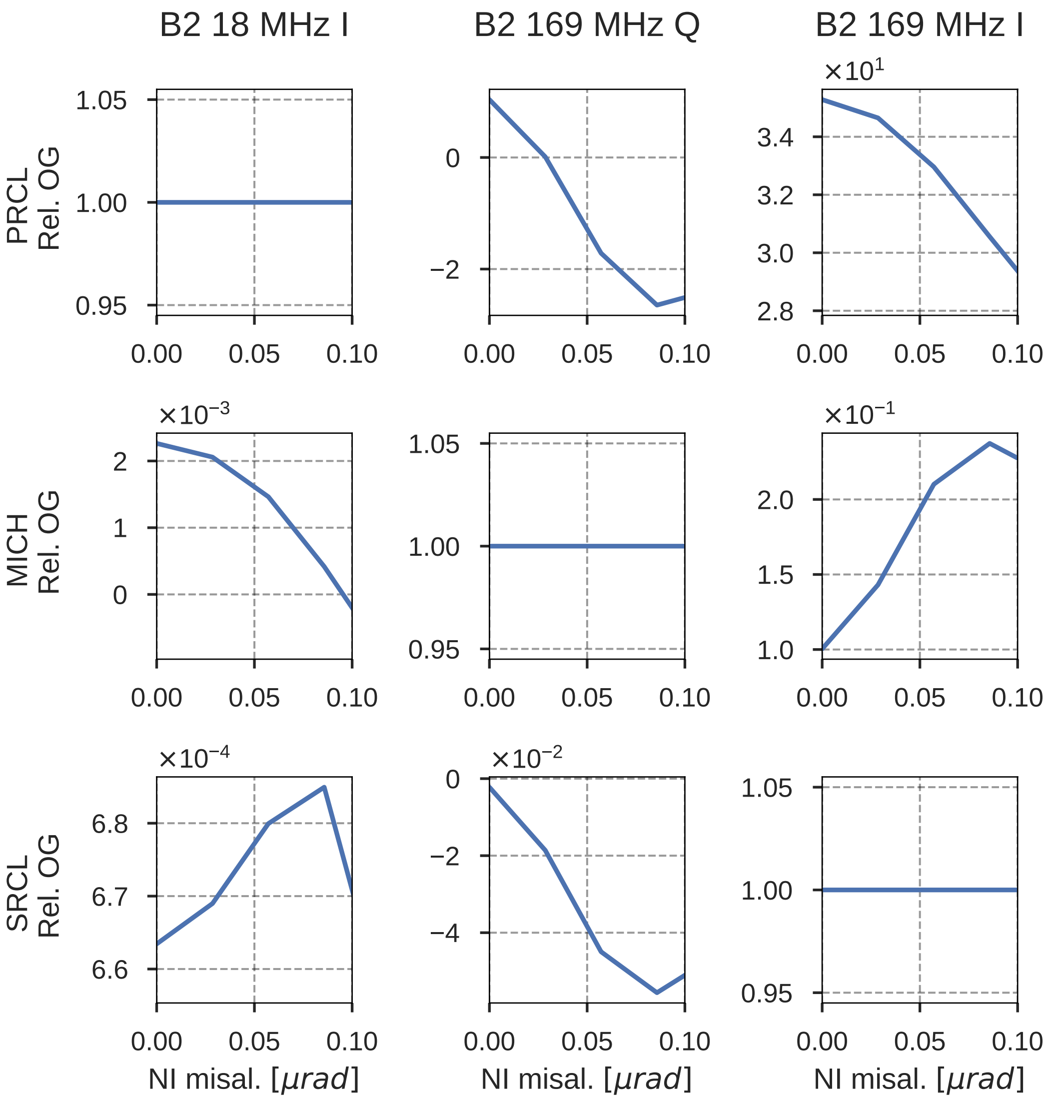

Figure A.17: Evolution of “3f” signals’ cross-couplings between CITF DOFs for misalignments of the NI mirror. Each column corresponds to a different error signal, each row to a different DOF. Each plot shows the relative OG of the respective error signal against displacements of the respective DOF. The OGs are divided by the OG of the diagonal elements, corresponding to the OG of the signals used in the feedback loops.

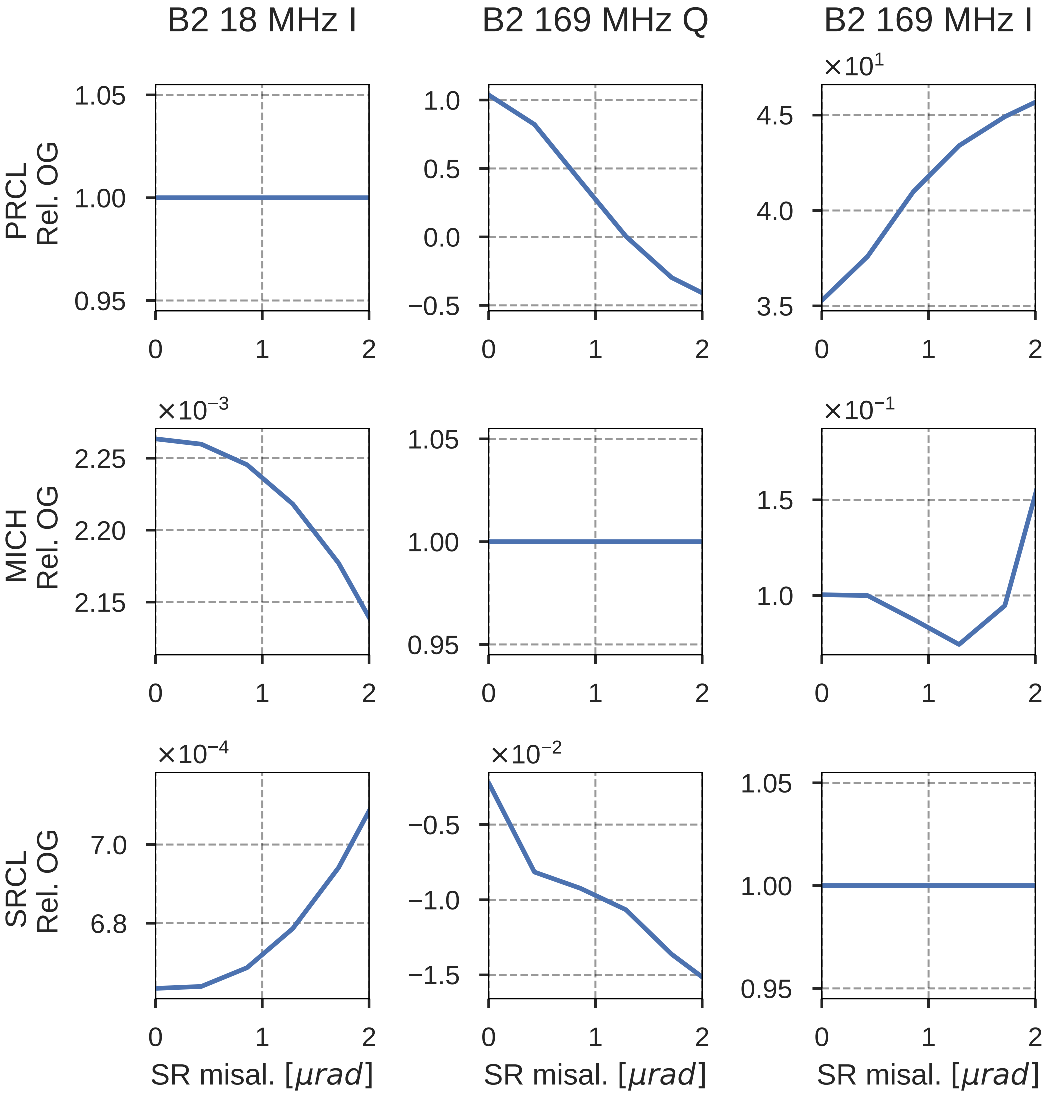

Figure A.18: Evolution of "3f" signals' cross-couplings between CITF DOFs for misalignments of the SR mirror. Each column corresponds to a different error signal, each row to a different DOF. Each plot shows the relative OG of the respective error signal against displacements of the respective DOF. The OGs are divided by the OG of the diagonal elements, corresponding to the OG of the signals used in the feedback loops.

Appendix B

Detailed study of LSC error signals

This appendix reports the detailed study of the main possible LSC error signals for the AdV+ phase 1 configuration. The context and methodology of this study are explained in section 4.4.

For each of these error signals, two different kinds of plots are reported in this appendix. These plots are in figure B.1, B.2, B.5, B.4, B.7, B.8, B.9, B.10 and B.11. In each of these figures, the plot on the bottom (called “compass plot”) contains pointers whose orientations represent the optimal demodulation phase for each DOF and whose lengths represent the respective optical gain (in $\mathrm{dB}_{\mathrm{W/m}}$). These plots allow having a preliminary estimate of the coupling between the various DOFs in a specific error signal. Indeed, if the optimal demodulation phase difference between two DOFs is exactly 90°, they can be perfectly decoupled by demodulating at the appropriate phase. Otherwise, the demodulated error signal will be influenced by the displacement of both (or more) DOFs at any chosen demodulation phase. The closer the optimal demodulation phase difference between two different DOFs is to 0°or 180°, the higher their inevitable cross-coupling will be. As mentioned above, however, the optical gain alone can give misleading information. Therefore we can obtain a complete overview of the error signal from the plots on the top. These plots represent, with two different zoom levels, the value of the error signal demodulated at the chosen phase with respect to the displacement of each LSC DOF. In addition to these lines, the plots include a dotted line representing the relative change of power at a relevant photodiode with respect to the displacement of the main DOF. This helps in comparing the error signal linear region with the cavities’ linewidth.

B.1 DARM: B1p 56 MHz

When the interferometer is at the ideal working point, the maximum sensitivity to DARM variations (and therefore to GWs) is seen at the antisymmetric port of the interferometer. As explained in chapter 3, different error signals are used to control this degree of freedom during the various steps of the locking sequence. In particular, the used signals are:

- During the first steps of the lock acquisition: auxiliary lasers beating signals;

- During the later stages of the CARM offset reduction and until the lock of the OMC: B1p 56 MHz (see below);
- After the addition of the DC offset and the OMC lock: B1 DC.

Since the use of B1 DC as the final signal was not under discussion (the benefits of a DC readout vs. an RF "heterodyne" detection are discussed here: [14]), the study focused on finding the best error signal for the dark fringe state. The simulation showed that, in this configuration, the B1p signal demodulated at 56 MHz is the optimal error signal for the control of DARM. The same photodiode signal demodulated at 6.27 MHz can also be used, but, as shown in Figures B.1 and B.2 and in table B.1, it has a lower optical gain and SNR. This is caused by the lower power than the 6.27 MHz sidebands have at this port since they are not transmitted by the SR cavity. Both these error signals do not show significant coupling with other DOFs except for MICH, which shows an optical gain that is two orders of magnitude lower than the DARM one, therefore not raising any concerns.

	B1p 56 MHz	B1p 6 MHz
Rel. OG [1/m]	4.2e+10	7.7e+09
Shot SNR [$1/(\mathrm{m}\sqrt{\mathrm{Hz}})$]	3.1e+18	4.2e+17
WP offset [m]	3e-14	2e-14
ΔWP [m]	5e-16	6e-17
Acc. Requirement [m]	1e-11	

Table B.1: Overview of DARM error signals' parameters. First row: relative-power optical-gain. Second row: expected shot noise SNR. Third row: signal working point offset WP at the optimal demodulation phase with respect to the WP found in the longitudinal pre-tune procedure explained in the "Length tunings" paragraph of section 4.1.1. Fourth row: working point shift ΔWP when a 10° offset is applied to the demodulation phase. Fifth row: accuracy requirement, taken from section 4.2.

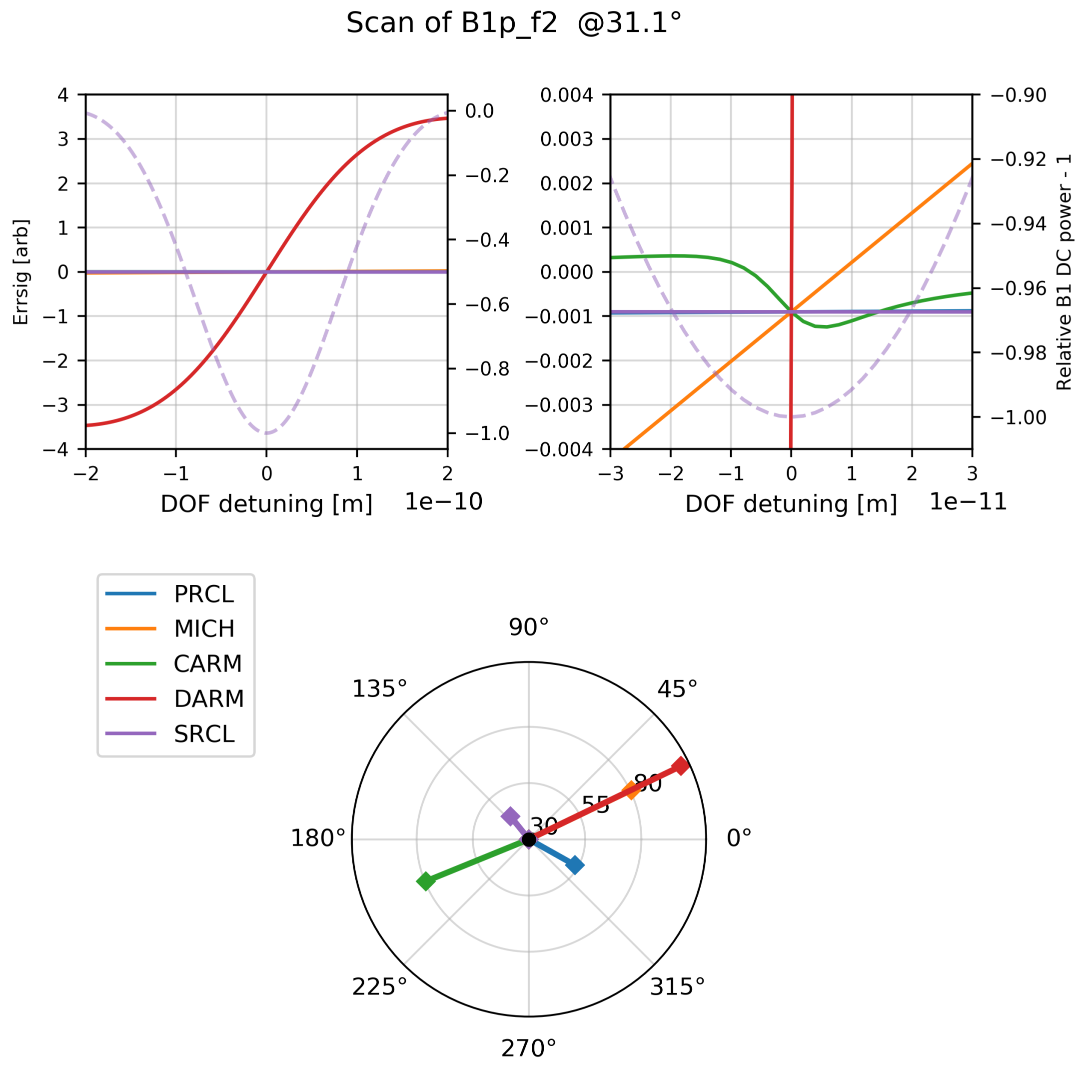

Figure B.1: B1p 56MHz error signal scan (with two different zoom levels) and compass plot, showing the dependence on the displacement of all the longitudinal DOFs, as explained in 4.4.2. This signal is meant to control the DARM DOF, which is indeed highly preeminent compared to the other DOFs. The dashed purple line corresponds to the power at the B1 photodiode, showing the interferometer dark-fringe. Note the higher optical gain of this error signal with respect to the alternative 6 MHz signal shown in figure B.2. Optical gain units in the compass plot are $\mathrm{dB}_{\mathrm{W/m}}$

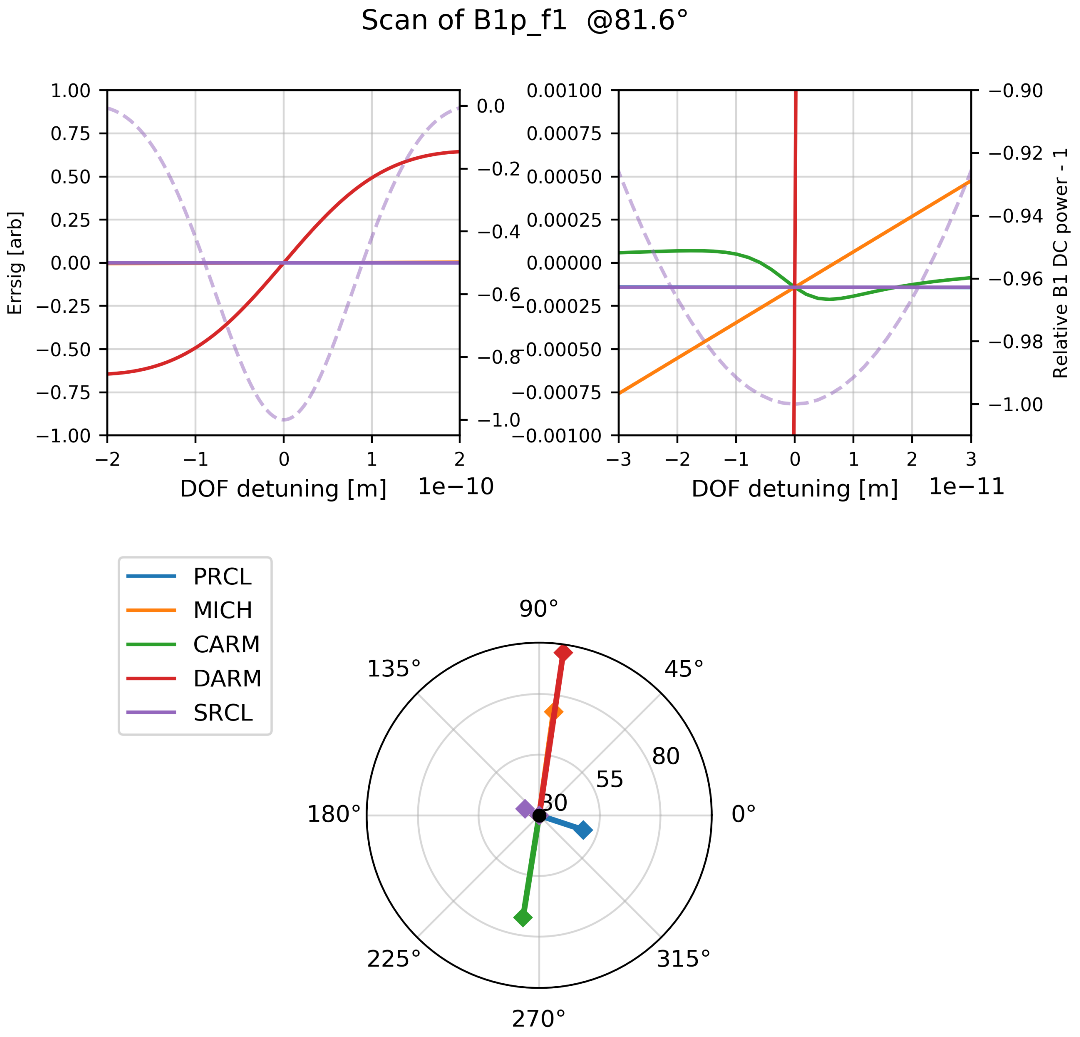

Figure B.2: B1p 6MHz error signal scan (with two different zoom levels) and compass plot, showing the dependence on the displacement of all the longitudinal DOFs, as explained in 4.4.2. This signal is a possible alternative to control the DARM DOF, which is indeed highly preeminent with respect to the other DOFs. The dashed purple line corresponds to the power at the B1 photodiode, showing the interferometer dark-fringe. Optical gain units in the compass plot are $\mathrm{dB}_{\mathrm{W/m}}$

B.2 CARM and SSFS: B2 6 MHz (I)

The SSFS loop controls different DOFs in different frequency bands: CARM, the Input Mode Cleaner IMC length, and the frequency of the main laser. Three different error signals are used by this loop, as explained in the note [72] and shown in figure B.3. These three error signals are acquired in the following systems:

- The IMC;
- The ReFerence Cavity (used when the main interferometer is not locked);
- **The main interferometer (studied in this document).**

Additionally, the RFC error signal can be used to stabilize the slow variations of CARM length with a low UGF (< 1 Hz) "CARM to RFC" loop.

Since this study focuses on the simulation of the main interferometer, we will consider only the choice and the behavior of the main interferometer error signal. This signal is used mainly in the control of the main laser frequency. However, for simplicity, the error signal has been studied against CARM displacement instead of laser frequency shift. This gives equivalent results due to the fact that the arm cavities have a much narrower linewidth with respect to other cavities considered in the simulations. Therefore, a small enough frequency variation has an equivalent effect as a CARM displacement.

An additional effect of the high finesse of the arm Fabry-Perot cavities is that most error signals acquired in the B4 and B2 ports show a much larger dependence on CARM displacement than on the displacement of any other DOF. Indeed, a small common displacement of the arm cavities or a small variation in the main laser frequency both cause a large phase shift in the carrier beam reflected by those cavities. This phase variation then heavily influences the carrier phase at the interferometer's B4 and B2 "symmetric" ports and, therefore, the PDH-like error signals. A wide variety of error signals can be therefore chosen for the control of CARM or the laser frequency, the best ones being the B2 or B4 beams demodulated at 6 or 56 MHz, as listed in table B.2. Both beams show a higher optical gain in the 6 MHz signals, shown in Figures B.4 and B.5, than in the 56 MHz ones. The highest relative optical gain and SNR is on the B2 6 MHz signal, which has been chosen as the primary error signal for the SSFS loop.

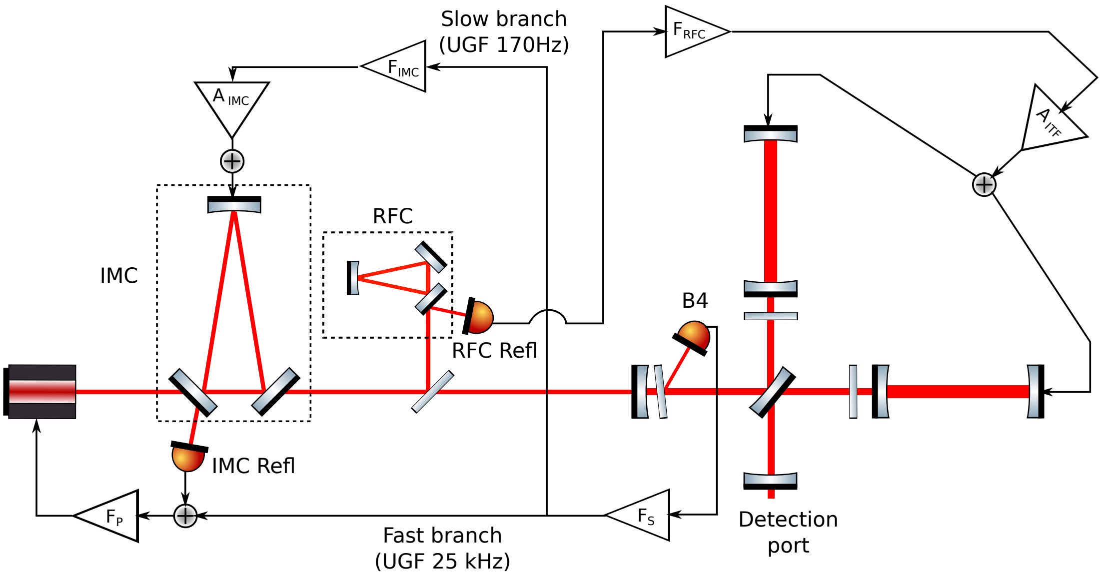

Figure B.3: Scheme of the SSFS loop, in this case, using B4 6 MHz as the primary error signal.

	B2 6 MHz	B4 6 MHz
Rel. OG [1/m]	1.0e+11	2.5e+10
Shot SNR [$1/(\mathrm{m}\sqrt{\mathrm{Hz}})$]	3.6e+18	2.0e+18
WP offset [m]	6.4e-15	8.8e-15
ΔWP [m]	2e-17	9e-17
Acc. Requirement* [m]	2e-13	

Table B.2: Overview of CARM/SSFS error signals' parameters. First row: relative-power optical-gain. Second row: expected shot noise SNR. Third row: signal working point offset WP at the optimal demodulation phase with respect to the WP found in the longitudinal pre-tune procedure explained in the "Length tunings" paragraph of section 4.1.1. Fourth row: working point shift ΔWP when a 10° offset is applied to the demodulation phase. Fifth row: accuracy requirement, taken from section 4.2. "*": Since this error signal is used mainly for the SSFS control, the displayed requirement is the CARM displacement corresponding to the SSFS frequency requirement, see section 5.2.

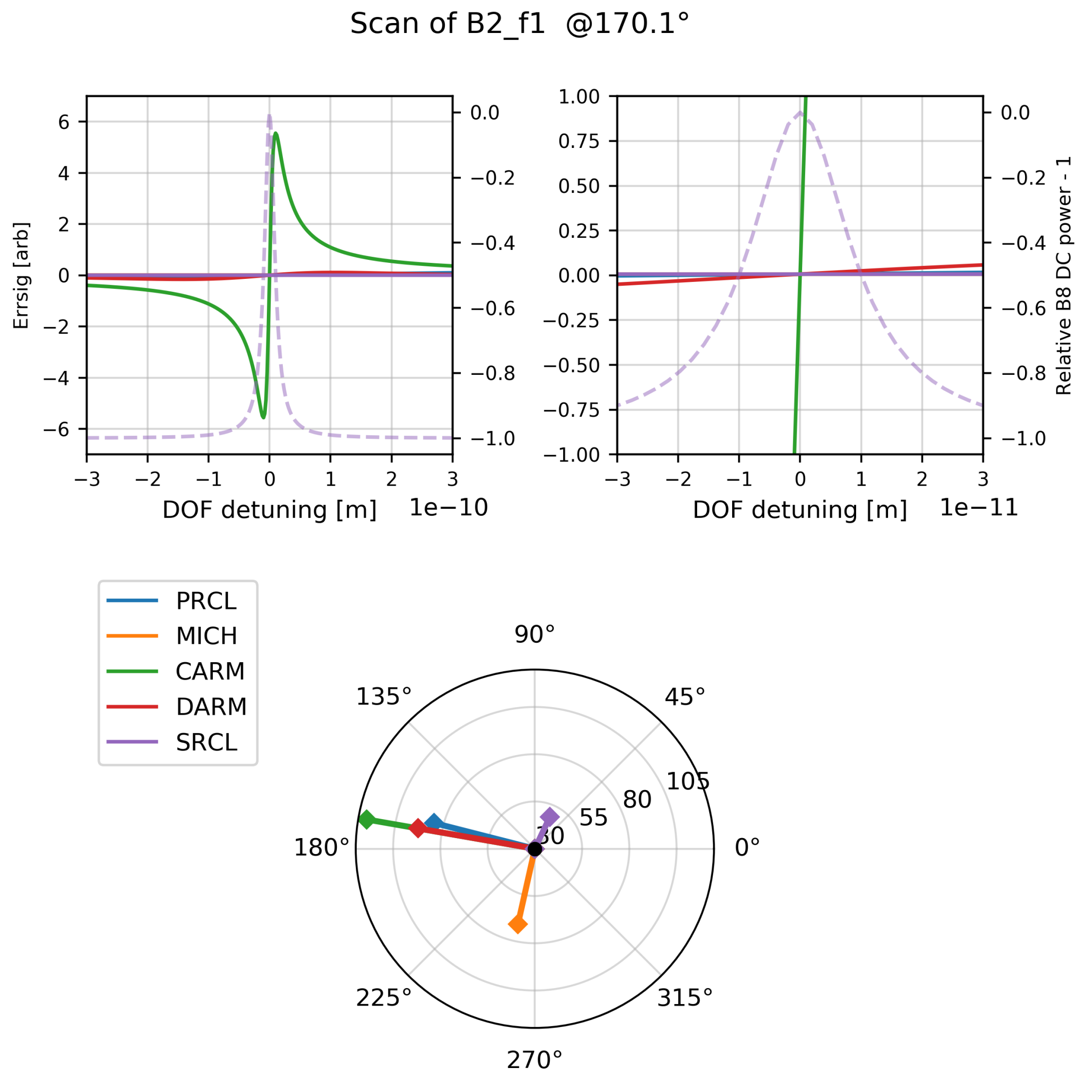

Figure B.4: B2 6 MHz error signal scan (with two different zoom levels) and compass plot, showing the dependence on the displacement of all the longitudinal DOFs, as explained in 4.4.2. This signal is meant to control the CARM DOF, which is highly preeminent with respect to the other DOFs. The dashed purple line corresponds to the power at the B8 photodiode, showing the arm cavity resonance. A quantitative comparison with the alternative signal B4 6 MHz (figure B.5) has to take into consideration the different powers shining on the two different B2 and B4 photodiodes. Optical gain units in the compass plot are $\mathrm{dB}_{\mathrm{W/m}}$

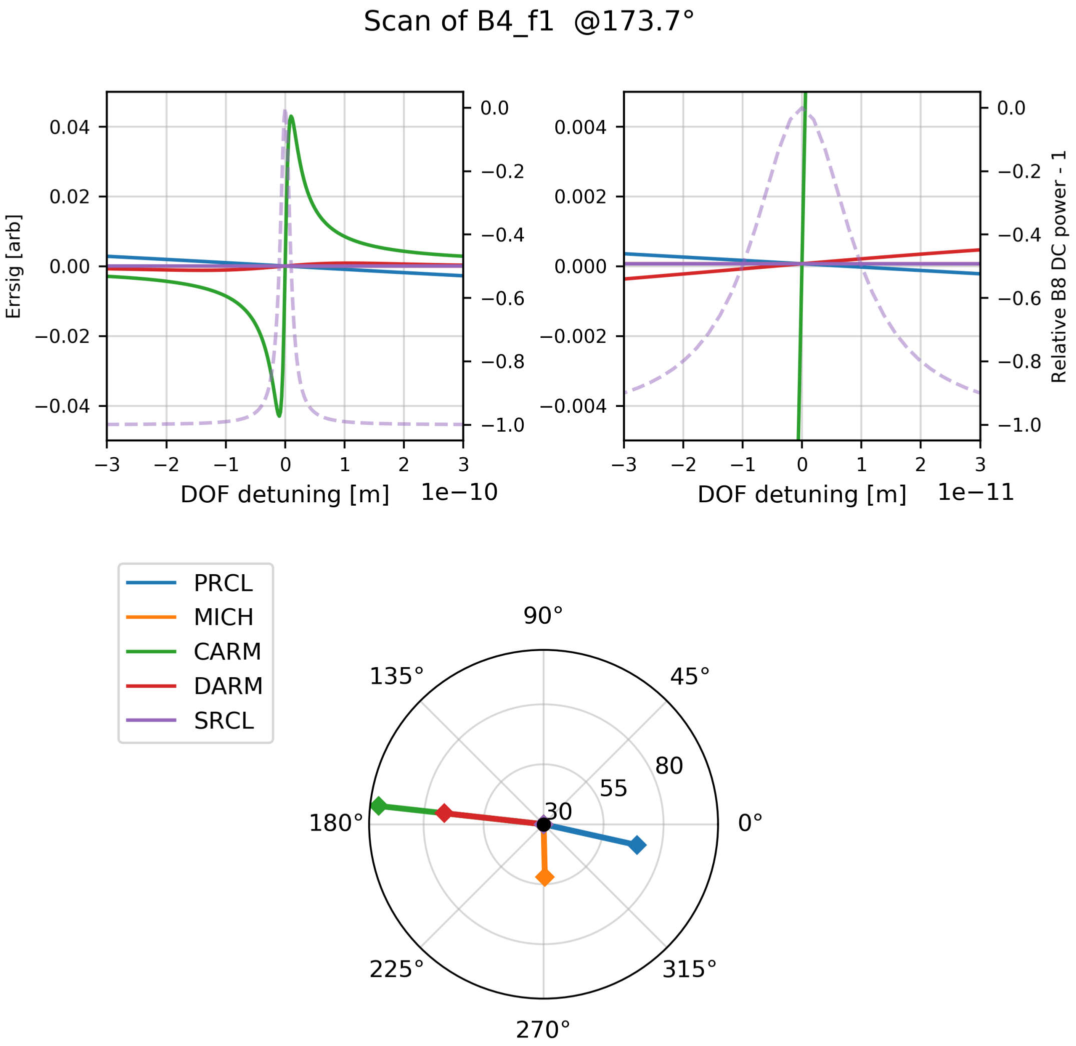

Figure B.5: B4 6 MHz error signal scan (with two different zoom levels) and compass plot, showing the dependence on the displacement of all the longitudinal DOFs, as explained in 4.4.2. This signal is an alternative signal to control the CARM DOF, which is highly preeminent with respect to the other DOFs. The dashed purple line corresponds to the power at the B8 photodiode, showing the arm cavity resonance. A quantitative comparison with the main signal B2 6 MHz (figure B.4) has to take into consideration the different powers shining on the two different B2 and B4 photodiodes. Optical gain units in the compass plot are $dB_{W/m}$

B.3 MICH: B2 56 MHz (Q)

The main signal chosen for the control of the MICH DOF is B2 demodulated at 56 MHz. B1p and B4 56 MHz error signals also show a clear dependence on the MICH displacement, but the first one is overshadowed by the DARM displacement, while B4 is a valid alternative, as shown in table B.3.

Demodulation phase noise: During the operation of the AdV detector in O3, the MICH DOF control has shown to be particularly sensitive to the effect phase noise in the demodulation chain [99]. This is due to the relatively low optical gain of the error signal, which makes it more vulnerable to noises and cross-coupling effects, also considering the strictness of its corresponding accuracy requirement. In order to minimize the effect of phase noise on the MICH error signal, the RMS of the residual noise in its quadrature has to be as low as possible. During the AdV operation, this was accomplished by controlling CARM and MICH using respectively the two quadratures of the same error signal (B4 56 MHz). With the addition of the SRCL cavity, a similar strategy can be used by controlling both SRCL and MICH using the two quadratures of B2 (or B4) 56 MHz.

DARM and PRCL displacement contribution to the MICH error signal: The sensing matrices 4.4 and 4.5 show a high optical gain of both B2 56 MHz Q and B4 56 MHz Q with the PRCL and DARM DOFs, compared to MICH.

However, figures B.7 and B.8 respectively show that DARM has an optimal demodulation phase that is almost 90° off with respect to the MICH optimal one and that the DARM contribution to these signals is actually extremely small and limited to a very small region.

A preliminary estimate of the contribution of PRCL to MICH has been made considering the PRCL displacement accuracy achieved during O3 $\Delta z_{\mathrm{PRCL}} = 8 \cdot 10^{-14}$ m [71]. One therefore obtains a PRCL contribution to MICH of:

$$\Delta z_{\mathrm{PRCL}\to\mathrm{MICH}} = \Delta z_{PRCL} \cdot \frac{OG_{\mathrm{PRCL}}}{OG_{\mathrm{MICH}}} = 3 \cdot 10^{-13} \text{ m} \tag{B.1}$$

The resulting PRCL contribution of $3 \cdot 10^{-13}$ m is well below the new MICH accuracy requirement of $3 \cdot 10^{-10}$ m, see section 4.2. However, we might still require subtracting this contribution to the error signal. The usage of the primary PRCL error signal B2 8 MHz in the subtraction will be avoided to prevent issues generated by the usage of the same PRCL error signal in two different coupled control loops. Therefore, alternative signals have been evaluated, with a focus on the 6 MHz signals, since they are not affected by the SRCL displacement. Simulations showed B4 6 MHz to be the best signal for this purpose, as long as it is not used by the CARM-SSFS loop. The effect of this subtraction on the MICH error signal can be observed in figure B.6.

	B2 56 MHz Q	B4 56 MHz Q
Rel. OG [1/m]	6.0e+06	2.2e+06
Shot SNR $[1/(\mathrm{m}\sqrt{\mathrm{Hz}})]$	2.2e+15	1.8e+15
WP offset [m]	1.6e-11	1.6e-11
Δ WP [m]	3.1e-11	3.1e-11
Acc. Requirement [m]	3e-10	

Table B.3: Overview of MICH error signals' parameters. First row: relative-power optical-gain. Second row: expected shot noise SNR. Third row: signal working point offset WP at the optimal demodulation phase with respect to the WP found in the longitudinal pre-tune procedure explained in the "Length tunings" paragraph of section 4.1.1. Fourth row: working point shift ΔWP when a 10° offset is applied to the demodulation phase. Fifth row: accuracy requirement, taken from section 4.2.

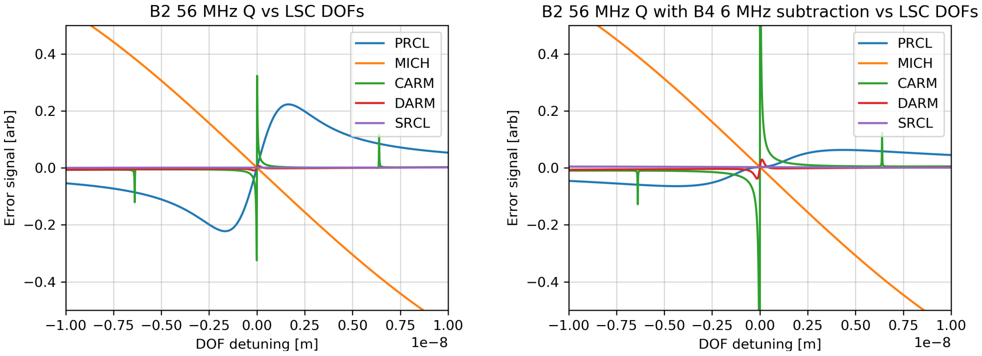

(a) No subtraction (b) With subtraction

Figure B.6: Primary MICH error signal with (right) vs. without (left) subtraction of PRCL contribution. Note that the increase in the CARM contribution is not an issue when SSFS is enabled due to the hierarchical control strategy mentioned in section 4.4.3.

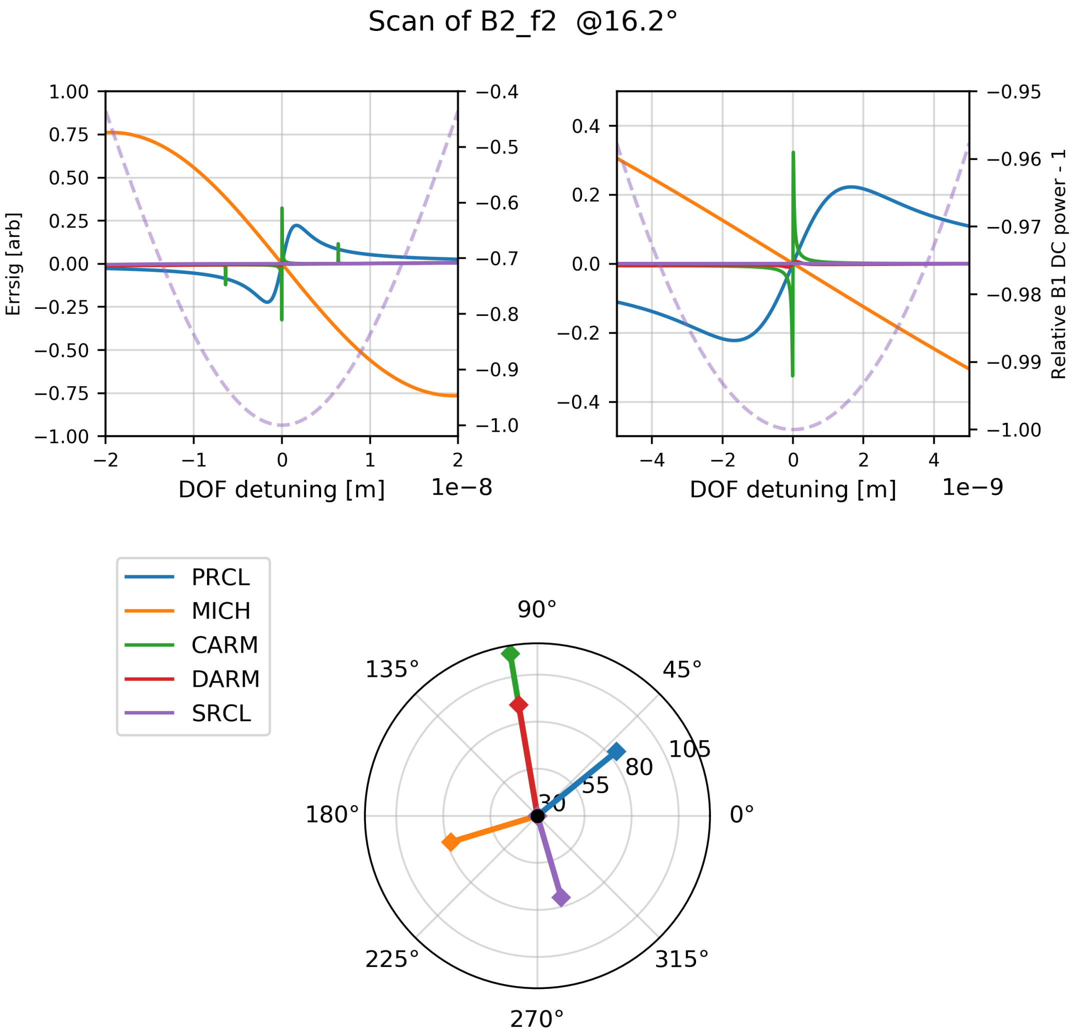

Figure B.7: B2 56 MHz Q error signal scan (with two different zoom levels) and compass plot, showing the dependence on the displacement of all the longitudinal DOFs, as explained in 4.4.2. This signal is meant to control the MICH DOF. The dashed purple line corresponds to the power at the B1 photodiode, showing the interferometer dark-fringe. Note that the PRCL displacement gives a non-negligible contribution. The DARM contribution, despite the high optical gain shown in the sensing matrix, gives a negligible contribution and is limited to a very small region compared to MICH. A quantitative comparison with the alternative signal B4 56 MHz Q (figure B.8) has to take into consideration the different powers shining on the two different B2 and B4 photodiodes. Optical gain units in the compass plot are $\mathrm{dB_{W/m}}$

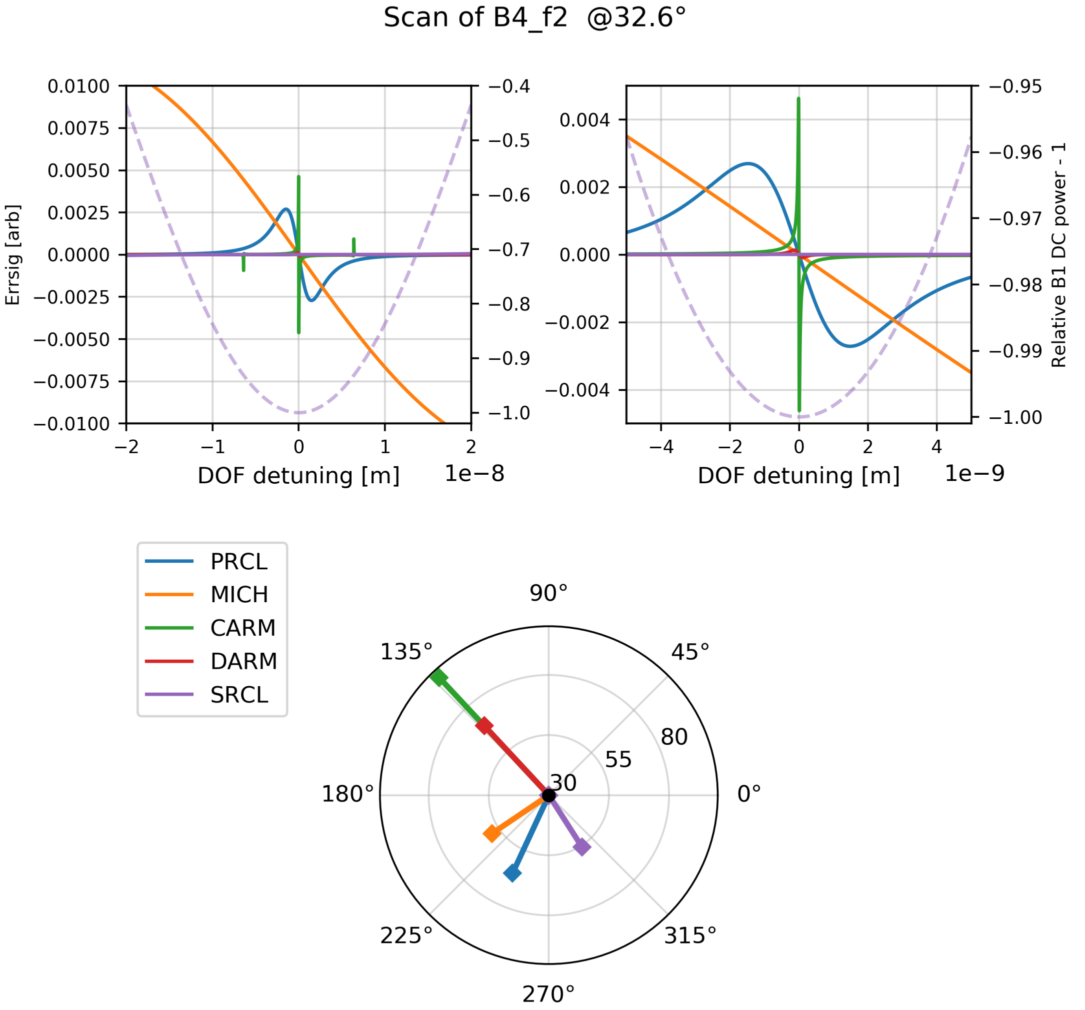

Figure B.8: B4 56 MHz Q error signal scan (with two different zoom levels) and compass plot, showing the dependence on the displacement of all the longitudinal DOFs, as explained in 4.4.2. This signal is an alternative for the control of MICH. The dashed purple line corresponds to the power at the B1 photodiode, showing the interferometer dark-fringe. Note that the PRCL displacement gives a non-negligible contribution. The DARM contribution, despite the high optical gain shown in the sensing matrix, gives a negligible contribution and is limited to a very small region compared to MICH. A quantitative comparison with the main signal B2 56 MHz Q (figure B.7) has to take into consideration the different powers shining on the two different B2 and B4 photodiodes. Optical gain units in the compass plot are $\mathrm{dB}_{\mathrm{W/m}}$

B.4 PRCL: B2 8 MHz

The 8 MHz sideband is reflected by the Power Recycling cavity and minimally influenced by the motion of other DOFs. Once the SSFS is locked and the phase of the carrier reflected by the input mirrors is therefore stable, the B2 signal demodulated at 8 MHz is the best error signal for the control of the PRCL cavity. The alternative signal B4 6 MHz listed in table B.4 is necessary for the subtraction of the PRCL contribution to the MICH error signal, as noted in the previous subsection B.3.

DARM displacement contribution to the PRCL error signal: The high optical gain shown in table 4.4 of B2 8 MHz with respect to displacements of the DARM DOF is misleading information. Indeed, as seen in figure B.9, the dependence of this error signal on DARM is extremely low except for a very small region, therefore not hampering the control of the PRCL DOF.

	B2 8 MHz	B4 6 MHz
Rel. OG [1/m]	2.7e+08	3.0e+07
Shot SNR [$1/(\mathrm{m}\sqrt{\mathrm{Hz}})$]	8.3e+16	1.8e+16
WP offset [m]	2.3e-13	7.5e-12
Δ WP [m]	1e-17	7.8e-14
Acc. Requirement [m]	5e-11	

Table B.4: Overview of PRCL error signals' parameters. First row: relative-power optical-gain. Second row: expected shot noise SNR. Third row: signal working point offset WP at the optimal demodulation phase with respect to the WP found in the longitudinal pre-tune procedure explained in the "Length tunings" paragraph of section 4.1.1. Fourth row: working point shift ΔWP when a 10° offset is applied to the demodulation phase. Fifth row: accuracy requirement, taken from section 4.2. The second signal, B4 6 MHz, is meant to be used for subtraction purposes only and is not planned to be used for the control of PRCL.

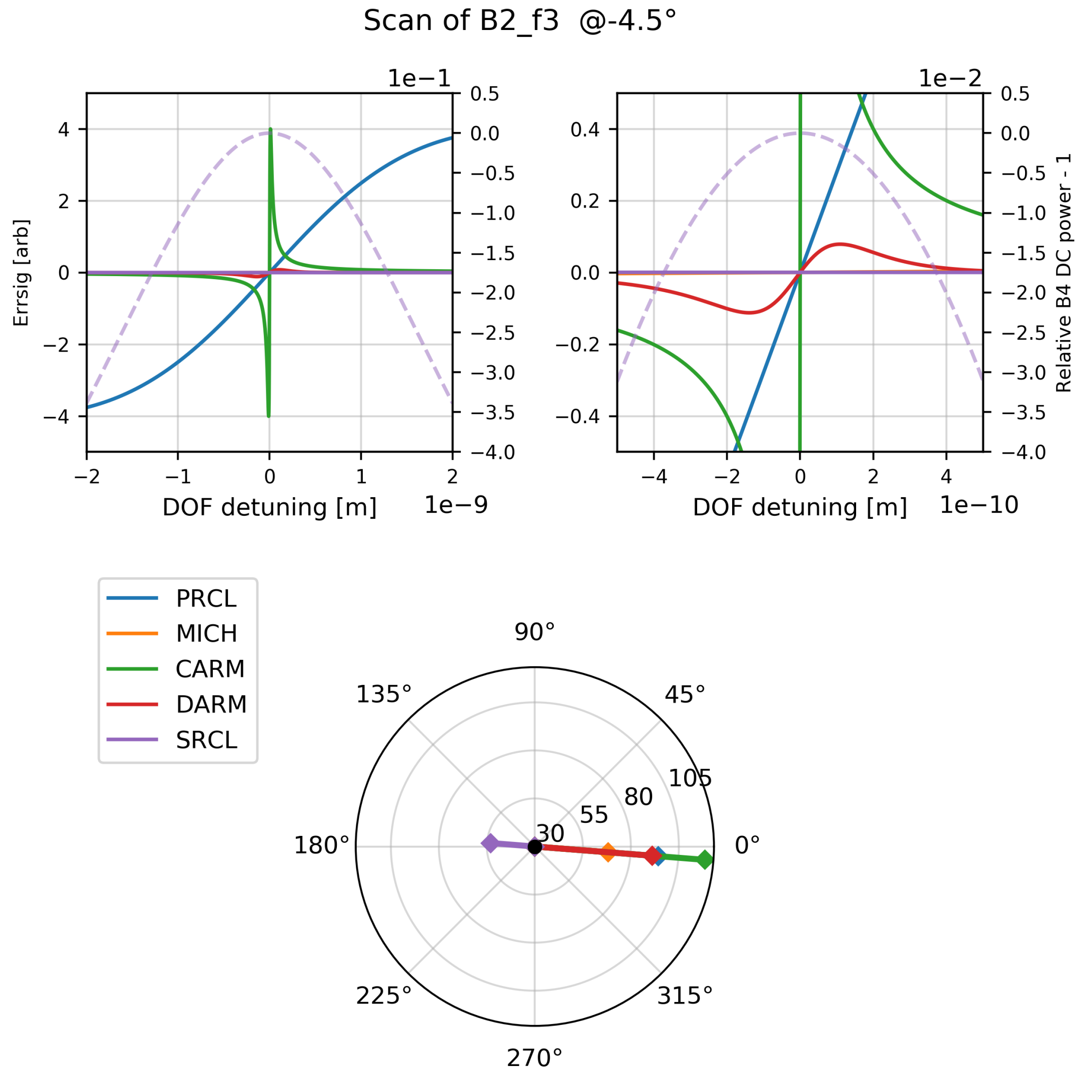

Figure B.9: B2 8 MHz error signal scan (with two different zoom levels) and compass plot, showing the dependence on the displacement of all the longitudinal DOFs, as explained in 4.4.2. This signal is the main choice to control the PRCL DOF. The dashed purple line corresponds to the power at the B4 photodiode, showing the resonance of the PRCL cavity. Note that the DARM contribution, despite the high optical gain shown in the sensing matrix, is limited to a very small region and negligible with respect to the contribution of the PRCL displacement. Optical gain units in the compass plot are $\mathrm{dB}_{\mathrm{W/m}}$

B.5 SRCL: B2 56 MHz (I)

The primary error signal chosen for the control of SRCL is B2 56 MHz I. B4 56 MHz I shows a very similar behavior and has been chosen as an alternative error signal in the eventuality of issues in the usage of B2 signals. As shown in table B.5 and comparing figures B.10 and B.11, B2 56 MHz shows a higher relative-power optical gain and a lower coupling with PRCL.

Analogously to MICH, the low finesse of the Signal Recycling cavities results in low optical-gain error signals when compared to the other LSC DOFs. This makes its error signals vulnerable to coupling with the displacement of other DOFs. Indeed, B2 56 MHz I shows higher optical gains for DARM and PRCL than for the displacement of SRCL, as shown in the sensing matrix 4.4. This is also true for B4 56 MHz I, shown in the alternative sensing matrix 4.5 instead.

PRCL and DARM displacement contributions to the SRCL error signals: The possibility of reducing the contribution of PRCL to the SRCL error signal has been studied, and the simulations resulted in a suppression of a factor over 50 of the PRCL displacement contribution to the SRCL error signal. However, the following reasons make the subtraction of the PRCL contribution to MICH a priority with respect to the subtraction to SRCL:

- Figure B.10 shows that, in the B2 56 MHz signal, the total contributions of both DARM and PRCL are limited in regions respectively of $\simeq 10^{-10}$ m and $\simeq 5 \cdot 10^{-10}$ m around the working point. The SRCL contribution instead is linear in a region larger than 10^{-7} m. There are, therefore, no concerns about the possibility of locking the Signal Recycling cavities, even in phases when the DARM and PRCL loops are not optimally operative (i.e., in dark fringe configuration).

- The influence of DARM and PRCL residual motion can be again estimated by "projecting" the DARM and PRCL residual motions to obtain the corresponding SRCL displacement, using as reference the residual motion values of the PRFPMI configuration measured during O3 [71] $\Delta z_{\text{DARM}} = 3 \cdot 10^{-16}$ m and $\Delta z_{\text{PRCL}} = 8 \cdot 10^{-14}$ m. As seen in equations B.2 and B.3, the resulting contributions are much smaller than the SRCL accuracy requirement of $2 \cdot 10^{-9}$ m (see 4.2).

$$\Delta z_{\text{PRCL}\rightarrow\text{SRCL}} = \Delta z_{\text{PRCL}} \cdot \frac{OG_{\text{PRCL}}}{OG_{\text{SRCL}}} = 2.5 \cdot 10^{-13}\ \text{m} \tag{B.2}$$

$$\Delta z_{\text{DARM}\rightarrow\text{SRCL}} = \Delta z_{\text{DARM}} \cdot \frac{OG_{\text{DARM}}}{OG_{\text{SRCL}}} = 9 \cdot 10^{-15}\ \text{m} \tag{B.3}$$

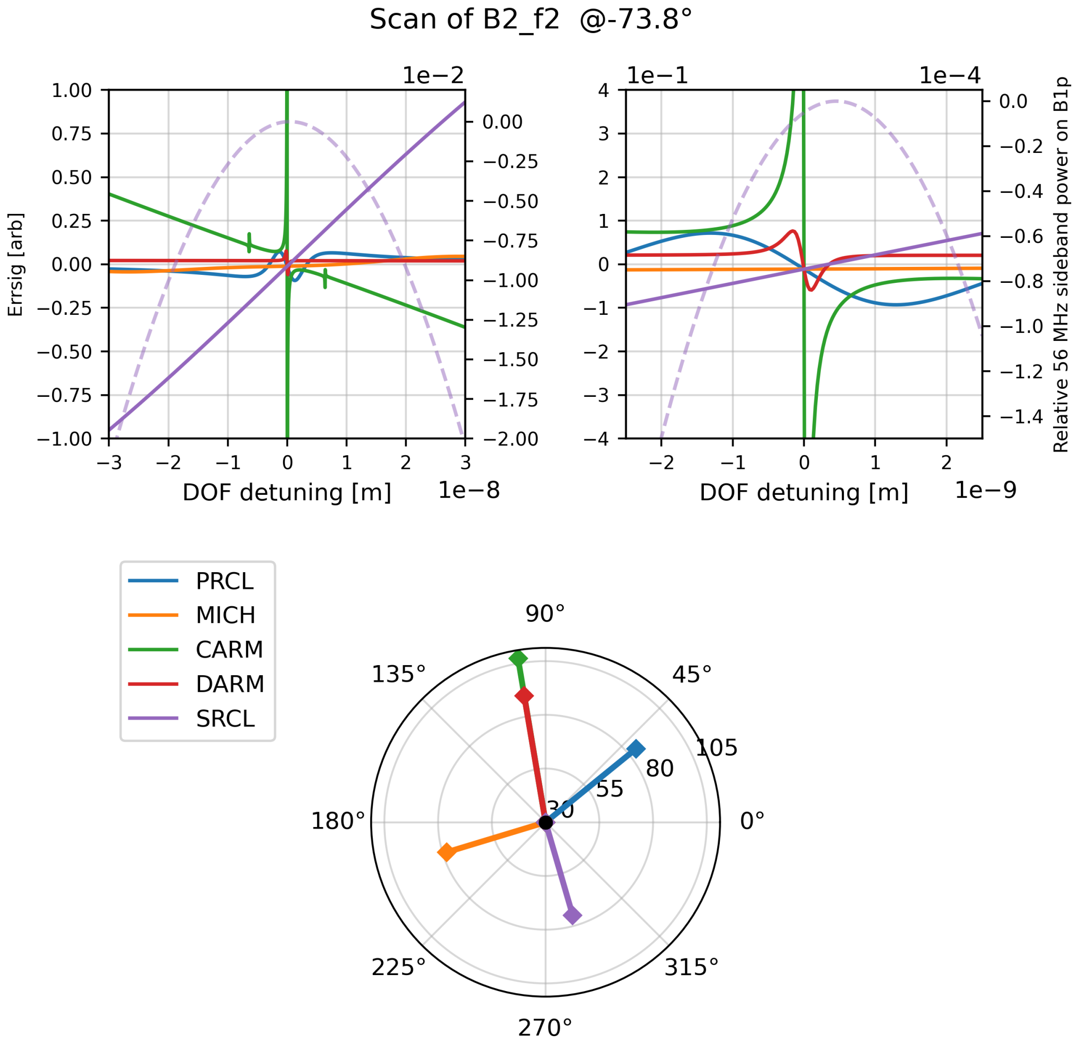

Figure B.10: B2 56 MHz I error signal scan (with two different zoom levels) and compass plot, showing the dependence on the displacement of all the longitudinal DOFs, as explained in 4.4.2. This signal is the main choice to control the SRCL DOF. The dashed purple line corresponds to the power of the 56 MHz sideband at the B1p photodiode, showing its resonance in the SRCL cavity. Note that while the PRCL displacement gives a non-negligible contribution to the error signal, it is much smaller than the one in the quadrature signal used for MICH B.7. Note also that the alternative signal B4 56 MHz I (figure B.11) is more affected by PRCL displacement. Despite the high optical gain shown in the sensing matrix, the DARM contribution is negligible and is limited to a very small region compared to SRCL. However, a quantitative comparison with this signal has to take into consideration the different powers shining onto the two different B2 and B4 photodiodes. Optical gain units in the compass plot are $\mathrm{dB}_{\mathrm{W/m}}$

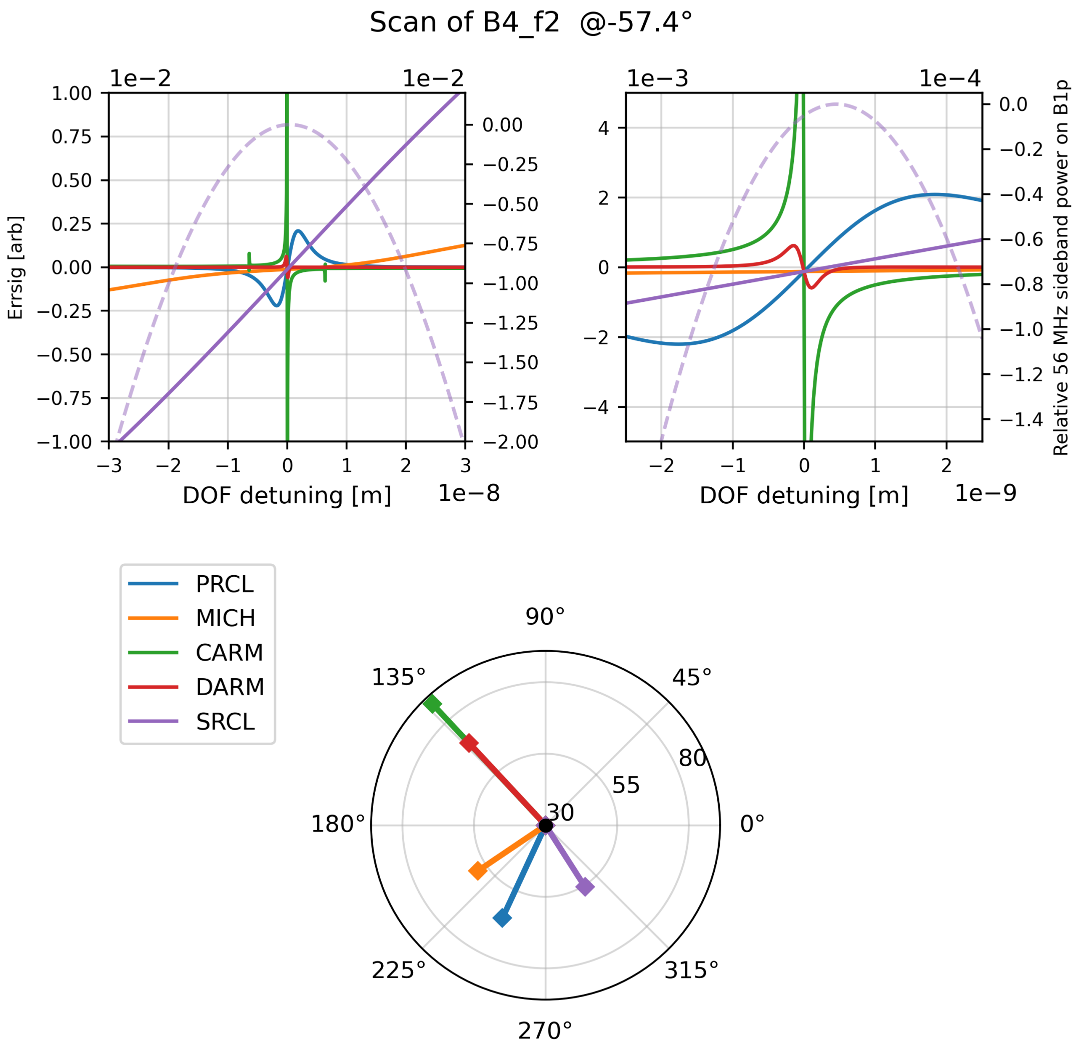

Figure B.11: B2 56 MHz I error signal scan (with two different zoom levels) and compass plot, showing the dependence on the displacement of all the longitudinal DOFs, as explained in 4.4.2. This signal is the main choice to control the SRCL DOF. The dashed purple line corresponds to the power of the 56 MHz sideband at the B1p photodiode, showing its resonance in the SRCL cavity. Note that while the PRCL displacement gives a non-negligible contribution, it is much smaller than the one given in the quadrature signal used for MICH B.8. The DARM contribution, despite the high optical gain shown in the sensing matrix, gives a negligible contribution and is limited to a very small region compared to SRCL. However, a quantitative comparison with this signal has to take into consideration the different powers shining onto the two different B2 and B4 photodiodes. Optical gain units in the compass plot are dB$_{\mathrm{W/m}}$

	B2 56 MHz I	B4 56 MHz I
Rel. OG [1/m]	3.1e+06	1.1e+06
Shot SNR $[1/(\mathrm{m}\sqrt{\mathrm{Hz}})]$	1.2e+15	9.4e+14
WP offset [m]	3.4e-10	3.3e-10
Δ WP [m]	5e-12	3.9e-12
Acc. Requirement [m]	2e-9	

Table B.5: Overview of SRCL error signals' parameters. First row: relative-power optical-gain. Second row: expected shot noise SNR. Third row: signal working point offset WP at the optimal demodulation phase with respect to the WP found in the longitudinal pre-tune procedure explained in the "Length tunings" paragraph of section 4.1.1. Fourth row: working point shift ΔWP when a 10° offset is applied to the demodulation phase. Fifth row: accuracy requirement, taken from section 4.2.

Acronyms

AA Automatic Alignment. 75

AdVGWINC Advanced Virgo GW Interferometer Noise Calculator. 25

ALS Auxiliary Laser System. 50, 52, 55–61, 66–73, 76, 78, 103, 104, 108, 109, 117, 122, 123, 126

AOM Acousto-Optic Modulator. 31, 56, 59

ASC Angular Sensing and Control. 36, 43, 46, 49, 54

ASD Amplitude Spectral Density. 6, 13, 24, 27, 29, 39, 40, 42, 65, 87–89, 100

BBH Binary Black Hole. 6, 7, 28

BH Black Hole. 5

BIBO Bound-Input-Bound-Output. 41

BNS Binary Neutron Star. 6, 7, 27–29

BPC Beam Pointing Control. 46, 53

BS Beam-Splitter. 8, 45, 48, 62, 87

CARM Common ARM length. 9, 47, 48, 52, 58, 60, 61, 64, 66–78, 83, 84, 86, 94, 97–100, 103–105, 108, 110, 115, 117, 122, 123, 125, 126, 150, 153–158

CBC Compact Binary Cohalescence. 3, 5, 6

CITF Central InTerFerometer. 50–52, 55, 57, 60–66, 69, 72, 74, 75, 103, 105, 108, 110, 125–130, 132–138, 142–148

CLTF Closed-Loop Transfer Function. 40

CP Compensation Plate. 45, 47

DARM Differential ARM length. 9–11, 36, 47, 52, 58, 60, 67–69, 72, 73, 75, 81–83, 85–87, 89–94, 97–101, 104, 106–110, 115–119, 126, 149–152, 157, 159–165

DC Direct Current (usually meant to indicate the constant component of a signal, as opposed to the high frequency components). 13, 32, 46, 52, 55, 62, 66, 70, 71, 75, 76, 78, 81, 85, 95, 104, 106, 108, 109, 115, 123, 150

DOF Degree Of Freedom. 20, 21, 31, 35, 36, 40, 43, 47–51, 61, 64, 68, 75, 79–83, 85–89, 91–100, 103–106, 109–113, 115–119, 121, 125–129, 131, 139, 142–153, 155–157, 159–165

DRFPMI Dual-Recycled Fabry-Perot Michelson Interferometer. 7, 43–45, 50, 80, 103, 123

DRMI Dual-Recycled Michelson Interferometer. 19, 21, 50, 60, 61, 72, 78, 103, 122, 125, 131

EM ElectroMagnetic. 5, 8, 13, 14, 23

EOM Electro-Optic-Modulator. 31, 32, 45, 46, 49, 53, 95

FDS Frequency-Dependent Squeezing. 24, 27, 28, 75

FP Fabry-Perot. 14–17, 20, 31–34, 37, 38, 50–52, 54, 55, 57, 59, 64, 66, 83, 103–105, 122

FSR Free Spectral Range. 15, 35, 37, 38, 47, 59, 60

FWHM Full-Width-Half-Maximum. 16, 17, 31, 35, 83, 84

GM Gain Margin. 41

GW Gravitational Wave. 3–9, 11, 13, 14, 16, 17, 19–22, 24, 25, 27, 30–32, 36, 39, 40, 46, 50, 75–77, 149

HOM Higher Order Mode. 60, 80, 101, 111, 113, 126

HR High Reflectivity. 81

IMC Input Mode Cleaner. 45, 46, 49, 53, 54, 70, 71, 74, 76, 77, 105, 153

IR InfraRed. 55, 57–60, 66–74, 78, 103–105, 122, 126

ISC Interferometer Sensing and Control. 49, 50, 77, 80, 122

KAGRA Kamioka Gravitational Wave Detector. 7, 26, 27, 29

LIGO Laser Interferometer Gravitational-Wave Observator. 7, 20–22, 26–28, 50, 55, 68, 103

LSC Longitudinal Sensing and Control. 36, 43, 44, 46–49, 54, 68, 74, 79, 86, 87, 89, 91, 94, 97, 99–101, 107, 110–112, 114–118, 120, 121, 126, 128, 149, 163

LTI Linear-Time-Invariant. 36, 39, 41

LVDT Linear Variable Differential Transducers. 30

LVK LIGO-Virgo-KAGRA. 26

MICH small MICHelson length. 48, 61, 65, 74, 81–83, 86, 90–94, 97–101, 103, 104, 106, 107, 115, 116, 118, 130, 131, 142, 150, 157–161, 163–165

MIMO Multiple-Input-Multiple-Output. 36, 39, 120

Nd:YAG Neodymium-doped Yttrium Aluminum Garnet. 44

NE North End. 45, 48

NI North Input. 45, 48, 62, 63, 82, 87, 126–128, 130–132, 134, 137, 139–142, 144, 147

NPRO Non-Planar Ring Oscillator. 44

NS Neutron Star. 5, 6

NSBH Neutron-Star-Black-Hole. 6, 7

OG Optical Gain. 63, 83, 115, 118, 131, 132, 142–148, 150, 154, 158, 161, 166

OLTF Open-Loop Transfer Function. 40–42, 87–89

OMC Output Mode Cleaner. 45, 46, 52, 75, 76, 81–84, 94, 109, 150

PD PhotoDiode. 33

PDH Pound-Drever-Hall. 30, 31, 41, 153

PLL Phase-Locked Loop. 55, 56

PM Phase Margin. 41

PMC Pre Mode Cleaner. 44, 46, 53

POP Pick-Off-Plate. 45–47, 94

PR Power Recycling. 17, 19, 20, 22, 45, 47–49, 51, 54, 57, 61–63, 69, 72, 75, 81–84, 87, 101–107, 114, 120–122, 125–127, 130–133, 136, 139–143, 146

PRC Power Recycling Cavity. 19, 20, 46

PRCL Power Recycling Cavity Length. 47, 48, 51, 61, 62, 65, 72, 74, 80, 83, 84, 86, 87, 90, 91, 93, 94, 97–100, 103, 105, 106, 115, 130, 131, 142, 157–165

PRFPMI Power-Recycled Fabry-Perot Michelson Interferometer. 19, 22, 79, 80, 83, 103, 108, 163

PRITF Power Recycled InTerFerometer. 94, 97

PRMI Power-Recycled Michelson Interferometer. 21, 120, 125

PSD Power Spectral Density. 11, 12

PSTAB Power STABilization. 53

QNR Quantum Noise Reduction. 45, 46, 54

RAM Residual Amplitude Modulation. 100

RF Radio Frequency. 23, 33, 67, 69, 72–77, 101, 104, 105, 150

RFC ReFerence Cavity. 45, 46, 53, 54, 58, 60, 70, 75, 77, 153

RMS Root Mean Square. 42, 65, 79, 80, 82, 157

ROC Radius Of Curvature. 81

RT Round Trip. 81, 82

SHG Second Harmonic Generation. 55, 56

SISO Single-Input-Single-Output. 36, 39, 47

SNR Signal-to-Noise-Ratio. 6, 11, 16, 36, 42, 75, 97, 101, 130, 139, 150, 153, 154, 158, 161, 166

SR Signal Recycling. 17, 19–21, 27, 36, 45, 47–49, 54, 57, 61–63, 79–83, 85, 87, 100, 102–121, 125–127, 129–132, 135, 138–141, 145, 148, 150

SRC Signal Recycling Cavity. 19, 119

SRCL Signal Recycling Cavity Length. 47, 48, 61, 65, 74, 80, 81, 83, 85–87, 91, 93, 94, 97–101, 103, 108, 110–113, 115–118, 120, 121, 131, 142, 157, 163–166

SRM Signal Recycling Mirror. 85

SSFS Second Stage Frequency Stabilization. 44, 47, 48, 52, 74, 76, 77, 83, 84, 86, 93, 97, 101, 105, 106, 108, 153, 154, 157, 158, 161

TCS Thermal Compensation System. 43, 47, 54, 75, 82, 120

TEM Transverse ElectroMagnetic. 46, 61, 75, 120, 126

TF Transfer Function. 12, 85, 90, 101, 116

TT Transverse-Traceless. 4

TWF Twin Variable Finesse. 103–106, 108–111, 116, 120

UGF Unity Gain Frequency. 41, 42, 74, 90, 94, 115, 116, 130, 142, 153

VCO Voltage-Controlled Oscillator. 56

WE West End. 45, 48

WI West Input. 45, 48, 82, 87

WP Working Point. 67, 112, 113, 127–129, 150, 154, 158, 161, 166

Bibliography

[1] K. Izumi. "LIGO-P1300001-v1: [Thesis] Multi-Color Interferometry for Lock Acquisition of Laser Interferometric Gravitational-wave Detectors". University of Tokyo. URL: https://dcc.ligo.org/cgi-bin/DocDB/ShowDocument?.submit=Identifier&docid=P1300001&version=.

[2] Bernard Schutz. *A First Course in General Relativity*. 2nd ed. Cambridge: Cambridge University Press, 2009. ISBN: 978-0-521-88705-2. DOI: 10.1017/CBO9780511984181. URL: https://www.cambridge.org/core/books/first-course-in-general-relativity/3805425203DD91A7436EF6E5F2082263.

[3] Eric Poisson and Clifford M. Will. "Gravitational Waves". In: *Gravity: Newtonian, Post-Newtonian, Relativistic*. Cambridge: Cambridge University Press, 2014, pp. 539–623. ISBN: 978-1-107-03286-6. DOI: 10.1017/CBO9781139507486.012. URL: https://www.cambridge.org/core/books/gravity/gravitational-waves/EC73A20ACAF26AC876A1D2AF2ADB0814.

[4] The LIGO Scientific Collaboration et al. *GWTC-2.1: Deep Extended Catalog of Compact Binary Coalescences Observed by LIGO and Virgo During the First Half of the Third Observing Run*. May 10, 2022. DOI: 10.48550/arXiv.2108.01045. arXiv: 2108.01045 [gr-qc]. URL: http://arxiv.org/abs/2108.01045.

[5] The LIGO Scientific Collaboration et al. "GWTC-3: Compact Binary Coalescences Observed by LIGO and Virgo During the Second Part of the Third Observing Run". Nov. 17, 2021. URL: http://arxiv.org/abs/2111.03606.

[6] Shasvath J. Kapadia et al. "A Self-Consistent Method to Estimate the Rate of Compact Binary Coalescences with a Poisson Mixture Model". In: *Classical and Quantum Gravity* 37.4 (Jan. 2020), p. 045007. ISSN: 0264-9381. DOI: 10.1088/1361-6382/ab5f2d. URL: https://doi.org/10.1088/1361-6382/ab5f2d.

[7] B. P. Abbott et al. "GWTC-1: A Gravitational-Wave Transient Catalog of Compact Binary Mergers Observed by LIGO and Virgo during the First and Second Observing Runs". In: *Phys. Rev. X* 9.3 (Sept. 2019), p. 031040. DOI: 10.1103/PhysRevX.9.031040. URL: https://link.aps.org/doi/10.1103/PhysRevX.9.031040.

[8] R. Abbott et al. "Observation of Gravitational Waves from Two Neutron Star–Black Hole Coalescences". In: *The Astrophysical Journal Letters* 915.1 (July 1, 2021), p. L5. ISSN: 2041-8205, 2041-8213. DOI: 10.3847/2041-8213/ac082e. URL: https://iopscience.iop.org/article/10.3847/2041-8213/ac082e.

[9] B. P. Abbott et al. “GW190425: Observation of a Compact Binary Coalescence with Total Mass $\sim 3.4\ M_{\odot}$”. In: *The Astrophysical Journal Letters* 892.1 (Mar. 20, 2020), p. L3. ISSN: 2041-8205, 2041-8213. DOI: 10.3847/2041-8213/ab75f5. URL: https://iopscience.iop.org/article/10.3847/2041-8213/ab75f5.

[10] B. P. Abbott et al. “Prospects for Observing and Localizing Gravitational-Wave Transients with Advanced LIGO, Advanced Virgo and KAGRA”. In: *Living Reviews in Relativity* 23.1 (Dec. 2020), p. 3. ISSN: 2367-3613, 1433-8351. DOI: 10.1007/s41114-020-00026-9. URL: https://link.springer.com/10.1007/s41114-020-00026-9.

[11] Hsin-Yu Chen et al. “Distance Measures in Gravitational-Wave Astrophysics and Cosmology”. In: *Classical and Quantum Gravity* 38.5 (Jan. 2021), p. 055010. ISSN: 0264-9381. DOI: 10.1088/1361-6382/abd594. URL: https://doi.org/10.1088/1361-6382/abd594.

[12] B. P. Abbott et al. “Characterization of Transient Noise in Advanced LIGO Relevant to Gravitational Wave Signal GW150914”. In: *Classical and Quantum Gravity* 33.13 (June 6, 2016), p. 134001. ISSN: 0264-9381. DOI: 10.1088/0264-9381/33/13/134001. URL: https://iopscience.iop.org/article/10.1088/0264-9381/33/13/134001/meta.

[13] J. Vinet. “The Virgo Physics Book Vol. II”. May 19, 2005. URL: https://tds.virgo-gw.eu/ql/?c=6361.

[14] S. Hild et al. “DC-readout of a Signal-Recycled Gravitational Wave Detector”. In: *Classical and Quantum Gravity* 26.5 (Feb. 2009), p. 055012. ISSN: 0264-9381. DOI: 10.1088/0264-9381/26/5/055012. URL: https://doi.org/10.1088/0264-9381/26/5/055012.

[15] Julia Casanueva Diaz. “Control of the Gravitational Wave Interferometric Detector Advanced Virgo”. Cham: Springer International Publishing, Oct. 27, 2017. DOI: 10.1007/978-3-319-96014-2. URL: http://link.springer.com/10.1007/978-3-319-96014-2.

[16] The Virgo Collaboration. *Advanced Virgo Technical Design Report.* 2012. URL: https://tds.virgo-gw.eu/ql/?c=8940.

[17] The Virgo collaboration. *AdVgwinc · GitLab.* URL: https://git.ligo.org/virgo/virgoapp/advgwinc.

[18] LIGO Scientific Collaboration and Virgo Collaboration et al. “Observation of Gravitational Waves from a Binary Black Hole Merger”. In: *Physical Review Letters* 116.6 (Feb. 11, 2016), p. 061102. DOI: 10.1103/PhysRevLett.116.061102. URL: https://link.aps.org/doi/10.1103/PhysRevLett.116.061102.

[19] J. Weber. “Observation of the Thermal Fluctuations of a Gravitational-Wave Detector”. In: *Physical Review Letters* 17.24 (Dec. 12, 1966), pp. 1228–1230. DOI: 10.1103/PhysRevLett.17.1228. URL: https://link.aps.org/doi/10.1103/PhysRevLett.17.1228.

[20] L. Baggio et al. “Resonant Detectors for Gravitational Waves”. In: *Advances in Space Research*. Fundamental Physics in Space 25.6 (Jan. 1, 2000), pp. 1171–1176. ISSN: 0273-1177. DOI: 10.1016/S0273-1177(99)00981-3. URL: https://www.sciencedirect.com/science/article/pii/S0273117799009813.

[21] Robert L. Forward. “Wideband Laser-Interferometer Graviational-Radiation Experiment”. In: *Physical Review D* 17.2 (Jan. 15, 1978), pp. 379–390. DOI: `10.1103/PhysRevD.17.379`. URL: `https://link.aps.org/doi/10.1103/PhysRevD.17.379`.

[22] T Akutsu et al. “Overview of KAGRA: Detector Design and Construction History”. In: *Progress of Theoretical and Experimental Physics* 2021.5 (May 1, 2021), 05A101. ISSN: 2050-3911. DOI: `10.1093/ptep/ptaa125`. URL: `https://doi.org/10.1093/ptep/ptaa125`.

[23] The Virgo Collaboration. *Advanced Virgo Plus Phase I - Design Report*. 2019. URL: `https://tds.virgo-gw.eu/ql/?c=14430`.

[24] Craig Cahillane and Georgia Mansell. “Review of the Advanced LIGO Gravitational Wave Observatories Leading to Observing Run Four”. In: *Galaxies* 10.1 (1 Feb. 2022), p. 36. ISSN: 2075-4434. DOI: `10.3390/galaxies10010036`. URL: `https://www.mdpi.com/2075-4434/10/1/36`.

[25] T. Accadia et al. “The Seismic Superattenuators of the Virgo Gravitational Waves Interferometer”. In: *Journal of Low Frequency Noise, Vibration and Active Control* 30.1 (Mar. 1, 2011), pp. 63–79. ISSN: 1461-3484. DOI: `10.1260/0263-0923.30.1.63`. URL: `https://doi.org/10.1260/0263-0923.30.1.63`.

[26] Govanni Losurdo. “Inertial Control of the VIRGO Superattenuator”. In: *AIP Conference Proceedings* 523.1 (June 15, 2000), pp. 332–337. ISSN: 0094-243X. DOI: `10.1063/1.1291876`. URL: `https://aip.scitation.org/doi/abs/10.1063/1.1291876`.

[27] R. W. P. Drever et al. “Laser Phase and Frequency Stabilization Using an Optical Resonator”. In: *Applied Physics B* 31.2 (June 1, 1983), pp. 97–105. ISSN: 1432-0649. DOI: `10.1007/BF00702605`. URL: `https://doi.org/10.1007/BF00702605`.

[28] Dana Z. Anderson. “Alignment of Resonant Optical Cavities”. In: *Applied Optics* 23.17 (Sept. 1, 1984), pp. 2944–2949. ISSN: 2155-3165. DOI: `10.1364/AO.23.002944`. URL: `https://opg.optica.org/ao/abstract.cfm?uri=ao-23-17-2944`.

[29] Annalisa Allocca et al. “Interferometer Sensing and Control for the Advanced Virgo Experiment in the O3 Scientific Run”. In: *Galaxies* 8.4 (Dec. 8, 2020), p. 85. ISSN: 2075-4434. DOI: `10.3390/galaxies8040085`. URL: `https://www.mdpi.com/2075-4434/8/4/85`.

[30] F. Acernese et al. “Calibration of Advanced Virgo and Reconstruction of the Detector Strain h(t) during the Observing Run O3”. In: *Classical and Quantum Gravity* 39.4 (Jan. 21, 2022), p. 045006. ISSN: 0264-9381. DOI: `10.1088/1361-6382/ac3c8e`. URL: `https://iopscience.iop.org/article/10.1088/1361-6382/ac3c8e/meta`.

[31] F. Acernese et al. “The Advanced Virgo Longitudinal Control System for the O2 Observing Run”. In: *Astroparticle Physics* 116 (Mar. 2020), p. 102386. ISSN: 09276505. DOI: `10.1016/j.astropartphys.2019.07.005`. URL: `https://linkinghub.elsevier.com/retrieve/pii/S0927650519301835`.

[32] Enzo Nicolas Tapia San Martin. “SC MIMO System Identification”. Apr. 5, 2022. URL: `https://tds.virgo-gw.eu/ql/?c=18014`.

[33] Enzo Nicolas Tapia San Martin. “Advanced Virgo LSC MIMO Scheme for Noise Projections”. July 19, 2021. URL: `https://tds.virgo-gw.eu/ql/?c=17148`.

[34] Dirk Schütte et al. “Experimental Demonstration of Frequency Autolocking an Optical Cavity Using a Time-Varying Kalman Filter”. In: *Physical Review Applied* 5.1 (Jan. 13, 2016), p. 014005. DOI: `10.1103/PhysRevApplied.5.014005`. URL: `https://link.aps.org/doi/10.1103/PhysRevApplied.5.014005`.

[35] Dirk Schütte. “Modern Control Approaches for Next-Generation Interferometric Gravitational Wave Detectors”. doctoralThesis. Hannover : Gottfried Wilhelm Leibniz Universität Hannover, 2016, XX, 159 S. DOI: `10.15488/8857`. URL: `https://www.repo.uni-hannover.de/handle/123456789/8910`.

[36] G. Vajente et al. “Machine-Learning Nonstationary Noise out of Gravitational-Wave Detectors”. In: *Physical Review D* 101.4 (Feb. 18, 2020), p. 042003. DOI: `10.1103/PhysRevD.101.042003`. URL: `https://link.aps.org/doi/10.1103/PhysRevD.101.042003`.

[37] H. Nyquist. “Regeneration Theory”. In: *Bell System Technical Journal* 11.1 (Jan. 1932), pp. 126–147. ISSN: 00058580. DOI: `10.1002/j.1538-7305.1932.tb02344.x`. URL: `https://ieeexplore.ieee.org/document/6773211`.

[38] Richard C. Dorf and Robert H. Bishop. *Modern Control Systems*. Thirteenth edition, global edition. Harlow, England London New York Boston San Francisco Toronto Sydney Dubai Singapore Hong Kong Tokyo Seoul Taipei New Delhi Cape Town São Paulo Mexico City Madrid Amsterdam Munich Paris Milan: Pearson, 2017. 1025 pp. ISBN: 978-0-13-440762-3 978-1-292-15297-4.

[39] A. Rocchi et al. “Thermal Effects and Their Compensation in Advanced Virgo”. In: *Journal of Physics: Conference Series* 363 (June 2012), p. 012016. ISSN: 1742-6596. DOI: `10.1088/1742-6596/363/1/012016`. URL: `https://doi.org/10.1088/1742-6596/363/1/012016`.

[40] L. Aiello et al. “Thermal Compensation System in Advanced and Third Generation Gravitational Wave Interferometric Detectors”. In: *Journal of Physics: Conference Series* 1226.1 (May 2019), p. 012019. ISSN: 1742-6596. DOI: `10.1088/1742-6596/1226/1/012019`. URL: `https://doi.org/10.1088/1742-6596/1226/1/012019`.

[41] B. Canuel et al. “Sub-Nanoradiant Beam Pointing Monitoring and Stabilization System for Controlling Input Beam Jitter in Gravitational Wave Interferometers”. In: *Applied Optics* 53.13 (May 1, 2014), pp. 2906–2916. ISSN: 2155-3165. DOI: `10.1364/AO.53.002906`. URL: `https://opg.optica.org/ao/abstract.cfm?uri=ao-53-13-2906`.

[42] F. Acernese et al. “The Variable Finesse Locking Technique”. In: *Classical and Quantum Gravity* 23.8 (Mar. 2006), S85–S89. DOI: `10.1088/0264-9381/23/8/s12`. URL: `https://doi.org/10.1088/0264-9381/23/8/s12`.

[43] Bersanetti Diego. “Development of a New Lock Acquisition Strategy for the Arm Cavities of Advanced Virgo”. PhD thesis. 2016. URL: `https://tds.virgo-gw.eu/ql/?c=13950`.

[44] Julia Casanueva Diaz and N. Leroy. *Auxiliary Laser System: Study of the Lock Acquisition Strategy*. Technical report. Virgo Collaboration, Apr. 1, 2019. URL: `https://tds.virgo-gw.eu/ql/?c=14154`.

[45] Denis V. Martynov. "Lock Acquisition and Sensitivity Analysis of Advanced LIGO Interferometers". PhD thesis. 2015. URL: https://resolver.caltech.edu/CaltechTHESIS:05282015-142013480.

[46] D. Bersanetti et al. "New Algorithm for the Guided Lock Technique for a High-Finesse Optical Cavity". In: *Astroparticle Physics* 117 (Jan. 1, 2020), p. 102405. ISSN: 0927-6505. DOI: 10.1016/j.astropartphys.2019.102405. URL: https://www.sciencedirect.com/science/article/pii/S0927650519302087.

[47] F. Acernese et al. "Automatic Alignment for the First Science Run of the Virgo Interferometer". In: *Astroparticle Physics* 33.3 (Apr. 1, 2010), pp. 131–139. ISSN: 0927-6505. DOI: 10.1016/j.astropartphys.2010.01.010. URL: https://www.sciencedirect.com/science/article/pii/S0927650510000290.

[48] Charlotte Bond et al. "Interferometer Techniques for Gravitational-Wave Detection". In: *Living Reviews in Relativity* 19.1 (Feb. 17, 2017), p. 3. ISSN: 1433-8351. DOI: 10.1007/s41114-016-0002-8. URL: https://doi.org/10.1007/s41114-016-0002-8.

[49] Kiwamu Izumi et al. "Multicolor Cavity Metrology". In: *JOSA A* 29.10 (Oct. 1, 2012), pp. 2092–2103. ISSN: 1520-8532. DOI: 10.1364/JOSAA.29.002092. URL: https://opg.optica.org/josaa/abstract.cfm?uri=josaa-29-10-2092.

[50] A. Staley et al. "Achieving Resonance in the Advanced LIGO Gravitational-Wave Interferometer". In: *Classical and Quantum Gravity* 31.24 (Nov. 2014), p. 245010. ISSN: 0264-9381. DOI: 10.1088/0264-9381/31/24/245010. URL: https://doi.org/10.1088/0264-9381/31/24/245010.

[51] Camilla De Rossi et al. "Development of a Frequency Tunable Green Laser Source for Advanced Virgo+ Gravitational Waves Detector". In: *Galaxies* 8.4 (4 Dec. 2020), p. 87. ISSN: 2075-4434. DOI: 10.3390/galaxies8040087. URL: https://www.mdpi.com/2075-4434/8/4/87.

[52] I. Flugge-Lotz. *Discontinuous Automatic Control*. Princeton Legacy Library. Princeton University Press, 2016. ISBN: 978-0-691-65325-9. URL: https://books.google.it/books?id=yG1wjwEACAAJ.

[53] Diego Bersanetti et al. "Simulations for the Locking and Alignment Strategy of the DRMI Configuration of the Advanced Virgo Plus Detector". In: *Galaxies* 10.6 (6 Dec. 2022), p. 115. ISSN: 2075-4434. DOI: 10.3390/galaxies10060115. URL: https://www.mdpi.com/2075-4434/10/6/115.

[54] Euan Morrison et al. "Automatic Alignment of Optical Interferometers". In: *Applied Optics* 33.22 (Aug. 1, 1994), p. 5041. ISSN: 0003-6935, 1539-4522. DOI: 10.1364/AO.33.005041. URL: https://www.osapublishing.org/abstract.cfm?URI=ao-33-22-5041.

[55] Mattia Boldrini et al. *Simulation of the Angular Sensing for the Central Interferometer in Advanced Virgo+*. Oct. 3, 2021. URL: https://tds.virgo-gw.eu/ql/?c=16597.

[56] Julia Casanueva Diaz and Mattia Boldrini. *ISC Shift: CITF Lock Robustness*. Logbook Entry. Mar. 26, 2021. URL: https://logbook.virgo-gw.eu/virgo/?r=51228.

[57] H. Yamamoto. *E2E (End-to-End) Simulation Software*. URL: https://labcit.ligo.caltech.edu/~e2e/.

[58] Paolo Ruggi. *Logbook Entry Green Carm Noise*. Logbook Entry. Mar. 1, 2021. URL: https://logbook.virgo-gw.eu/virgo/?r=50931.

[59] Michele Valentini. "ISC Arm Lock Status and Plans". Apr. 20, 2021. URL: https://tds.virgo-gw.eu/ql/?c=16641.

[60] Maddalena Mantovani. "ISC Status Presentation". July 13, 2021. URL: https://tds.virgo-gw.eu/ql/?c=17119.

[61] Maddalena Mantovani and Marco Vardaro. *Tests @ CARM Null - CARM and PRCL Set*. Mar. 4, 2022. URL: https://logbook.virgo-gw.eu/virgo/?r=55077.

[62] Mattia Boldrini, Diego Bersanetti, and Paolo Ruggi. *ISC Shift: CARM Hand-off to IR Rf Signals, CARM Offset Zero*. Logbook Entry. July 15, 2021. URL: https://logbook.virgo-gw.eu/virgo/?r=52549.

[63] Diego Bersanetti, Paolo Ruggi, and Marco Vardaro. *9 Hours and 45 Min of Lock: SRCL Longitudinal Offset Scan, SRCL, and DARM Boost, 1f Automation Test*. Logbook Entry. Jan. 14, 2022. URL: https://logbook.virgo-gw.eu/virgo/?r=54476.

[64] Daniel D. Brown et al. "Pykat: Python Package for Modelling Precision Optical Interferometers". In: *SoftwareX* 12 (July 1, 2020), p. 100613. ISSN: 2352-7110. DOI: 10.1016/j.softx.2020.100613. URL: https://www.sciencedirect.com/science/article/pii/S2352711020303265.

[65] The Virgo collaboration. *Common Virgo File for Finesse*. URL: https://git.ligo.org/virgo/isc/finesse/common_virgo_file/-/tree/master/finesse2.

[66] L. Pinard and J. Degallaix. *Signal Recycling Mirror Substrate to Be Selected for the Coating*. Dec. 1, 2014. URL: https://tds.virgo-gw.eu/ql/?c=10648.

[67] L. Pinard and J. Degallaix. *Power Recycling Mirrors Substrates to Be Selected for the Coating*. Dec. 1, 2014. URL: https://tds.virgo-gw.eu/ql/?c=10646.

[68] Michele Valentini et al. *Update of the LSC Accuracy Requirements for AdV +*. Technical report. Mar. 29, 2021. URL: https://tds.virgo-gw.eu/ql/?c=15030.

[69] Gabriele Vajente. *Advanced Virgo Length Sensing and Control Steady State Design*. Dec. 20, 11. URL: https://tds.virgo-gw.eu/ql/?c=8797.

[70] S. Goßler et al. "Damping and Tuning of the Fibre Violin Modes in Monolithic Silica Suspensions". In: *Classical and Quantum Gravity* 21.5 (Feb. 2004), S923–S933. ISSN: 0264-9381. DOI: 10.1088/0264-9381/21/5/082. URL: https://doi.org/10.1088/0264-9381/21/5/082.

[71] Julia Casanueva Diaz. *Error Signals Calibration*. Logbook Entry. Sept. 30, 2019. URL: https://logbook.virgo-gw.eu/virgo/?r=47052.

[72] E. Calloni and Gabriele Vajente. *Conceptual Design of the Second Stage of Frequency Stabilization for Advanced Virgo*. VIR-0013C-12. May 9, 2012. URL: https://tds.virgo-gw.eu/ql/?c=8815.

[73] R. Gouaty and DET team. "DET Plans for AdV+". Apr. 17, 2019. URL: https://tds.virgo-gw.eu/ql/?c=14264.

[74] Mattia Boldrini et al. *Optomechanical Response of DARM in Presence of Signal Recycling and Radiation Pressure*. Technical report. Feb. 13, 2020. URL: https://tds.virgo-gw.eu/ql/?c=15329.

[75] R. Maggiore and ISC team. "Longitudinal Optical Spring in AdV+ - Talk for the Joint IS / Comm. / DetChar-Tuesday-I Session at the March 2022 LVK Meeting". Mar. 15, 2022. URL: `https://tds.virgo-gw.eu/ql/?c=17928`.

[76] J. R. Smith et al. "Linear Projection of Technical Noise for Interferometric Gravitational-Wave Detectors". In: *Classical and Quantum Gravity* 23.2 (Dec. 2005), pp. 527–537. ISSN: 0264-9381. DOI: `10.1088/0264-9381/23/2/016`. URL: `https://doi.org/10.1088/0264-9381/23/2/016`.

[77] Enzo Nicolas Tapia San Martin. "LSC MIMO System Identification". Apr. 5, 2022. URL: `https://tds.virgo-gw.eu/ql/?c=18014`.

[78] Gabriele Vajente. "Analysis of Sensitivity and Noise Sources for the Virgo Gravitational Wave Interferometer". Scuola Normale Superiore di Pisa, 2008. URL: `https://tds.virgo-gw.eu/ql/?c=7469`.

[79] P. Amico et al. "Thermal Noise Limit in the Virgo Mirror Suspension". In: *Nuclear Instruments and Methods in Physics Research Section A: Accelerators, Spectrometers, Detectors and Associated Equipment.* 8th Pisa Meeting on Advanced Detectors 461.1 (Apr. 1, 2001), pp. 297–299. ISSN: 0168-9002. DOI: `10.1016/S0168-9002(00)01256-0`. URL: `https://www.sciencedirect.com/science/article/pii/S0168900200012560`.

[80] Eric Black. *LIGO-T980045-x0: Notes on the Pound-Drever-Hall Technique.* Apr. 16, 1998. URL: `https://dcc.ligo.org/cgi-bin/DocDB/ShowDocument?.submit=Identifier&docid=T980045&version=`.

[81] R. Gouaty. "Expected DC Powers on the Control Photodiodes for O4". June 17, 2020. URL: `https://tds.virgo-gw.eu/ql/?c=15467`.

[82] Bas Swinkels et al. *Longitudinal Noise Subtraction: The Alpha-, Beta- and Gamma-Technique.* June 9, 2008. URL: `https://tds.virgo-gw.eu/ql/?c=2055`.

[83] F. Acernese et al. "Performances of the Virgo Interferometer Longitudinal Control System". In: *Astroparticle Physics* 33.2 (Mar. 1, 2010), pp. 75–80. ISSN: 0927-6505. DOI: `10.1016/j.astropartphys.2009.11.006`. URL: `https://www.sciencedirect.com/science/article/pii/S0927650509001765`.

[84] Annalisa Allocca, Antonino Chiummo, and Maddalena Mantovani. *Locking Strategy for the Advanced Virgo Central Interferometer.* 2016. URL: `https://tds.virgo-gw.eu/ql/?c=11495`.

[85] Michele Valentini et al. *Error Signals for the Longitudinal Controls in Dual Recycled Advanced Virgo Interferometer - Steady State.* May 11, 2020. URL: `https://tds.virgo-gw.eu/ql/?c=15570`.

[86] Michele Valentini. "Alternative LSC Sensing and SNR". June 23, 2020. URL: `https://tds.virgo-gw.eu/ql/?c=15690`.

[87] Julia Casanueva Diaz et al. *Requirements on the Relative Amplitude Modulation Form the ISC Point of View.* Technical report. Apr. 23, 2020. URL: `https://tds.virgo-gw.eu/ql/?c=15504`.

[88] M. Gosselin et al. *Technical Noise : Relative Amplitude Modulation.* Technical report. Feb. 10, 2022. URL: `https://tds.virgo-gw.eu/ql/?c=17818`.

[89] Enzo Nicolas Tapia San Martin, Diego Bersanetti, and Maddalena Mantovani. "LSC Sensing Noise Projections for O4 V2". Oct. 29, 2021. URL: `https://tds.virgo-gw.eu/ql/?c=17369`.

[90] Maddalena Mantovani. *Frequency Noise Injections Results, Logbook Entry*. Logbook Entry. July 27, 2021. URL: https://logbook.virgo-gw.eu/virgo/?r=52673.

[91] Maddalena Mantovani. *Analysis of MICH Noise Injections*. Logbook Entry. Aug. 2, 2021. URL: https://logbook.virgo-gw.eu/virgo/?r=52728.

[92] Paolo Ruggi. *Further Analysis of Error Signals for SSFS*. Logbook Entry. Aug. 10, 2021. URL: https://logbook.virgo-gw.eu/virgo/?r=52834.

[93] M Salle, R. Maggiore, and Andreas Freise. "Effects of Shifting the PRM". Apr. 20, 2022. URL: https://tds.virgo-gw.eu/ql/?c=18094.

[94] R. Maggiore and Andreas Freise. "Investigation of the Tuning of the Compensation Plates Focal Length - Follow-Up". June 7, 2022. URL: https://tds.virgo-gw.eu/ql/?c=18246.

[95] Daniel David Brown and Andreas Freise. *Finesse*. May 19, 2014. DOI: 10.5281/zenodo.821364. URL: https://zenodo.org/record/821364.

[96] R. Maggiore et al. "Studying DARM Optomechanical Plant with Finesse When Adding Offsets to the SRM". Jan. 17, 2022. URL: https://tds.virgo-gw.eu/?content=3&r=19969.

[97] Priyanka Giri et al. "Effects of Cold Aberrations on the Longitudinal Error Signals and Its Compensation". In: *Proceedings of The European Physical Society Conference on High Energy Physics — PoS(EPS-HEP2021)*. The European Physical Society Conference on High Energy Physics. Vol. 398. SISSA Medialab, May 12, 2022, p. 069. DOI: 10.22323/1.398.0069. URL: https://pos.sissa.it/398/069.

[98] Michele Valentini et al. *Effects of CITF Misalignments on the Longitudinal Error Signals during the CARM Offset Phase of AdV+*. VIR-0446B-20. May 11, 2020. URL: https://tds.virgo-gw.eu/ql/?c=15571.

[99] Michal Was. *Testing Mich Offset*. Logbook Entry. Nov. 30, 2018. URL: https://logbook.virgo-gw.eu/virgo/?r=43823.